

**Response of Building Structure and its Components to Blast
Loads**

by

Danesh Nourzadeh

A thesis submitted to the Faculty of Graduate and Postdoctoral Affairs in
partial fulfillment of the requirements for the degree of

Doctor of Philosophy
in
Civil Engineering

Carleton University
Ottawa, Ontario

© 2017
Danesh Nourzadeh

Abstract

In the present work, both the local response of the components of a building structure and the global response of the structure itself to blast loading are studied. The local response of the columns on the front face of a building, which experience high reflected pressures, is of utmost importance in the analysis and design of structures subjected to blast and is the subject of the first section of this study. The beams on the side faces and roof of the buildings experience loads produced by a travelling blast wave, which makes their response analysis somewhat complex. Analysis of such response is the second component of this study.

For the two types of members mentioned above, the impact of simplifications and assumptions inherent in the current methodologies for calculating blast loading and for the determination of their dynamic response is examined. The response obtained from these methodologies is compared with that obtained from a refined analysis that uses a more accurate representation of the blast loading as well as of the members. The objective is to find whether there are any inaccuracies in the current practice, and to suggest modifications, as well as new tools to improve the reliability of the response analysis, while maintaining the efficiency and simplicity of the current methodologies.

The final part of the study is related to the analysis of the global response of the structures to blast loading. Different aspects of the global response of buildings to blast loads are analysed in a case study of a 10-story reinforced concrete building. The impact of different assumptions in application of the blast loads to the building and loading

area of the frames are studied. Also, the global response of building structures to blast loading are compared to the individual member-by-member analysis for blast loading. In addition, comparison is made between the response of the building to blast and to seismic forces.

The study shows that the number of degrees of freedom in the analytical model of the columns and second-order deflections ($P-\delta$) both have important effect on the calculated response to blast load. On the other hand, shear deformations have only a minor effect on the response. Also, it is shown that the analytical response of columns to blast loads, when they are modeled individually can be different from when they are modeled as part of the lateral load resisting system of the building.

It is observed that the simplified methodologies used for the analysis of roof and side beams spanning in a direction perpendicular to the shockfront lead to large overestimation of the response. For a more reliable estimate of the response, analysis should be carried out using multi-degree-of-freedom models of such elements and the blast loading imposed by a travelling wave. A computer code is developed to facilitate such analysis. In the final part of the thesis, it is shown that a global response analysis of the buildings can be important even if progressive collapse does not occur. It is also shown that the lateral drifts in the buildings produced by blast loads can be even more significant than the drifts caused by design level earthquake. Also, several recommendations for accurate and efficient modeling of the global response are presented.

Acknowledgement

First, I would like to express my utmost gratitude to my supervisors Professor Jagmohan Humar and Professor Abass Braimah for their continuous support of my research and study, in addition to setting the best examples of commitment to excellence, hard work, knowledge and accomplishment. During my time in Carleton University, they inspired and pushed me constantly to become a better researcher and engineer.

My sincere appreciations also go to staff, faculty and fellow researchers in Department of Civil and Environmental Engineering in Carleton University. The experimental part of the studies would have not been possible without the help of the staff of Canadian Explosives Research Laboratory (CERL), Natural Resources Canada, especially Mr. Rick Guilbeault.

Finally, I thank my lovely family: my wife Sepideh, my parents and my siblings, from the bottom of my heart for their support and unconditional love through my study and my life in general.

Table of Contents

Acknowledgement	iv
Table of Contents	v
List of Tables	x
List of Figures	xiii
Notations	xx
Chapter 1. Introduction	1
1.1. Motivation and Objective	1
1.2. Background	3
1.2.1. Blast Waves	4
1.2.2. Interaction of Blast Waves and Structure	8
1.2.3. Local Response of Structural Components to Blast Load	10
1.2.4. Global Response of Structures to Blast Load	15
1.3. Scope of Present Research	17
Chapter 2. Response of Columns to Blast Loading	20
2.1. Introduction	20
2.2. Literature Review	23
2.3. Cases Studied	30
2.3.1. Material Models	33
2.3.1.1. Unconfined concrete	33

2.3.1.2. Confined concrete.....	34
2.3.1.3. Reinforcing steel model	38
2.3.2. Blast Loading.....	39
2.4. Analytical Models.....	40
2.4.1. Traditional single degree of freedom (SDOF) analysis.....	40
2.4.2. More precise multi-degree of freedom (MDOF) analysis.....	46
2.5. Results of Numerical Analyses and Discussions.....	47
2.5.1. Effect of shear deformation.....	47
2.5.2. Effects of number of degrees of freedom	53
2.5.3. Effects of axial load and P-delta.....	58
2.5.4. Response of multi-story columns	63
2.5.4.1. Effects of loading patterns.....	66
2.5.4.2. Comparison with response of single column.....	71
2.6. Verification of Numerical Model.....	76
2.6.1. Material models	77
2.6.2. Analytical model.....	80
2.6.3. Results.....	81
2.7. Summary and Conclusion	84
Chapter 3. Blast Induced Roof Loads in Building Structures.....	87
3.1. Introduction	87

3.2. Study on the Validity of Current Methodologies.....	95
3.2.1. Structure and Blast Load Description	96
3.2.2. Analysis for Equivalent Uniform Loading.....	100
3.2.2.1. Calculation of equivalent uniform loads.....	100
3.2.2.2. SDOF analysis of the roof beams for equivalent uniform loads	105
3.2.2.3. MDOF analysis of the roof beams for equivalent uniform loads	112
3.2.3 Analysis for the Traveling Blast Wave Loading	119
3.2.4. Results and Discussion	129
3.2.4.1. Accuracy of equivalent SDOF model.....	129
3.2.4.2. Accuracy of equivalent uniform loads	135
3.3. Experimental Study.....	144
3.3.1. Tests Setup.....	145
3.3.2. Blast Scenarios	151
3.3.3. Numerical Simulation of the Experiments	153
3.3.4. Discussion and Conclusion.....	158
3.4. Computer Code for Nonlinear Dynamic Analysis.....	160
3.4.1. General flow of the code	161
3.4.2. Calculation of initial parameters.....	163
3.4.3. Generation of loading function.....	163
3.4.4. Dynamic Analysis	164

3.4.4.1. Dynamic solver.....	165
3.4.4.2. Nonlinear beam element.....	166
3.4.5. Summary of the assumptions	170
3.4.6. Validation and verification.....	170
3.5. Summary and Conclusion	173
Chapter 4. Global Response of Buildings to Blast Loading	175
4.1. Introduction	175
4.2. Case Study of Global Response of a Building to Blast.....	176
4.2.1. Geometric models.....	177
4.2.2. Material Models.....	180
4.2.2.1. Unconfined Concrete.....	180
4.2.2.2. Confined Concrete	181
4.2.2.3. Reinforcing Steel	185
4.2.3. Structural Members Generation.....	185
4.2.5. Blast Loading.....	189
4.2.6. General Model Preparations and Modifications	197
4.2.7. Static Pushover Analysis	198
4.2.8. Dynamic Analysis and Results.....	200
4.2.8.1. 2D and 3D Modelling Techniques.....	201
4.2.8.2. Blast Load Patterns	203

4.2.8.3. Cladding and Transmitted Load Effects	208
4.2.8.4. Comparison of the response of an isolated column to that of the same column as a part of the global model	209
4.2.8.5. Comparison with the deflections produced under earthquake loads	223
4.3. Summary and Conclusions	233
Chapter 5. Summary and conclusions	236
5.1 Introduction	236
5.2. Summary and conclusion on response of columns to blast loading.....	238
5.3. Summary and conclusion on response of roof beams to blast loading.....	242
5.4. Summary and conclusion on global response of buildings to blast loading.....	245
5.5. Recommendations for future research.....	249
5.5.1. General Recommendations	249
5.4.2. Further Research on Column Response to Blast Loading	250
5.4.3. Further Research on Roof Beam Response to Blast Loading.....	251
5.4.4. Further Research on Global Response of Buildings to Blast Loading	251
References	253

List of Tables

Table 2.1. Selected blast scenarios and the load properties of each case.....	39
Table 2.2. Mid-height displacement and bending moment in MDOF model of 400×400 columns with and without shear deformation	50
Table 2.3. End reactions in MDOF model of 400×400 columns with and without shear deformation	50
Table 2.4. Mid-height displacement and bending moment in MDOF model of 500×500 columns with and without shear deformation	51
Table 2.5. End reactions in MDOF model of 500×500 columns with and without shear deformation	51
Table 2.6. Maximum response of 400×400-mm columns in blast scenarios without P-delta effects	59
Table 2.7. Maximum response of 400×400-mm columns in blast scenarios with P-delta effects.....	59
Table 2.8. Maximum response of 500×500 columns in blast scenarios without P-delta effects.....	60
Table 2.9. Maximum deflection (mm) of continuous columns under different load patterns.....	67
Table 2.10. Comparison of response of first story columns in single and continuous models.....	72
Table 2.11. Comparison of response of second story columns in single and continuous models.....	72

Table 2.12. Blast load scenarios applied to the columns based on experiments	80
Table 2.13. Comparison of numerical and experimental results	82
Table 3.1. Drag coefficient for roof beams (DoD 2008)	89
Table 3.2. Definition of selected blast scenarios (calculated for front point of the roof)	97
Table 3.3. Structural properties of steel beams of the roof.....	98
Table 3.4. Array for the selected analysis cases.....	99
Table 3.5. Equivalent uniform load characteristics based on ASCE 2010 and UFC 3-340-02 methodologies	101
Table 3.6. Equivalent uniform load characteristics based on TM 5-855 methodology .	102
Table 3.7. SDOF model properties for the different analytical cases	107
Table 3.8. Results of SDOF analysis for equivalent uniform loads.....	108
Table 3.9. Results of MDOF analysis for equivalent uniform loads	115
Table 3.10. Results of MDOF analysis for exact moving blast loads	125
Table 3.11. Differences beams response in exact and equivalent uniform blast loads (MDOF models).....	139
Table 3.12. Characteristics of the analytical model for numerical simulation of the experiments	154
Table 3.13. Equivalent uniform loading for the experimental cases based on UFC/ASCE method.....	154
Table 3.14. Equivalent uniform loading for the experimental cases based on TM 5-855 method.....	154

Table 3.15. Comparison of the maximum mid-span deflections obtained from numerical analyses and experiments	156
Table 3.16. Blast wave parameters for hemispherical 500 kg TNT at 20 m standoff	172
Table 4.1. Definition of section properties for members.....	186
Table 4.2. Peak blast loads on joints in front, side and back faces of the buildings	193
Table 4.3. Peak blast loads on joints in the roof	196
Table 4.4. Simplified progressive blast pressures, with incident angles	204
Table 4.5. Simplified progressive blast pressures, without incident angles	205
Table 4.6. Planar shock front loading pressures	205
Table 4.7. Blast load properties applied on first story column	210
Table 4.8. Comparison of lateral deflections at individual column mid-heights, and when they are part of the global model with loads applied at both story and mid-height levels	214
Table 4.9. Maximum chord displacements of 1 st story columns in global model compared to maximum mid-height column deflections in individual model	216
Table 4.10. Maximum displacements of 1 st story columns in global models with 4 and 16 sub-elements	217
Table 4.11. Blast load properties applied on first story column in 500 kg TNT at 30 m standoff.....	219
Table 4.12. Simplified progressive blast loads (considering incident angle for each story) applied to structure from 1000 kg at 30 m scenario	231

List of Figures

Figure 1.1. Free-field pressure time-history.....	5
Figure 1.2. Different situations for interaction of blast waves and structures	9
Figure 1.3. Blast pressure time-history for members on the front-face of buildings	12
Figure 1.4. Different types of beam members in the roof of a building	14
Figure 1.5. Global excitation of building structure in blast loads.....	16
Figure 2.1. SDOF representation of individual members in blast using different stiffness states.....	21
Figure 2.2. Schematic detailing of the columns	32
Figure 2.3. Details of transverse reinforcement in columns	32
Figure 2.4. Hognestad’s model for unconfined concrete (after Hognestad, 1951)	34
Figure 2.5. Chang and Mander model definition for concrete (after Chang and Mander, 1994)	35
(figure 2.6. Effective confined core in members based on Chang and Mander (1994)	36
Figure 2.7. Definition of SDOF model and the resistance function for the studied column	43
Figure 2.8. P-M Interaction curves for (a) 500×500 column, (b) 400×400 column	45
Figure 2.9. Response of the 400x400 column in blast scenario 1 in MDOF model.....	49
Figure 2.10. Comparison of mid-height displacement and bending moment models with and without shear deformations	52
Figure 2.11. Comparison of end reactions for models with and without shear deformations.....	53

Figure 2.12. Maximum response of the 400×400-mm column in blast scenario 1 versus number of DOFs	55
Figure 2.13. Normalized maximum response of the 400×400-mm column under different blast scenarios.....	56
Figure 2.14. Normalized maximum response of the 500×500-mm column in different blast scenarios.....	57
Figure 2.15. Maximum deformations for 400×400 columns with and without P-delta effects.....	61
Figure 2.16. Maximum deformations for 500×500 columns without P-delta effects	62
Figure 2.17. Geometrical model of 2-story column (a) bottom column is 500×500 mm	64
Figure 2.18. Step-by-step loading of continuous columns.....	66
Figure 2.19. Comparison of maximum deflections in continuous columns with 400×400-mm column in 1 st story	68
Figure 2.20. Comparison of maximum deflections in continuous columns with 500×500 column in 1 st story	69
Figure 2.21. Comparison of response of bottom columns in single and continuous models.....	73
Figure 2.22. Comparison of response of top columns in single and continuous models	74
Figure 2.23. Rectangular column sections used for verification of numerical model	77
Figure 2.24. Comparison of the experimental and numerical results for columns	83
Figure 3.1. Different members in the roof subject to blast loading.....	87
Figure 3.2. Shock wave propagation along the roof span	89

Figure 3.3. Pressure time-history on roof beams in UFC 3-340-02 (DoD 2008).....	91
Figure 3.4. Pressure time-history on roof beams in (Glasstone and Dolan 1977)	91
Figure 3.5. Definition of parameters in blast time-histories, based on (B) ASCE (2010) and (C) TM 5-855 (DOA 1986).....	92
Figure 3.6. Equivalent load coefficient in UFC 3-340-02 and TM-855 documents	93
Figure 3.7. Nominal Static and actual dynamic behavior of G40.21 (ASTM A588) steel material.....	98
Figure 3.8. Blast load time-histories for the equivalent uniform loads derived from different methodologies	103
Figure 3.8. (Contd.) Blast load time-histories for the equivalent uniform loads derived from different methodologies	104
Figure 3.9. Plastic hinge generation and definition of resistance function for the beams	106
Figure 3.10. Blast pressure time-histories generated for the exact analysis.....	121
Figure 3.10 (Cont'd). Blast pressure time-histories generated for the exact analysis...	122
Figure 3.10 (Cont'd). Blast pressure time-histories generated for the exact analysis...	123
Figure 3.11. Difference in maximum response measures between the SDOF and MDOF models subject to uniform blast loads	131
Figure 3.12. Mid-span displacement time-history of SDOF and MDOF models in Case 1	134
Figure 3.13. Mid-span moment time-history of SDOF and MDOF models in Case 1.....	134

Figure 3.14. Mid-span displacement time-history of SDOF and MDOF models in Case 15	134
Figure 3.15. Mid-span moment time-history of SDOF and MDOF models in Case 15...	135
Figure 3.16. Difference in response for MDOF models subject to moving blast loads and uniform loads from UFC 3-340-02	137
Figure 3.17. Difference in response for MDOF models subject to moving blast loads and uniform loads from TM 5-855.....	138
Figure 3.18. Midspan displacement time-history in simplified and exact loads for Case 1	142
Figure 3.19. Midspan moment time-history in simplified and exact loads for Case 1...	142
Figure 3.20. Midspan displacement time-history in simplified and exact loads for Case 15	143
Figure 3.21. Midspan moment time-history in simplified and exact loads for Case 15.	143
Figure 3.22. Plane view of blast table and the experimental setup.....	146
Figure 3.23. Elevation views of blast table and experimental setup	147
Figure 3.24. Experimental setup in the field	148
Figure 3.25. Plan of the measuring instruments in the test.....	149
Figure 3.26. Inside view of the roof and measuring instruments in the tests	150
Figure 3.27. Completed setup for the tests in the field	150
Figure 3.28. Comparison of measured pressures with those obtained from CONWEP	152
Figure 3.28 (Cont'd.) Comparison of measured pressures with those obtained from CONWEP.....	153

Figure 3.29. Results summary for the different cases.....	156
Figure 3.30. Comparison of mid-span deflections for different cases	157
Figure 3.30. (Cont'd.) Comparison of mid-span deflections for different cases	158
Figure 3.31. Snapshot of the input data in the designed computer code GUI	161
Figure 3.32. General flowchart of the written code for analysis of roof beams.....	162
Figure 3.33. Elastic beam with plastic hinges at the end used in the code.....	166
Figure 3.34. Blast pressure time histories for the internal nodes.....	171
Figure 3.35. Comparison of mid-span deflections of 6-m beam obtained from computer code and D2DX.....	173
Figure 4.1. Geometrical model of the building and the blast source.....	178
Figure 4.2. Floor plan of the building being studied	178
Figure 4.3. 2D model of the 10-story buildings	180
Figure 4.4. Details of transverse reinforcement in beams of moderate ductility frames	183
Figure 4.5. Results of the moment-curvature analysis of beam sections	187
Figure 4.6. Results of the moment-curvature analysis of column sections	188
Figure 4.7. Hysteretic and monotonic moment- curvature behavior of sections.....	189
Figure 4.8. The shortest standoff distance for points on the side face.....	191
Figure 4.9. The shortest standoff distance for points on the roof	192
Figure 4.10. Pushover curve for moderate ductility moment resisting frame using different elements	199
Figure 4.11. Top floor displacement in 2D and 3D model.....	202

Figure 4.12. Maximum story drift ratios in 2D and 3D model.....	202
Figure 4.13. Top floor displacement for different types of loading patterns	206
Figure 4.14. Maximum story drift ratios for different types of loading patterns	207
Figure 4.15. Top floor displacement for different types of loading area	208
Figure 4.16. Maximum story drift ratios for different types of loading area	209
Figure 4.17. Response at mid-height in individual columns versus first story displacement in the global model	211
Figure 4.18. Loading areas for a typical frame	212
Figure 4.19. Lateral displacements at mid-heights of individual columns and the first story (columns end) deformations in the global model in which the loads are applied at both column mid-heights and story levels	213
Figure 4.20. Comparison of maximum story drifts under progressive loading with loads applied at story levels or at both story and mid-height levels	214
Figure 4.21. Deformed shape of 1st and 2nd story columns at the time mid-height chord deflections in 1st story columns peak in global response	215
Figure 4.22. Comparison of deformed shape of peak 1 st story columns chord displacements versus deflections in single columns modeled individually	220
Figure 4.23. Deformed shape of 1 st and 2 nd story columns at the time 1 st story deflections peak in global model in 1000 kg TNT at 15 m scenario	222
Figure 4.24. Tributary area of the columns subject to blast loads.....	223
Figure 4.25. Scaled ground motion time-histories for the eastern Canada (Atkinson 2009)	225

Figure 4.26. Scaled ground motion time-histories for the western Canada (Atkinson
2009) 226

Figure 4.27. Maximum story drift ratios obtained from earthquake and blast analyses
..... 231

Notations

A, B	confinement stress factors
A_{cc}	net cross-sectional area of concrete core (without area of steel bars)
A_{ch}	cross-sectional area of core of RC member
A_e	effective confined area
A_g	gross cross-section of RC member
A_{sh}	cross-sectional area of transverse reinforcement
$A_{sh,min}$	minimum cross-sectional area of transverse reinforcement allowed by design code
A_{st}	cross-sectional area of longitudinal reinforcement
A_{sv}	cross-sectional area of transverse reinforcement
A_{sx}, A_{sy}	cross-sectional area of transverse reinforcement in x and y directions
b	exponential decay coefficient in Friedlander equation
b_c	confined width (center to center of transverse rebar) of rectangular RC section
b_{max}	greater dimension in rectangular RC member
b_{min}	smaller dimension in rectangular RC member
b_{sh}	strain-hardening ratio of steel
\mathbf{C}	damping matrix of structure
C_D	drag coefficient
C_E	uniform load equivalent coefficient

d	effective depth of RC member
D	critical point on the roof, if the shockfront is located at this point it creates maximum internal efforts
$d_{b,min}$	smallest diameter of longitudinal rebars used
d_c	confined depth (center to center of transverse rebar) of rectangular RC section
DIF	dynamic increase factor
d_{sv}	diameter of transverse reinforcement
E_c	modulus of elasticity of concrete
EI	bending stiffness of member
EI_{ave}	average bending stiffness of RC member
E_s	modulus of elasticity of steel
E_{sh}	strain-hardening modulus of steel
$f'_c = f'_{c0}$	specified compressive strength of concrete
f'_{cc}	compressive strength of confined concrete
f'_{cd}	dynamic compressive strength of concrete
f'_{cu}	ultimate compressive strength of concrete
f'_{lx}, f'_{ly}	confinement stress in concrete core
f_c	stress in concrete
f_r	modulus of rupture of concrete
\mathbf{F}_i	global force matrix in step i
f_t	tensile strength of concrete

f_u	ultimate stress of steel
f_{ud}	ultimate dynamic ultimate stress of steel
f_y	yield stress of steel
f_{yd}	dynamic yield stress of steel
f_{yh}	yield stress of transverse reinforcement
G_c	shear modulus of concrete
h	height of rectangular RC section
h_c	height of column
I	moment of inertia of member
i^*	elastic beam element node, connected to node i via nonlinear spring
I_{cr}	cracking moment of inertia of RC member
$I_e = I_{eff}$	effective moment of inertia of RC member
I_g	gross moment of inertia of RC member
I_r	reflected impulse
I_{so}	incident impulse
K	stiffness of structure in SDOF model
k	post peak slope in stress-strain relationship of unconfined concrete based on Hognestad's model
\mathbf{K}	stiffness matrix of structure
k_1, k_2	increasing stress and strain factors in confined concrete core
K_e	elastic stiffness of member in SDOF analysis
k_e	effective confined area ratio

K_{ep}	post yield stiffness of member in SDOF analysis
K_L	load factor in SDOF analysis
K_{LM}	load-mass factor in SDOF analysis
K_M	mass factor in SDOF analysis
k_n	factor accounting for the number of longitudinal reinforcing bars in RC columns
K_p	plastic stiffness of member in SDOF analysis
k_p	factor accounting for compression on column or wall
K_R	stiffness factor in SDOF analysis
$k_{s,i}$	stiffness of springs at node i of the member
\mathbf{K}_i^t	tangential stiffness matrix in step i
L	length of member
l_0	length of special region (possible plastic hinge region) in members
L_{wb}	blast wavelength at the back point of the roof
L_{wf}	blast wavelength at the front point of the roof
m	mass of structure in SDOF model
\mathbf{M}	mass matrix of structure
M_a	applied moment on RC section
M_{cr}	cracking moment of RC section
M_i	bending moment at node i
M_{i^*}	bending moment at node i^*
M_{max}	maximum bending moment in dynamic analysis

M_n	negative plastic moment of section
M_p	positive plastic moment of section
$\bar{m}(x)$	mass function per unit length
n	confined concrete factor
N	axial load applied to the column
$p(t)$	blast pressure as function of time
$P(t)$	blast load as function of time
P_{so}^-	peak incident pressure in negative phase of blast
P_0	ambient (atmospheric) pressure
P_r	peak reflected pressure in the positive phase
P_s	peak stagnation blast pressure
P_{so}	peak incident pressure in positive phase of blast
p_{sob}	peak incident pressure at the back point of roof
p_{sod}	peak incident pressure at point D on the roof
p_{sof}	peak incident pressure at the front point of roof
q	ratio of confinement stresses in each direction
\mathbf{q}	vector of total rotations at the end nodes of the element
q_0	peak dynamic pressure
q_{ob}	peak dynamic pressure at back point of the roof
q_{of}	peak dynamic pressure at front point of the roof
R	distance (range) from centre of detonation to point of interest
r	confined concrete factor

$R(u)$	resistance function of the element
R_{max}	maximum resistance of member found from dynamic analysis
R_u	peak resistance of the element
s	spacing of transverse reinforcement
S	elastic section modulus
s'	clear spacing of transverse reinforcement
s_{max}	maximum spacing of transverse reinforcement
t	time
\bar{t}_d^-	duration of negative phase of blast
t_p^+	duration of the positive phase of blast
t_a	time of arrival of blast wave at point of interest
t_b	arrival time of blast wave at back point of the roof
t_c	clearing time of blast wave
t_d	duration of positive phase of blast
t_{db}	duration of positive phase of blast loads at back point of the roof
t_{df}	fictitious duration of positive phase of blast (triangular form)
t_f	arrival time of blast loads at front point of the roof
t_{of}	duration of positive phase of blast at the front point of the roof
t_r	rise time of simplified blast loads
U	shockfront velocity at point of interest
u, \dot{u}, \ddot{u}	displacement, velocity and acceleration, respectively, in dynamic analysis
U_b	shockfront velocity of blast wave at back point of the roof

U_f	shockfront velocity of blast wave at front point of the roof
u_{max}	maximum displacement in dynamic analysis
$u_{max,n}$	maximum displacement in n -th cycle of response
V_i	shear force at node i
V_{i^*}	shear force at node i^*
W	mass of blast charge
w'	clear spacing between adjacent longitudinal rebars
x'	ratio of confinement stresses to dynamic compressive strength
x_n	compressive strain parameter in concrete
x_p	tensile strain parameter in concrete
y_t	distance from the centroidal axis to the extreme fibre in tension
Z	scaled distance of blast to the intended point
Z	plastic section modulus
α_0	mass proportional damping factor
α_1	stiffness proportional damping factor
Γ	vector of stiffness ratio of end springs to bending stiffness of the member
γ_i	ratio of stiffness of springs at node i to bending stiffness of the member
δ	deflection of member
Δ	plastic hinge parameter
$\delta(x)$	displacement produced in the member
δ_{max}	maximum displacement produced in the member
ΔP_i	load increment vector

Δt	time-step used in dynamic analysis
$\Delta \mathbf{u}_i$	incremental displacement vector in step i
Δx	length of sub-elements used in discretization
$\epsilon_0 = \epsilon_{c0}$	concrete strain at peak compressive stress
ϵ_c	strain in concrete
ϵ_{cc}	strain of confined concrete at maximum compressive strength
ϵ_{crk}	ultimate tensile strain of concrete in Chang and Mander's model
ϵ_{sp}	ultimate compressive strain of concrete in Chang and Mander's model
ϵ_t	strain at maximum tensile stress in concrete
ϵ_u	ultimate strain of steel
ϵ_y	yield strain of steel
θ	exponential decay factor in Friedlander equation
κ	bending curvature of section
κ_y	yield curvature of section
μ	displacement ductility ratio
ξ_i	damping ratio in i -th mode of vibration
ρ_x, ρ_y	transverse reinforcement density in x and y directions
$\phi(x)$	displacement shape function
φ_i	total rotations at the end nodes of the element
φ_{i^*}	sum of rotations at the node i^* of the elastic beam
Φ^p	vector of rotations at the plastic hinge at node i
φ^p_i	rotation of the plastic hinge at node i

ψ interpolation parameter

ω_i frequency of i -th mode of vibration

Chapter 1. Introduction

1.1. Motivation and Objective

Blast loading is one of the most harmful and destructive loads that a structure can experience during its design life span. Blast loads could be caused by terrorist attacks, accidental explosions or other explosions intended for excavations or mining. Although the probability of occurrence of this phenomenon during the life span of an ordinary structure is very small, the very severe consequences of this hazard requires designers to consider it in analysis and design of structures that are deemed critical or have a high probability of being exposed to blast loading. Examples of such structures are high-profile government buildings and monuments or structures in proximity to petrochemical facilities. Therefore, it is important to develop analytical methods and procedures that can predict the response of the structures to blast loads with reasonable accuracy.

A majority of the current guidelines and procedures for blast load analysis date back several decades and are based on data from military experimentations on hardened structures. The suggested simplified methodologies in the guidelines do not always provide good and reliable estimates of the response of structural elements and often compromise accuracy for simplification. It is therefore necessary to take an in-depth look into such methodologies to examine their accuracy and reliability. Most of the simplifications suggested in the current guidelines are not necessary today, because of the availability of powerful computational tools that are also available in many design

offices. The application of such tools to obtain more accurate estimates of the response to blast loads can significantly improve the design practice, and lower the cost of blast resistant structures.

Response of building structures to blast loading is very complex in nature and depends on many variables including the magnitude of the loads and characteristics of the structure itself. Blast waves reflect from the surfaces of the structure that are in direct line-of-sight to the charge (front face), and when the blast magnitude is large enough, diffract to the other surfaces of the structure including roof, sides and rear faces. This complex interaction of the blast wave and structure leads to varying effects on the various components of the structure. For instance, the elements on the front face experience reflected pressures, which have higher magnitude in comparison to the incident pressures that the elements on the roof, sides and back faces experience, because of the smaller distance to the charge and the reflection of the wave. Another difference between the members on the front face and other sides of the buildings is that the components on the front face are loaded almost simultaneously and with a uniform level of load along their span from blast waves caused by far-field explosions. On the other hand, the blast wave traverses the span of the components on the sides and roof of the structure and the characteristics of the load changes during this motion. Throughout the propagation and interaction of the blast wave with the structure, if any of the individual members fail or lose their load bearing capacity, the global integrity of the structure could be at risk. This issue is discussed in the literature as probability of progressive collapse of the structure, and there are different methodologies to examine

the possibility of this type of failure. On the other hand, if the failure of the external members of the buildings is prevented, global response of the structure can still be excited, provided the loads are large enough. In this case, the structure is subject to a complex distribution of external dynamic loadings that act on different faces, which can cause the structure to experience excessive deformations and inter-story drifts.

A building structure subjected to blast loading may experience one or more of the type of responses described in the preceding paragraphs. In each case, the behavior of the structure must be examined carefully to determine the performance level achieved by the structure under the given blast scenario. The current codes of practice use various simplifying assumptions to find the local or global response of the structure in any of the scenarios mentioned above. In the present study, the accuracy of these assumptions is examined, in order to make suggestions that could improve the accuracy and reliability of the analysis and design. More specifically, improved methods are developed that could lead to a more accurate estimate of the local and global response to blast loads.

1.2. Background

In this section, background information on propagation of blast loads, and their interaction with the structures is summarized. This information is used throughout other chapters of the thesis. The nature of the blast loads and the characteristics of air blast are first discussed. The possible scenarios of interaction between the blast waves and the structure and the response of the structure under each scenario are discussed next. Also, an overview of the methodologies used in current practice is presented.

1.2.1. Blast Waves

After an explosive material detonates, part of its internal energy is released in a very rapid reaction (detonation reaction), in which the original material converts into extremely hot and high-pressure gases. The expanding gases form a shock front that spreads spherically through the surrounding medium in which the detonation occurred. This effect of the explosion is called shock wave propagation. As the waves expand through the media, their pressure and velocity decrease, while their duration increases. These shock waves impose pressures on the surfaces of the structures that are in their propagation path. The resulting forces are commonly referred to as blast loads (DoD 2008, Smith & Hetherington 1994).

The blast loads are classified into different categories based on the confinement of the blast waves and the boundary conditions that are applied to their propagation.

Explosions can be categorized as confined or unconfined blasts depending on the boundaries of confinement. Confined blasts occur within the boundaries of the barrier structures and do not form part of this study. Unconfined explosions occur in free air or on the surface of the earth. The unconfined explosions are further categorized as air burst (spherical blast) and surface burst (hemispherical blast), based on the height of explosion above the ground (height of burst (HOB)). The only difference between these two cases is that in surface burst, the explosive charge is on the ground or close to it, so the initial blast waves are instantaneously reflected from the ground, and amplified.

As the blast wave propagates, the pressure at points in its path instantaneously increases from the ambient pressure when the shock front arrives at them. The pressure builds up to a maximum value, which is called peak incident (side-on) pressure, and then drops to the ambient pressure or even less than the ambient pressure (negative or under-pressure). The negative pressure phase lasts longer than the positive phase but eventually the pressure returns to the ambient pressure. The variation of the pressure at a typical point on the propagation path is shown in Figure 1.1. In the figure, P_{so} and P_{so}^- are peak positive and negative incident pressures, respectively. t_a is the time of arrival of the blast shock front at the point of interest, t_d and t_d^- are the durations for the positive and negative phases of the blast wave, respectively.

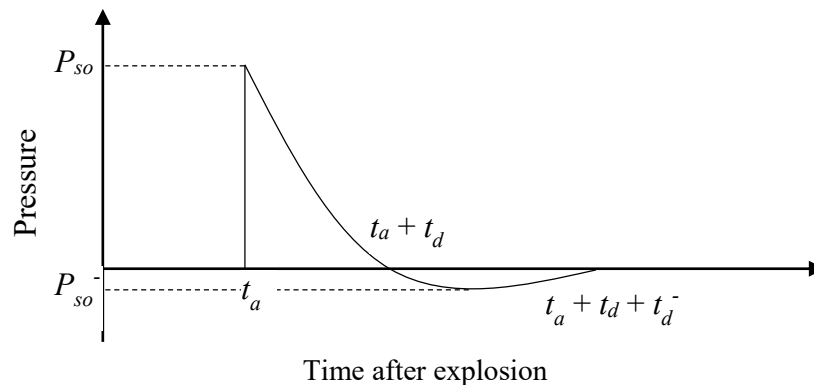


Figure 1.1. Free-field pressure time-history

The parameters shown in Figure 1.1 depend on the characteristics of the blast, including explosive charge mass, distance from the centre of explosion (centre of explosive charge) to the point of interest (standoff distance), and the HOB. The formulations and charts available in the literature for finding the afore-mentioned blast pressure

parameters are expressed in terms of the scaled distance, Z , which is defined in Equation 1.1.

$$Z = \frac{R}{W^{1/3}} \quad (1.1)$$

where, R is the standoff distance and W is the mass of the explosive charge. The latter is generally expressed in terms of the equivalent amount of TNT providing the same released internal energy as the explosive of interest.

As can be observed from Figure 1.1, the blast pressure decay is approximately in the form of an exponential curve. Since the magnitude of the peak negative blast pressure is small compared to peak positive incident pressure, in most of cases, the negative phase of the blast pressure is neglected. The exponential decay of the blast pressure in the positive phase can be represented by the well-known modified Friedlander equation shown in Equation 1.2.

$$P(t) = \begin{cases} P_{so} \left(1 - \frac{t-t_a}{t_d}\right) e^{-b(t-t_a)/t_d}, & t_a \leq t \leq t_d \\ 0, & t > t_d \end{cases} \quad (1.2)$$

where, b is the exponential decay coefficient, which can be calculated from curves or tables given in different references (e.g. DoD 2008) or by a method of trial and error.

Another parameter which is important is the area under the incident pressure time-history, called the impulse. Impulse has also a physical meaning, which is an indicator of the change of energy and momentum due to the blast wave propagation. When the

incident pressure time-history graph is considered, the impulse is the incident impulse (I_{so}) and can be calculated from Equation 1.3.

$$I_{so} = \int_{t_a}^{t_a+t_d} P(t)dt \quad (1.3)$$

In many cases, for simplifying the problem, the time-history of the positive blast pressure is assumed as being triangular. Thus, retaining unchanged the peak positive incident pressure and the incident impulse, a fictitious positive phase duration t_{df} can be calculated from Equation 1.4. It is also possible to maintain the duration and find a fictitious peak pressure, which is usually the case for structures sensitive to duration.

$$t_{df} = \frac{2I_{so}}{P_{so}} \quad (1.4)$$

As the blast wave propagates through air, and the distance from the blast source increases, peak pressure, impulse, and the speed of the shock front decrease, while the duration increases.

The parameters described in the foregoing are related to the propagation of the blast wave in air, before it reaches an obstacle or barrier surface. As soon as the wave reaches the interface with a medium denser than the medium it is propagating in, the wave is reflected. The interaction of the blast wave and the structure is discussed further in the following paragraph.

1.2.2. Interaction of Blast Waves and Structure

When a wave encounters a denser medium in its path, it gets reflected from the interface; and the incident pressure is amplified several times, up to eight times in magnitude, depending on the angle between the direction of the propagation and the normal to the surface (incident angle) and the peak incident pressure (Glasstone and Dolan 1977). The highest incident pressure amplification occurs when the incident angle is zero, so that the shockfront is parallel to the surface of the barrier. It is assumed that the reflected pressure at a point on the external surfaces of the barrier structure or obstacle has the same duration time as that of the incident pressure.

As the blast wave reaches an obstacle in its propagation path, different scenarios can occur depending on the scale of the barrier and magnitude of the blast wave at that point. As shown in Figure 1.2 (a), the first scenario occurs when the structure is smaller, while the blast wave has a significant magnitude so that it can either move the target or separate it from its anchorage and base. In this case, the blast load will move the object since the large reflected pressures on the front combined with smaller incident pressures, equal to the incident pressure, on the side and rear faces leads to a net force in the direction of the wave propagation. In the second scenario, shown in Figure 1.2(b), a stable structure experiences significant load in the direction of propagating wave, which excites response of the entire structure. For the smaller scale blast wave in the third scenario, shown in Figure 1.2(c), depending on the characteristics of the blast wave namely the wavelength, the elements in the structure could be loaded sequentially and

only specific portions of the structure may be loaded. In this case, the front face of the building might be the most vulnerable to blast loading.

The focus of the present study is on the analysis of structural response for cases b and c of Figure 1.2. In case b, the front face of the structure experiences significant reflected pressures. Also, if the HOB is not greater than the height of the structure and the centre of explosion is within the width of the front face, members in the roof of the structure, and those on the side and rear faces experience the incident blast pressures as the wave traverses their spans. If the intensity of the blast loads is large enough, the lateral load resisting system of the structure is excited and the structure may face strong vibrations.

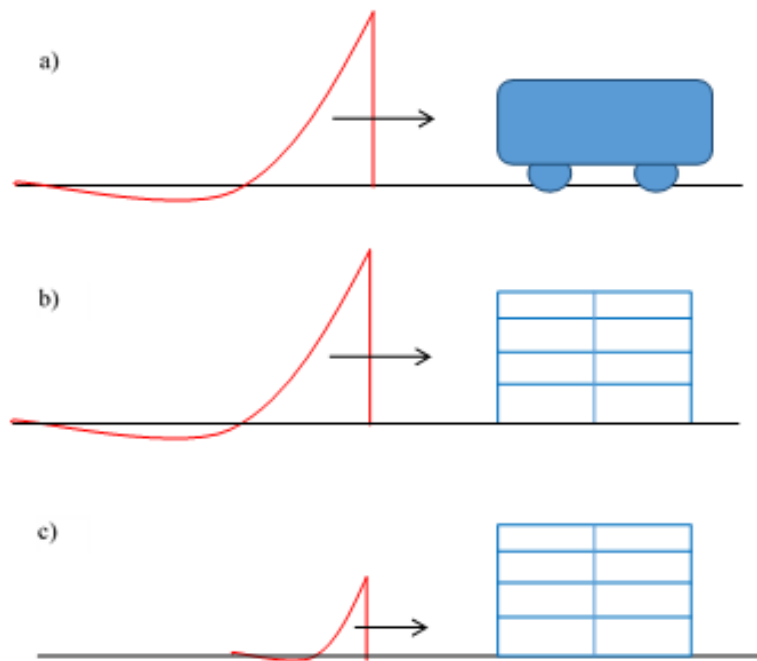


Figure 1.2. Different situations for interaction of blast waves and structures

In case of Figure 1.2(c), small-scale blast cannot induce significant lateral motion of structure, however, the local response of some of the members that experience higher pressures or are exposed to the reflected pressures on the front face of the structure, would be important. The blast pressures can cause local damage in components on the front face of the structure, and such local failure may lead to instability in the structure, which should be prevented.

1.2.3. Local Response of Structural Components to Blast Load

In the literature on blast load effects and protective design, the term local response of members refers to the situations where the members fail as a result of intense effects from mostly near-field blasts. Some examples of this type of failure are: perforation, scabbing, cratering and shattering of exterior walls and façade members. However, in this thesis, the local response of members is used to refer to the behavior of the structural members such as beams and columns when subjected to blast pressures, and not the local instabilities and failures which can occur before the global response of the members.

The local response of the structural members to blast load is classified into two major categories. The first category of response is that of members that are on the front façade of the structure. They are the first to be subjected to the blast shockfront and experience high-magnitude reflected blast pressures. The other category of response is that of members that do not have a direct path to the blast source, and thus experience the blast wave as it reaches them and traverses their spans, applying decaying incident

pressures. In order to analyze the local response of the members during blast, columns on the front face and the beams in the roof of buildings are selected for detailed study in this work.

The columns on the front-face of the buildings experience reflected pressures with a comparatively short duration. For columns of usual span lengths, the time of arrival of the blast wave at different points along the height of the column and the magnitudes of the blast pressure are quite similar. Therefore, it can be assumed with reasonable accuracy that these members are loaded with a uniformly distributed load having the time-history of the reflected pressure multiplied by the tributary width supported by the column. The time history of the blast load is similar to that shown in Figure 1.1 but with peak reflected pressure.

The members on the front face experience reflected pressures until the blast wave reaches an edge in the structure. As the blast wave wraps around the edges and diffracts to the sides and roof of the building, the magnitude of the pressure on the front face drops from the reflected pressure to the stagnation pressure value (incident pressure plus drag pressure). This is due to generation of rarefaction waves from the points experiencing reflected pressures in the front face to the points experiencing incident pressures, to balance the high pressure differences. The time it takes for the reflected blast pressure to decay to the stagnation pressure is called clearing time (Figure 1.3).

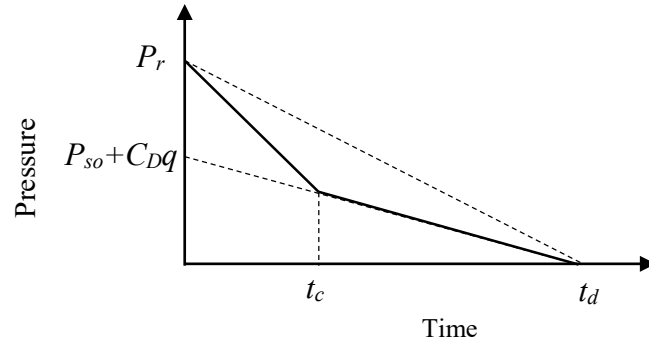


Figure 1.3. Blast pressure time-history for members on the front-face of buildings

The stagnation pressure P_s includes two terms, one being the incident pressure and the other, the dynamic pressure caused by the motion of the hot gases behind the shock front. Pressure P_s can be obtained from Equation 1.5, as shown in Figure 1.3.

$$P_s = P_{s0} + C_d q_0 \quad (1.5)$$

In Equation 1.5, q_0 is the dynamic pressure, while C_D is the drag coefficient that depends on the geometry of the surface, and the magnitude of the pressure of the gases in motion over the surface; it can be assumed as being equal to 1.0 for the front face members (DoD, 2008). The dynamic pressure q_0 can be derived from the empirical expression given in Equation 1.6 (Newmark 1956)

$$q_0 = \frac{2.5P_{s0}^2}{P_{s0} + 7P_0} \quad (1.6)$$

where $P_0 = 101.3$ kPa is the ambient pressure.

Analysis of the response of columns on the front-face of building involves the application of the pressure time-histories discussed in the foregoing to the columns and finding the dynamic response of the members by single or multi-degree of freedom

analysis. However, several factors affect the response of these members and must be considered. They include the effect of gravity loads on the columns, shear deformations, and P-delta effects. Assumptions made in modeling the columns include the number of degrees-of-freedom and material models. Only some of these effects are considered in the current design guidelines, thus the response predictions may not be accurate. In the present study, the methodologies used in the current design practice are studied and the effects of the important factors on the response of the single columns on the front-face of the building are analyzed.

Loading of the roof beams in the buildings is more complex when compared to that of a column on the front face. The loading depends on the direction of the blast wave motion. As highlighted in Figure 1.4, the members that are aligned parallel to the shock front, experience similar pressure time-histories at all points along their span, since there is no significant change in the distance between these points and the blast source for typical tributary widths and span lengths. On the other hand, beams that are oriented in a direction perpendicular to the shock front, may experience significantly different blast loads at different points along their span.

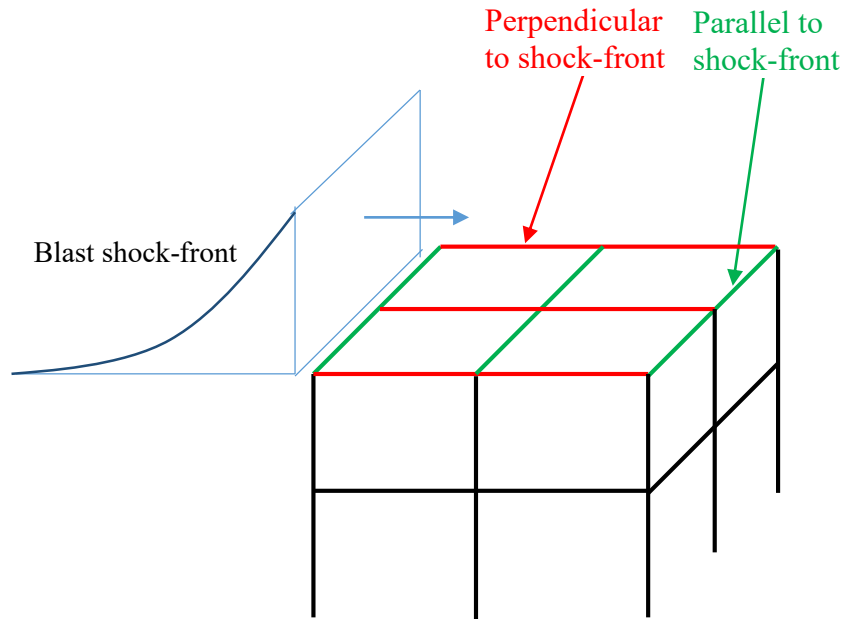


Figure 1.4. Different types of beam members in the roof of a building

The time-history of the blast pressure that any point on the roof or on a side face of a building experiences is similar to that shown in Figure 1.1. The magnitude of the peak pressure is, however, different from the incident pressure, because of the drag pressure that is imposed on the surface. Equation 1.5 can again be used to calculate the pressure at any point on the surface, where the drag coefficient C_D is a function of the dynamic pressures and the geometry of the roof or side surfaces.

Because of the differences between the pressure time-histories at different points along the roof, the response analysis of the beam perpendicular to the shockfront is done by a step-by-step integration of the equation of motion. However, in the current guidelines (ASCE 2010, DoD 2008, DoA 1986) the load on these members is simplified as a uniformly distributed time-varying dynamic pressure, so that a simplified methodology based on an equivalent single degree of freedom (SDOF) model can be used. This

simplification makes the analysis very efficient and straight-forward, however it often compromises the accuracy of the analysis. The evaluation of present methodologies for such analysis is the subject of an important part of the present study. The evaluation is based on the determination of the exact response by a step-by-step integration of the equation of motion for a moving load, and comparing the response with that obtained from the current methodologies.

1.2.4. Global Response of Structures to Blast Load

If the blast loads have a large enough magnitude and duration, the entire building structure can be excited and vibrate laterally as shown in Figure 1.5. This situation would occur when premature local failure of the façade members, walls, columns, beams, and fenestration, is prevented. The failure of a critical member, such as a column or a major girder in the structure, would also affect the structure globally. In this case, the local failure of the member may result in an interruption in the load transmission path in the structure, and a portion or possibly the whole building structure may become unstable or collapse. This type of failure in the structures is called “progressive collapse”, and is a major damage mode that most current design codes urge the engineers to prevent in buildings (DoD 2009, Smith et al. 2009, ASCE 2010, ASCE/SEI 2010, ACI 2014).

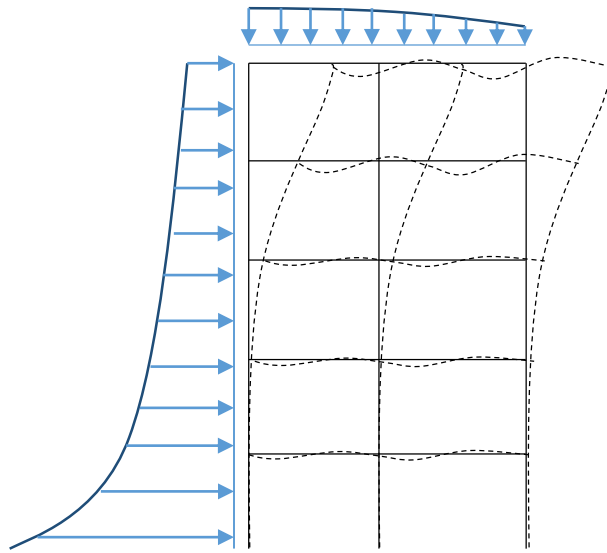


Figure 1.5. Global excitation of building structure in blast loads

Two different methodologies are commonly used in the current practice to prevent the progressive collapse of buildings. In the first methodology, the problem is dealt by various direct or explicit measures. One way to do this is by providing alternate load paths to bridge over the member which is susceptible to failure, so that the extent of the failure in the structure is limited and localized. The other way is to provide some critical members with specific load resistance and design them for higher load levels, so that the failure of such members, and therefore an instability in the structure, is prevented (DoD 2009, ASCE/SEI 2010).

Another methodology for the prevention of progressive collapse in the building is to provide additional strength, continuity and ductility in the building so that the integrity of the structure is improved. The measures suggested in the current guidelines include the use of a good plan layout with less irregularities, having redundant load paths, and ductile detailing (DoD 2009, ASCE/SEI 2010).

The different ways of improving the integrity of a structure and preventing the occurrence of progressive collapse are discussed in details in the references cited in the previous paragraphs, but are not part of the present study. Instead, the steps that could be followed to prevent premature local failure of critical members are discussed. This topic is not appropriately or fully covered in the literature, and there is need for additional in-depth study of the local and global response of structures to blast loads.

The global response of the buildings under blast depends on many parameters, from the characteristics of the blast loads and the configuration of the structural members, to the models and assumptions used in the response analysis. It is, therefore, important to understand the effects and consequences of each assumption and simplification in the analysis. Also, it would be a good idea to compare the lateral deformations of the structure under blast loads to the ones due to earthquake ground motions, to understand the differences and similarities in the response of the building to these dynamic forces.

1.3. Scope of Present Research

The scope of the present study can be summarized as follows:

1. Analysis of the response of individual columns on the front face of the building subjected to blast loading
2. Analysis of the response of beams in the roof of a building to blast load, when such beams are oriented in a direction that is perpendicular to the shock front.

3. Analysis of the global response of a building to blast load, while testing the effects of different assumptions on the response.

1.4. Organization of the Thesis

Various parts and chapters of the thesis are designed based on the scope of the research described above. Hence, the organization of the thesis is as follows.

Chapter 2 of this thesis presents the analysis of the response of columns on the front face of the buildings. The current practice for the analysis and design of these members is reviewed. The impact of simplifications and assumptions incorporated in the current methodologies, such as SDOF system representation, secondary forces due to P-delta effects also studied the response of multiple story columns.

In Chapter 3, local response of beams in the roof of a building to blast loading is studied. As discussed earlier, response of beams which are oriented parallel to the blast shock-front is similar to that of members on the front face. Therefore, only the beams with orientation perpendicular to the shock-front are discussed. The methodologies suggested in the different guidelines and codes which are currently used in the blast resistant design community are reviewed. The assumptions and simplifications outlined in the literature are studied and compared, also the response obtained from the use of the current methodologies is compared with the more accurately simulated response of the members to a propagating blast wave. Based on this study, a new computer code is developed for a more precise yet efficient analysis of the roof beams for their response to blast loads.

In Chapter 4 of this thesis, global response of building structures to blast loading is studied. The importance of such response is discussed through the case study of a benchmark building, and the effects of different parameters and simplifications made in modelling the structure on the accuracy of the analysis are assessed. The response of individual columns when modeled as part of the lateral load resisting system in blast are compared to their response to blast when modeled as individual members. In addition, the lateral deformations of the buildings under blast loads and earthquake ground motions are compared to highlight the significance of the differences in the two types of response.

Chapter 2. Response of Columns to Blast Loading

2.1. Introduction

Traditionally, in analyzing the building structures for blast loads, the main focus is on assessment of the response of individual members. The most important and critical members in this analysis are the columns on the external façade, which are the first to be impacted by the blast waves from external explosion and also experience the highest magnitude blast loading. The integrity of these columns has significant effect on the response of the structure to blast, since their damage could lead to an abrupt change in their stiffness and load resistance and consequently to progressive collapse of the building.

In the current practice, the response of individual columns in buildings is determined by using the single degree of freedom (SDOF) idealization. In the SDOF model, the effective mass of a column (depending on the end conditions) is lumped at the middle of its height and its equivalent stiffness is derived based on beam deformation theory. The equivalent stiffness depends on the boundary conditions, elastic modulus, section properties and height of the column. During the response of the column the force-deformation relationship of the material goes through different states: elastic, elasto-plastic and fully plastic. The stiffness of the column is different in the three states, as shown in Figure 2.1. The springs at the ends of the columns in Figure 2.1 represent different possible boundary conditions while the filled circles represent locations of plastic hinge.

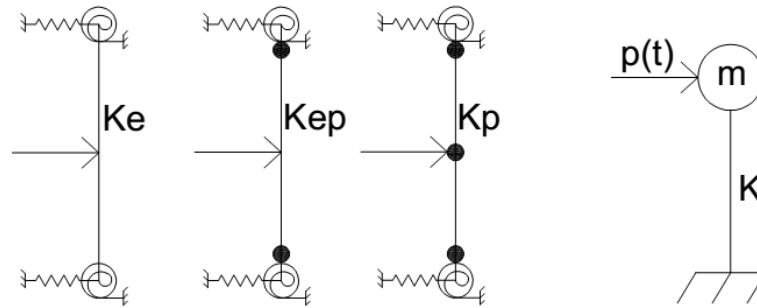


Figure 2.1. SDOF representation of individual members in blast using different stiffness states

The current methodology takes the effect of nonlinearity in the member into consideration by assuming a tri-linear force-deformation relationship for the member (Biggs 1964, DoD 2008). At low loads and deformations, the stiffness of the element (K_e) is derived for elastic state of the section. For a reinforced concrete column such a state takes into account the cracking of concrete under tension. As the loads increase, the first pair of plastic hinges is formed at the fixed supports and reduces the stiffness to the elasto-plastic stiffness (K_{ep}). After this, if the loading continues to increase, an additional plastic hinge is formed within the height of the loaded element, which produces an unstable mechanism with stiffness K_p , before collapse occurs. The relations that provide the equivalent mass and stiffness of the element are provided by Biggs (1964) and DoD (2008).

The current methodology for analysing blast-loaded columns includes many simplifications that may affect its accuracy. The use of SDOF representation ignores the higher modes of vibration, which are known to make significant contribution to the response of the column under different types of dynamic loads including blast loads

(Ebeling et al. 1997). The reliability of the SDOF idealization has been assessed in a research study by El-Dakhkhni et al. (2009), where the sensitivity of the response of an element to the number of degrees of freedom used in the analysis was investigated. El-Dakhkhni et al. (2009) studied different RC beams with fixed and simply supported end conditions using different number of degrees of freedom (DOF's). It was shown that the response of an element to blast loading was sensitive to the number of DOF's used, especially in the post-yield and near failure states of the beam.

Studies by Razaqpur et al (2007) and Magnusson (2007) provide additional evidence on the sensitivity of the response of an element to the number of degrees of freedom used in the analysis. It was shown in these studies that the response to blast load is strongly affected by higher modes of vibration. The two studies also point out the importance of shear deformations and the need to consider them in the analytical models. Another limitation of the SDOF analysis procedure is in the way it handles different nonlinear states of the section. This is because the plasticity is not concentrated at one location; it initiates at the first set of plastic hinges and then spreads throughout the length of the element. In SDOF modeling, there is also uncertainty in how the moment of inertia of a reinforced concrete (RC) column is defined in the empirical formulations. The moment of inertia used in the analysis may be that of the gross transformed section (I_g), cracked transformed section (I_{cr}), average of gross and cracked transformed sections, or the effective moment of inertia (I_{eff}). The effective moment of inertia is defined differently in various design codes, but generally as a function of the moment acting on the

member and the cracking moment. In the next section a more detailed review of the state of research on the column's response to blast loading is presented.

2.2. Literature Review

Saatcioglu et al. (2009) analyzed the response of RC columns of a benchmark 10-story building under several blast scenarios. The columns were designed and detailed for seismic forces representative of Ottawa and Vancouver. A SDOF model was used to analyse the column with due consideration being given to the effect of column confinement. The force-deformation relationship for the concrete section was based on the backbone curves derived from a moment-curvature analysis. Constant values for the dynamic and strength increase factors (DIF and SIF), were used throughout the analysis. The tributary area that imposed the blast load on the column was varied from the column face alone to an area that included the cladding around the column. The results showed that the columns with higher levels of seismic detailing, (closer stirrup spacing) performed better under blast load.

El-Dakhkhni et al. (2009(a)) carried out response analysis on RC beams subjected to blast loading using a MDOF model which accounted for nonlinear behavior of the RC section. The strain rate effects on the nonlinear behavior were taken into consideration by using DIF's that were functions of the strain-rates. However, these factors were assumed to remain constant during the response history and were calculated using an approximate strain-rate value for each scenario. The analytical cases consisted of two different RC beam sections with fixed-fixed and simply-supported boundary conditions.

Two (2) to forty (40) DOF's were used in the numerical analysis and a uniformly distributed pressure time-history of blast was applied on the beams. The study showed that in order to accurately predict the response of the RC beams, especially in near-failure conditions, it was necessary to use a large number of DOF's. The study also compared the results of the MDOF analyses to those from the traditional SDOF analysis using different values for the flexural rigidity of the beams (EI). The comparison showed significant errors in the SDOF analysis. Among the different values of EI for the beams, including gross transformed moment of inertia, cracked transformed moment of inertia, average and effective moment of inertia, the effective moment of inertia suggested by CSA provided better consistency between the results of SDOF and MDOF analyses. For most cases in which the response was in the elastic range and the blast was not of very short duration (impulsive scenarios), the closed-form solutions for end reactions in the beams as given by Biggs (1964) proved to be reasonable and close to the results of MDOF analyses.

In another paper, El-Dakhkhni et al. (2009(b)) provided a more detailed description of the MDOF model used in their previous paper. In this paper, a fixed-fixed rectangular RC column with various heights and different axial loads was analyzed. Analyses using different moment-curvature relationships obtained under different strain-rates showed the inability of constant, code-based DIF's in capturing the strain-rate effects when the strain-rate was high (higher than 1 s^{-1}). The effect of axial load levels on the response of the columns was also analyzed. It was shown that the axial load significantly reduced the ultimate (failure) curvature of the sections by increasing the depth of compression

zone in concrete. Therefore, it was suggested that the probability of increased axial loads in the columns as a result of partial collapse of other parts of the buildings, should be accounted for in the protective design of the columns. Pressure-Impulse (P-I) diagrams for two different detailing of the column ends (ductile seismic detailing and non-ductile detailing) were generated using the same analytical model. Failure in the columns with non-ductile detailing was assumed to occur when ultimate curvature was reached at an end. On the other hand, for columns with ductile detailing the formation of three plastic hinges represented failure. The effect of high axial load had a more marked influence on the P-I diagrams for the columns, especially in the impulsive regime. Another conclusion derived from the results was that a finer ductile detailing (closer ties spacing) in the column yielded higher deformation and strength capacity. In addition, it was shown that contrary to the suggestion in the current guidelines, the end rotation angle of the columns at failure depended on the level of the axial load, and for high levels of axial load, it could be much smaller than the suggested constant value. A new methodology for rapid post-blast assessment of RC columns based on variations in the axial load levels and the consequent changes in the P-I diagram was proposed.

Nassr et al. (2012) carried out experimental tests on wide flange steel beams subjected to the effects of explosions. The results of the experiments were compared to those obtained from numerical simulations using both SDOF and MDOF models. The SDOF models were built using constant code-based DIF's. As an alternative, the models used moment-curvature curves obtained from the application of DIF's considering both temporal and spatial distribution of strain-rate in the sections. The MDOF models

consisted of fiber elements with 24 nodes along the length of the beams. The variation in stress and strain rates was included in the models as well. In both SDOF and MDOF models, an elastic-perfectly-plastic strength model was used for the steel members. The study showed a reasonable match between the results obtained from both SDOF and MDOF models and the experiments. In addition, the closed-form solutions for end reactions in the beams (Biggs 1964) were proven to be accurate and consistent with the numerical models. The assumption of a constant DIF based on the codes was found to underestimate the forces transmitted to the connections. A power spectral density (PSD) analysis was carried out as a part of the research to determine the contributions of various modes of vibration on the response of the beam. It showed that the most significant (around 90%) contribution was from the first mode, along with a small contribution from the third mode of vibration, which was the reason for the accuracy of the SDOF model.

Nassr et al. (2013) repeated the experimental tests referred to in the preceding paragraph on wide flange steel sections in the presence of an axial load equal to 25% of the axial load capacity of the section, and compared the results of these tests to those for the beams without any axial load. The axial loads were imposed by pre-stressing the steel sections before the test. The comparison showed that the presence of axial loads on the columns reduced rather than magnifying the lateral displacements in the elastic range, most probably due to an elongation in the vibration period of the column caused by the presence of axial load. In addition, it was found that the $P-\delta$ effects did not have any significant effect on the response of the columns in the elastic response range.

However, when the columns were strained into the plastic range, axial loads and P- δ effects significantly increased the deformations (more than 150% increase from no axial load). Presence of axial loads also increased the contribution of higher modes, and the strain-rate in the members. The authors suggested a linear distribution of strain-rate across the depth of the columns, similar to that for beams without axial loads.

Abladey and Braimah (2014) obtained the response of RC columns in the near-field blast scenarios (scaled distances of less than $1 \text{ m/kg}^{1/3}$) using high-fidelity physics-based simulations in AUTODYN. The analytical results were verified against experimental data. The emphasis in this research was on the response of seismically detailed columns, therefore three different types of transverse reinforcement spacing were selected for the RC columns. The effect of charge mass on the response of the columns within a constant scaled distance was analyzed in the study. The analysis showed that the deflections in the columns increased with higher charge masses, due to higher impulses. The simulations also showed that for hemispherical blasts or those with near-ground charges, maximum deflection in the column occurred in the lower third of the column length, which means that the traditional SDOF model analysis would most likely underestimate the support rotations in these cases. In addition, it was found that for similar charge masses the effect of closer transverse reinforcement spacing on the response of the columns was more significant for lower scaled distances. Thus, the columns with higher confinement would be expected to suffer lower damage levels in close-in explosions. Another conclusion of the study was that higher levels of seismic

detailing for the columns would improve their response to near-field blasts in terms of both the maximum deflections and the extent of damage.

Burrel et al. (2015) experimentally investigated the response of RC and steel fiber reinforced concrete (SFRC) columns in the shock tube of University of Ottawa. A constant axial load equal to 30% of the section axial capacity was applied on the specimens using hydraulic jacks. In addition to the assessment of response of SFRC columns, the effect of seismic detailing and closer transverse reinforcement spacing was tested. The results showed that the use of smaller spacing for transverse reinforcement, as suggested in the seismic detailing of columns, improved the response of columns at moderate and high blast levels by reducing both the maximum and the residual deflections. Another benefit of the seismic detailing was in preventing premature failure through compression rebar buckling at mid-height of the column. The damage mode for the seismically detailed RC columns was observed to be rupture of the tension rebars for higher blast levels. This was evidently because the higher confinement of the core concrete resulted in higher strength, ductility and integrity, enabling the column to behave predominantly in the flexural mode.

Crawford et al. (2014) recommended consideration of additional failure/response modes for columns besides the more common flexural modes, especially for columns subjected to close-in or contact blasts. These additional modes include diagonal shear, direct shear and also complete or partial breach of the columns. It was observed that the post-blast capacity of the columns depended on both structural response and the material damage level predominantly affected by the shock front intensity and the

confinement of the concrete. It was reasoned that the local damage to the column caused by the shock front was more important than the structural response for near-field blasts. Such local damage is much harder to evaluate with the traditional analysis tools such as the response analysis of SDOF models. Another limitation of the traditional analysis tools, including SDOF models and simple finite element models using beam elements, addressed by Crawford et al. (2014) and Crawford and Morrill (2015) was the use of external failure criteria such as allowable support rotations and ductility. These criteria were reported to be misleading and poor indicators of the residual axial capacity of a column. A new design metric, called residual capacity index (RCI), was defined using the results of verified high fidelity physics based (HFPB) models. A combination of CFD calculations and HFPB models was suggested for obtaining the data required to generate simplified tools for the design of columns. The study by Crawford and Morrill (2015) also suggested a few measures to enhance the response of the RC columns and to retrofit them.

In this chapter, different assumptions and techniques used in the analysis of the response of building columns are critically examined. The effect of parameters that affect the response of columns including the number of DOF used in the analysis, shear deformations, axial gravity loads and P-delta effects are investigated through analyses carried out with the help of OpenSEES software. Different versions of the numerical model are generated and analyzed, and the response results are compared with those obtained from the current empirical methods such as those based on SDOF models. In addition, the response of continuous building columns is studied and the response

results are compared to those from single columns in order to have a better understanding of the effects of the assumptions inherent in the traditional member-by-member analysis.

It should be noted that since beam-column elements are used in the numerical models, only the response of the columns in far-range blasts are examined, so that it could be compared with that available in the literature cited in this chapter. Thus, the type of failures that a column may experience in the close-in range blast, including shear failures or direct damages from the shockfront, are not considered.

2.3. Cases Studied

In the present study, response of two different RC column sections to blast loads is analyzed. The height of both columns is 4 meters. The first column has a 500×500-mm section with 12-25M steel reinforcing bars, while the other has a 400×400-mm section with 8-25M longitudinal bars. The columns are modeled with fixed end conditions. The transverse reinforcement is designed for medium ductility, according to the provisions of National Building Code of Canada (NRCC 2010) and the related Reinforced Concrete Design Standard (CSA 2004). The transverse reinforcement calculations are carried out for one of the column sections and then used for the other section as well. For this purpose, the 400×400-mm column with 8-25M rebars and 50 mm concrete cover is selected.

The columns are required to have a minimum amount of transverse reinforcement throughout their length. This amount is the same as the requirements for beams, based on CSA A23.3-04 (CSA, 2004), and is determined as follows:

$$\text{Size assumed: } 10M \Rightarrow A_{sv} = 100 \text{ mm}^2$$

$$\text{Max. spacing, } s = \min \left\{ \begin{array}{l} d = 350 \text{ mm} \\ 16d_{b,\min} = 16 \times 20 = 320 \text{ mm} \\ 48d_{sv} = 48 \times 11.3 = 542.4 \text{ mm} \\ 300 \text{ mm} \end{array} \right\} = 300 \text{ mm}$$

In calculations above, A_{sv} is the area of the transverse reinforcement, d is the effective depth of section, $d_{b,\min}$ is diameter of smallest longitudinal bar used and d_{sv} is diameter of the transverse reinforcement.

For moderate ductility moment resisting frames, Clause 21.7.2.2 of the code specifies that a given amount of transverse reinforcement must be provided in the region close to the beam/column joint, as follows:

$$s_{\max} = \min \left\{ \begin{array}{l} b_{\min} / 2 = 350 / 2 = 175 \text{ mm} \\ 8d_{b,\min} = 8 \times 20 = 160 \text{ mm} \\ 24d_{sv} = 24 \times 10 = 240 \text{ mm} \end{array} \right\} = 160 \text{ mm} \quad \Rightarrow \text{say } 150 \text{ mm}$$

$$A_{sh,\min} = \max \left\{ \begin{array}{l} 0.15k_n k_p \frac{A_g}{A_{ch}} \frac{f_c'}{f_{yh}} s.b_c \rightarrow \text{unlikely to govern} \\ 0.09 \frac{f_c'}{f_{yh}} s.b_c = 0.09 \frac{30}{400} 150 \times 500 = 506.25 \text{ mm}^2 \end{array} \right\} = 506.25 \text{ mm}^2$$

$$\text{use } \boxed{3 \text{ legs of } 15M @ 150 \text{ mm}} \quad \Rightarrow A_{sh} = 3 \times 200 = 600 \text{ mm}^2$$

$$\text{length of probable plastic hinge region, } l_0 = \max \left\{ \begin{array}{l} h_c / 16 = 3600 / 16 = 225 \text{ mm} \\ b_{\max} = 500 \text{ mm} \\ 450 \text{ mm} \end{array} \right\} = 500 \text{ mm}$$

In above calculations, b_{min} and b_{max} are the smaller and larger dimension of the section respectively, $A_{sh,min}$ is minimum cross-sectional area of transverse reinforcement, k_n and k_p are factors accounting for the number of longitudinal bars and compressive strength of concrete respectively, A_g is gross cross-section of the section, A_{ch} is area of the concrete core, f_{yh} is yield stress of transverse reinforcement, and b_c and h_c are the confined width and height of the section respectively.

The layout of the transverse reinforcement is shown in Figure 2.2.

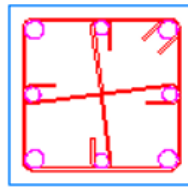


Figure 2.2. Schematic detailing of the columns

The schematic details of the designed transverse reinforcement are shown in Figure 2.3.

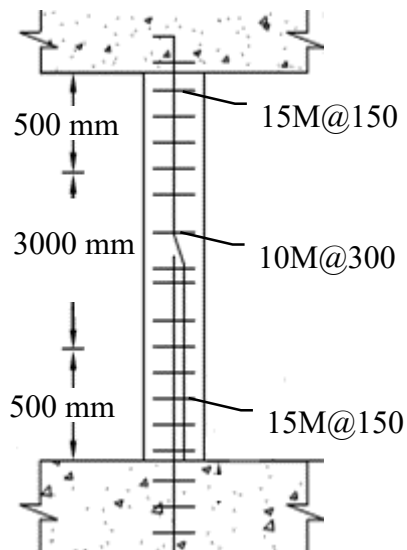


Figure 2.3. Details of transverse reinforcement in columns

In the numerical analyses whose details are presented in this chapter, only the transverse reinforcement provided at the mid-height of the columns is considered, thus the variation in the transverse reinforcement along the length of the column is not considered in the models. Based on the geometry and design of the sections of the columns, the material models selected are discussed in the following sections. Also discussed are the loading and the other parameters used in the simulations.

2.3.1. Material Models

Based on the sections of the RC columns defined in the preceding paragraph, material models to be used in the numerical simulations are selected for different parts of the column section. The selected models are described in the following.

2.3.1.1. Unconfined concrete

For modeling unconfined concrete in the cover of the column section, Hognestad's model (Hognestad, 1951) is used. Based on the assumed properties for the concrete, and applying the constant DIF's (DOD 2008), the following parameter values are obtained:

$$\begin{aligned}
 f'_c = 30 \text{ MPa} & \Rightarrow \boxed{E_c = 4700\sqrt{f'_c} = 25.74 \text{ GPa}} \\
 f'_{cd} = DIF \cdot f'_c & \quad \& \quad DIF = 1.25 \Rightarrow \boxed{f'_{cd} = 37.5 \text{ MPa}} \\
 \boxed{\varepsilon_0 = 2f'_{cd} / E_c = 0.00291} \\
 \Rightarrow \boxed{k = 169.2} & \quad \& \quad \boxed{f'_{ca} = 0.85f'_{cd} = 31.875 \text{ MPa}}
 \end{aligned}$$

The parameters defined above are based on the definitions of the Hognestad's model shown in Figure 2.4. It should be noted that the dynamic properties of the materials are used instead.

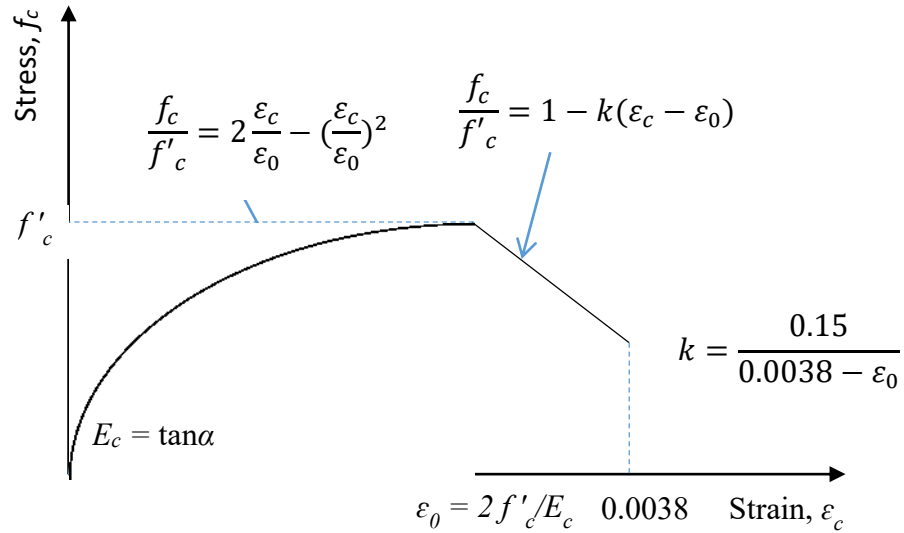


Figure 2.4. Hognestad's model for unconfined concrete (after Hognestad, 1951)

In order to use this model in the OPENSEES code, concrete01 model was selected since tension softening is not significant in the cover concrete. In order to reflect the cracking of the concrete cover in the members, the ultimate cracking stress was selected as 10% of the maximum compressive strength. The command line for using this material model in OpenSEES is as follows:

```
uniaxialMaterial Concrete01 $matTag $fpc $sepsc0 $fpcu $sepsU
```

2.3.1.2. Confined concrete

One of the most used models for simulating the confined concrete material is the concrete07 material model available in OpenSEES. This model is based on a derivation by Chang and Mander (1994) and is shown in Figure 2.5. The calculations of the

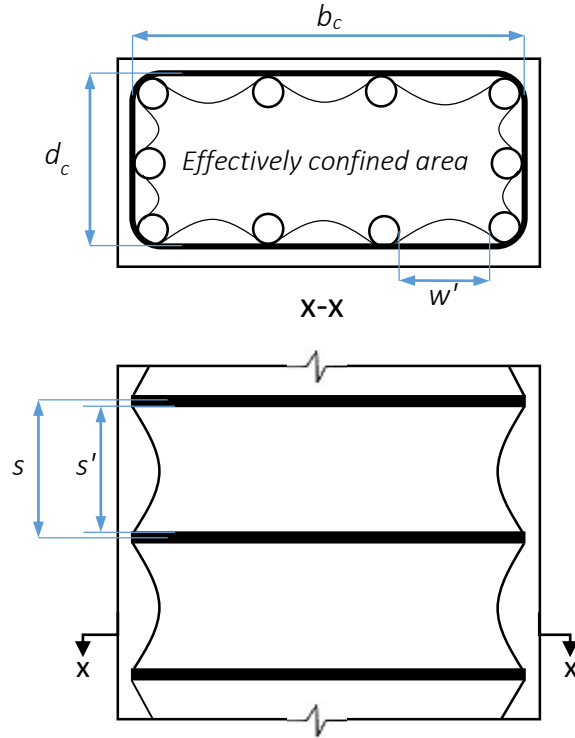


Figure 2.6. Effective confined core in rectangular members based on Chang and Mander (1994)

Properties of confined concrete in special regions in moderate ductility columns:

$$\begin{aligned}
 \text{effective confined area, } A_e &= \left(b_c d_c - \sum \frac{(w'_i)^2}{6} \right) \left(1 - 0.5 \frac{s'}{b_c} \right) \left(1 - 0.5 \frac{s'}{d_c} \right) \\
 &= \left(275 \times 275 - 8 \times \frac{(112.5)^2}{6} \right) \left(1 - 0.5 \times \frac{125}{275} \right) \left(1 - 0.5 \times \frac{125}{275} \right) \\
 &= 33448.66 \text{ mm}^2
 \end{aligned}$$

$$\text{concrete core area, } A_{cc} = b_c d_c - A_{st} = 275 \times 275 - 8 \times 500 = 71625 \text{ mm}^2 \Rightarrow k_e = A_e / A_{cc} = 0.467$$

$$\rho_x = \rho_y = \frac{A_{sx}}{s.d_c} = \frac{3 \times 200}{150 \times 275} = 1.45 \times 10^{-2} \quad \Rightarrow \text{confinement stress, } f'_l = k_e \rho_x f_{yh} = 2.72 \text{ MPa}$$

$$q = f'_{lx} / f'_{ly} = 1.0 \quad \& \quad x' = \frac{f'_{lx} + f'_{ly}}{2f'_{cd}} = 0.072$$

$$A = 6.8886 - (0.6096 + 17.275q)e^{-4.989q} = 6.767 \quad \& \quad B = \frac{4.5}{\frac{5}{A}(0.9849 - 0.6306e^{-3.8939q}) - 0.1} = 7.28$$

$$k_1 = A(0.1 + \frac{0.9}{1 + Bx'}) = 4.67 \quad \Rightarrow \quad \boxed{f'_{cc} = f'_{cd}(1 + k_1x') = 50.12 \text{ MPa}}$$

$$k_2 = 5k_1 = 23.35 \quad \Rightarrow \quad \boxed{\varepsilon_{cc} = \varepsilon_{c0}(1 + k_2x') = 0.0058}$$

$$\boxed{x_n = 30} \& \boxed{x_p = 2} \quad n = \frac{E_c \varepsilon_{cc}}{f'_{cc}} = \frac{29.36 \times 10^3 \times 0.0058}{50.12} = 3.38 \quad \Rightarrow \quad \boxed{r = n / (n - 1) = 1.42}$$

Properties of concrete in other regions in moderate ductility columns:

$$\begin{aligned} A_e &= \left(b_c d_c - \sum \frac{(w'_i)^2}{6} \right) \left(1 - 0.5 \frac{s'}{b_c} \right) \left(1 - 0.5 \frac{s'}{d_c} \right) \\ &= \left(275 \times 275 - 8 \times \frac{(112.5)^2}{6} \right) \left(1 - 0.5 \times \frac{275}{275} \right) \left(1 - 0.5 \times \frac{275}{275} \right) \\ &= 13638.74 \text{ mm}^2 \end{aligned}$$

$$A_{cc} = b_c d_c - A_{st} = 275 \times 275 - 8 \times 500 = 71625 \text{ mm}^2 \Rightarrow k_e = A_e / A_{cc} = 0.190$$

$$\rho_x = \rho_y = \frac{A_{sx}}{s \cdot d_c} = \frac{3 \times 100}{300 \times 275} = 3.64 \times 10^{-3} \quad \Rightarrow \quad f'_i = k_e \rho_x f_{yh} = 0.276 \text{ MPa}$$

$$q = f'_{lx} / f'_{ly} = 1.0 \quad \& \quad x' = \frac{f'_{lx} + f'_{ly}}{2f'_{cd}} = 0.0074$$

Because of very small confinement stress calculated above, it can be concluded that the confinement effect in the regular regions of the columns in moderate ductility frames is not significant. Therefore, the unconfined properties of the concrete are used in concrete07 model, as shown below:

$$f'_{c0} = 30 \text{ MPa} \Rightarrow E_c = 8200 f'_{c0}{}^{3/8} = 29.36 \text{ GPa} \quad \& \quad f'_{cd} = DIF \cdot f'_{c0} = 37.5 \text{ MPa}$$

$$\varepsilon_{c0} = \frac{f'_{cd}{}^{1/4}}{1152.63} = 0.00215$$

$$f_t = 0.62 \sqrt{f'_{cd}} = 3.8 \cong 0.1 f'_{cd} \quad \& \quad \varepsilon_t = 2 f_t / E_c = 0.00026$$

$$x_p = 2.0$$

$$x_n = 2.3$$

$$r = \frac{f'_{cd}}{5.2} - 1.9 = 5.31$$

2.3.1.3. Reinforcing steel model

For the modeling of reinforcing steel, the Giuffre-Manegotto-Pinto material model without isotropic hardening was used (Filippou et al. 1983). This model is included in the OpenSEES code as steel02 model. Based on the given information on the steel rebar, the parameters used in this model are defined as follows:

$$f_y = 400 \text{ MPa} ; DIF = 1.23 \Rightarrow f_{yd} = 492 \text{ MPa} \quad E_s = 200 \text{ GPa}$$

$$f_u = 500 \text{ MPa} ; DIF = 1.05 \Rightarrow f_{ud} = 525 \text{ MPa}$$

$$\varepsilon_y = f_{yd} / E_s = 0.00246$$

$$\varepsilon_u = 0.035$$

$$E_{sh} = \frac{f_{ud} - f_{yd}}{\varepsilon_u - \varepsilon_y} = 1014.14 \text{ MPa} \Rightarrow b_{sh} = \frac{E_{sh}}{E_s} = 0.0051$$

In the calculations above, f_{yd} and f_{ud} are dynamic yield and ultimate stress of steel respectively, E_s is modulus of elasticity of steel, ε_y and ε_u are yield and ultimate strain, E_{sh} and b_{sh} are strain-hardening modulus and ratio of steel respectively.

For other parameters in the model (R values for controlling the hysteretic curve), the values as recommended in the manual of the software are used. The command line for using the Giuffre-Manegotto-Pinto material model is given as follows.

uniaxialMaterial Steel02 \$matTag \$Fy \$Es \$bsh \$R0 \$cR1 \$cR2

2.3.2. Blast Loading

For analyzing the response of the single columns, five different hemispherical blast scenarios with scaled distance ranging from 1.59 m/kg^{1/3} to 5.39 m/kg^{1/3} are selected as defined in Table 2.1. The load parameters for the selected scenarios are also shown in the table. The total load on the columns is assumed to vary with time according to an exponential or as a triangular pulse time-history. The corresponding duration times are derived for different cases using the CONWEP program (DoA 1986), and are also shown in Table 2.1.

Table 2.1. Selected blast scenarios and the load properties of each case

Scenario		1	2	3	4	5
W (kg)	Charge weight	100	250	250	200	250
R (m)	Standoff dist.	25	25	20	15	10
Z (m/kg ^{0.33})	Scaled distance	5.39	3.97	3.18	2.57	1.59
P_r (kPa)	Peak reflected pressure	87.08	165.20	285.00	509.00	2130.00
I_r (kPa.msec)	Reflected impulse	536.80	1025.00	1323.00	1577.00	3053.00
t_d (msec)	Positive phase duration time	18.08	21.48	18.66	13.86	13.30
Θ (msec)	Exponential decay coefficient	19.31	14.49	9.71	9.57	2.72
t_{df} (msec)	fictitious duration time = $2I_{sof}/P_{sof}$	12.33	12.41	9.28	6.20	2.87

For all the blast cases shown in Table 2.1, the blast loads are applied to the columns using a 4-m tributary width, from which the loads are transmitted to the columns. Also accounted for is the mass of the tributary wall assumed to be 40 kg/m².

2.4. Analytical Models

2.4.1. Traditional single degree of freedom (SDOF) analysis

Response of individual elements under blast load is traditionally carried out using a SDOF model as described in Section 2.1. This model takes only the first mode of vibration into consideration by concentrating the total mass and stiffness of the member and the applied load on the member at a single point, for instance, the midspan (DoD 2008, Biggs 1964, Mays and Smith 1995). The properties of the SDOF model are defined through mass (K_M), resistance (K_R) and load (K_L) factors, obtained by equating the energy terms in the actual member and the equivalent SDOF model as described in the following paragraphs.

A shape function $\phi(x)$ is selected to represent the displaced shape of the column. The selected function is given by equation 2.1.

$$\phi(x) = \frac{\delta(x)}{\delta_{max}} \quad (2.1)$$

where $\delta(x)$ is the displacement produced in the member under a uniformly distributed lateral load and δ_{max} is the maximum value of $\delta(x)$.

On equating the kinetic energy in the actual member to that in the SDOF representation, the following is derived.

$$K_M = \frac{\int_0^L \bar{m}(x) \phi^2(x) dx}{\int_0^L \bar{m}(x) dx} \quad (2.2)$$

On equating the work done by the distributed load on the member to the work done by equivalent concentrated load to the equivalent SDOF system gives

$$K_L = \frac{\int_0^L p(x) \phi(x) dx}{\int_0^L p(x) dx} \quad (2.3)$$

In Equations 2.2 and 2.3 $\bar{m}(x)$ and $p(x)$ are, respectively, the mass and load functions per unit length and L is the span of the element.

Using the same approach, the resistance of an element is defined as its internal force that restores the element to its unloaded static condition. The resistance of the elements can be defined in terms of the applied load distribution. Since the same load distribution is used in deriving both factors, resistance factor K_R is always equal to the load factor K_L defined in Equation 2.3.

The nonlinearity of the member is considered in defining the mass, load and resistance factors, which take different values depending on the end conditions of the elements, and on the formation of plastic hinges along the length. After finding the properties of the equivalent SDOF system, the dynamic equation of motion for the element can be expressed as in Equation 2.4, using load-mass factor (K_{LM}) which is defined as $K_{LM}=K_M/K_L$.

$$K_{LM}m\ddot{u}(t) = P(t) \quad (2.4)$$

where, m is the total mass of the element including the tributary mass of the wall, $u(t)$ and $\ddot{u}(t)$ are the displacement and acceleration of the equivalent SDOF system, respectively. $R(u)$ is the resistance function of the element, and $P(t)$ is the blast load acting on the element.

For the column with fixed end conditions, the mechanism of formation of plastic hinges is shown in Figure 2.7. The response of the member has three different stages: elastic, elasto-plastic and fully plastic. K_{LM} factors for these three stages are determined as 0.77, 0.78 and 0.66, respectively (DoD 2008). The resistance function of the column is also shown in Figure 2.7, where M_n and M_p are, respectively, the negative and positive plastic moments of the section at the shown locations, and EI is the bending stiffness of the member.

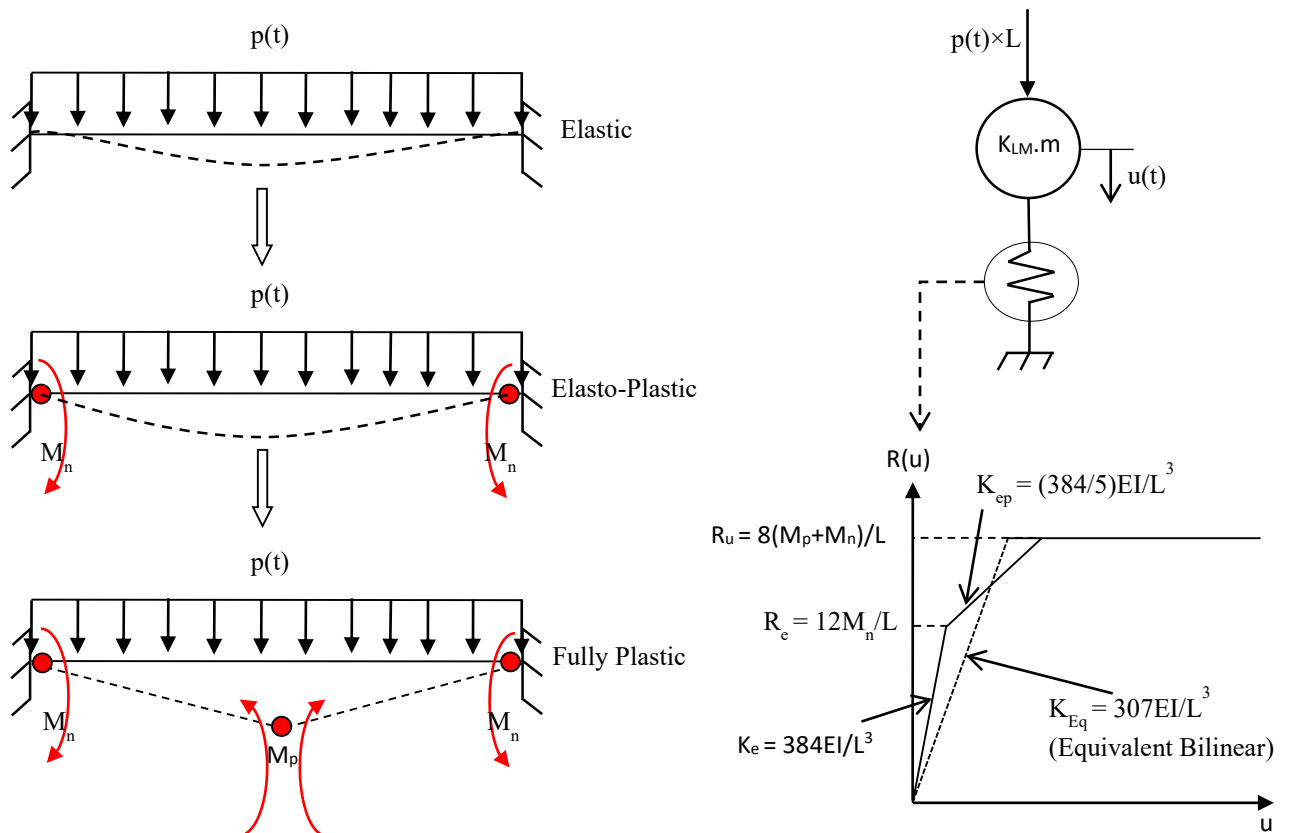


Figure 2.7. Definition of SDOF model and the resistance function for the studied column

As shown in Figure 2.7, an equivalent bilinear curve for the resistance function of the system can be used. An important factor in defining the resistance function is the effective bending stiffness (EI) of the member. In the traditional methodology, it has been suggested that for concrete an average of the bending rigidities of the cracked and gross section of the section, EI_{ave} (Biggs 1964) may be used. On the other hand, reinforced concrete design codes suggest different formulations for this parameter. For instance, ACI 318-14 and CSA A23.3-04 suggest the expression shown in Equation 2.5, using cracking bending moment (M_{cr}), the maximum moment applied to the section

(M_a), and a combination of cracked and gross section moments of inertia of the member (ACI 2014, CSA 2004).

$$I_e = \left(\frac{M_{cr}}{M_a} \right)^3 + \left[I - \left(\frac{M_{cr}}{M_a} \right)^3 \right] I_{cr} \leq I_g \quad (2.5)$$

where,

$$M_{cr} = \frac{f_r \cdot I_g}{y_t}, \quad f_r = 0.62 \sqrt{f'_{cD}} \quad (2.6)$$

In Equation 2.5, f_r is the modulus of rupture of concrete, and y_t is the distance from the centroidal axis to the extreme fibre in tension. Based on this formulation, cracking moment of rectangular sections can be simplified to $bh^2f_r/6$, where b and h are width and height of the section, respectively.

In the present study, the effective moment of inertia (I_e) based on ACI and CSA formulations is used to determine the stiffness of the concrete column in a SDOF model. For this, the maximum applied moment (M_a) is assumed to be the maximum unfactored bending moment capacity of the section in absence of axial loads. Also, in finding the referenced parameters, the effect of confinement is neglected and the material properties of unconfined concrete and steel reinforcement, as amplified by the dynamic strength reduction factors, are used.

The other important parameter in the SDOF model is the bending moment capacity of the sections at the midspan and supports (M_p and M_n in Figure 2.7). For the RC columns discussed here, the positive and negative moment capacities are the same because of

identical reinforcement on both sides, and are functions of the applied axial loads. In this respect, the moment capacity of the column under different gravity axial loads is obtained from the P-M interaction curve of the section. This interaction curve without the application of strength reduction factors, is obtained using SAP 2000 software, and is shown in Figure 2.8 for the internal and external column sections.

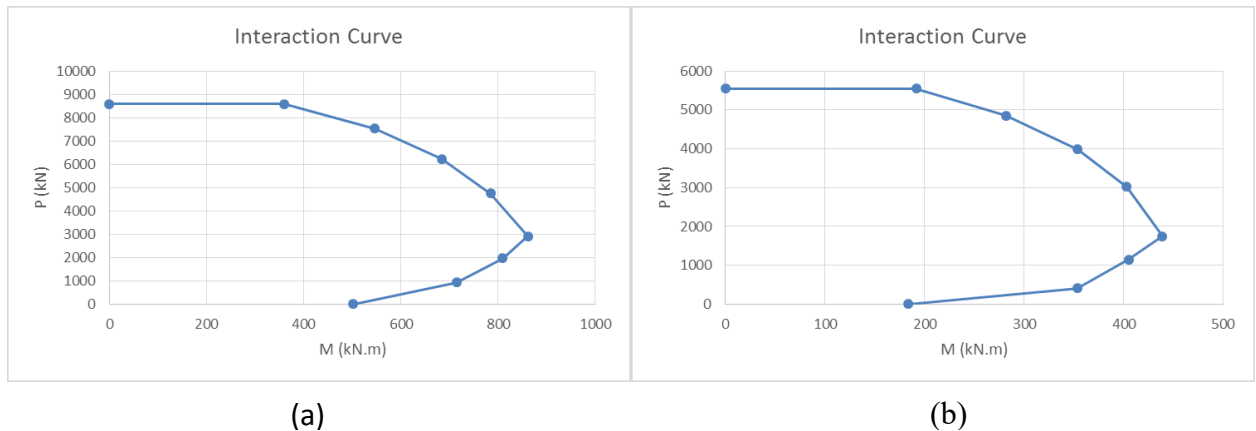


Figure 2.8. P-M Interaction curves for (a) 500x500 column, (b) 400x400 column

After generating the SDOF model based on the parameters referred to in the foregoing for the different analytical cases, a dynamic analysis of the SDOF system with equivalent bilinear resistance function is carried out by using step-by-step time integration (Newmark's average acceleration) method, considering 5% damping ratio and 0.01 msec time step. The results that include the maximum displacement at the midspan of the columns and the support reactions are presented and are compared to those obtained from more precise (multi-degree of freedom) models in the following sections.

2.4.2. Multi-degree of freedom (MDOF) analysis

A more accurate methodology for analyzing a members' response to blast is used in addition to the SDOF model. In this methodology, the columns are modeled using fibre elements with nonlinear material properties based on the models described in Section 2.3. In fibre elements model, the cross-section of the beams is discretized into different subparts (fibres) which can represent different materials such as concrete (confined or unconfined) and reinforcing steel. In this 2D model, which is generated using OpenSEES code, the columns are discretized into a number of different elements, modeled by fibre elements. Force-based integration using "nonlinearBeamColumn" command is employed in the analysis. The individual elements are modeled with 5 integration points along the length. The mass of each element is lumped at the nodes, where the blast loads are also applied.

For the assessment of response of the members, first a static analysis is carried out to find the internal efforts in the members under the applied gravity loads. After this, a nonlinear dynamic analysis is carried out applying 5% Rayleigh damping to the 1st and the 3rd modes of vibration of the member. The dynamic solver uses Newmark's average acceleration method with 0.01 msec time step. This time step is selected after a sensitivity analysis with smaller and larger time steps, which shows using this time step is both efficient and accurate in the analysis. The results are recorded in the form of displacements of the nodes and the reactions at the end of the members. These are compared with the results obtained from the SDOF models, in the following sections.

2.5. Results of Numerical Analyses and Discussions

Numerical analyses for many cases, that measure the sensitivity of the response to different parameters, are carried out and the results are presented in this section.

Different variables are selected for testing their effect on the response of the member and the analytical models are changed accordingly, as presented in the following.

2.5.1. Effect of shear deformation

In this sub-section, the effect of shear deformations on the response of the members to blast loading is examined. For this purpose, the two column sections, each with a gravity axial load of $0.125f'_cA_g$ (axial load ratio or ALR of 12.5%) are considered. The blast loads from the scenarios defined in Table 2.1 are applied to the MDOF models assuming a tributary span of 4 m and an exponentially decaying time-history. In the simulation, 15 translational degrees of freedom are assigned to the members, and the lengths of the members are meshed accordingly. The beam-column elements are generated using the material properties of the unprotected region of the columns (middle of the column) with moderate ductility design level without special seismic detailing. Also, the P-delta effects are neglected in the analysis.

For considering shear deformations in the analyses, elastic shear behavior is assumed and a stiffness of $G_cA_g/12$ is added to the members (G_c is the shear modulus of concrete) using the “section aggregator” command in OpenSEES. The difference between the responses of the 400×400-mm column to the first blast scenario, with and without shear

deformation is shown in Figure 2.9. The results for all analyzed cases are shown in Tables 2.2 to 2.5, and in Figures 2.10 and 2.11.

From a comparison of the results for the models with and without shear deformations, several points can be observed as follows:

- 1- The maximum displacements in the models with shear deformations are slightly greater than those in the models without shear deformation since the structure is softer. However, this difference is less than 12% for all cases (Table 2.2 and Table 2.4).
- 2- The difference in the maximum displacement is more pronounced in the 500×500-mm columns, since the shear deformations are more important in deeper sections. The maximum difference between maximum displacements in models with and without shear deformations is 5.3% for 400×400-mm columns (Table 2.2), compared to 11.3% for 500×500-mm columns (Table 2.4).
- 3- The differences in the maximum moments at mid-height and ends of the columns vary randomly, but are within 5% percent of the values in the models with no shear deformations (Table 2.3 and Table 2.5).
- 4- The least sensitive parameters are the end reactions and the fixed end moments in the columns. The difference between the results for different cases reaches up to 5% between models with and without shear deformation.
- 5- Based on the above observations, it is seen that the difference between results for the models with and without shear deformations are not significant.

Therefore, it can be concluded that considering shear deformations in the models is not very important.

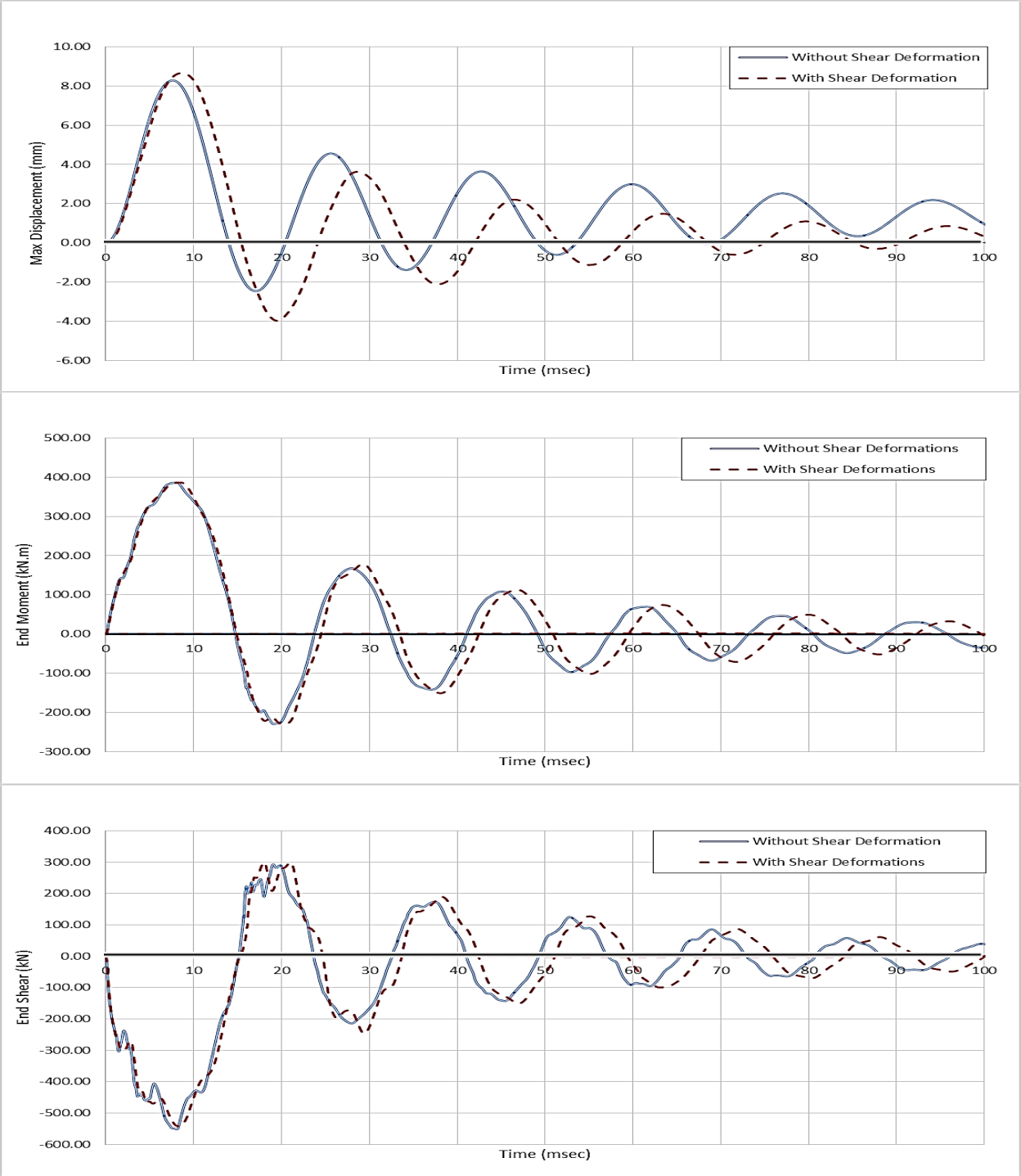


Figure 2.9. Response of the 400x400 column in blast scenario 1 in MDOF model

Table 2.2. Mid-height displacement and bending moment in MDOF model of 400×400 columns with and without shear deformation

Element model	Blast 1		Blast 2		Blast 3		Blast 4		Blast 5	
	Max. displacement (mm)	Max. moment (kN.m)								
	No Shear Def.	8.20	247.56	25.19	385.56	56.0	401.22	133.89	417.57	462.09
With Shear	8.66	241.57	26.29	386.59	57.7	400.61	138.74	419.06	473.28	465.58
Difference*	5.31%	-2.48%	4.18%	0.27%	2.95%	-0.15%	3.50%	0.36%	2.36%	5.23%

* Positive values mean the results in models with shear deformations are greater, negative values show otherwise.

Table 2.3. End reactions in MDOF model of 400×400 columns with and without shear deformation

Element model	Blast 1		Blast 2		Blast 3		Blast 4		Blast 5	
	Max. moment (kN.m)	Max. shear (kN)								
	No Shear Def.	385.74	551.45	412.61	775.08	454.44	901.46	489.26	1025.59	585.27
With Shear	385.72	540.86	413.13	762.59	456.36	888.70	488.91	1030.10	586.18	2081.07
Difference*	-0.01%	-1.96%	0.13%	-1.64%	0.42%	-1.44%	-0.07%	0.44%	0.16%	0.31%

* Positive values mean the results in models with shear deformations are greater, negative values show otherwise.

Table 2.4. Mid-height displacement and bending moment in MDOF model of 500×500 columns with and without shear deformation

Element model	Blast 1		Blast 2		Blast 3		Blast 4		Blast 5	
	Max. displacement (mm)	Max. moment (kN.m)								
	No Shear Def.	2.86	289.60	7.12	507.68	15.55	711.42	43.81	770.85	202.62
With Shear	3.22	304.21	7.72	497.11	17.31	672.19	45.96	772.42	205.19	824.36
Difference*	11.18%	4.80%	7.77%	-2.13%	10.17%	-5.84%	4.68%	0.20%	1.25%	-1.39%

* Positive values mean the results in models with shear deformations are greater, negative values show otherwise.

Table 2.5. End reactions in MDOF model of 500×500 columns with and without shear deformation

Element model	Blast 1		Blast 2		Blast 3		Blast 4		Blast 5	
	Max. moment (kN.m)	Max. shear (kN)								
	No Shear Def.	478.69	664.16	744.30	1099.15	780.76	1343.10	880.25	1757.76	967.84
With Shear	476.74	668.04	746.15	1104.38	784.07	1336.00	884.86	1712.50	1018.05	3034.13
Difference*	-0.41%	0.58%	0.25%	0.47%	0.42%	-0.53%	0.52%	-2.64%	4.93%	2.97%

* Positive values mean the results in models with shear deformations are greater, negative values show otherwise.

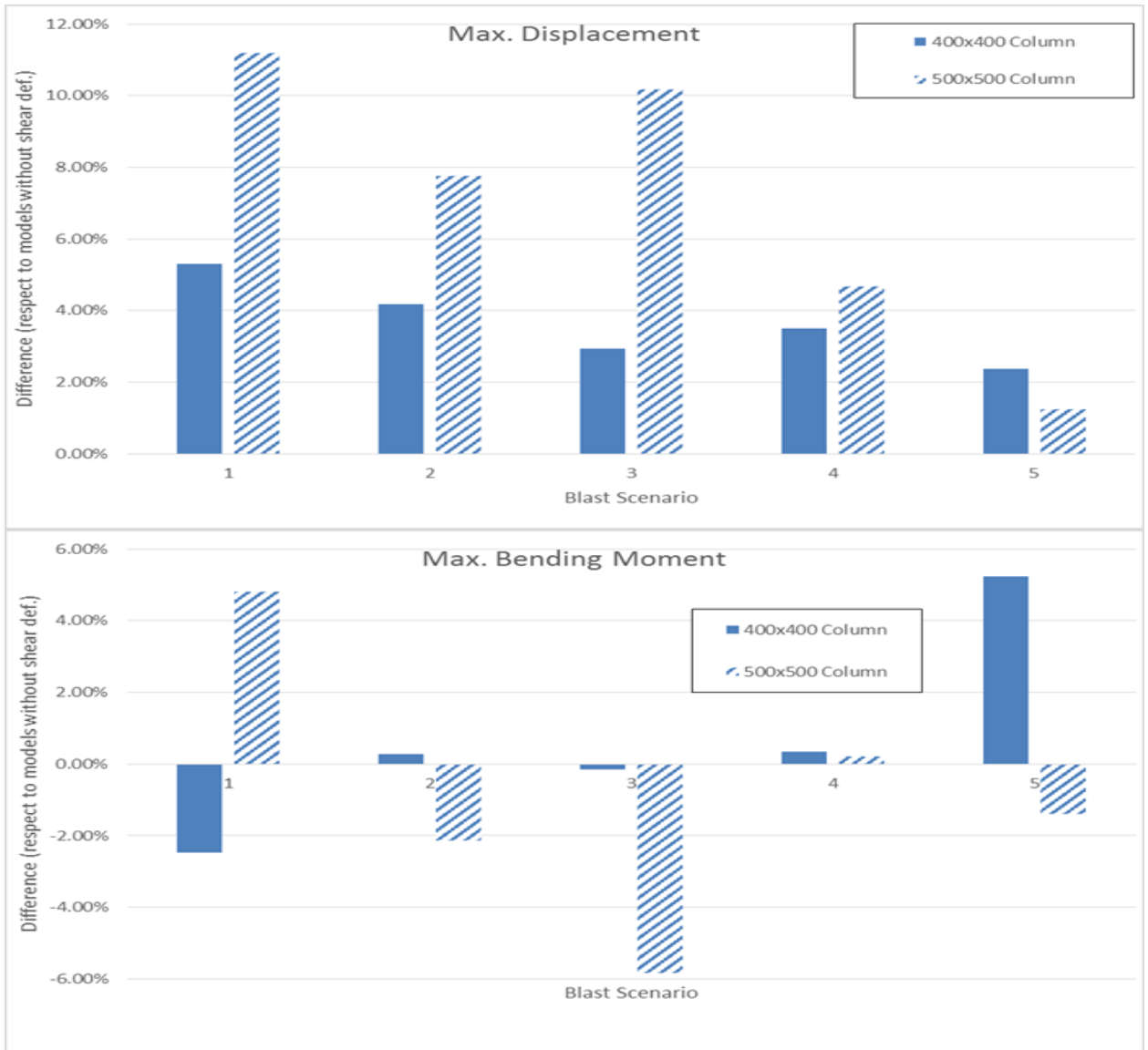


Figure 2.10. Comparison of mid-height displacement and bending moment models with and without shear deformations

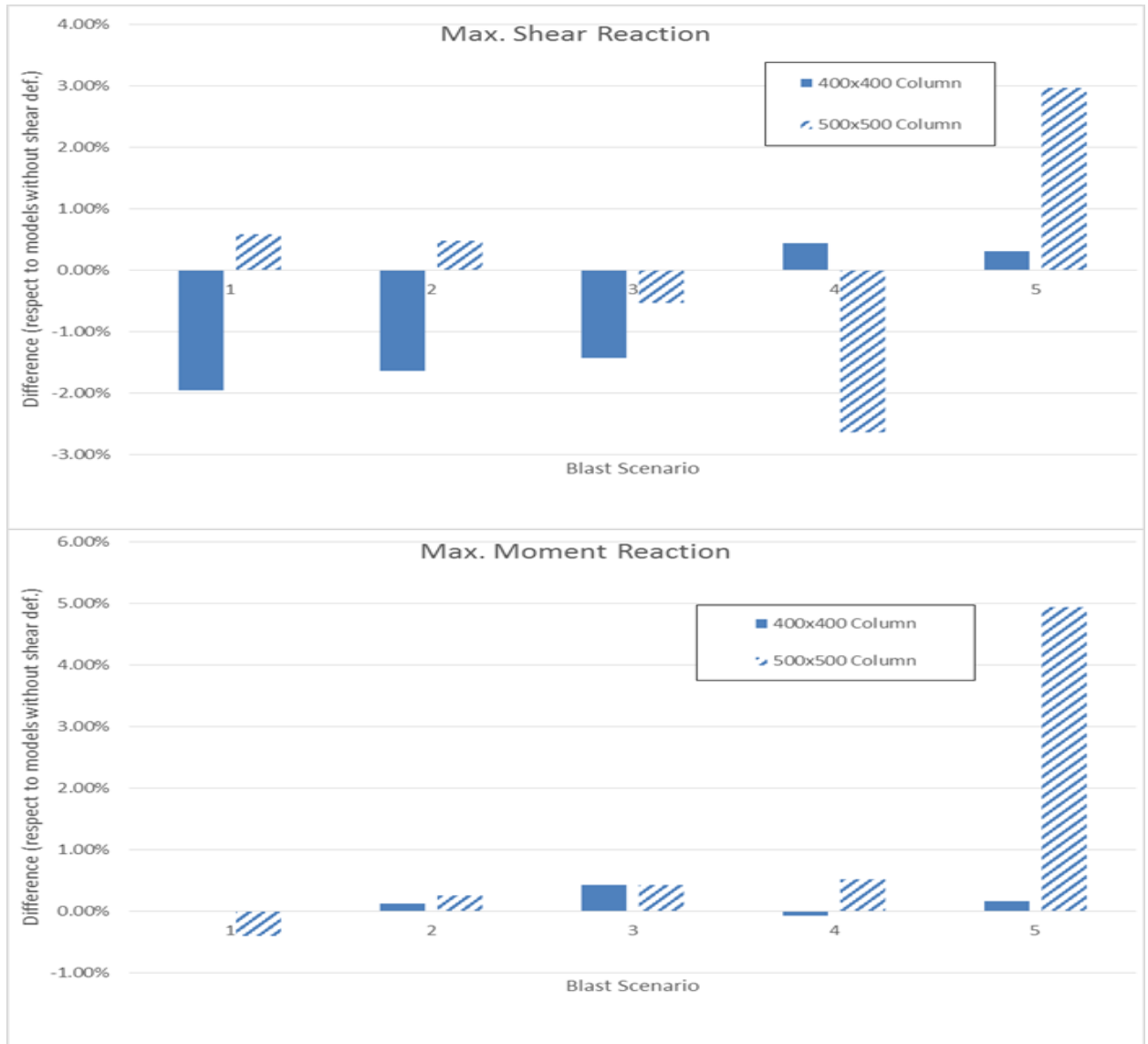


Figure 2.11. Comparison of end reactions for models with and without shear deformations

2.5.2. Effects of number of degrees of freedom

In this sub-section, the effect of number of DOF on the response of the models is examined. For this purpose, the two different column sections, each with an ALR of 12.5% are considered. The blast loads from the defined scenarios in Table 2.1 are applied to the MDOF models. In the simulations, number of degrees of freedom

assigned to the member is varied from 1 to 25, and the length of the member is meshed accordingly. Also, P-delta effects is neglected.

The maximum response parameters for the 400×400-mm column under blast scenario 1 are shown in Figure 2.12. The normalized results for each blast scenario for the columns are presented in Figures 2.13 and 2.14. For the normalization, the maximum responses in the different models are divided by the maximum response of the model with largest number of degrees of freedom, which is assumed to be more accurate.

Several conclusions can be drawn from the results presented here. As shown, the maximum displacement of the members can be predicted with good accuracy even with a small number of DOF's (say 5 DOF's for instance) in the models. In contrast, the maximum shear (column reaction force) in the members is quite sensitive to the number of DOF's. Maximum shear will be underestimated when fewer degrees of freedom are used. However, the maximum moments at mid-height and ends of the elements are not significantly sensitive to the number of DOFs used. Also, for the analysis cases selected for this study, 15 degrees of freedom appears to be a reasonable number and can be used to obtain a balance between accuracy and efficiency.

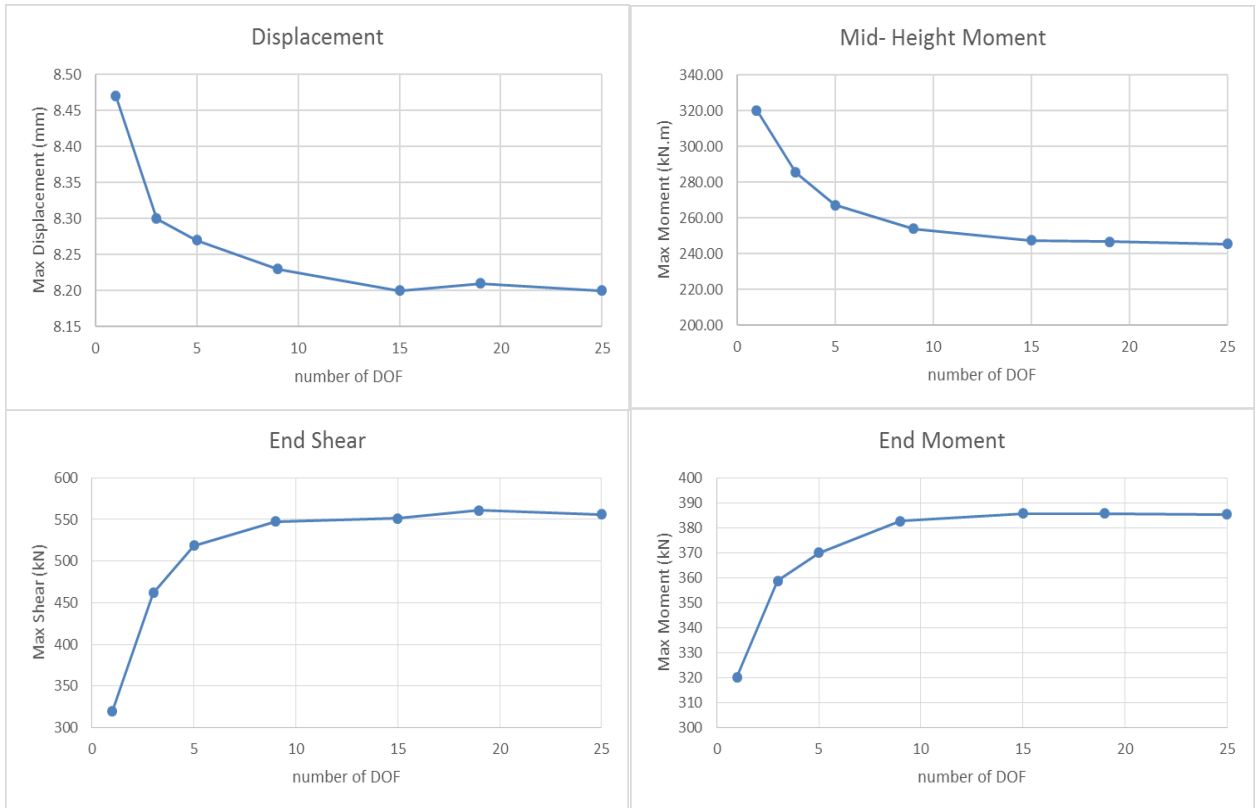


Figure 2.12. Maximum response of the 400×400-mm column in blast scenario 1 versus number of DOFs

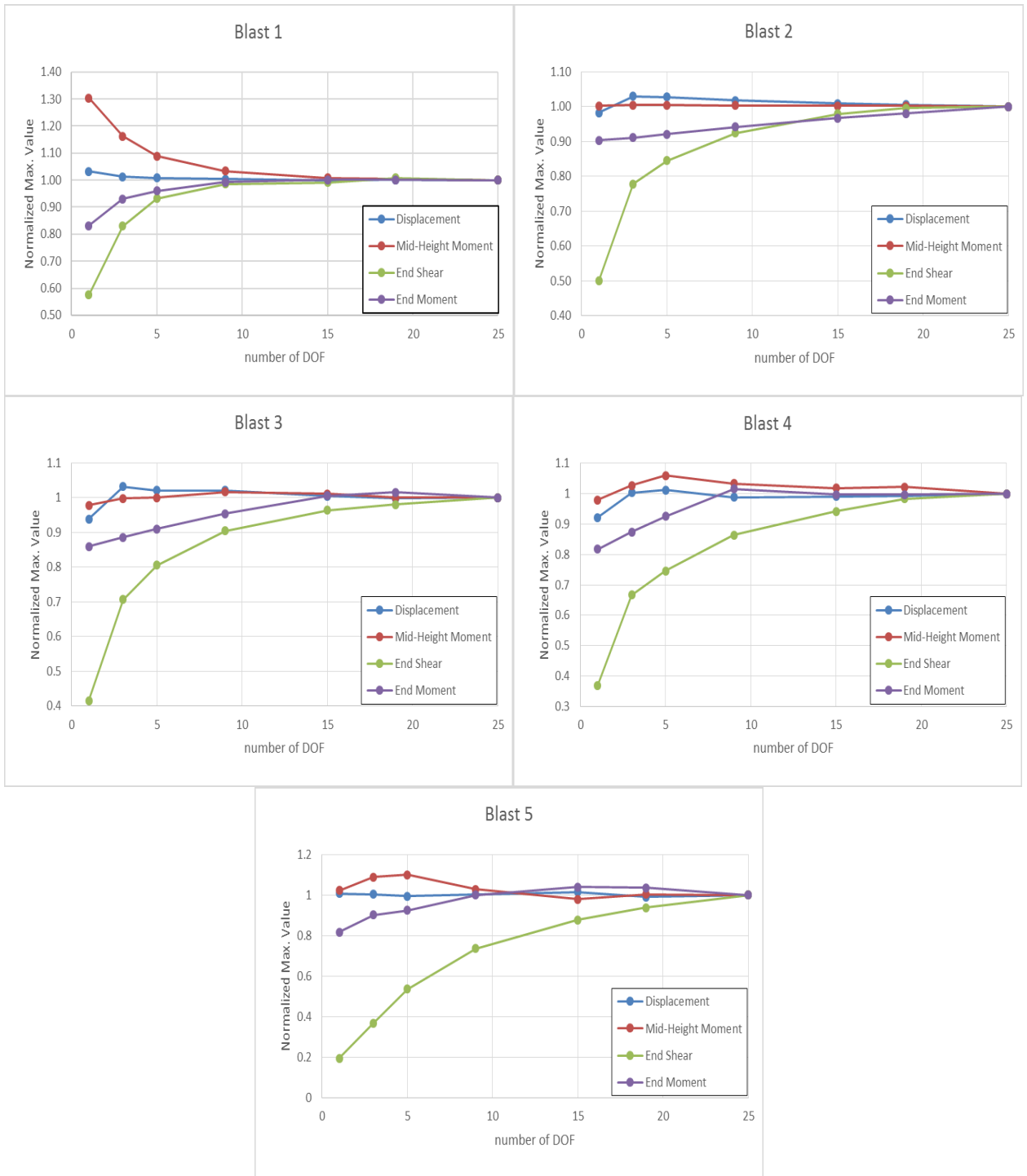


Figure 2.13. Normalized maximum response of the 400×400-mm column under different blast scenarios

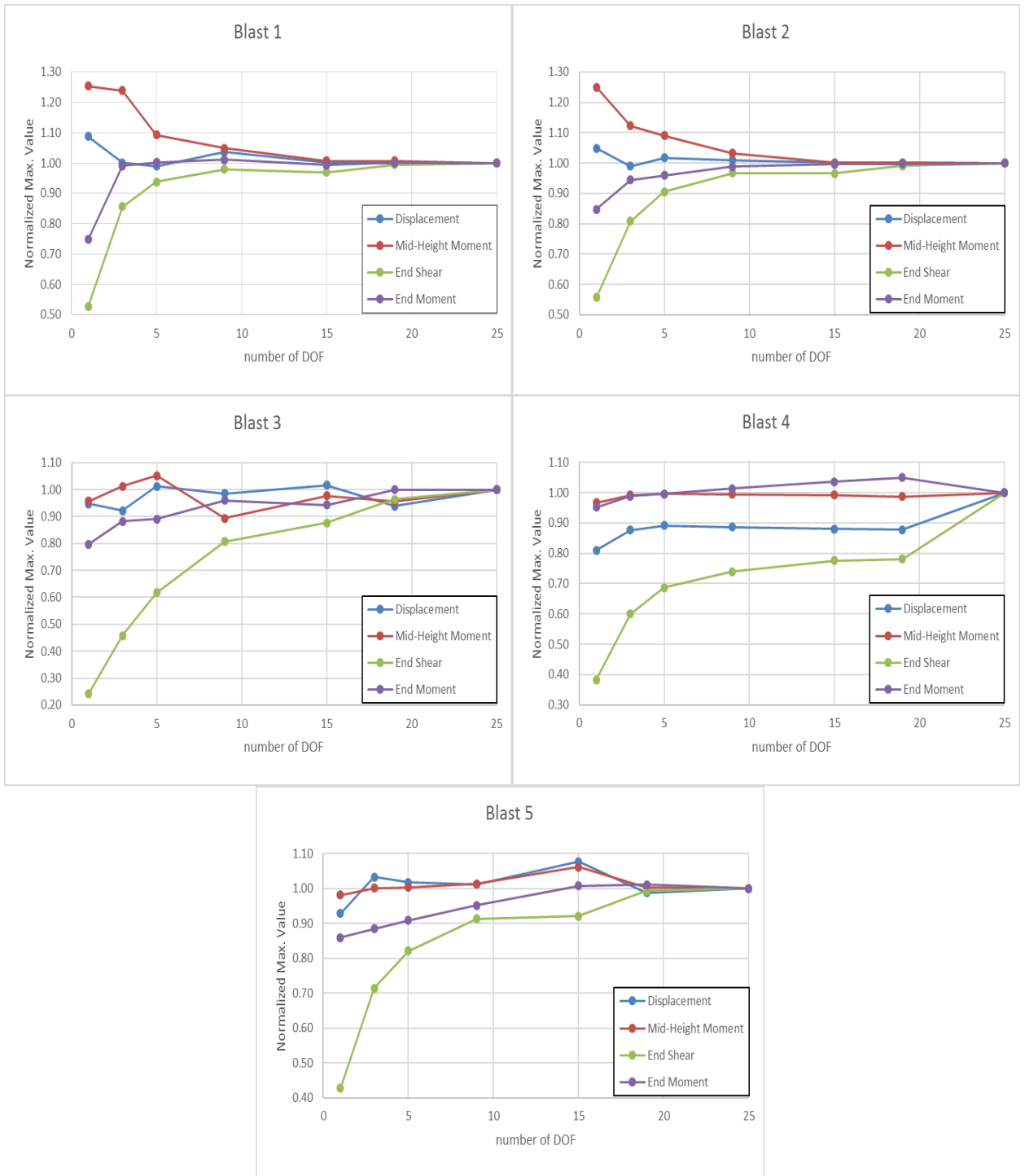


Figure 2.14. Normalized maximum response of the 500×500-mm column in different blast scenarios

2.5.3. Effects of axial load and P-delta

In this sub-section, the effect of axial loads on the response of the columns to blast loading is examined. For this purpose, the two different column sections, each with different ALR's of 12.5%, 25%, and 40%, are considered. The blast loads from the defined scenarios in Table 2.1 are applied to the MDOF models assuming tributary width of 4 m and an exponentially decaying time-history. In the simulations, 15 DOF's are assigned to the members, since it was shown that 15 DOF's for the current analytical cases can lead to sufficient accuracy, with reasonable computation costs.

The beam-column elements are generated using the material properties of the portion of the middle (unprotected) region of the columns with moderate ductility design level without the special seismic detailing. In order to investigate the effects of P-delta, the simulations are carried out with and without second order analysis in OpenSEES. The results of the numerical simulations are presented in Table 2.6 (no P-delta effect), and Table 2.7 (with P-delta effects) for 400×400-mm columns and Table 2.8 for 500×500-mm columns without P-delta effects. Since the results for both column sizes are observed to have a similar trend for P-delta effect, only the smaller columns (400×400 mm) are used in the analysis. The maximum mid-height displacements of the columns are also shown in Figure 2.15 and 2.16.

Table 2.6. Maximum response of 400×400-mm columns in blast scenarios without P-delta effects

$N / f'_c A_g$	Blast 1			Blast 2			Blast 3			Blast 4			Blast 5		
	Deflection (mm)	Moment (kN.m)	Shear (kN)												
12.5 %	8.12	385.74	551.45	22.90	412.61	755.08	52.99	454.44	901.46	131.44	489.26	1025.59	454.24	585.27	2074.59
25 %	6.73	424.52	609.01	19.20	452.73	834.28	48.29	452.71	980.61	126.95	476.34	1133.50	456.21	603.85	2169.40
40 %	5.95	455.62	632.35	17.10	473.27	821.99	48.29	471.55	1015.74	131.56	491.68	1165.04	433.99	608.92	2275.58

Table 2.7. Maximum response of 400×400-mm columns in blast scenarios with P-delta effects

$N / f'_c A_g$	Blast 1			Blast 2			Blast 3			Blast 4			Blast 5		
	Deflection (mm)	Moment (kN.m)	Shear (kN)												
12.5 %	8.17	385.85	548.40	23.24	413.16	748.87	54.44	455.96	889.89	137.14	488.57	1022.73	503.57	569.12	2066.17
25 %	6.81	426.10	606.18	19.74	452.74	812.85	51.12	452.74	961.91	139.94	496.79	1134.96	Column failed!		
40 %	6.04	457.96	626.55	17.72	473.24	808.79	52.88	471.56	1009.64	155.53	471.50	1167.51	Column failed!		

Table 2.8. Maximum response of 500×500 columns in blast scenarios without P-delta effects

$N / f'_c A_g$	Blast 1			Blast 2			Blast 3			Blast 4			Blast 5		
	Deflection (mm)	Moment (kN.m)	Shear (kN)												
12.5 %	2.86	478.69	664.16	7.12	744.30	1099.15	15.55	780.76	1343.10	43.81	880.25	1757.76	202.62	967.84	2944.05
25 %	2.35	529.75	734.85	5.69	851.51	1252.03	13.24	857.75	1472.59	48.78	857.63	2629.17	202.79	1039.41	3118.01
40 %	2.23	565.46	757.62	4.96	913.12	1275.79	13.95	915.16	1723.90	49.52	913.86	2171.03	204.54	1102.24	3457.59

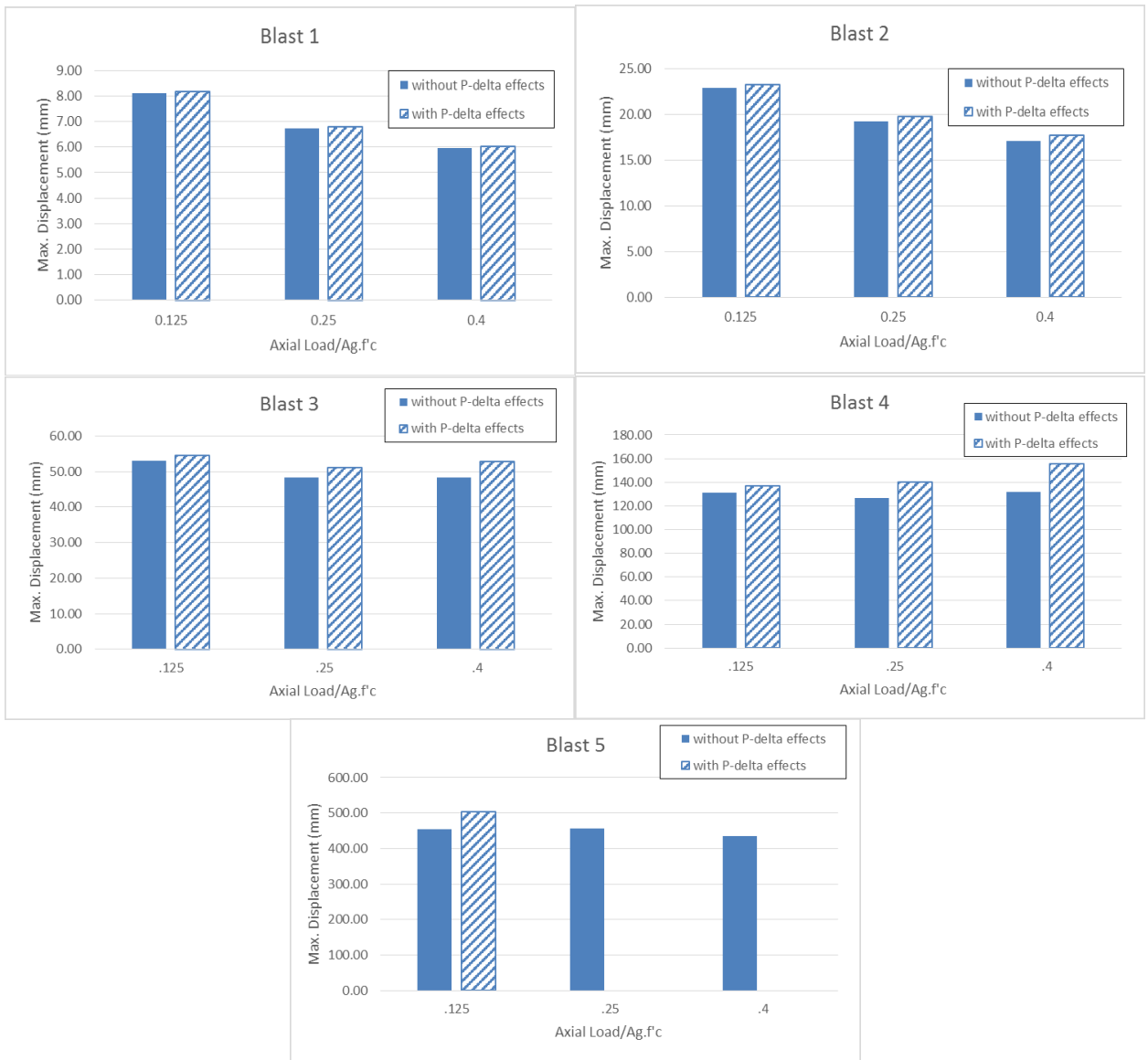


Figure 2.15. Maximum deformations for 400×400 columns with and without P-delta effects

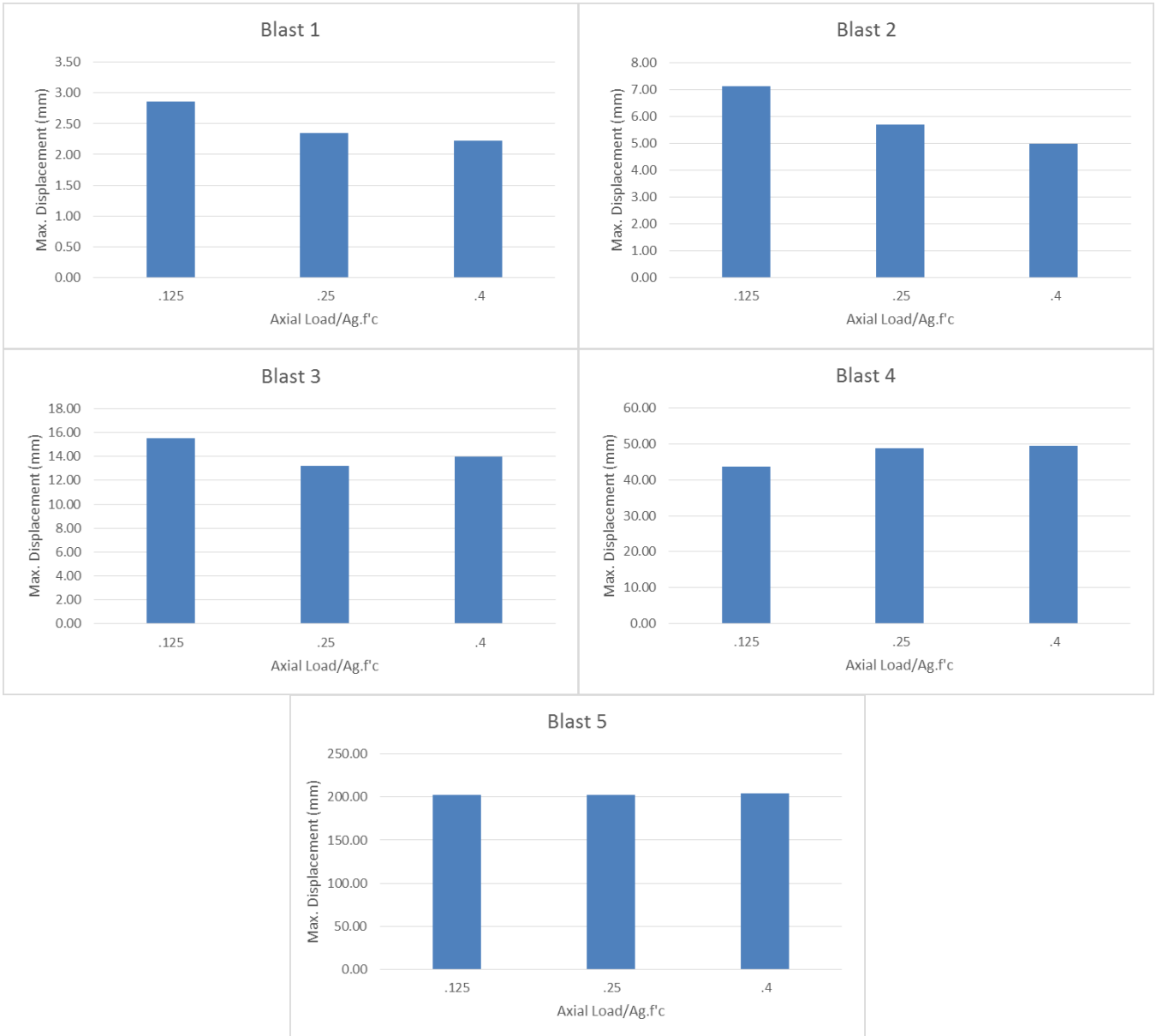


Figure 2.16. Maximum deformations for 500×500 columns without P-delta effects

From the results presented above, several conclusions can be drawn as follows:

1- Under smaller blast loads, higher axial load level improves the response of the columns and reduces the deformations.

2- The P-delta effects are less significant under smaller blast loads, as the difference between the deformations are less than 5% for blast scenarios 1 and 2.

3- Under higher blast loads, where the blast loads impose higher deformations giving support rotations (mid-height deformation divided by half the column height) of more than 0.34 degrees, the axial load level does not have a significant effect on the results, when the P-delta effects are neglected.

4- Under higher blast loads, the P-delta effects amplify the results by up to 15% or more. This amplification is more significant under the higher axial load levels. As shown in Table 2.8, the columns fail under the highest level of blast load defined in Table 2.1 when the axial load ratios are 25 and 40%.

5- When P-delta effects are included, the differences between the moments and shear reactions under different levels of axial loads are less pronounced compared to those observed in the deflections. This is because only small changes occur in the maximum capacity of the sections even as the axial load is varied.

2.5.4. Response of multi-story columns

The response of columns in multi-story buildings is examined next as a part of the study. For this purpose, the analytical model is constructed to include a continuous two-story column with two variations as shown in Figure 2.17. The height of each story is 4 m. The ALR in all the columns is assumed to be 25%. The other characteristics of the columns are the same as those used in the analysis on single columns. In the numerical analysis in this section, P-delta effects are considered as well.

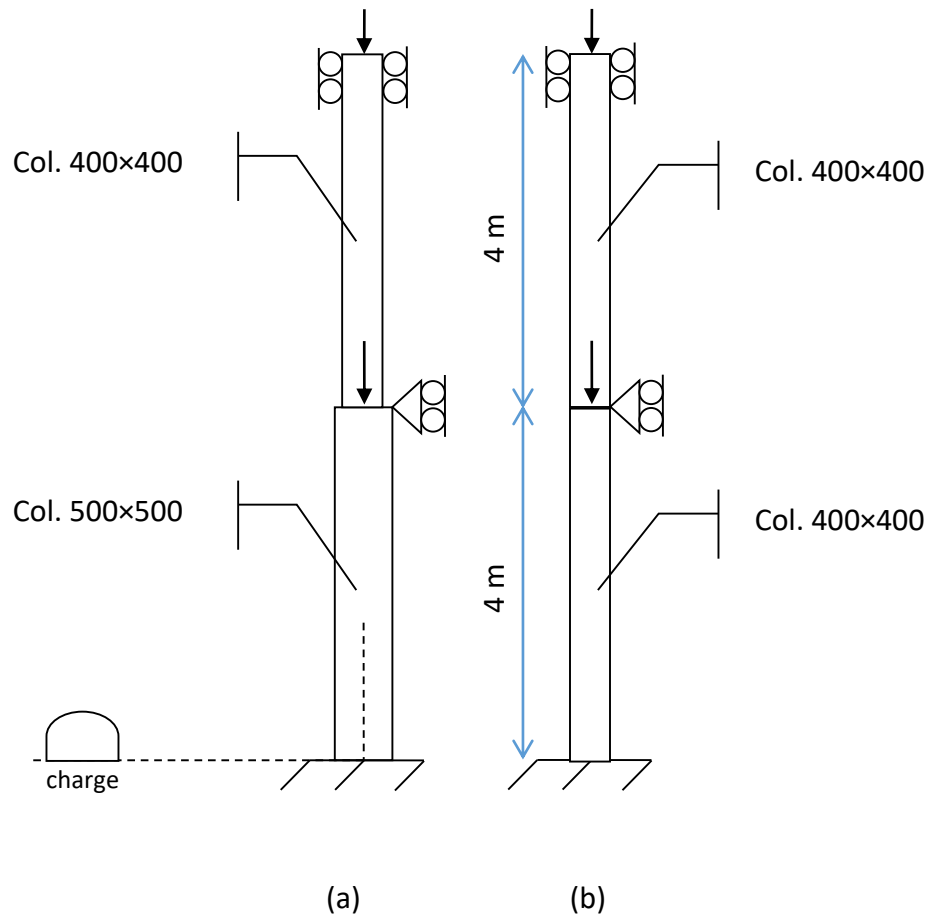


Figure 2.17. Geometrical model of 2-story column (a) bottom column is 500×500 mm and upper column is 400×400 mm, (b) both top and bottom columns are 400×400 mm

It should be noted that the fixed and pinned end conditions used here are not completely realistic since achieving complete or zero fixity in the beam-column and column to foundation connections in the actual building structures is close to impossible. However, choosing any other end conditions for the models will limit the scope of the study, since the level of fixity depends on the stiffness and characteristics of the beams and foundation. The effect of the lateral restraint at story levels on the

mid-height deflections of the columns will be studied in detail in chapter 4, where the global response of the buildings is studied.

In order to examine the response of the columns to blast loading, the continuous columns are subjected to the same 5 blast scenarios as those introduced in Section 2.3.2. For applying the blast loads to the columns, three different patterns are used as follows:

- 1- Applying a uniform load on both columns, based on the standoff distance of the first story column to the explosive charge (the same as that used previously for the single columns).
- 2- Applying a uniform blast load in each story's column, based on the distance and incident angle of the mid-height of the individual columns to the charge (the upper story column has a different load time-history than the column in the first story).
- 3- Dividing each column into three regions along height, and applying a uniform load to individual segments using the distance and incident angle corresponding to the mid-height of the segment as shown in Figure 2.18.

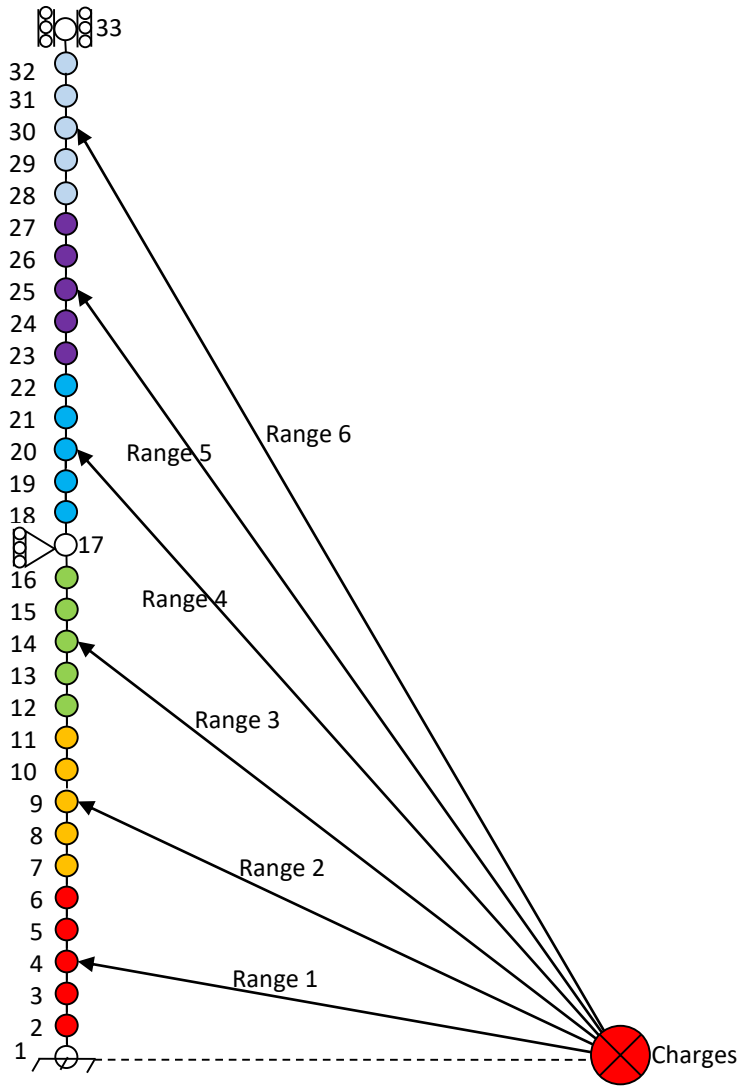


Figure 2.18. Step-by-step loading of continuous columns

2.5.4.1. Effects of loading patterns

The analytical models described above are generated with the same 15 degrees of freedom for each column and a tributary width of 4m. The blast loads with three different patterns described before are applied on the continuous columns. The resulting response values are presented in Table 2.9 and Figure 2.19-20. The values

above the bar charts show the ratio of the maximum values in each pattern to the maximum deflection for the most detailed model (segment-by-segment loading).

Table 2.9. Maximum deflection (mm) of continuous columns under different load patterns

case	1 st Story column	Loading pattern	Blast scenario	Max. deflection in 1 st st. col.	Max. deflection in 2 nd st. col.
1	400×400 mm (Fig. 2.13b)	Uniform on both columns	1	7.03	7.84
2			2	21.14	23.99
3			3	56.99	63.36
4			4	163.83	166.99
5			5	1499.17	1599.14
6		Different uniform load in each story	1	7.92	5.56
7			2	22.08	16.82
8			3	57.55	38.06
9			4	116.90	61.18
10			5	1808.01	241.69
11		Segment-by-segment loading	1	7.67	5.66
12			2	21.24	17.07
13			3	55.86	36.91
14			4	115.60	66.39
15			5	2621.64	263.36
16	500×500 mm (Fig. 2.13a)	Uniform on both columns	1	2.82	7.26
17			2	7.38	22.78
18			3	16.49	60.38
19			4	57.22	162.55
20			5	308	912.24
21		Different uniform load in each story	1	3.33	5.37
22			2	7.92	16.14
23			3	17.16	35.84
24			4	41.62	59.66
25			5	281.32	230.25
26		Segment-by-segment loading	1	3.10	5.46
27			2	7.53	16.09
28			3	16.31	35.82
29			4	39.24	65.39
30			5	267.03	241.63

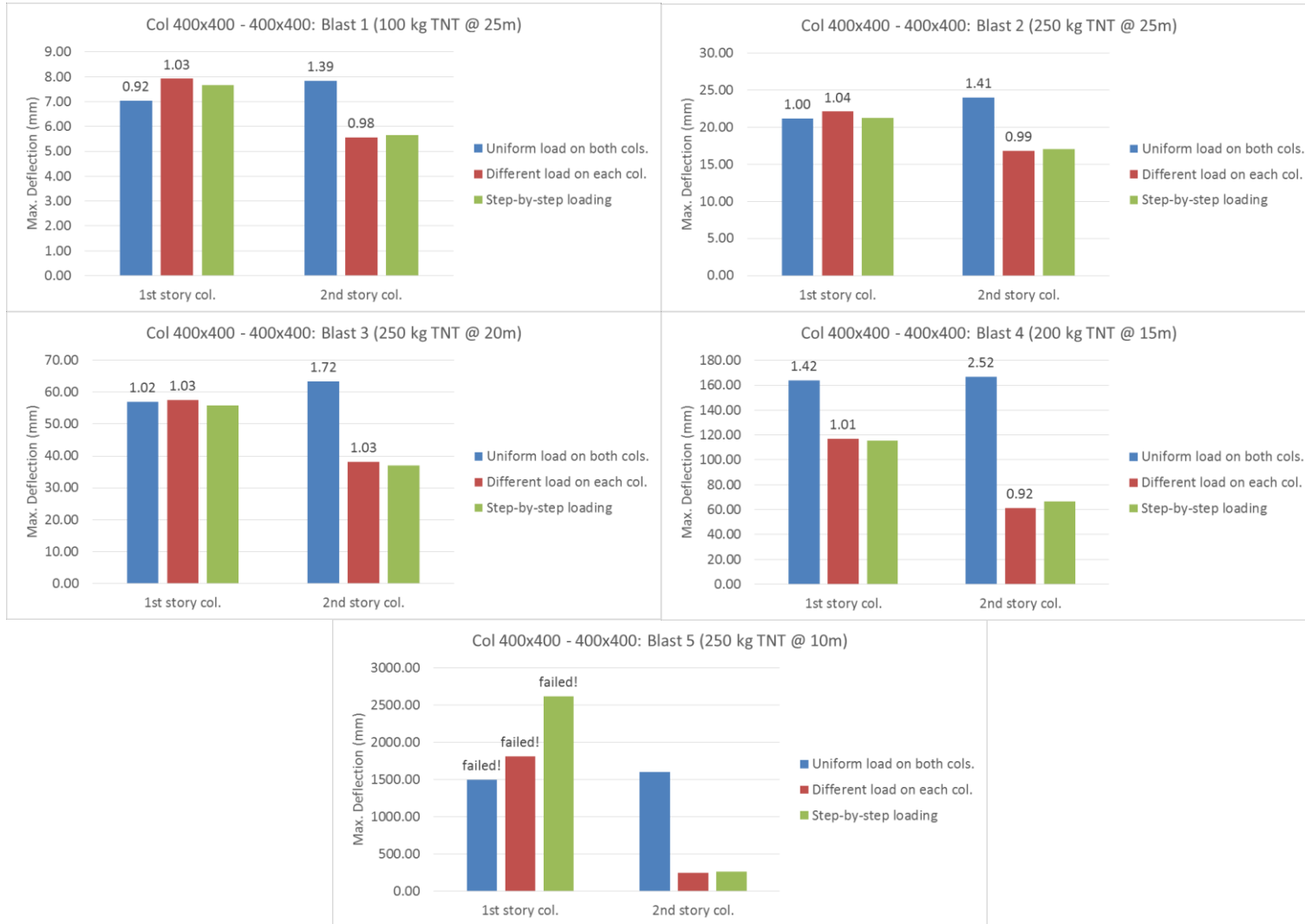


Figure 2.19. Comparison of maximum deflections in continuous columns with 400x400-mm column in 1st story

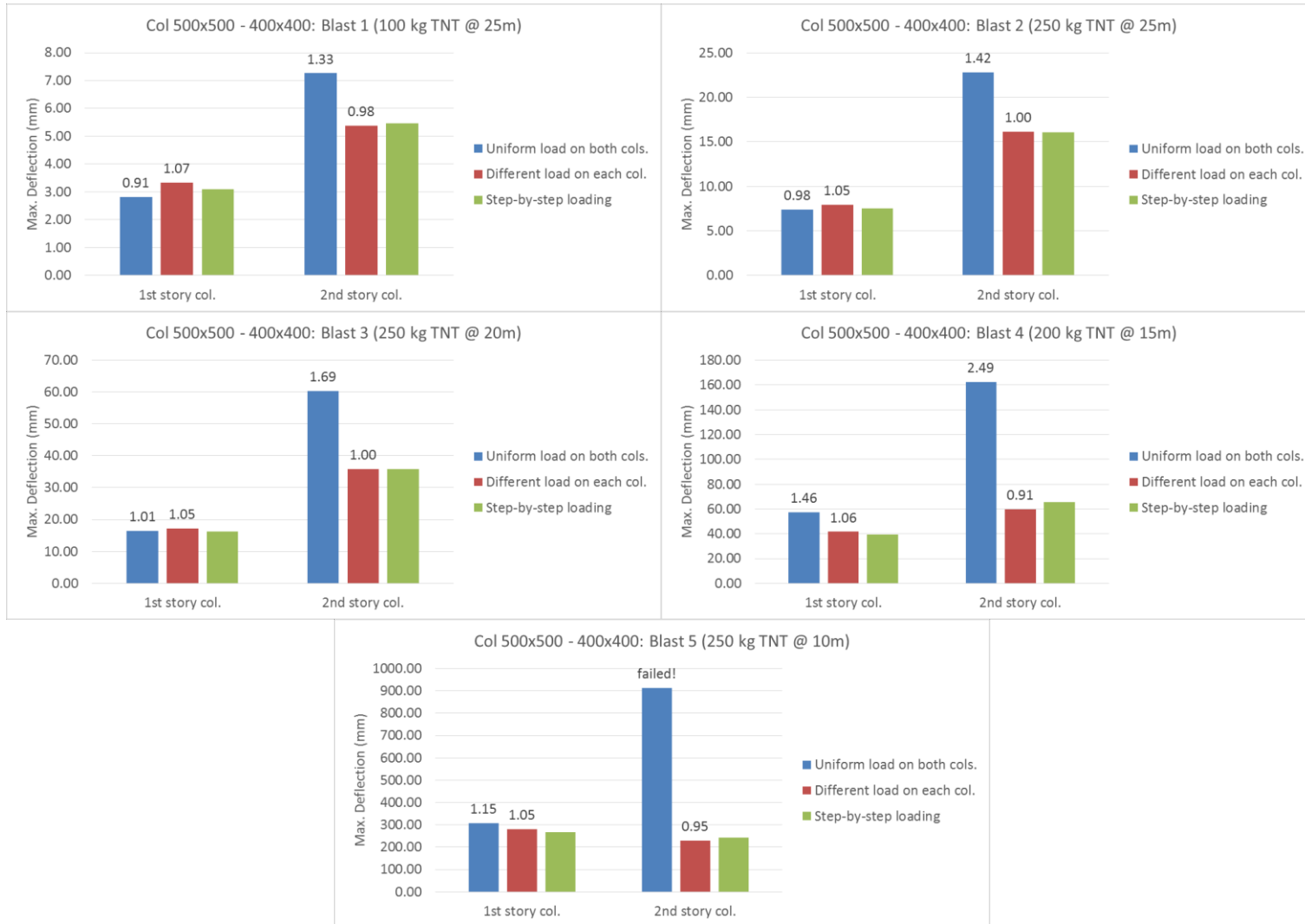


Figure 2.20. Comparison of maximum deflections in continuous columns with 500x500 column in 1st story

From the results shown above, several observations are made and conclusions drawn as follows. These observations and conclusions are based on the cases where the columns do not experience significant damage, which is assumed as having occurred when a support rotation exceeds 4 degrees (ASCE, 2010). A support rotation of 4 degrees is equivalent to 140 mm mid-height deflection in the analysed cases. The conclusions listed below do not apply to the cases that lead to these significant damages.

- 1- As is observed from the results, when the uniform simultaneous loading is applied to both columns, there is up to 46% overestimation in response of the lower-story column with respect to the more accurate segment by segment loading, when the response of the columns is in the nonlinear range (blast 4). Under smaller blast loads (scenarios 1 to 3), the response of the first story columns when subjected to all three load patterns are quite close to each other.
- 2- When the uniform simultaneous loading is applied to both columns, there is up to 72% overestimation in response of the second story column with respect to the more accurate segment by segment loading. The difference in the response of the second story column to simultaneous loading pattern and to segment-by-segment pattern is very large (between 33% to 72%) for all the cases in both elastic and inelastic response ranges.
- 3- When different uniform loading patterns are used for the columns in each story, there is up to 7% over-estimation in lower-story deflection, and up to 9% under-estimation in upper-story deflection with respect to the response of the columns under stage-by-stage loading.

4- Considering all of the results, and the cost and time required for analyzing the columns by each of the three loading patterns, it can be concluded that applying uniform loads on each column separately based on the distance and incidence angle of the mid-height of the columns can lead to relatively accurate results with less computational costs. This applies for blast loads that are in the far-field category, which is the assumption in the present analysis as discussed at the beginning of the chapter.

2.5.4.2. Comparison with response of single column

The analysis of columns for blast loading is traditionally carried out on a member-by-member fashion. Individual members are modeled with fixed or simple boundary conditions, depending on the situation, and the loads are applied uniformly and simultaneously. In this sub-section, the continuous columns described in the previous paragraphs are modeled as single members to investigate how that will affect the numerical responses.

In practice, columns in the first story are modeled with fixed boundary conditions. Therefore, the analyses described in this sub-section are carried out on columns with fixed-fixed boundary conditions. The same axial load level is applied on the members, and all the analytical parameters for both lower and upper story columns are assumed to be the same as described earlier. The loads are applied based on the reflected pressure resulting from distance and incidence angle to the mid-height of the columns (pattern 2 introduced earlier).

The numerical analyses are carried out in OpenSEES and the results in terms of maximum deflections in the columns are compared for both top and bottom columns. The results are

compared in Tables 2.10-2.11, and Figures 2.21-2.22. The values on top of the bar charts in the figures show the ratio of the results to the results for single columns.

Table 2.10. Comparison of response of first story columns in single (under first story blast loads) and continuous models

Column	Blast scenario	Max. deflection in continuous column	Max. deflection in single column	Ratio of continuous columns response to single cols.
400x400	1	7.92	6.81	1.16
	2	22.08	19.74	1.12
	3	57.55	51.12	1.13
	4	116.90	104.41	1.12
	5		Column failed!	
500x500	1	3.33	2.37	1.41
	2	7.92	5.75	1.38
	3	17.16	11.83	1.45
	4	41.62	29.98	1.39
	5	281.32	228.36	1.23

Table 2.11. Comparison of response of second story columns in single (under second story blast loads) and continuous models

Column	Blast scenario	Max. deflection in single column	Max. deflection in continuous column: On top of 400x400 col.	Ratio to single column	Max. deflection in continuous column: On top of 500x500 col.	Ratio to single column
400x400	1	6.7	5.56	0.83	5.37	0.80
	2	18.11	16.82	0.93	16.14	0.89
	3	39.11	38.06	0.97	35.84	0.92
	4	63.93	61.18	0.96	59.66	0.93
	5	230.32	Bottom col. failed!	-	230.25	1.00

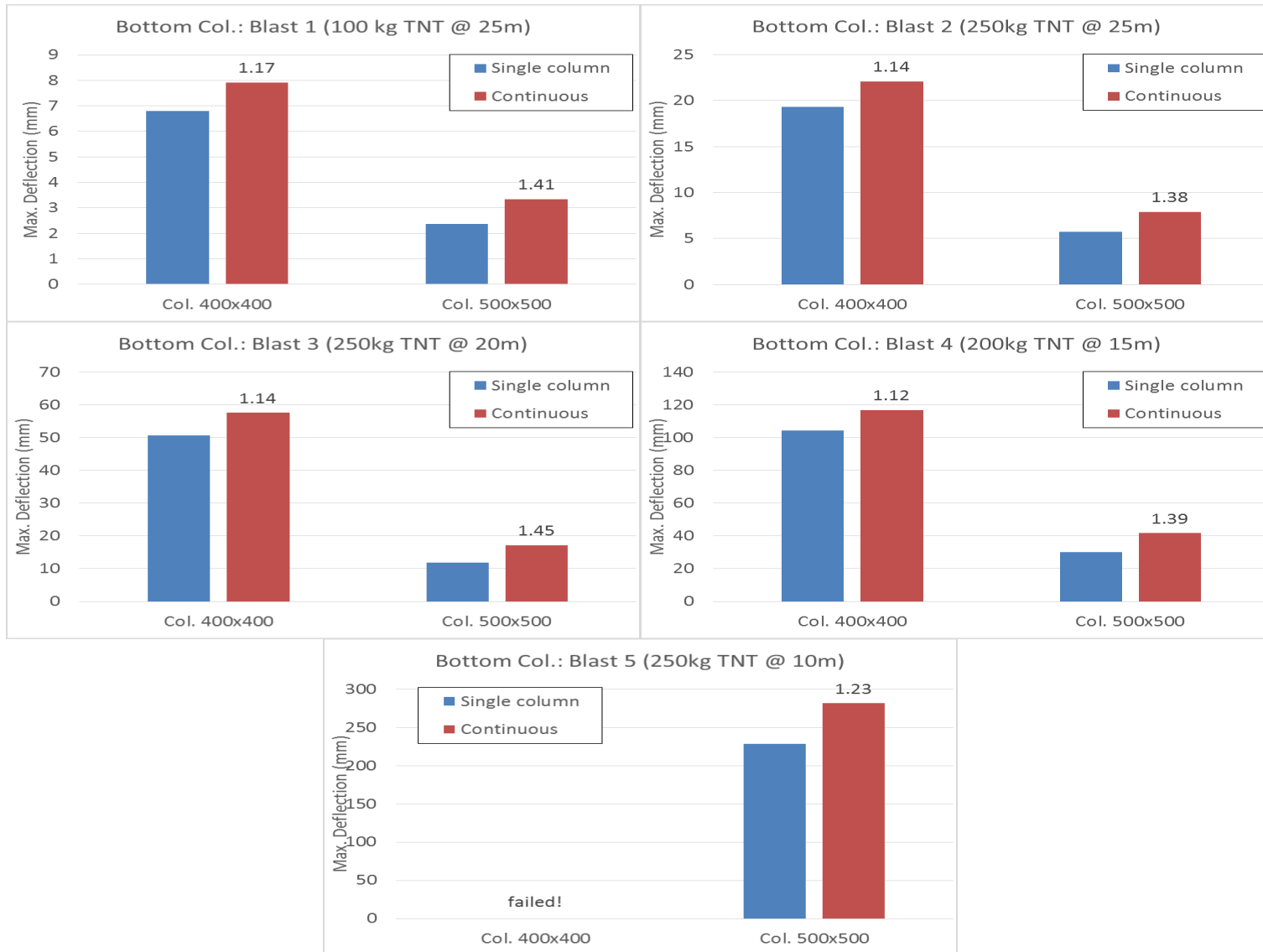


Figure 2.21. Comparison of response of bottom columns in single and continuous models

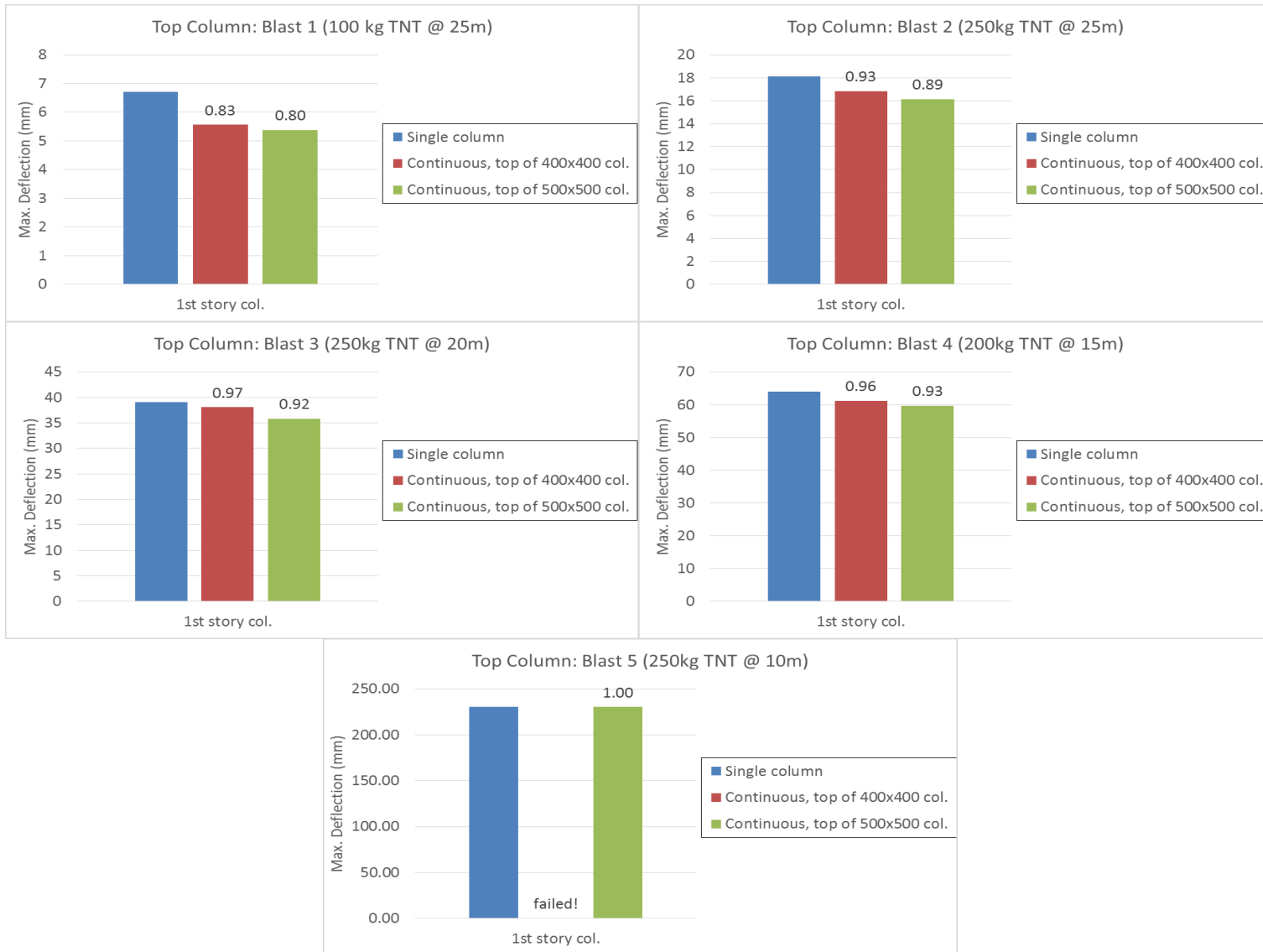


Figure 2.22. Comparison of response of top columns in single and continuous models

From the results shown above, several conclusions can be drawn as follows. It should be noted that for blast 5, in all the cases the support rotation exceeds 4 degrees and therefore the results for this blast scenarios are not included in the conclusions. These conclusions do not apply to the cases that lead to large damage (support rotation of greater than 4 degrees).

- 1- Modeling the first story columns as single elements leads to underestimation of the deflections. This is because the top end of the column is restrained against lateral deflection as well as rotation imparting to it higher stiffness. By comparison, the upper end of the first story column is restrained against only lateral displacement in the two-column model.
- 2- This difference increases for the 500×500-mm columns, as the smaller column at the top provides smaller rotational stiffness than a fixed end for the bottom columns. Thus, the difference between the results of continuous and single columns reaches up to 45% when the first story columns are 500×500 mm, compared to 17% when first story columns are 400×400 mm.
- 3- The situation is different for the top columns, where the single model yields larger deformations. This is due to the effect that the deformation of the bottom column has on the top column. Thus, the deflections are less when the bottom column is stiffer (500×500 mm).
- 4- It is concluded that modeling the columns as single elements in the traditional element-by-element fashion can lead to underestimation of the deflections for first story columns by up to 45%, while overestimating the deflections for the

second story columns. This overestimation is up to 20% in the cases analyzed here.

- 5- The differences between the results of single and continuous columns is less pronounced under more significant blasts. This is due to the fact that in higher intensity blasts, plastic hinges develop at the column ends making the difference between the continuous and fixed end conditions less important.

2.6. Verification of Numerical Model

This section presents the results of a verification of the numerical model used in this study to simulate the response of reinforced concrete columns by comparing such response against experimental results from shock tube testing of reinforced concrete columns. For this purpose, two experimental cases from Burrell et. al (2015) are selected. The columns in those tests had a height of 2468 mm, a 152-mm square cross-section, and two different transverse reinforcement details (spacing of 38 and 75 mm) as shown in Figure 2.23. The compressive strength (f'_c) and modulus of rupture (f_r) of the concrete were 51.6 MPa and 6.6 MPa, respectively. The steel rebar had yield and ultimate strengths of 483 and 675 MPa, respectively.

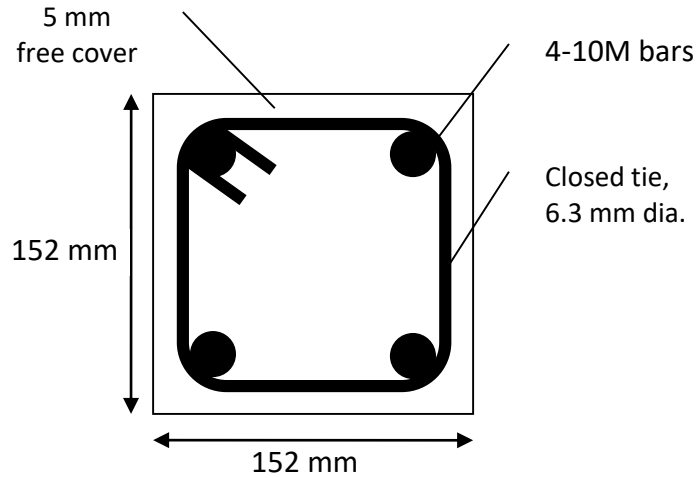


Figure 2.23. Rectangular column sections used for verification of numerical model

2.6.1. Material models

In order to use the same numerical model as that described in the earlier sections of this chapter, the confinement effects and dynamic increase factors are applied to the strength of concrete and reinforcing steel. In this regard, for the concrete, a DIF of 1.25 is used, and for the steel rebars; *DIF* of 1.23 and 1.05 are used for the yielding and ultimate strength, respectively. Also, the confinement effects are calculated by the Chang and Mander model (1994), as follows:

$$f'_{c0} = 51.6 \text{ MPa} \quad \Rightarrow \quad \boxed{E_c = 8200 f'_{c0}{}^{3/8} = 35.98 \text{ GPa}} \quad \& \quad f'_{cd} = \text{DIF} \cdot f'_{c0} = 64.5 \text{ MPa}$$

$$\varepsilon_{c0} = \frac{f'_{cd}{}^{1/4}}{1152.63} = 0.00246$$

$$\boxed{f_t = 6.6} \quad \& \quad \boxed{\varepsilon_t = 2f_t / E_c = 0.000367}$$

- For column with 38 mm spacing of transverse reinforcement (SCC-0%-38):

$$\begin{aligned}
 A_e &= \left(b_c d_c - \sum \frac{(w'_i)^2}{6} \right) \left(1 - 0.5 \frac{s'}{b_c} \right) \left(1 - 0.5 \frac{s'}{d_c} \right) \\
 &= \left(135.7 \times 135.7 - 4 \times \frac{(106.8)^2}{6} \right) \left(1 - 0.5 \times \frac{31.7}{135.7} \right) \left(1 - 0.5 \times \frac{31.7}{135.7} \right) \\
 &= 8432.48 \text{ mm}^2
 \end{aligned}$$

$$A_{cc} = b_c d_c - A_{st} = 135.7 \times 135.7 - 4 \times 100 = 18014.49 \text{ mm}^2 \Rightarrow k_e = A_e / A_{cc} = 0.468$$

$$\rho_x = \rho_y = \frac{A_{sx}}{s.d_c} = \frac{2 \times 100}{38 \times 135.7} = 3.88 \times 10^{-2} \quad \Rightarrow \quad f'_l = k_e \rho_x f_{yh} = 10.97 \text{ MPa}$$

$$q = f'_{lx} / f'_{ly} = 1.0 \quad \& \quad x' = \frac{f'_{lx} + f'_{ly}}{2f'_{cd}} = 0.17$$

$$A = 6.8886 - (0.6096 + 17.275q)e^{-4.989q} = 6.767 \quad \& \quad B = \frac{4.5}{\frac{5}{A}(0.9849 - 0.6306e^{-3.8939q}) - 0.1} = 7.28$$

$$k_1 = A \left(0.1 + \frac{0.9}{1 + Bx'} \right) = 3.40 \quad \Rightarrow \quad \boxed{f'_{cc} = f'_{cd} (1 + k_1 x') = 101.76 \text{ MPa}}$$

$$k_2 = 5k_1 = 17 \quad \Rightarrow \quad \boxed{\varepsilon_{cc} = \varepsilon_{c0} (1 + k_2 x') = 0.0096}$$

$$\boxed{x_n = 30} \quad \& \quad \boxed{x_p = 2} \quad n = \frac{E_c \varepsilon_{cc}}{f'_{cc}} = \frac{35.98 \times 10^3 \times 0.0096}{101.76} = 3.39 \quad \Rightarrow \quad \boxed{r = n / (n - 1) = 1.42}$$

- For column with 75 mm spacing of transverse reinforcement (SCC-0%-75):

$$\begin{aligned}
 A_e &= \left(b_c d_c - \sum \frac{(w'_i)^2}{6} \right) \left(1 - 0.5 \frac{s'}{b_c} \right) \left(1 - 0.5 \frac{s'}{d_c} \right) \\
 &= \left(135.7 \times 135.7 - 4 \times \frac{(106.8)^2}{6} \right) \left(1 - 0.5 \times \frac{68.7}{135.7} \right) \left(1 - 0.5 \times \frac{68.7}{135.7} \right) \\
 &= 6030.13 \text{ mm}^2
 \end{aligned}$$

$$A_{cc} = 18014.49 \text{ mm}^2 \Rightarrow k_e = A_e / A_{cc} = 0.335$$

$$\rho_x = \rho_y = \frac{A_{sx}}{s.d_c} = \frac{2 \times 100}{75 \times 135.7} = 1.94 \times 10^{-2} \quad \Rightarrow \quad f'_l = k_e \rho_x f_{yh} = 3.93 \text{ MPa}$$

$$q = f'_{lx} / f'_{ly} = 1.0 \quad \& \quad x' = \frac{f'_{lx} + f'_{ly}}{2 f'_{cd}} = 0.061$$

$$A = 6.8886 - (0.6096 + 17.275q)e^{-4.989q} = 6.767 \quad \& \quad B = \frac{4.5}{\frac{5}{A}(0.9849 - 0.6306e^{-3.8939q}) - 0.1} = 7.28$$

$$k_1 = A(0.1 + \frac{0.9}{1 + Bx'}) = 4.89 \quad \Rightarrow \quad \boxed{f'_{cc} = f'_{cd}(1 + k_1x') = 83.76 \text{ MPa}}$$

$$k_2 = 5k_1 = 24.5 \quad \Rightarrow \quad \boxed{\varepsilon_{cc} = \varepsilon_{c0}(1 + k_2x') = 0.0061}$$

$$\boxed{x_n = 30} \& \boxed{x_p = 2} \quad n = \frac{E_c \varepsilon_{cc}}{f'_{cc}} = \frac{35.98 \times 10^3 \times 0.0061}{83.76} = 2.62 \quad \Rightarrow \quad \boxed{r = n / (n - 1) = 1.62}$$

For the unconfined concrete in the cover of the section the following parameters are used in concrete01 model in OpenSEES, based on Hognestad's model.

$$f'_{cd} = 64.5 \text{ MPa} \quad \Rightarrow \quad \boxed{E_c = 4700 \sqrt{f'_c} = 37.75 \text{ GPa}}$$

$$\boxed{\varepsilon_0 = 2f'_{cd} / E_c = 0.00342}$$

$$\Rightarrow \boxed{k = \frac{0.15}{0.0038 - \varepsilon_0} = 392.18} \quad \& \quad \boxed{f'_{ca} = 0.85f'_{cd} = 54.83 \text{ MPa}}$$

For the modeling of reinforcing steel, the same Giuffre-Manegotto-Pinto material model without isotropic hardening is used (Filippou et al. 1983) as follows.

$$f_y = 483 \text{ MPa} ; DIF = 1.23 \quad \Rightarrow \quad \boxed{f_{yd} = 594.1 \text{ MPa}} \quad \boxed{E_s = 200 \text{ GPa}}$$

$$f_u = 675 \text{ MPa} ; DIF = 1.05 \quad \Rightarrow \quad \boxed{f_{ud} = 708.75 \text{ MPa}}$$

$$\boxed{\varepsilon_u = f_{yd} / E_s = 0.00297}$$

$$\boxed{\varepsilon_u = 0.035}$$

$$E_{sh} = \frac{f_{ud} - f_{yd}}{\varepsilon_u - \varepsilon_y} = 3579.5 \text{ MPa} \quad \Rightarrow$$

$$\boxed{b_{sh} = \frac{E_{sh}}{E_s} = 0.018}$$

2.6.2. Analytical model

Using the material models described above, the analytical models of the columns are generated in OpenSEES. The stiffness of the semi-rigid supports is calculated to be 903 kN.m/rad in the experiments, and is considered using rotational springs at the ends of the columns in the numerical model. Also, an axial load of 294 kN, equivalent of $0.247f'_cA_g$, is applied on the specimens initially. However, the axial load drops momentarily from this level throughout the experiment, because of the difference in the rate of the deflections in the column and the rate at which the gravity loads follow the column (Saatcioglu et al. 2011). The total mass and the loaded area of the columns are taken as 315 kg and 4.129 m² (shock tube opening area) based on the experiments. Various blast loads are applied to the specimens in the experiments. The characteristics of these loads are presented in Table 2.12. Based on the data obtained from the experiments, an ideal triangular load pulse is generated to be used in the simulations. The fictitious positive phase duration is calculated and is presented in Table 2.12.

Table 2.12. Blast load scenarios applied to the columns based on experiments

Column	Blast no.	Shock wave properties			fictitious duration
		P_r (kPa)	t_d (msec)	I_r (kPa.msec)	time (msec)
SCC-0%-75	1	13.7	22.2	130.0	19.0
	2	42.4	22.2	381.0	18.0
SCC-0%-38	1	12.7	12.9	123.2	19.4
	2	40.9	24.4	401.4	19.6
	3	79.2	32.1	755.8	19.1

It should be noted that in the original research, a total number of 7 repeated blast loads were applied to the columns. However, as the columns experience relatively large permanent deformations under the larger blast loads, the properties of the columns change drastically making it difficult to use them in the numerical simulations. Therefore, in this part of the study, only the smaller blast loads (5 cases shown in Table 2.12) are applied to the columns (modelled using 15 DOF's) and the results are compared with the experimental data in the following.

2.6.3. Results

After running the numerical analysis with the details mentioned above, the results are presented in terms of maximum displacements and support rotations, as shown in Table 2.13.

Table 2.13. Comparison of numerical and experimental results

Column	Blast no.	Experimental results		Numerical results		Numerical result / Experimental result ratio	
		Max. displacement (mm)	Max. support rotation (°)	Max. displacement (mm)	Max. support rotation (°)		
SCC-0%-75	1	6.4	0.37	6.2	0.39	0.97	1.05
	2	24.6	1.73	25.2	1.35	1.02	0.78
SCC-0%-75	1	6.6	0.38	5.7	0.36	0.86	0.95
	2	29.68	1.45	25.4	1.37	0.86	0.94
	3	90.5	5.31	80.5	2.64	0.89	0.50

In order to have a better comparison between the numerical and experimental results, the time-history of mid-height displacement of the columns from Burrell (2012) are plotted against the results from the numerical analysis in Figure 2.24.

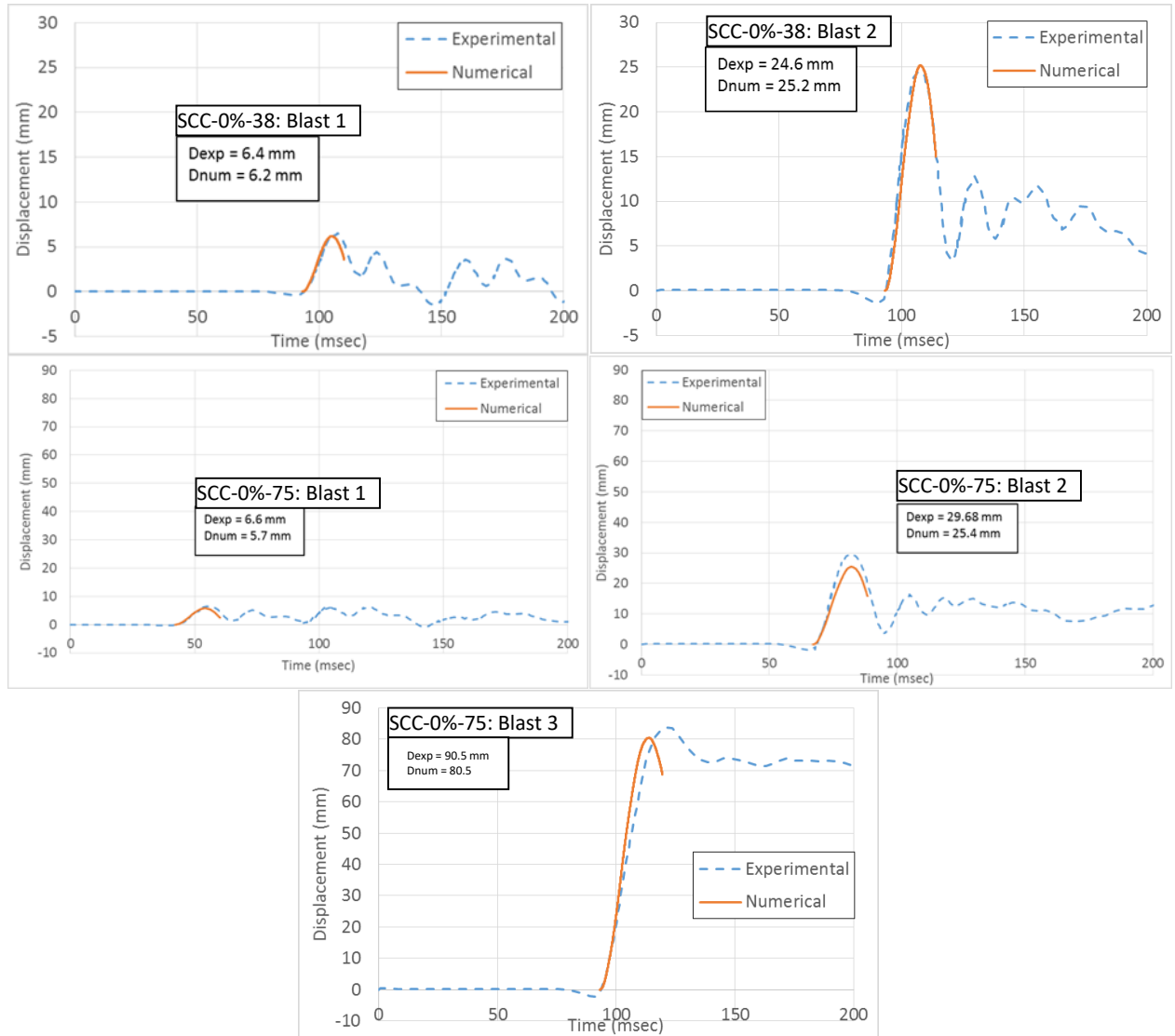


Figure 2.24. Comparison of the experimental and numerical results for columns

As can be observed from the comparison shown in Figure 2.24 and Table 2.13, the numerical model was able to capture the response of the columns in terms of both the maximum displacements and support rotations. The response of the members after the

peak can be strongly affected by the secondary blast pulses and negative pressures, which are not included in the numerical simulations. In addition, other nonlinearities and the inherent damping in the setup, as well as residual stresses and conditions of the members can significantly influence the response after the peak. This is the reason the response of the members only up to the peak displacement is compared. However, the peak response is the most important parameter for the purpose of design and analysis of the members under blast loading. Therefore, the numerical models and assumptions used in this chapter seem to be accurate and acceptable.

2.7. Summary and Conclusion

In this chapter, the effects of different parameters on the response of columns in building structures subjected to blast loads are examined numerically. The numerical model consisted of nonlinear 2D beam-column elements with spread plasticity, which modeled reinforced concrete rectangular column with two different dimensions subjected to five different far-field blast scenarios.

The study shows that the effect of shear deformations in the response of columns is quite small, being less than 15% in the maximum deflections and less than 5 % in moments in all investigated cases. Analyses using different number of degrees of freedom in modeling the columns show that the results are highly sensitive to this parameter, especially in terms of the shear forces, and the accuracy of the results depend on the number of elements into which the column is divided (or on the number

of DOF's). The amplifying effects of P-delta on the deformations of the columns, especially under higher axial load levels are also demonstrated by the analytical results.

Also, the response of a model in which both the first and second story columns are included, was examined and compared to the response obtained when the two columns are analysed independently. Different load patterns were applied to the columns. The load patterns ranged from uniform and simultaneous loads to segment by segment loading. It is shown that loading the columns in each story with a uniform load separately can give reasonable estimates of the response. The numerical analysis also shows that the traditional element-by-element analysis of single columns underestimates the response of the column in the lower story by up to 45%, while overestimates the response of the column in the higher story by up to 20%.

Toward the end of the chapter, the numerical model of cross-sectional properties used in the simulations is verified against experimental results obtained from the published literature. The maximum responses found from the numerical and experimental tests are compared. The comparison shows acceptable match between the two sets of results indicating that the models used in this study can be trusted for the cases analyzed here.

From the results described above several conclusions can be drawn as follows:

- The effect of shear deformations can be neglected in the analysis of the response of columns to blast loading.
- For accurately capturing the response of columns to blast loads, it is essential to discretize the members into a sufficient number of sub-elements. The most

response parameters most sensitive to the number of DOF's of the model are end reactions. It is recommended that at least 15 DOF's be used in the model to obtain good estimates of such reactions.

- Higher axial loads on the columns lead to smaller deflections under blast loads, when the response level is within elastic range.
- Under moderate to high axial loads, the P- δ effects need to be considered in the analysis of the response of columns to blast loading.
- Blast response of continuous columns can be different from the response that is obtained when they are modelled individually.

Chapter 3. Blast Induced Roof Loads in Building Structures

3.1. Introduction

The structural elements of the roof in a building structure that resist blast loads can be categorized into two groups. As shown in Figure 3.1, the first group is comprised of beams that span in a direction parallel to the blast shock front. The blast overpressure on these members can be assumed as being uniform across the span since the distance from the explosive charge to different points on the beam is not significantly different. Analysis of these roof beams is carried out in the same way as of the columns on the front face of the building to blast load from far-field explosion, where the blast loads are generally uniformly distributed along the length of the member. The other group is comprised of beams that span in a direction perpendicular to the blast shockfront. For these beams, the blast loads may vary significantly along the span. This chapter deals with the challenges in the analysis of the beams that are perpendicular to the blast wave shockfront, and throughout the remainder of the chapter this type of members is meant when roof beams are mentioned.

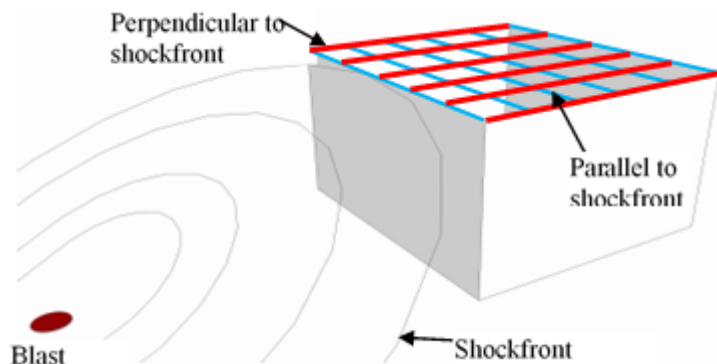


Figure 3.1. Different members in the roof subject to blast loading

The theory that governs the propagation of the blast wave along the roof span has been discussed in several different references including Glasstone and Dolan 1977, DoD 2008, and ASCE 2010. As discussed earlier, when the blast wave from an explosion reaches the front face of a building, it is reflected from the surface. The reflected overpressure decays to the stagnation pressure within the clearing time. After a while, the blast wave diffracts around the structure, and exerts pressure on the roof as well as on the side walls. For a flat roof, reflection does not occur and the pressure instantaneously rises to the incident overpressure. The net pressure on the roof is a combination of the incident overpressure and the dynamic wind pressure. The latter, also referred to as drag pressure, is negative in this case as it exerts suction on the roof members (Glasstone and Dolan 1977, DoD 2008).

As the blast wave propagates along the span of the roof, the maximum incident pressure decays while the wavelength increases as illustrated in Figure 3.2. It is evident from Figure 3.2 that the distribution of pressure along the length of the beam is a function of both the space and the time. At any specific time, only a portion of the roof may be loaded, depending on the location of the shock front and the wavelength of the travelling wave as well as the length of the roof.

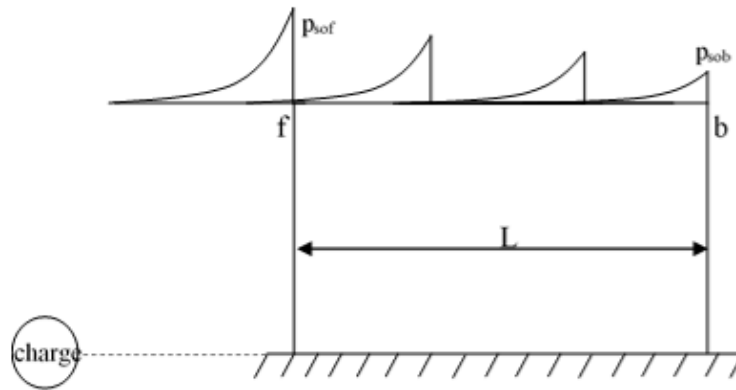


Figure 3.2. Shock wave propagation along the roof span

The total pressure at any point on the roof surface can be determined from Equation 3.1.

$$P(t) = P_{so}(t) + C_D q_o(t) \quad (3.1)$$

where $P_{so}(t)$ is the side-on (incident) pressure, $q_o(t)$ is the dynamic pressure, and C_D is the drag coefficient, which can be obtained from Table 3.1.

Table 3.1. Drag coefficient for roof beams (DoD 2008)

Peak dynamic pressure, q_o (kPa)	Drag coefficient, C_D
0 – 170	-0.40
170 – 350	-0.30
350 - 1000	-0.20

Calculation of the exact blast wave forces that act on the roof of a structure is complicated because of the spatial and temporal variation of the blast load. In order to develop a simple methodology for the design and analysis of buildings and structures

subject to blast, it has been suggested that the blast pressure be assumed as being spatially-uniform over the span, but varying with time. The proposed methodologies are valid only when the cross-sectional properties of the roof member remain uniform across the span length (DOD, 2008).

There are, however, differences in how the magnitude of the uniform load and its variation with time is defined by different sources in the literature. UFC 3-340-02 (DoD 2008) uses the pressure values at the front of the roof (point f in Figure 3.2), P_{sof} and q_{of} along with an equivalent uniform load coefficient C_E in the determination of the maximum pressure (q_{of} is based on the equivalent side-on pressure $C_E P_{sof}$). The equivalent uniform load coefficient depends on the ratio of the blast wavelength at the instant it arrives at point f, L_{wf} , to the span of roof, L . The time it takes for the uniform pressure on the surface to rise to its maximum value, t_d and also the duration of the loads t_{of} can be obtained from charts given in UFC 3-340-02 (DoD 2008), as a function of the wavelength to span ratio. The maximum equivalent pressure is given by Equation 3.2, and the proposed time-history for the uniform load is shown in Figure 3.3.

$$P_r = C_E P_{sof} + C_D q_{of} \quad (3.2)$$

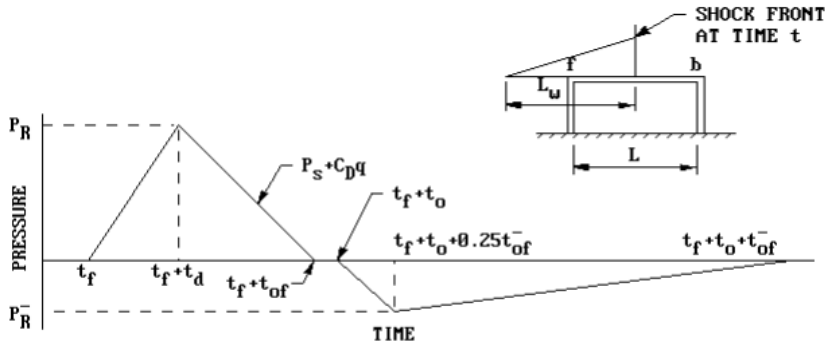


Figure 3.3. Pressure time-history on roof beams in UFC 3-340-02 (DoD 2008)

Unlike UFC 3-340-02 (DoD 2008), Glasstone and Dolan (1977) uses the mid-span of the roof as the reference for calculating the equivalent uniform load, and a different rise time equal to L/U , where U is the blast wave velocity at mid-span, and a different pressure-time history as shown in Figure 3.4. In Figure 3.4, t_p^+ is the duration of the positive phase of blast at midspan of the roof.

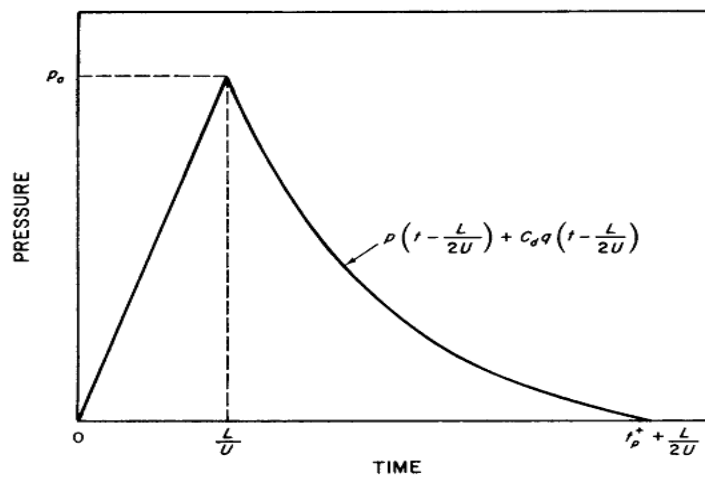


Figure 3.4. Pressure time-history on roof beams in (Glasstone and Dolan 1977)

ASCE (2010) suggests the blast load magnitude as that based on UFC 3-340-02, but the rise time calculated based on roof span and shock front velocity. In TM 5-855 (DoA 1986), the manual associated with CONWEP computer program, an expression similar to Equation 3.2 is suggested for determining the peak pressure, but instead of using the blast wave parameters at the front, the blast wave parameters at the rear (b) in Figure 3.2) of the roof are used, as shown in Equation 3.3. The blast pressure time-history profiles as given by ASCE (2010) and TM 5-855 (DOA 1986) are illustrated in Figures 3.5(B) and 3.5(C), respectively.

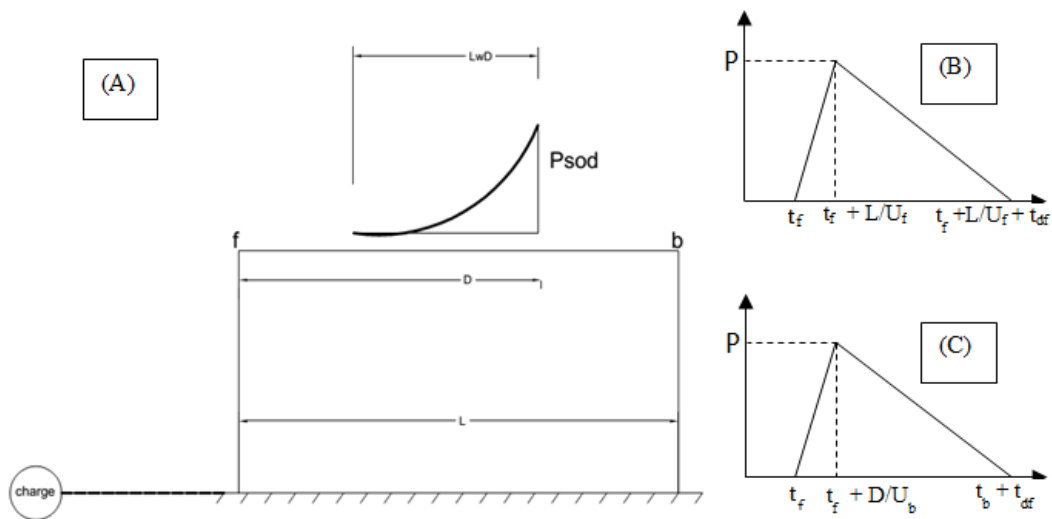


Figure 3.5. Definition of parameters in blast time-histories, based on (B) ASCE (2010) and (C) TM 5-855 (DOA 1986)

$$P = C_E P_{sob} + C_D q_{ob} \quad (3.3)$$

In the time-histories shown in the Figure 3.5, t_f and t_b are the arrival times of the blast wave at points f and b respectively, and D is the location of a point along the span at which the shock front causes the highest deflection and stresses in the beams. The

location of point D is determined from empirical charts given in TM 5-855 (DOA 1986) where D is given as a function of the wavelength to roof span ratio. Parameters U_b , U_D and U_f are the shock front velocities at points b, D and f, respectively. Also, t_{db} and t_{df} are the positive phase durations of the blast wave calculated from parameters at points b and f.

The suggested curves given in UFC 3-340.02 and TM-855 for determining the equivalent load coefficients C_E are compared in Figure 3.6. It should be noted that the reference points for calculating the wavelength of the blast are different in the two methodologies, as discussed above.

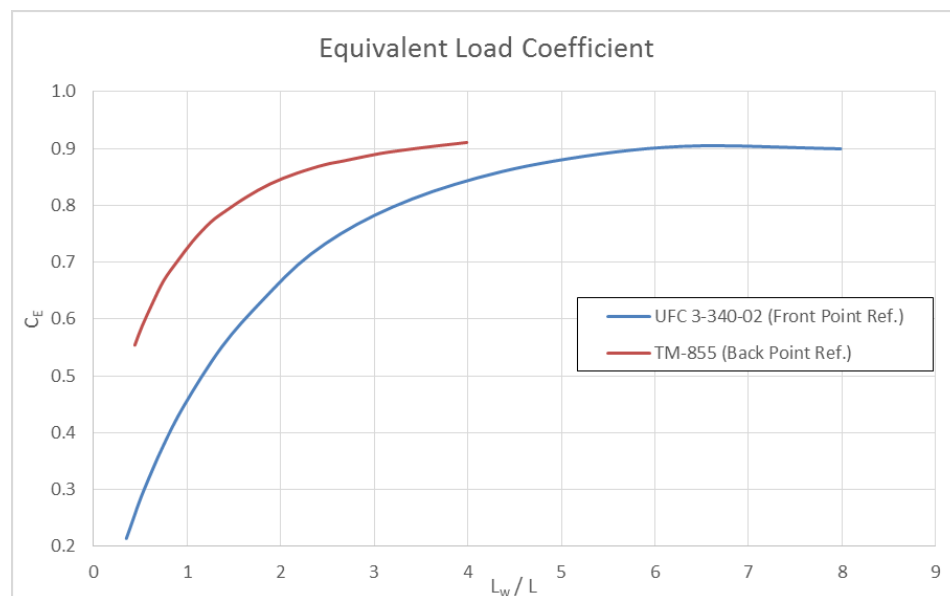


Figure 3.6. Equivalent load coefficient in UFC 3-340-02 and TM-855 documents

The methodologies described in the foregoing have been used for many years in protective design and analysis of buildings; however, there are several research studies in which the exact moving blast loads are used instead of the equivalent uniform distributions. Recognizing the availability of high performance computing in recent

years, a more accurate response of the building structures is assessed based on comprehensive models taking advantage of Computational Fluid Dynamics (CFD) in many research studies (Luccioni et al. 2004, Tadepalli & Mullen 2008, Jan & Gurbuz 2008). In all of the referenced studies, the loading produced by the propagating blast wave is used in association with a Finite Elements Method (FEM) of analysis.

A recent research study has attempted to verify the validity of the equivalent blast loading of the roof systems by means of numerical simulation and experimental tests (McClendon 2007). In that study, the roof beams were modeled by beam elements and analyzed by FEM in LS-DYNA software. The blast load properties were obtained by CONWEP, and applied to the beams in an equivalent uniform method, and also as dynamic moving loads considering both the positive and negative phases. The peak deflections of the beams, under simply supported conditions, were derived by both methods and compared to the results of the field tests. The comparison showed satisfactory consistency between the FEA results and the tests, despite the insufficient precision in the equivalent uniform method.

In the McClendon study, a simply supported steel beam with a length of 6.1 m was modeled in LS-DYNA. The beam was divided into five elements, in which the blast load characteristics, such as the peak blast load, varied. For the analysis, a hemispherical surface explosive of 453.6 kg of TNT located 9.14 m from the front side of the roof was selected, and the blast wave parameters at the middle of the five different elements were calculated by CONWEP and applied to the beam elements (McClendon, 2007).

Different shapes of blast time history, with the same value of impulse, were considered and the deflections of the beam at the quarter-length points were investigated. The maximum deflection of the beam occurred at the mid-point in all cases when the blast load neglected the negative phase. The analyses were repeated with the blast loading including the negative phase, which showed a lower initial deflection, but a higher peak deflection on the rebound.

The comparison of the numerical results obtained from the travelling wave loading and the equivalent uniform loading of the beam with the field tests showed some important observations. First, the response of the beams in the travelling wave simulations closely matched the experimental results in the first cycle of response. After the first peak, the numerical deflections were higher than in the tests, since the effect of damping was neglected in the simulations. Second, the equivalent load method was unable to predict the maximum deflection; in some cases, it gave values that were up to 50% higher than the experimental results.

3.2. Study on the Validity of Current Methodologies

The validity of the different approaches to the analysis of roof beams for blast loading described in the previous sections is examined in this part of the thesis. For this purpose, blast loads based on different selected scenarios are applied on single-span, simply supported steel beams as equivalent uniform loads, or as the loads produced by a traversing blast wave. Dynamic analyses for the uniform loads are performed based on both the traditional SDOF analysis, and an MDOF simulation. These are followed by a

MDOF analysis for the blast load produced by the traversing wave. The objective here is to highlight the differences between the response produced by traditional simplified methodologies and those obtained from the analyses for a more accurate representation of the blast loads.

3.2.1. Structure and Blast Load Description

In the research by McClendon (2007), it was shown that the negative phase of the blast wave may be ignored, especially in determining the first and largest peak of the deflection. Therefore, in the present study only the positive phase of the blast is considered. Also, it is evident from the background presented in the previous section that according to the current methodologies the most important variables in the problem are the blast wavelength and roof span. Consequently, a range of blast wavelength to span length ratios is considered in the present study. The selected blast scenarios, along with the distances from the charges to the first point of the roof are presented in Table 3.2. The blast wave parameters related to the front point on the roof calculated using CONWEP are also presented in Table 3.2.

The selected blast scenarios shown in the table are all from the category of far-field explosions, since the selection of near-field explosions would add to the complexity of the problem, and also the model used is not capable of capturing the direct damages from the shockfront and shear damages due to the near-field blasts. Also, the selection of the blast scenarios ensures that a wide range of wavelength to span length ratios is investigated.

Table 3.2. Definition of selected blast scenarios (calculated for front point of the roof)

Parameter		Blast 1	Blast 2	Blast 3	Blast 4	Blast 5
W (kg)	Charge weight	100	250	250	500	2000
R (m)	Standoff dist.	25	25	10	10	15
Z (m/kg ^{1/3})	Scaled dist. to front	5.39	3.97	1.59	1.26	1.19
P_{sof} (kPa)	Peak Incident Pres.	37.99	65.89	483.40	819.00	929.40
q_{of} (kPa)	Peak Dynamic Pres.	4.82	13.99	489.11	1095.42	1315.54
t_f (msec)	Arrival time	42.85	35.96	6.90	5.70	8.10
t_{df} (msec)	Positive phase duration time (exponential form)	18.08	21.48	13.30	17.50	27.30
U_f (m/s)	Shock front velocity	391.1	425.1	764.0	953.1	1077.0
L_{wf} (m)	Wavelength = $U_f \cdot t_{df}$	7.07	9.13	10.16	16.68	29.40

For the structural properties used in this study, single span, simply-supported steel beams with W610x101, and W360x101 sections are selected. The properties of these two sections are presented in Table 3.3. Modulus of elasticity, yield stress, and ultimate stress of steel are assumed to be 200 GPa, 345 MPa, and 485 MPa, respectively. Considering that the in-situ steel strength is generally higher than the specified strength and that the high strain rates associated with response to blast loads cause significant increase in the yield and ultimate strengths, a strength increase factor (SIF) of 1.10 and dynamic increase factors (DIF) of 1.19 and 1.05 for yield and ultimate strength, respectively, are used in the analysis (DoD 2008). The steel is assumed to conform to CSA G40.21 (similar to ASTM A588). Based on the design manuals (ASCE 2010), the stress-strain relationship of the steel material used is shown in Figure 3.7 for static and dynamic behavior.

Table 3.3. Structural properties of steel beams of the roof

Parameter	W610 x 101	W360 x 101
total depth (mm)	603	357
flange width (mm)	228	255
flange thickness (mm)	14.9	18.3
web thickness (mm)	10.5	10.5
mass per unit length (kg/m)	101.7	101.2
section modulus, S (mm ³)	2530×10^3	1690×10^3
plastic section modulus, Z (mm ³)	2900×10^3	1880×10^3
moment of inertia, I (mm ⁴)	764×10^6	301×10^6

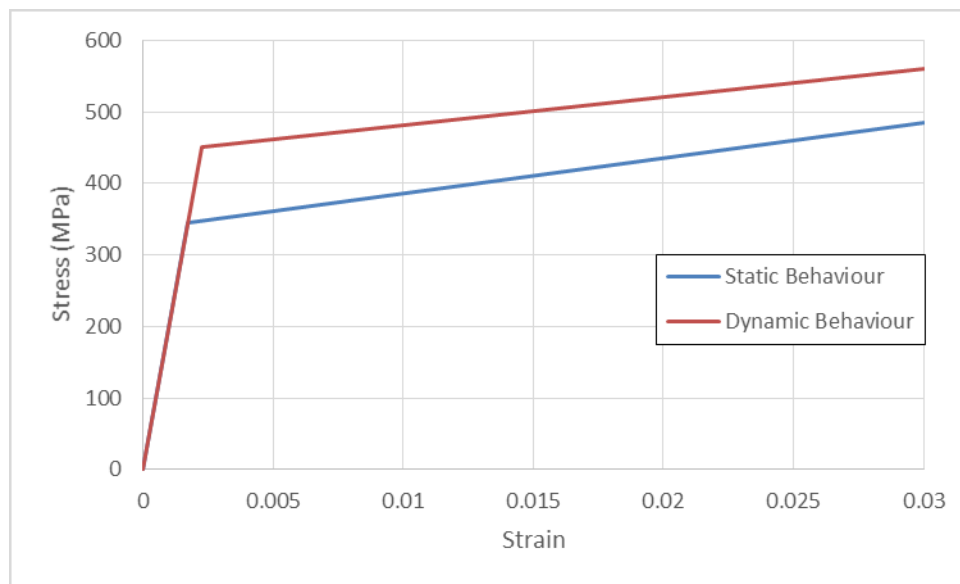


Figure 3.7. Nominal Static and actual dynamic behavior of G40.21 (ASTM A588) steel material

The roof beams are assumed to carry the dead load and blast pressure loads from tributary slab widths of 3 and 6 meters. The dead load is comprised of the weight of a 120-mm concrete slab (8.5 and 17.0 kN/m for 3-m and 6-m tributary widths,

respectively). No composite action is assumed between the concrete slab and steel beam. Three different span lengths for the steel beams are considered (4 m, 6 m and 12 m). Based on the definition of the blast scenarios, the beam spans, tributary width and the roof beams selected, 60 different analysis cases are generated as shown in Table 3.4.

Table 3.4. Array for the selected analysis cases

Case no.	Blast scenario	Beam span length (m)	Roof width (m)	Beam section
1 - 3	B 1	4, 6, 12		
4 - 6	B 2	4, 6, 12		
7 - 9	B 3	4, 6, 12	3	
10 - 12	B 4	4, 6, 12		
13 - 15	B 5	4, 6, 12		
16 - 18	B 1	4, 6, 12		W610x101
19 - 21	B 2	4, 6, 12		
22 - 24	B 3	4, 6, 12	6	
25 - 27	B 4	4, 6, 12		
28 - 30	B 5	4, 6, 12		
31 - 33	B 1	4, 6, 12		
34 - 36	B 2	4, 6, 12		
37 - 39	B 3	4, 6, 12	3	
40 - 42	B 4	4, 6, 12		
43 - 45	B 5	4, 6, 12		
46 - 48	B 1	4, 6, 12		
49 - 51	B 2	4, 6, 12		
52 - 54	B 3	4, 6, 12	6	
55 - 57	B 4	4, 6, 12		
58 - 60	B 5	4, 6, 12		

3.2.2. Analysis for Equivalent Uniform Loading

The responses of the roof beams are obtained by the simplified methodologies presented in the UFC 3-340-02 and TM 5-855 documents. The uniform load calculations for deriving the time-history of the dynamic load are presented first followed by the results of the dynamic analyses of the beams for the derived equivalent loads, using both SDOF and MDOF models.

3.2.2.1. Calculation of equivalent uniform loads

As discussed earlier, major differences exist between methodologies suggested by different sources for determining the equivalent uniform load on the side walls and roof of buildings. The two most used methodologies based on technical manuals (TM5-855) and task committees (ASCE 2010) which is based on UFC 3-340-02 methodology (DoD 2008) are used here for generating the simplified uniform loads for the different analysis cases. The two procedures differ not only in how the peak equivalent pressure (P_E) is determined, but also in the calculation of the rise time (t_r) and the total duration of the simplified uniform load (t_0), as shown in Figure 3.5. The uniform load characteristics derived on the basis of the two methodologies are presented in Tables 3.5 and 3.6, and the blast time-histories generated based on the two methodologies are compared in Figures 3.8 and 3.9. As discussed in the literature review, the blast loads depend only on the span of the roof and the blast scenario, therefore variations in the tributary width of the roof and the beam sections do not change the pressures and blast time-histories. Thus, the calculations are carried out for cases 1-15 according to Table 3.4, and all other cases use the same pressure time-histories.

Table 3.5. Equivalent uniform load characteristics based on ASCE 2010 and UFC 3-340-02 methodologies

Case no.	Blast Type	Span (m)	L_{wf} (m)	L_{wf}/L	C_E	P_{sof} (kPa)	q_{of} (kPa)	C_D	P_e (kPa)	U_f (m/sec)	t_{df} (msec)	t_r (msec)	t_0 (msec)	Impulse (kPa.msec)
1	B 1	4	7.07	1.77	0.63	37.99	1.96	-0.4	23.21	391.10	13.55	10.2	23.8	276.20
2	B 1	6	7.07	1.18	0.51	37.99	1.27	-0.4	18.69	391.10	13.55	15.3	28.9	270.07
3	B 1	12	7.07	0.59	0.32	37.99	0.50	-0.4	11.84	391.10	13.55	30.7	44.2	261.66
4	B 2	4	9.13	2.28	0.71	65.89	7.19	-0.4	43.76	425.10	13.87	9.4	23.3	509.80
5	B 2	6	9.13	1.52	0.59	65.89	4.97	-0.4	36.56	425.10	13.87	14.1	28.0	511.84
6	B 2	12	9.13	0.76	0.38	65.89	2.13	-0.4	24.17	425.10	13.87	28.2	42.1	508.78
7	B 3	4	10.16	2.54	0.74	483.40	298.06	-0.3	267.04	764.00	4.37	5.2	9.6	1281.79
8	B 3	6	10.16	1.69	0.62	483.40	221.62	-0.3	232.48	764.00	4.37	7.9	12.2	1418.13
9	B 3	12	10.16	0.85	0.41	483.40	107.53	-0.4	154.48	764.00	4.37	15.7	20.1	1552.52
10	B 4	4	16.68	4.17	0.85	819.00	864.42	-0.2	524.53	953.10	4.00	4.2	8.2	2150.57
11	B 4	6	16.68	2.78	0.76	819.00	728.90	-0.2	477.54	953.10	4.00	6.3	10.3	2459.33
12	B 4	12	16.68	1.39	0.56	819.00	446.02	-0.2	366.74	953.10	4.00	12.6	16.6	3043.94
13	B 5	4	29.4	7.35	0.90	929.40	1131.81	-0.2	610.20	1077.00	5.84	3.7	9.6	2928.96
14	B 5	6	29.4	4.90	0.88	929.40	1093.63	-0.2	598.43	1077.00	5.84	5.6	11.4	3411.05
15	B 5	12	29.4	2.45	0.73	929.40	825.12	-0.2	511.20	1077.00	5.84	11.1	17.0	4345.20

Table 3.6. Equivalent uniform load characteristics based on TM 5-855 methodology

Case no.	Blast Type	Span (m)	P_{sob} (kPa)	U_b (m/s)	t_{db} (msec)	L_{wb} (m)	L_{wb}/L	C_E	q_{ob} (kPa)	C_D	P_e (kPa)	D/L	t_f (msec)	t_b (msec)	t_r (msec)	t_0 (msec)	Impulse (kPa.msec)
1	B 1	4	29.70	380.40	19.1	7.27	1.82	0.83	2.08	-0.4	23.86	0.806	42.9	53.3	8.5	24.0	286.32
2	B 1	6	26.80	376.60	19.5	7.34	1.22	0.77	1.44	-0.4	19.95	0.724	42.9	58.6	11.5	29.3	292.27
3	B 1	12	20.40	368.30	20.7	7.62	0.64	0.63	0.57	-0.4	12.61	0.555	42.9	74.7	18.1	45.4	286.25
4	B 2	4	50.01	406.13	23.0	9.36	2.34	0.86	6.21	-0.4	40.75	0.848	36.0	54.7	8.4	32.6	664.23
5	B 2	6	44.41	399.19	23.7	9.46	1.58	0.81	4.34	-0.4	34.22	0.78	36.0	50.7	11.7	28.6	489.35
6	B 2	12	32.88	384.53	25.3	9.73	0.81	0.68	1.72	-0.4	21.73	0.623	36.0	66.1	19.4	44.0	478.06
7	B 3	4	223.18	577.69	13.3	7.70	1.93	0.84	97.88	-0.4	148.21	0.815	6.9	13	5.6	10.5	778.10
8	B 3	6	165.63	527.48	14.8	7.79	1.30	0.78	49.37	-0.4	108.89	0.738	6.9	16.6	8.4	14.1	767.67
9	B 3	12	84.63	446.39	19.9	8.90	0.74	0.66	10.28	-0.4	51.99	0.598	6.9	29	16.1	26.5	688.87
10	B 4	4	378.95	695.21	16.3	11.30	2.83	0.88	268.94	-0.3	254.52	0.869	5.7	10.6	5.0	8.9	1132.61
11	B 4	6	278.66	622.13	16.3	10.13	1.69	0.82	139.33	-0.3	186.83	0.793	5.7	13.7	7.6	12.0	1120.98
12	B 4	12	136.91	500.39	20.7	10.37	0.86	0.70	28.17	-0.4	83.94	0.638	5.7	24.5	15.3	22.8	956.92
13	B 5	4	544.05	801.37	27.1	21.75	5.44	0.9 *	829.65	-0.2	389.66	0.9 *	8.1	12.6	4.5	10.3	2006.75
14	B 5	6	431.92	730.90	26.2	19.12	3.19	0.89	340.28	-0.3	284.05	0.878	8.1	15.2	7.2	12.9	1832.12
15	B 5	12	242.37	593.44	26.3	15.60	1.30	0.78	98.75	-0.4	148.79	0.738	8.1	24.3	14.9	22.0	1636.69

* These values were derived using extrapolation of the curves outside the given range.

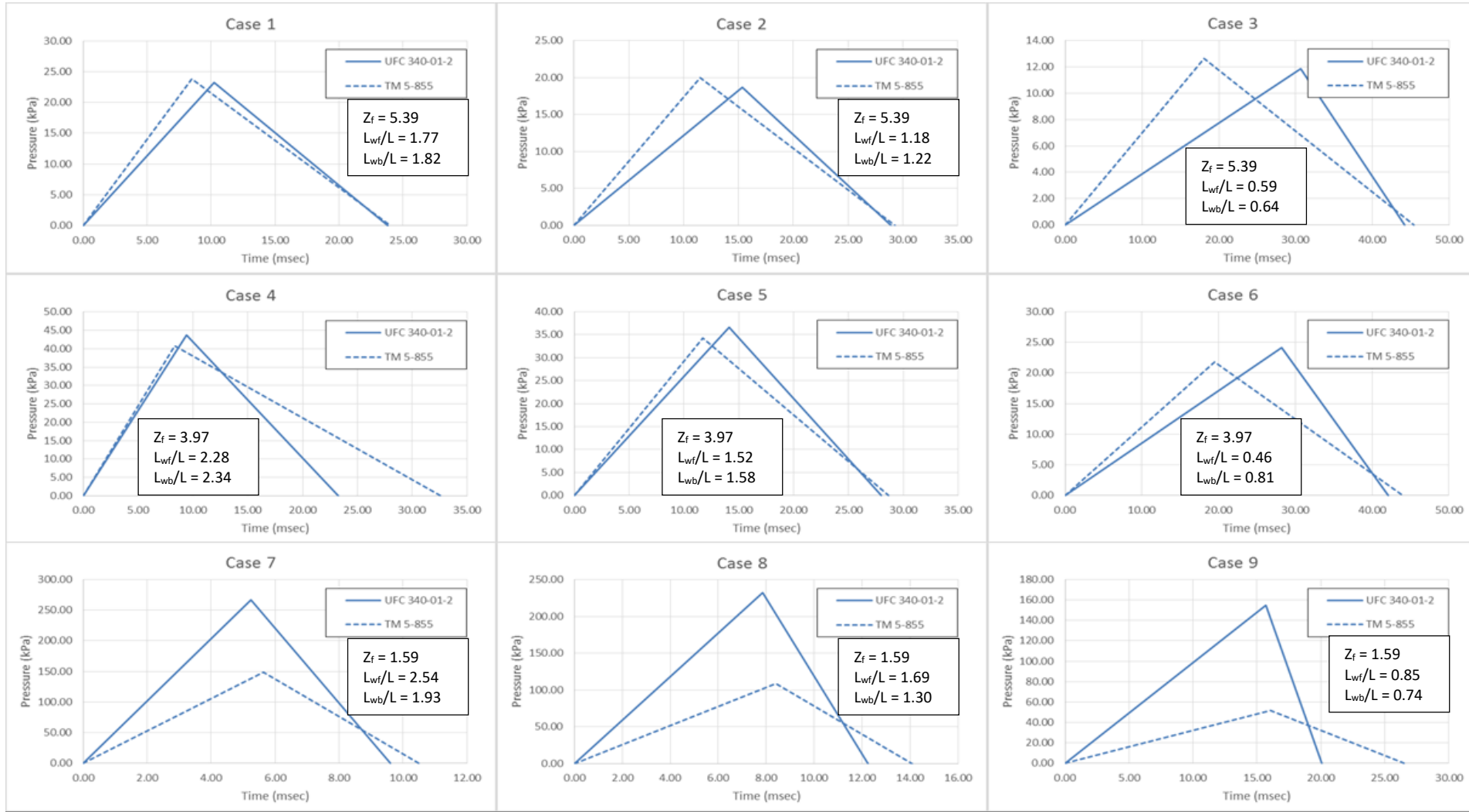


Figure 3.8. Blast load time-histories for the equivalent uniform loads derived from different methodologies

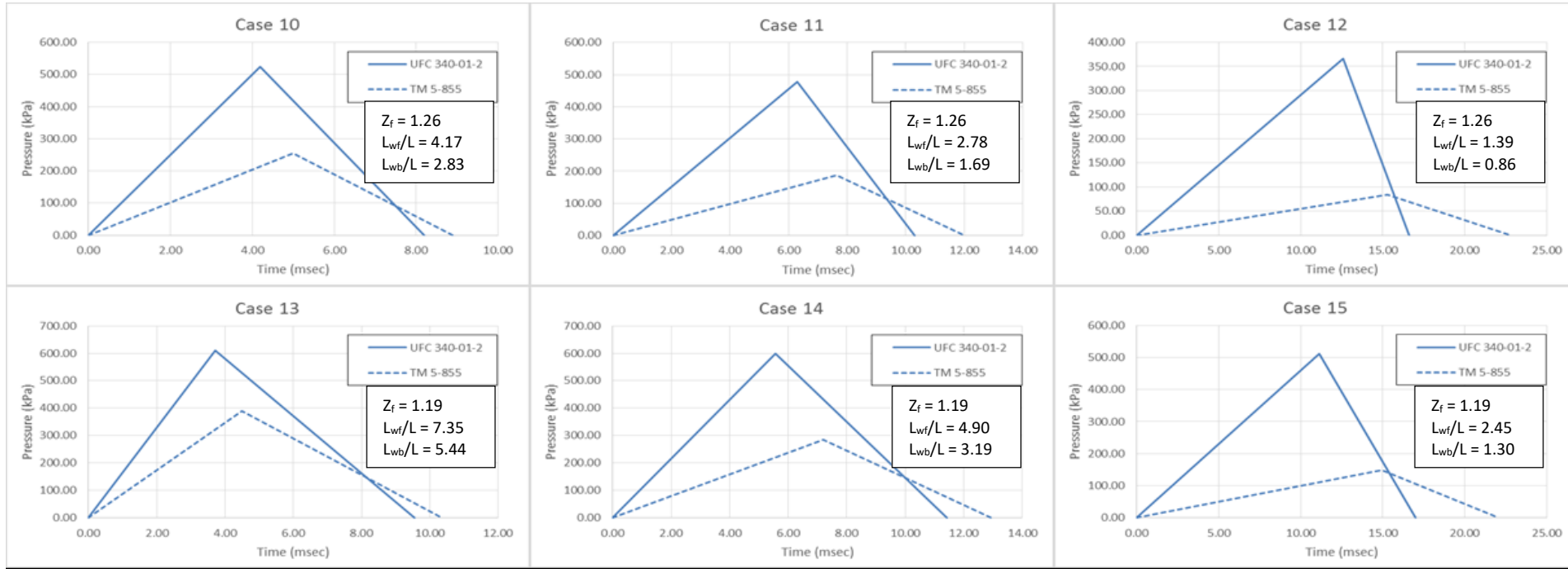


Figure 3.8. (Contd.) Blast load time-histories for the equivalent uniform loads derived from different methodologies

As shown in Figure 3.8, the two methodologies generate very different blast time-histories. The difference between the time-histories reaches up to 336% in the maximum pressure, and 217% in the impulse (area under the curves). The time-histories obtained from UFC 340-01-2 and ASCE (2010) provide higher pressures and impacts in most cases. Also, the difference between the time-histories of the two methodologies increases for longer spans of the roof and stronger blast scenarios (smaller scaled distances). The peak pressures increase in both methodologies by decreasing the scaled distance as expected.

3.2.2.2. SDOF analysis of the roof beams for equivalent uniform loads

As discussed earlier, the response of the structural members is traditionally determined by means of the equivalent SDOF model discussed in Section 2.3.1. The same model is used here to simulate the response of the roof beams, however some of the parameters are different from the models used for columns, because of the different boundary conditions of the beams as discussed in the following.

For the simply supported roof beams used in this study, the only applicable plastic mechanism is the formation of a plastic hinge at the midspan as shown in Figure 3.9. Thus, the nonlinear behavior of the beams has only two phases: elastic and fully-plastic, that is, before and after the formation of the plastic hinge. Using appropriate shape functions, the K_{LM} factor is 0.78 and 0.66 for the elastic and plastic stages respectively (DoD 2008). The average value of 0.72 is used in the dynamic analysis. The resistance function of a simply-supported beam is presented in Figure 3.9 based on the task committee manual and UFC 3-340-02 (ASCE 2010, DoD 2008).

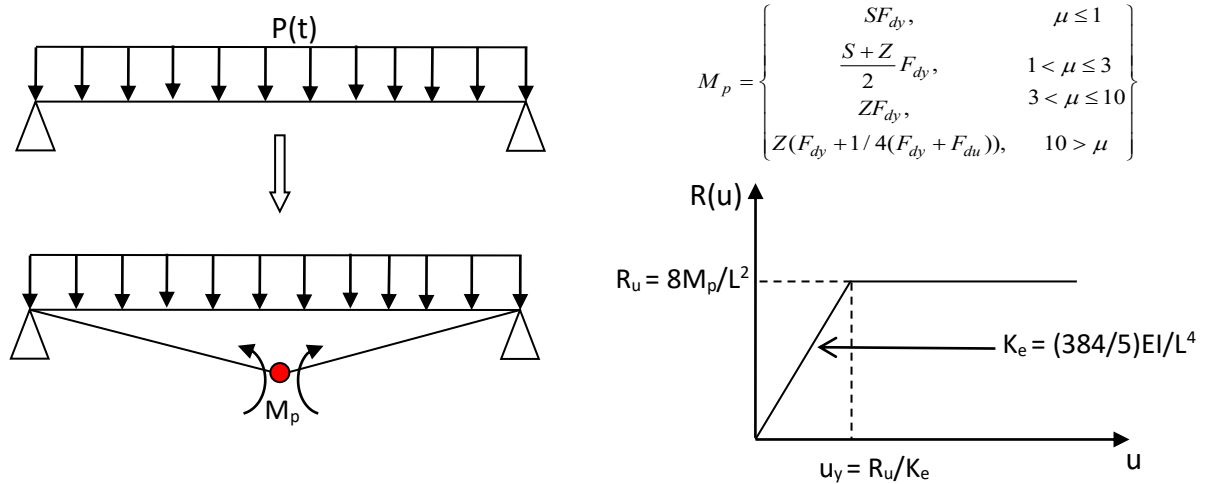


Figure 3.9. Plastic hinge generation and definition of resistance function for the beams

In Figure 3.9, S and Z are the elastic and plastic section moduli, respectively, F_{dy} and F_{du} are the dynamic yield and ultimate stresses of steel, EI is the bending stiffness of the beam, and μ is the ductility ratio defined as the maximum displacement divided by the yield displacement (u_y). The properties of the equivalent SDOF system for the different analytical cases are calculated based on the methodology described here and are presented in Table 3.7.

The dynamic analysis of the SDOF system is conducted by step-by-step time integration using Newmark's average acceleration method and assuming a damping of 2.5%. The results include the maximum displacement and moment at the mid-span of the beam, which are presented Table 3.8 for the equivalent uniform loads according to both ASCE 2010 and TM 8-855 methodologies.

Table 3.7. SDOF model properties for the different analytical cases

Case no.	Beam section	Trib. width (m)	Beam span (m)	K _{LM} .m (kg/m)	M _p (kN.m)				R _u (kN/m)				K (kN/m ²)
					μ ≤ 1	1 < μ ≤ 3	3 < μ ≤ 10	μ > 10	μ ≤ 1	1 < μ ≤ 3	3 < μ ≤ 10	μ > 10	
1,4,7,10,13	W610x101	3	4	622.1	1140	1230	1310	2040	571.0	613.0	655.0	1020.0	45800
2,5,8,11,14			6						254.0	272.0	291.0	454.0	9050
3,6,9,12,15		12	63.5						68.1	72.8	114.0	566	
16,19,22,25,28		4	571.0						613.0	655.0	1020.0	45800	
17,20,23,26,29		6	254.0						272.0	291.0	454.0	9050	
18,21,24,27,30		12	63.5						68.1	72.8	114.0	566	
31,34,37,40,43	W360x101	3	4	622.1	763	806	849	1320	382.0	403.0	425.0	662.0	18100
32,35,38,41,44			6						170.0	179.0	189.0	294.0	3570
33,36,39,42,45		12	42.4						44.8	47.2	73.6	223	
46,49,52,55,58		4	382.0						403.0	425.0	662.0	18100	
47,50,53,56,59		6	170.0						179.0	189.0	294.0	3570	
48,51,54,57,60		12	42.4						44.8	47.2	73.6	223	

Table 3.8. Results of SDOF analysis for equivalent uniform loads

Case no.	Blast type	Span length (m)	Trib. width (m)	Beam Section	UFC 3-340-02 and ASCE 2010 Methodology				TM 5-855 Methodology				Ratio of TM results to UFC/ASCE	
					u_{max} (mm)	μ	R_{max} (N/m)	M_{max} (kN.m)	u_{max} (mm)	μ	R_{max} (N/m)	M_{max} (kN.m)	u_{max}	M_{max}
1		4		W610x101	2.33	0.19	106750.00	213.50	2.46	0.20	112540.00	225.08	1.06	1.05
2	B 1	6			8.17	0.29	74000.00	333.00	8.80	0.31	79619.00	358.29	1.08	1.08
3		12			39.66	0.35	22450.00	404.10	43.34	0.39	24532.00	441.58	1.09	1.09
4		4			4.43	0.36	202700.00	405.40	4.35	0.35	199390.00	398.78	0.98	0.98
5	B 2	6			15.86	0.57	143500.00	645.75	14.99	0.53	135640.00	610.38	0.95	0.95
6		12			77.42	0.69	43800.00	788.40	72.65	0.65	41122.00	740.20	0.94	0.94
7		4			20.86	1.67	613000.00	1226.00	11.49	0.92	526270.00	1052.54	0.55	0.86
8	B 3	6	3		62.23	2.22	272000.00	1224.00	28.50	1.02	272471.37	1226.12	0.46	1.00
9		12			302.99	2.70	68100.00	1225.80	107.18	0.96	60666.00	1091.99	0.35	0.89
10		4			47.63	3.82	655000.00	1310.00	18.16	1.46	613000.00	1226.00	0.38	0.94
11	B 4	6			150.98	5.38	291000.00	1309.50	44.69	1.59	272000.00	1224.00	0.30	0.93
12		12			931.77	8.31	72800.00	1310.40	152.96	1.36	68100.00	1225.80	0.16	0.94
13		4			79.88	6.41	655000.00	1310.00	39.23	3.15	655000.00	1310.00	0.49	1.00
14	B 5	6			273.31	9.75	291000.00	1309.50	89.01	3.17	291000.00	1309.50	0.33	1.00
15		12			1226.00	10.93	114000.00	2052.00	316.37	2.82	72800.00	1310.40	0.26	0.64
16	B 1	4	6		4.47	0.36	204904.80	409.81	4.61	0.37	211322.40	422.64	1.03	1.03

Case no.	Blast type	Span length (m)	Trib. width (m)	Beam Section	UFC 3-340-02 and ASCE 2010 Methodology				TM 5-855 Methodology				Ratio of TM results to UFC/ASCE	
					u_{max} (mm)	μ	R_{max} (N/m)	M_{max} (kN.m)	u_{max} (mm)	μ	R_{max} (N/m)	M_{max} (kN.m)	u_{max}	M_{max}
17		6			13.22	0.47	119704.65	538.67	14.29	0.51	129393.30	582.27	1.08	1.08
18		12			57.19	0.51	32365.30	582.58	62.61	0.56	35432.62	637.79	1.09	1.09
19		4			8.39	0.67	384597.60	769.20	8.50	0.68	389640.00	779.28	1.01	1.01
20	B 2	6			25.25	0.90	228634.07	1028.85	24.00	0.86	217315.56	977.92	0.95	0.95
21		12			111.42	0.99	63055.47	1135.00	104.35	0.93	59054.37	1062.98	0.94	0.94
22		4			39.22	3.15	613060.58	1226.12	18.40	1.48	613060.58	1226.12	0.47	1.00
23	B 3	6			107.57	3.84	291037.56	1309.67	43.66	1.56	272471.37	1226.12	0.41	0.94
24		12			520.89	4.64	72759.39	1309.67	156.91	1.40	68117.84	1226.12	0.30	0.94
25		4			96.10	7.71	654834.50	1309.67	32.64	2.62	613060.58	1226.12	0.34	0.94
26	B 4	6			293.18	10.46	291037.56	1309.67	76.60	2.73	272471.37	1226.12	0.26	0.94
27		12			1218.80	10.87	113512.04	2043.22	247.22	2.20	68117.84	1226.12	0.20	0.60
28		4			113.86	9.14	1021608.38	2043.22	81.27	6.52	654834.50	1309.67	0.71	0.64
29	B 5	6			365.03	13.02	454048.17	2043.22	167.54	5.97	291037.56	1309.67	0.46	0.64
30		12			2351.00	20.96	113512.04	2043.22	570.76	5.09	72759.39	1309.67	0.24	0.64
31		4			5.43	0.26	98065.80	196.13	5.60	0.27	101136.00	202.27	1.03	1.03
32	B 1	6	3	W360x101	15.34	0.32	54724.03	246.26	16.50	0.35	58862.22	264.88	1.08	1.08
33		12			64.70	0.34	14425.70	259.66	70.74	0.37	15772.40	283.90	1.09	1.09
34	B 2	4			10.15	0.48	183309.00	366.62	10.45	0.49	188727.00	377.45	1.03	1.03

Case no.	Blast type	Span length (m)	Trib. width (m)	Beam Section	UFC 3-340-02 and ASCE 2010 Methodology				TM 5-855 Methodology				Ratio of TM results to UFC/ASCE	
					u _{max} (mm)	μ	R _{max} (N/m)	M _{max} (kN.m)	u _{max} (mm)	μ	R _{max} (N/m)	M _{max} (kN.m)	u _{max}	M _{max}
35		6			29.30	0.62	104525.04	470.36	27.89	0.59	99494.99	447.73	0.95	0.95
36		12			125.99	0.66	28091.10	505.64	118.38	0.62	26394.36	475.10	0.94	0.94
37		4			36.72	1.74	403061.93	806.12	20.30	0.96	366618.00	733.24	0.55	0.91
38	B 3	6			100.99	2.12	179138.63	806.12	47.10	0.99	168024.89	756.11	0.47	0.94
39		12			473.60	2.49	44784.66	806.12	172.17	0.91	38387.53	690.98	0.36	0.86
40		4			81.48	3.86	424513.40	849.03	31.39	1.49	403061.93	806.12	0.39	0.95
41	B 4	6			242.52	5.10	188672.62	849.03	72.48	1.52	179138.63	806.12	0.30	0.95
42		12			1454.50	7.65	47168.16	849.03	243.30	1.28	44784.66	806.12	0.17	0.95
43		4			137.93	6.53	424513.40	849.03	70.26	3.33	424513.40	849.03	0.51	1.00
44	B 5	6			439.20	9.24	188672.62	849.03	150.99	3.18	188672.62	849.03	0.34	1.00
45		12			1925.40	10.12	73587.12	1324.57	514.65	2.71	44784.66	806.12	0.27	0.61
46		4			9.11	0.43	164526.60	329.05	9.39	0.44	169583.40	339.17	1.03	1.03
47	B 1	6			22.78	0.48	81265.54	365.69	24.69	0.52	88079.29	396.36	1.08	1.08
48		12			92.20	0.48	20557.19	370.03	100.96	0.53	22510.34	405.19	1.10	1.10
49		4	6		17.00	0.80	307020.00	614.04	18.69	0.88	337541.40	675.08	1.10	1.10
50	B 2	6			43.26	0.91	154326.04	694.47	41.28	0.87	147262.58	662.68	0.95	0.95
51		12			179.40	0.94	39999.56	719.99	168.12	0.88	37484.53	674.72	0.94	0.94
52	B 3	4			62.77	2.97	403061.93	806.12	30.88	1.46	403061.93	806.12	0.49	1.00

Case no.	Blast type	Span length (m)	Trib. width (m)	Beam Section	UFC 3-340-02 and ASCE 2010 Methodology				TM 5-855 Methodology				Ratio of TM results to UFC/ASCE	
					u_{max} (mm)	μ	R_{max} (N/m)	M_{max} (kN.m)	u_{max} (mm)	μ	R_{max} (N/m)	M_{max} (kN.m)	u_{max}	M_{max}
53		6			171.42	3.61	188672.62	849.03	70.23	1.48	179138.63	806.12	0.41	0.95
54		12			814.17	4.28	47168.16	849.03	248.75	1.31	44784.66	806.12	0.31	0.95
55		4			156.43	7.40	424513.40	849.03	53.61	2.54	403061.93	806.12	0.34	0.95
56	B 4	6			461.90	9.72	188672.62	849.03	121.25	2.55	179138.63	806.12	0.26	0.95
57		12			1904.40	10.01	73587.12	1324.57	386.70	2.03	44784.66	806.12	0.20	0.61
58		4			273.47	12.94	662284.05	1324.57	135.31	6.40	424513.40	849.03	0.49	0.64
59	B 5	6			578.77	12.17	294348.47	1324.57	266.97	5.62	188672.62	849.03	0.46	0.64
60		12			3667.00	19.28	73587.12	1324.57	892.10	4.69	47168.16	849.03	0.24	0.64

In Table 3.7, u_{max} denotes the maximum displacement. Also, R_{max} and M_{max} are the maximum resistance function and the corresponding maximum bending moment of the beam ($R_{max}L^2/8$), respectively. The difference between the response of the beams obtained from the two methodologies reaches up to 509% for the displacements and 67% for the bending moments.

Also, this difference increases for longer spans and higher levels of the blast. In most cases, the displacement and moments from UFC/ASCE uniform loads are higher than the results from TM 5-855, which is expected because of the same pattern in the peak loads and impulses of the time-histories. In the cases where the length of the beams and the scaled standoff distances are smaller, the results from both methods are comparable, since the difference between the pressures at front and back point of the roof is not substantial.

3.2.2.3. MDOF analysis of the roof beams for equivalent uniform loads

The response obtained for cases that were analyzed by a SDOF model reported in the previous section is compared to that obtained for the same set of loads but using an MDOF model. The purpose of this study is to check the accuracy of the SDOF model and to obtain a more accurate response of the roof beams when equivalent uniform blast loading is used.

In the MDOF analysis, OpenSEES software (available at www.opensees.berkeley.edu) is used, and the roof beams are modeled as nonlinear fibre elements. The steel beams are divided into fibre sections across their depths and the dynamic stress-strain behavior based on Figure 3.7 is assigned to the fibres. The discretization of the I-beams includes

eight fibres for the web and two fibres in each flange. The beam is divided into a number of elements across its length, each of a length of 0.5m, and the mass of the roof slab is lumped at each node. The 0.5-m length of each element was used because it provides sufficient number of degrees of freedom for the accuracy of the analysis, while maintaining the computational efficiency. The equivalent uniform loads, derived from the UFC 3-340 and TM5-855 methodologies and presented in Table 3.7, were applied as uniformly distributed loads on the beam.

The material model “Steel01”, used to model the steel fibres, provides a simple bilinear behaviour with kinematic hardening of the steel (hardening modulus ratio used here is 1.96%). In order to take advantage of the selected type of material properties, a nonlinear beam-column element based on an iterative force-based integration is used. This type of element can be constructed using the “nonlinearBeamColumn” command line in OpenSEES. In this analysis, 2 Gauss-Lobatto (Neuenhofer & Filippou 1997) integration points are assigned to each element's ends.

Rayleigh proportional damping of 2.5% of critical damping is assigned to the 1st and 4th modes of vibration. Based on this, the proportional damping matrix, \mathbf{C} is generated using Equation 3.4 (Humar 2012).

$$\mathbf{C} = \alpha_0 \mathbf{M} + \alpha_1 \mathbf{K} \quad (3.4)$$

where, \mathbf{M} and \mathbf{K} are mass and stiffness matrices, respectively, and the coefficients α_0 and α_1 are obtained from Equation 3.5. As shown in Equation 3.5, the coefficients

depend on the frequencies of vibration and damping ratios in modes i and j , ω_i , ω_j , ξ_i and ξ_j .

$$1/2 \begin{bmatrix} 1/\omega_i & \omega_i \\ 1/\omega_j & \omega_j \end{bmatrix} \begin{Bmatrix} \alpha_0 \\ \alpha_1 \end{Bmatrix} = \begin{Bmatrix} \xi_i \\ \xi_j \end{Bmatrix} \quad (3.5)$$

The transient analysis is carried out using Newmark's average acceleration method (Humar 2012), and the nonlinear solution is handled by a modified Newton-Raphson algorithm. Also, the maximum time increment is selected as 0.01 msec for the analysis. The results of the analysis for different cases under the application of the uniform loads from the two selected methodologies are presented in Table 3.9.

Table 3.9. Results of MDOF analysis for equivalent uniform loads

Case no.	Blast type	Span length (m)	Trib. width (m)	Beam Section	UFC 3-340-02 and ASCE 2010 Methodology			TM 5-855 Methodology			Ratio of TM results to UFC/ASCE	
					u_{max} (mm)	μ	M_{max} (kN.m)	u_{max} (mm)	μ	M_{max} (kN.m)	u_{max}	M_{max}
1		4		W610x101	2.36	0.19	213.00	2.46	0.20	222.49	1.04	1.04
2	B 1	6			7.99	0.28	326.00	8.56	0.31	349.36	1.07	1.07
3		12			37.70	0.34	399.00	41.13	0.37	424.64	1.09	1.06
4		4			4.46	0.36	404.00	4.40	0.35	397.06	0.99	0.98
5	B 2	6			15.40	0.55	627.00	14.51	0.52	591.92	0.94	0.94
6		12			73.60	0.66	776.00	68.84	0.61	705.71	0.94	0.91
7		4			20.66	1.66	1311.87	11.09	0.89	1016.41	0.54	0.77
8	B 3	6	3		60.00	2.14	1348.02	27.11	0.97	1117.50	0.45	0.83
9		12			290.06	2.59	1365.09	100.74	0.90	1105.72	0.35	0.81
10		4			46.79	3.75	1423.89	18.05	1.45	1287.89	0.39	0.90
11	B 4	6			142.78	5.09	1477.14	43.54	1.55	1309.48	0.30	0.89
12		12			850.38	7.58	1551.22	148.29	1.32	1292.16	0.17	0.83
13		4			73.97	5.94	1509.35	39.14	3.14	1397.08	0.53	0.93
14	B 5	6			237.85	8.48	1581.44	87.48	3.12	1394.46	0.37	0.88
15		12			1495.17	13.33	1718.49	313.93	2.80	1377.24	0.21	0.80
16	B 1	4	6		4.41	0.35	399.98	4.55	0.36	412.23	1.03	1.03

Case no.	Blast type	Span length (m)	Trib. width (m)	Beam Section	UFC 3-340-02 and ASCE 2010 Methodology			TM 5-855 Methodology			Ratio of TM results to UFC/ASCE	
					u_{max} (mm)	μ	M_{max} (kN.m)	u_{max} (mm)	μ	M_{max} (kN.m)	u_{max}	M_{max}
17		6			12.69	0.45	517.89	13.66	0.49	555.93	1.08	1.07
18		12			54.05	0.48	578.48	58.89	0.53	613.41	1.09	1.06
19		4			8.26	0.66	748.78	8.44	0.68	763.81	1.02	1.02
20	B 2	6			24.21	0.86	987.43	23.01	0.82	935.96	0.95	0.95
21		12			105.14	0.94	1131.78	98.43	0.88	1035.97	0.94	0.92
22		4			37.47	3.01	1386.50	18.14	1.46	1288.42	0.48	0.93
23	B 3	6			104.83	3.74	1419.18	42.47	1.51	1307.65	0.41	0.92
24		12			510.28	4.55	1447.09	152.53	1.36	1303.94	0.30	0.90
25		4			86.56	6.95	1525.47	31.43	2.52	1361.32	0.36	0.89
26	B 4	6			254.58	9.08	1593.80	73.05	2.61	1370.48	0.29	0.86
27		12			1491.91	13.30	1710.56	239.31	2.13	1347.49	0.16	0.79
28		4			140.03	11.24	1651.30	74.95	6.01	1507.49	0.54	0.91
29	B 5	6			426.86	15.22	1777.56	156.87	5.59	1492.18	0.37	0.84
30		12			2594.18	23.13	1959.08	553.49	4.93	1460.29	0.21	0.75
31		4			5.35	0.25	191.76	5.49	0.26	197.22	1.03	1.03
32	B 1	6	3	W360x101	14.62	0.31	235.60	15.76	0.33	253.03	1.08	1.07
33		12			60.90	0.32	262.33	66.34	0.35	280.71	1.09	1.07

Case no.	Blast type	Span length (m)	Trib. width (m)	Beam Section	UFC 3-340-02 and ASCE 2010 Methodology			TM 5-855 Methodology			Ratio of TM results to UFC/ASCE	
					u_{max} (mm)	μ	M_{max} (kN.m)	u_{max} (mm)	μ	M_{max} (kN.m)	u_{max}	M_{max}
34		4			9.98	0.47	357.91	10.38	0.49	371.95	1.04	1.04
35	B 2	6			27.86	0.59	448.55	26.51	0.56	425.45	0.95	0.95
36		12			118.46	0.62	514.51	110.90	0.58	473.74	0.94	0.92
37		4			36.25	1.72	862.38	19.32	0.91	699.40	0.53	0.81
38	B 3	6			96.69	2.03	874.43	44.50	0.94	737.32	0.46	0.84
39		12			464.45	2.44	885.34	161.36	0.85	757.01	0.35	0.86
40		4			79.16	3.75	925.36	30.99	1.47	847.90	0.39	0.92
41	B 4	6			231.75	4.87	955.26	70.90	1.49	858.11	0.31	0.90
42		12			1353.80	7.12	999.70	237.40	1.25	853.40	0.18	0.85
43		4			126.46	5.98	975.00	68.76	3.25	909.86	0.54	0.93
44	B 5	6			386.01	8.12	1018.60	142.83	3.00	903.68	0.37	0.89
45		12			2374.24	12.48	1099.63	501.91	2.64	891.53	0.21	0.81
46		4			8.82	0.42	317.26	9.08	0.43	326.53	1.03	1.03
47	B 1	6			21.65	0.46	351.38	23.35	0.49	377.42	1.08	1.07
48		12	6		86.50	0.45	396.19	94.38	0.50	431.12	1.09	1.09
49		4			16.37	0.77	588.73	18.26	0.86	656.44	1.12	1.12
50	B 2	6			41.14	0.87	665.19	39.19	0.82	632.29	0.95	0.95

Case no.	Blast type	Span length (m)	Trib. width (m)	Beam Section	UFC 3-340-02 and ASCE 2010 Methodology			TM 5-855 Methodology			Ratio of TM results to UFC/ASCE	
					u_{max} (mm)	μ	M_{max} (kN.m)	u_{max} (mm)	μ	M_{max} (kN.m)	u_{max}	M_{max}
51		12			168.33	0.89	775.79	157.79	0.83	724.90	0.94	0.93
52		4			62.28	2.95	905.14	30.37	1.44	846.42	0.49	0.94
53	B 3	6			169.72	3.57	919.63	68.61	1.44	854.76	0.40	0.93
54		12			806.31	4.24	933.09	243.72	1.28	858.60	0.30	0.92
55		4			141.62	6.70	986.17	51.51	2.44	884.93	0.36	0.90
56	B 4	6			408.09	8.58	1027.91	117.05	2.46	886.56	0.29	0.86
57		12			2217.74	11.66	1084.22	382.13	2.01	875.13	0.17	0.81
58		4			229.96	10.88	1067.47	124.29	5.88	971.76	0.54	0.91
59	B 5	6			682.49	14.36	1139.50	254.57	5.35	968.56	0.37	0.85
60		12			3456.50	18.18	1175.06	874.81	4.60	941.91	0.25	0.80

The trend observed in the results of the MDOF simulation of the uniformly distributed blast loads, is much similar to the ones obtained from SDOF simulations. Thus, UFC/ASCE method leads to higher responses than the TM 5-855 method, and the differences in the results increase with the length of the beams. The major reason for this difference in responses is the large differences in the loads as explained in Section 3.2.2.1. The difference in the loads is due to the nature of the two different methodologies.

3.2.3 Analysis for the Traveling Blast Wave Loading

As stated earlier, a relatively more accurate way of analyzing the roof and side beams that are oriented perpendicular to the shock front is a step-by-step analysis for the moving load (DoA 1986, DoD 2008). In this section, the roof beams are analyzed for their response to the blast loads produced by the traversing wave. For this purpose, the beams are discretized into sub-elements of length $\Delta x = 1.5$ m. The blast pressures at different points along the length of the beams are calculated by placing the blast wave shock front sequentially at the nodes of the sub-elements, beginning from the front end of the roof and moving to the rear end, and constructing the exponentially-decaying blast pressure time-history for each node. The blast pressures are then multiplied by the tributary area of each node to generate the blast load time-histories.

Using this method, an array of blast loads is generated for each node. Depending on the blast wave properties and the beam length, different scenarios can occur as the blast wave traverses the beam. If the wavelength of the blast is greater than or equal to the

beam span, the entire length of the beam is loaded at the time the shock front reaches the rear end of the roof. On the other hand, if the wavelength is less than the beam span, only a portion of the beam is loaded at any time, even at the time the shock front reaches the rear end. Based on this methodology, more accurate blast load time-histories are generated for the selected blast scenarios, and are applied to the beams. These time-histories are presented in Figure 3.10 for the five blast scenarios. In this figure, the blast pressures on the internal nodes of the beam are generated for the nodes located at 0.5 m distance from each other, starting from the roof front point.

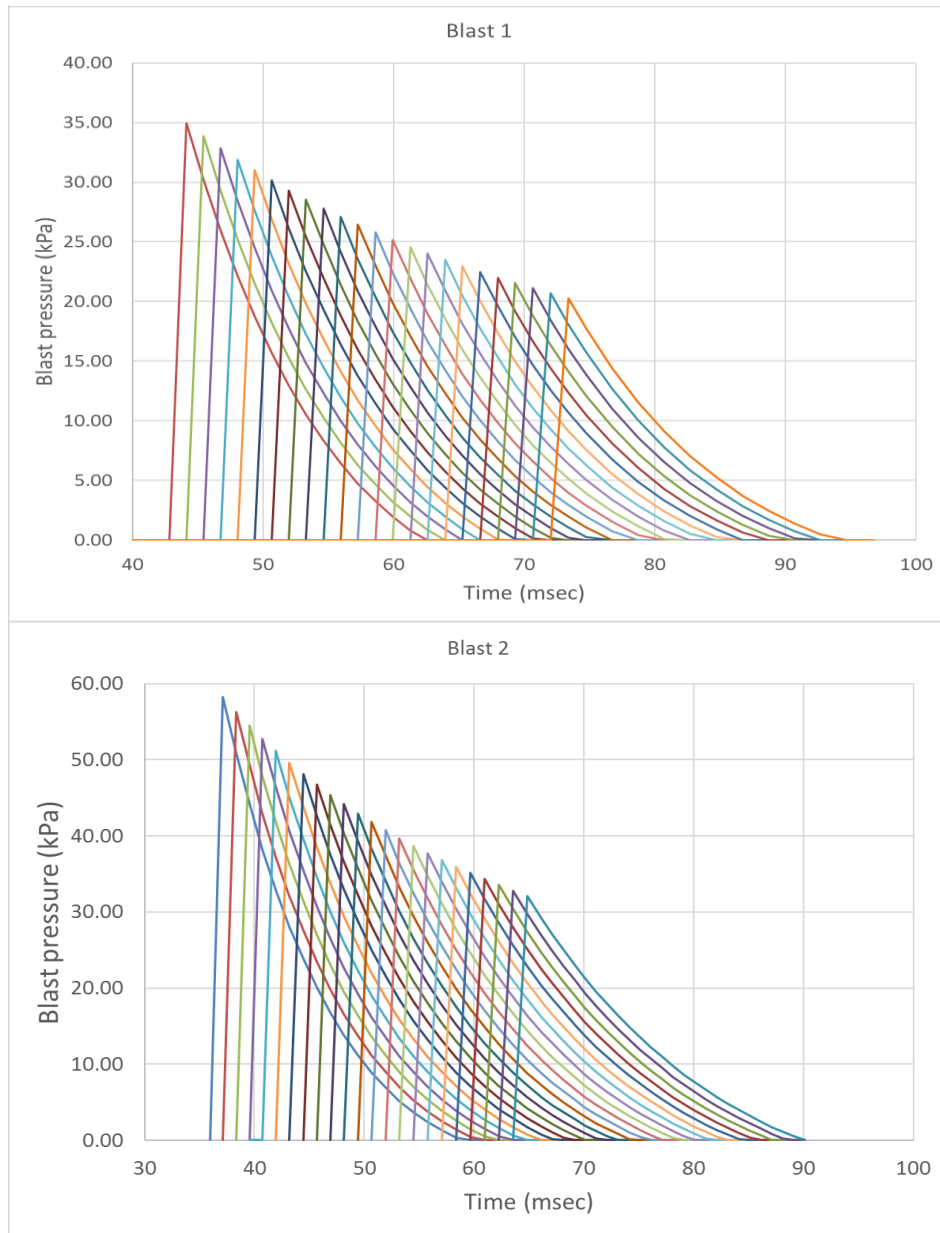


Figure 3.10. Blast pressure time-histories generated for the travelling load analysis

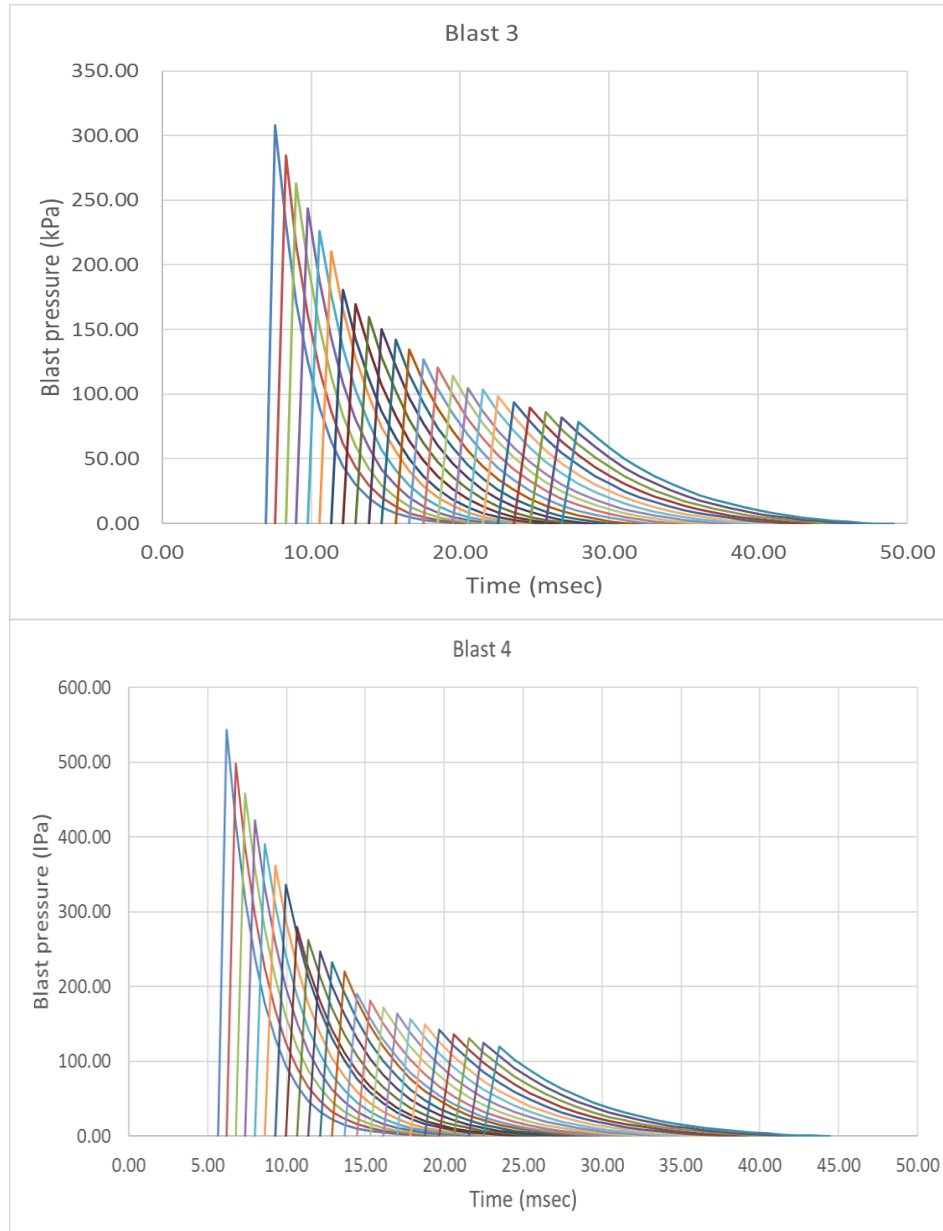


Figure 3.10 (Cont'd). Blast pressure time-histories generated for the travelling load analysis

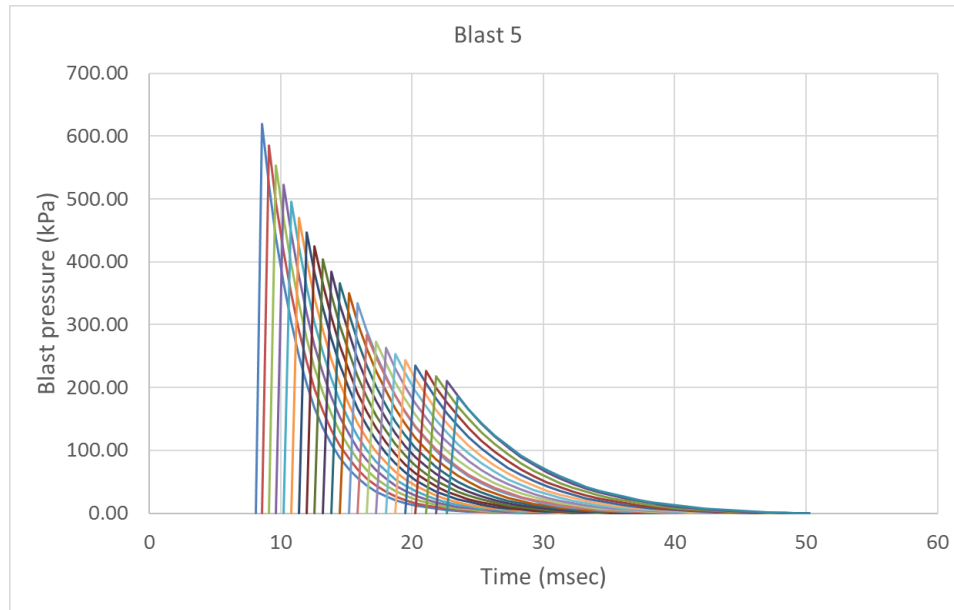


Figure 3.10 (Cont'd). Blast pressure time-histories generated for the travelling load analysis

After generating the time-histories of the loads produced by the blast wave traversing the roof spans as described above, these load records are applied to the same fibre element models as in the previous section (3.2.2.3) as nodal loads. The tributary width of the slabs is specified in the computer codes as scale factors for the blast time-histories and the dynamic nonlinear analysis is carried out for different cases in the same way as described in the previous section of this thesis. The maximum displacements, ductility ratios and the bending moments in the elements are reported as the results of the analysis in Table 3.10. It should be noted that unlike in the case of uniformly distributed loads, in a few cases the maximum response is not observed at the mid-span of the beams. The 12-m span beams tend to show the maximum displacement and bending moment at the first node before the mid-span point. Therefore, the

maximum response parameters in Table 3.9 are not exclusively from the mid-span of the beams.

Table 3.10. Results of MDOF analysis for moving blast loads

Case no.	Blast type	Span length (m)	Tributary width (m)	Beam section	u_{max} (mm)	μ	M_{max} (kN.m)
1		4			1.86	0.15	169.17
2	B 1	6			5.72	0.20	244.35
3		12			27.57	0.25	354.40
4		4			3.22	0.26	293.01
5	B 2	6			9.96	0.36	413.98
6		12			50.65	0.45	590.15
7		4			7.03	0.56	634.71
8	B 3	6	3	W610x101	18.26	0.65	915.00
9		12			78.20	0.70	986.68
10		4			11.70	0.94	1096.61
11	B 4	6			29.86	1.06	1171.02
12		12			111.22	0.99	1118.43
13		4			23.04	1.85	1309.48
14	B 5	6			62.91	2.24	1299.96
15		12			242.73	2.16	1301.76

Case no.	Blast type	Span length (m)	Tributary width (m)	Beam section	u_{max} (mm)	μ	M_{max} (kN.m)
16		4			3.46	0.28	318.39
17	B 1	6			9.56	0.34	416.02
18		12			38.67	0.34	513.12
19		4			5.91	0.47	529.08
20	B 2	6			15.74	0.56	716.11
21		12			69.71	0.62	884.45
22		4			11.41	0.92	1214.71
23	B 3	6	6		27.40	0.98	1149.62
24		12			101.60	0.91	1102.27
25		4			20.11	1.61	1304.36
26	B 4	6			46.62	1.66	1287.80
27		12			158.62	1.41	1167.20
28		4			48.99	3.93	1400.13
29	B 5	6			111.62	3.98	1365.01
30		12			385.35	3.44	1335.75
31		4			3.94	0.19	147.62
32	B 1	6			10.98	0.23	196.32
33		12	3	W360x101	42.11	0.22	223.44
34	B 2	4			6.87	0.32	246.40
35		6			18.66	0.39	343.37

Case no.	Blast type	Span length (m)	Tributary width (m)	Beam section	u_{max} (mm)	μ	M_{max} (kN.m)
36		12			78.55	0.41	390.48
37		4			13.57	0.64	586.27
38	B 3	6			31.75	0.67	608.07
39		12			115.69	0.61	516.94
40		4			21.50	1.02	797.22
41	B 4	6			48.55	1.02	792.77
42		12			166.04	0.87	713.00
43		4			43.24	2.05	863.86
44	B 5	6			104.72	2.20	845.99
45		12			366.76	1.93	834.91
46		4			6.61	0.31	257.10
47	B 1	6			16.23	0.34	299.57
48		12			59.09	0.31	265.70
49		4			11.46	0.54	430.81
50	B 2	6			28.04	0.59	525.43
51		12	6		109.33	0.57	448.57
52		4			20.67	0.98	801.76
53	B 3	6			46.05	0.97	769.55
54		12			159.14	0.84	679.26
55	B 4	4			34.87	1.65	822.39

Case no.	Blast type	Span length (m)	Tributary width (m)	Beam section	u_{max} (mm)	μ	M_{max} (kN.m)
56		6			70.42	1.48	826.02
57		12			240.02	1.26	844.51
58		4			81.16	3.84	891.89
59	B 5	6			180.08	3.79	884.26
60		12			645.99	3.40	893.54

These results are discussed and compared to the results obtained from SDOF and MDOF analyses of the beams for equivalent uniform loads in the next section to highlight the differences between the response results obtained for the more precise blast loads and the uniform loads suggested by the methodologies specified in the standard references.

3.2.4. Results and Discussion

Response of the selected roof beams to selected set of blast scenarios was obtained as described in the previous sections. In this section, the various results are compared to assess the validity of the assumptions used in the simplified methodologies for roof and side member analysis. Accuracy of the SDOF models are first studied by comparing their response to results obtained from the MDOF models under the equivalent uniform blast loads. Secondly, the response of the MDOF models subjected to uniform loads based on UFC 3-340-02 and TM 5-855 methodologies are compared to the response of beams to the blast loads produced by travelling wave to study the reliability of the equivalent load methodologies.

3.2.4.1. Accuracy of equivalent SDOF model

As discussed earlier, the simplest model used in blast load analysis of a roof beam is a SDOF model derived by assuming a predefined deflected shape. In order to check the accuracy of this assumption, the response of the roof beams subject to the equivalent uniform loads and a SDOF representation is compared to that obtained for the same set of loads but a MDOF representation. The differences between the maximum response for different cases are shown in Figure 3.11. In this figure, the relative differences are calculated with respect to the values obtained for the MDOF models, therefore the

negative values in the vertical axis mean the SDOF system underestimates the response in the given case.

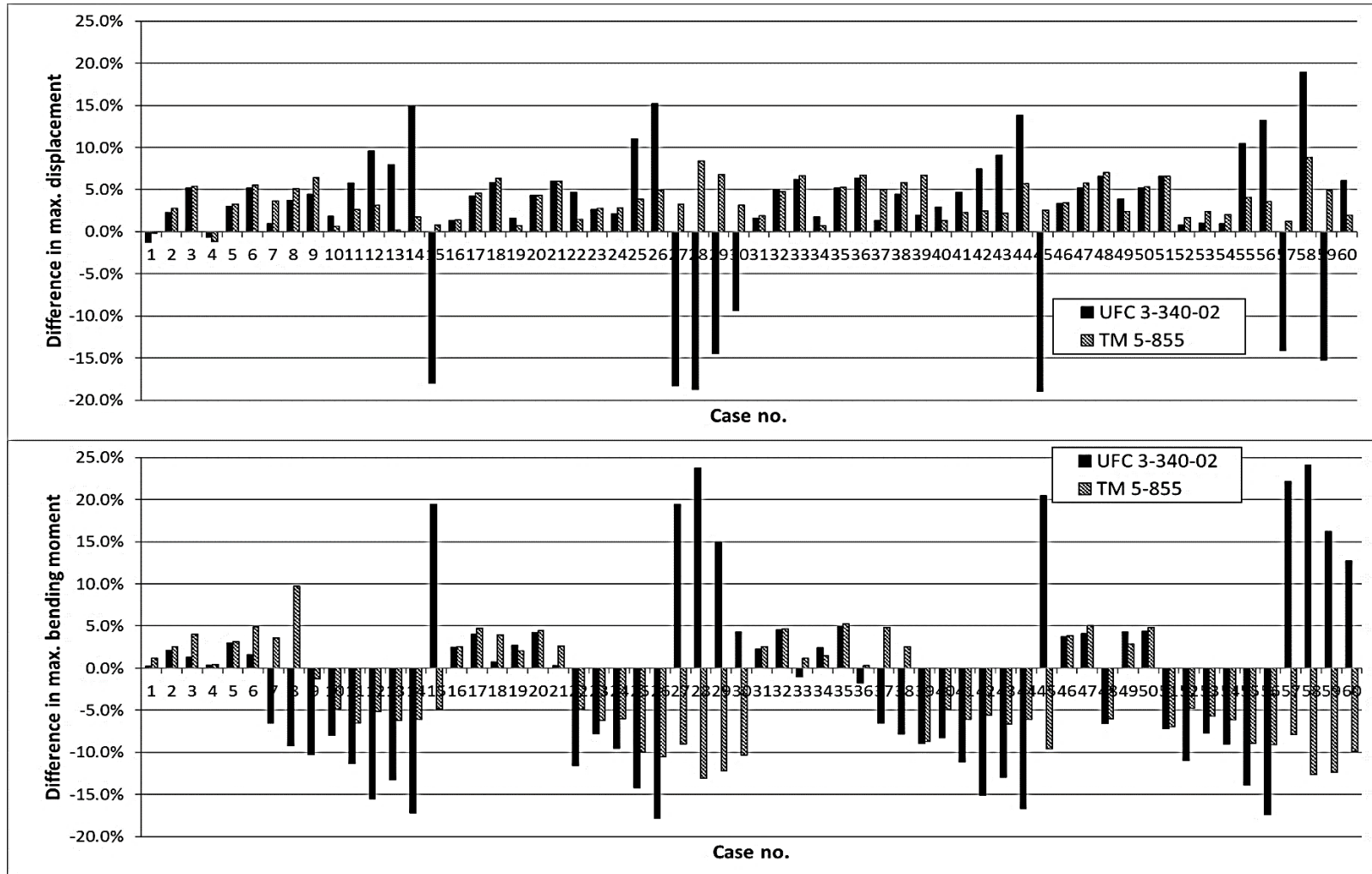


Figure 3.11. Difference in maximum response measures between the SDOF and MDOF models subject to uniform blast loads

Based on the comparison of the responses of SDOF and MDOF models shown above, several conclusions can be made as following.

1- The maximum difference in all of the analyzed cases reaches up to just under 20% in UFC/ASCE method and 10% in TM 5-855 method for the displacements, and 25% for the moments in UFC/ASCE method and 15% in TM 5-855 method.

2- In a majority of cases, the maximum displacements are overestimated while the maximum bending moments are underestimated when using the SDOF simplification. A portion of this difference could be explained by observing that the SDOF model uses an elastic-perfectly plastic resistance function, while a bilinear curve with post yield hardening behavior is used for the MDOF model. Consequently, the MDOF model leads to slightly higher displacements and larger forces. Although the post-yielding behavior of the material is taken into consideration by defining different yield stress and plastic moments for various ductility demands, the SDOF models struggle in capturing the exact hardening behavior in these cases.

3- The differences between the two sets of results do not grow as the magnitude of the blast loads increases (from Blast 1 to Blast 5). On the other hand, the difference in maximum displacement is seen to increase with the length of the beams (from case 1 to 3, 4 to 6, etc.). This could be explained by observing that the effect of higher modes of vibration tends to increase with the length of the beam.

4- The patterns of the differences are very similar when the same loads are applied on different beam sections (i.e. cases 1- 15 and 31-45), and do not change significantly with

the section type. Also, the differences are higher when the equivalent loads are determined from UFC 3-340-02 than from TM 5-855. This is because the former are larger in both the magnitude of the peak blast pressure and the impulse.

5- In cases with more significant blast loads (Blast 4 and 5) and longer spans (12 m), the maximum response, in terms of displacement and bending moment, occurs not at the mid-span point, but at a node just before the mid-span.

6- In order to get a better understanding of the results and nature of the differences, the time-histories of the displacement and bending moments at the midpoint of the span in two cases are compared for SDOF and MDOF models. This comparison for a case with very small difference, Case 1 (elastic response) and a case with a large difference, Case 15 (nonlinear response) are presented in Figures 3.12 to 3.15. In these figures, only the results for the models that use the UFC 3-340-02 loads are shown, since the corresponding loads and consequently the differences in the response are more severe in comparison to those for the TM 5-855 loads.

7- As observed from Figures 3.12 to 3.15 and in the response results of other cases, the apparent period of vibration for the MDOF models is greater than for the SDOF models. Also the vibration damps more quickly in the MDOF models.

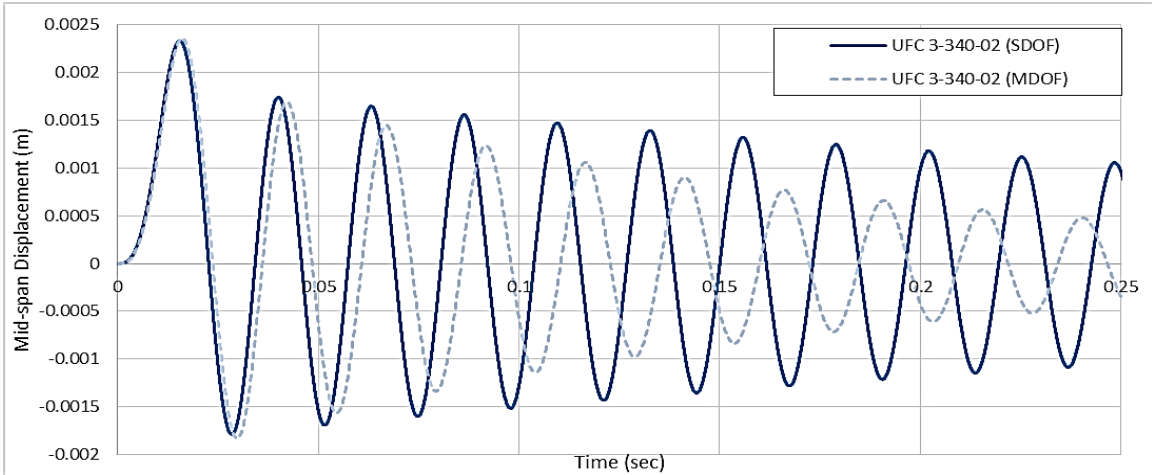


Figure 3.12. Mid-span displacement time-history of SDOF and MDOF models in Case 1

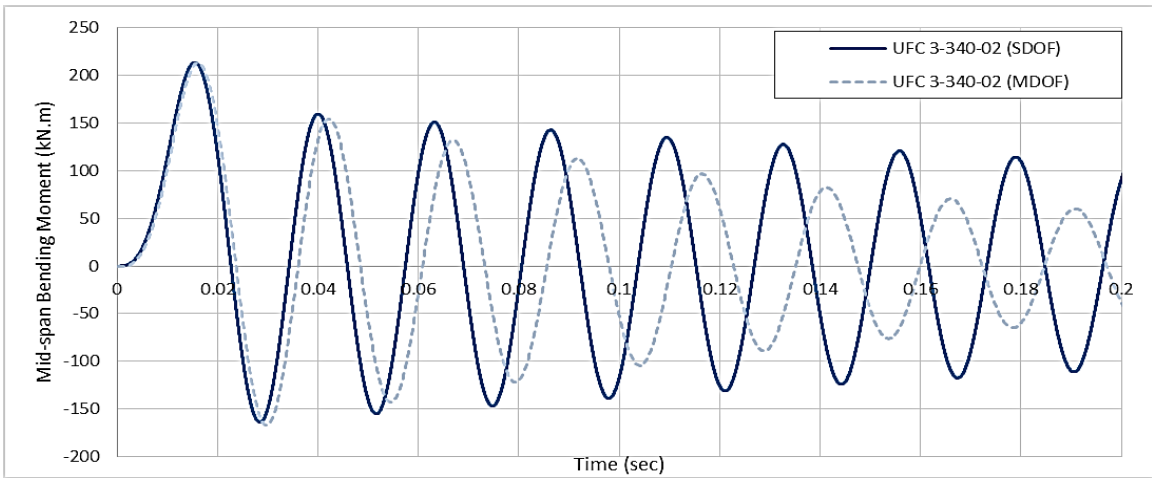


Figure 3.13. Mid-span moment time-history of SDOF and MDOF models in Case 1

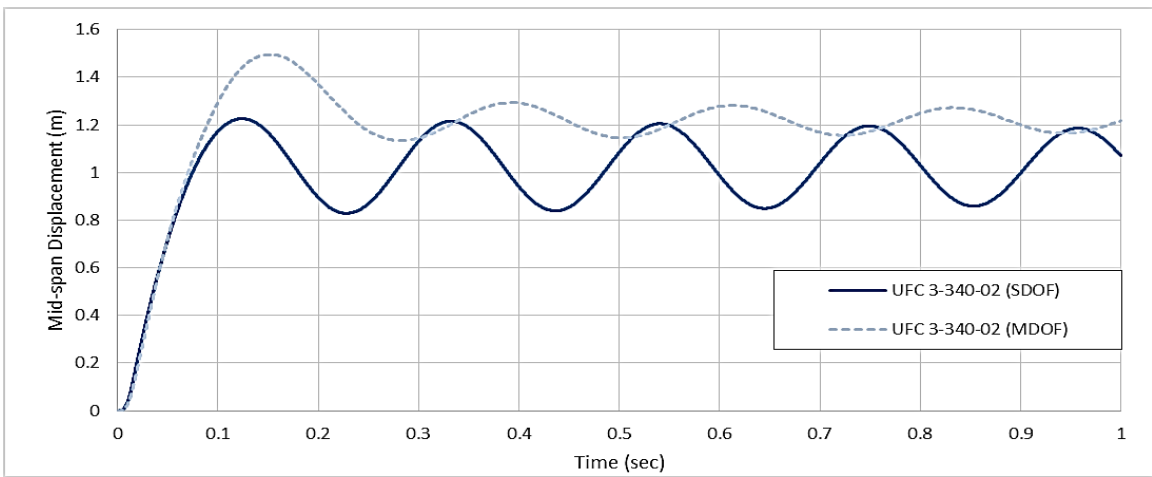


Figure 3.14. Mid-span displacement time-history of SDOF and MDOF models in Case 15

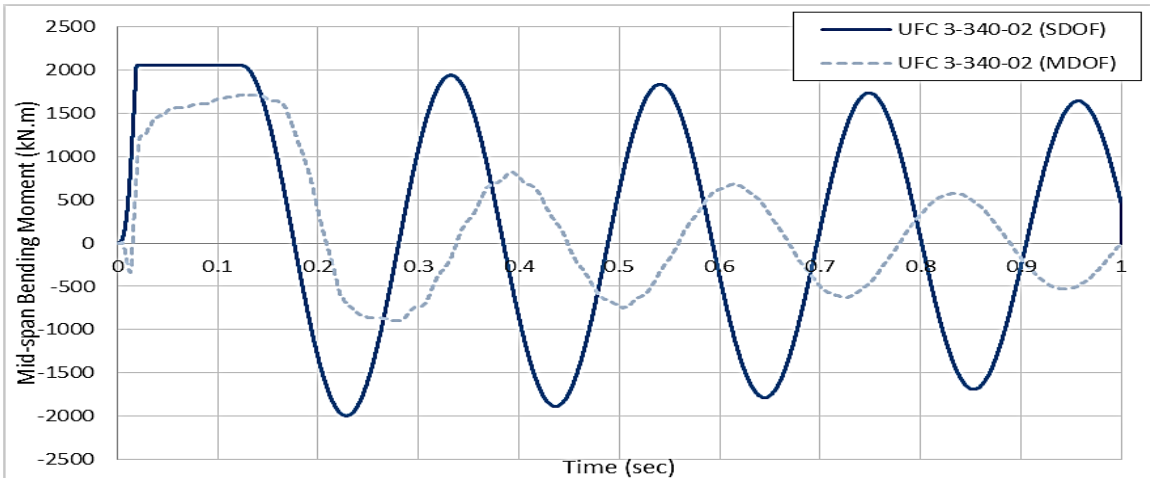


Figure 3.15. Mid-span moment time-history of SDOF and MDOF models in Case 15

8- Another important observation and conclusion that can be drawn from Figures 3.14 and 3.15 and from other cases not shown, is that the definition of plastic moment in the SDOF model for a high level of ductility level ($\mu \geq 10$) seems to be excessive and inconsistent, since in all cases that lead to this level of ductility, the differences between the SDOF and MDOF responses are comparatively quite large.

3.2.4.2. Accuracy of equivalent uniform loads

The major simplification in analyzing the members oriented in the direction perpendicular to the blast shock front is in using the equivalent uniformly distributed loads, derived by the procedures presented in earlier sections. In order to study the reliability of this simplification, the response of the beams to the more realistic moving blast loads is compared to their response to the two equivalent uniform loads. For the comparison to be valid, the results of only the MDOF models are used to investigate the beam response.

As discussed earlier, the equivalent uniform loads are primarily related to the span ratio (the ratio of blast wavelength to the span length of the beam) corresponding to the blast load attributes when the wave arrives either at the front of the roof (UFC 3-340-02 and ASCE 2010), or at the back (end) of the roof (TM 5-855). The differences between the response of beams to the moving load and uniform load are presented in Figures 3.16 and 3.17 as functions of the span ratio. Figure 3.16 relates to the procedure defined in UFC 3-340-02, while Figure 3.17 relates to the procedure of TM 5-585. From the data presented in these figures, several conclusions can be drawn as discussed in the following:

1- Response of the beams obtained according to UFC 3-340-02 significantly overestimates the more precise response obtained from travelling wave representation; the difference in the predictions of maximum displacement and maximum bending moment reaching up to 840% and 106%, respectively. The difference between the response obtained by the TM 5-855 method and that obtained for the exact loads is smaller, but still considerable, ranging up to 70% overestimation in maximum displacement and 62% in maximum bending moment.

2- In both methodologies, the differences between the maximum bending moments for equivalent loads and for moving loads are less than those in the maximum displacements. This is because after yield the bending moment does not change much, the hardening ratios considered in the models being quite small (less than 2%).

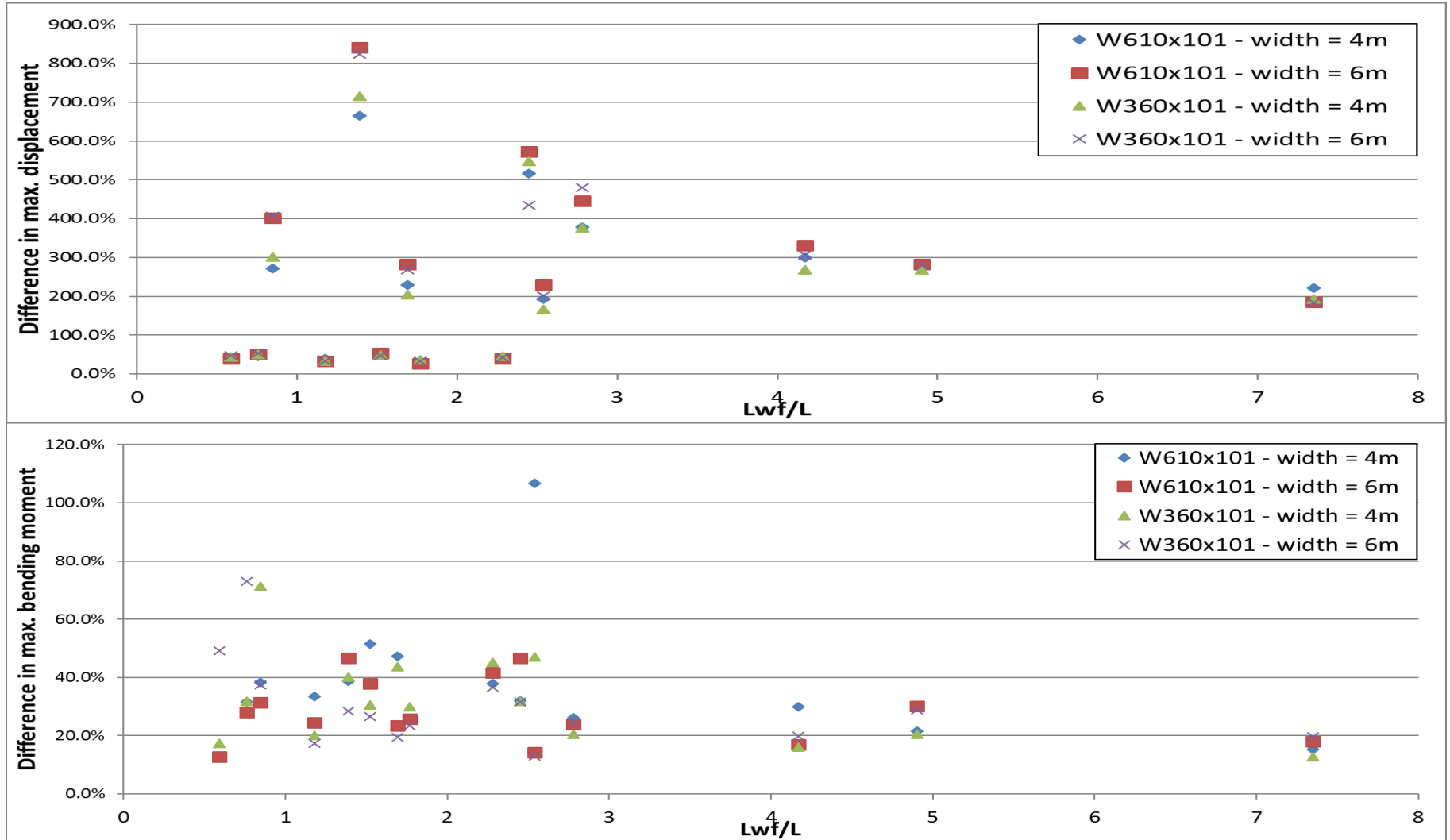


Figure 3.16. Difference in response for MDOF models subject to moving blast loads and uniform loads from UFC 3-340-02

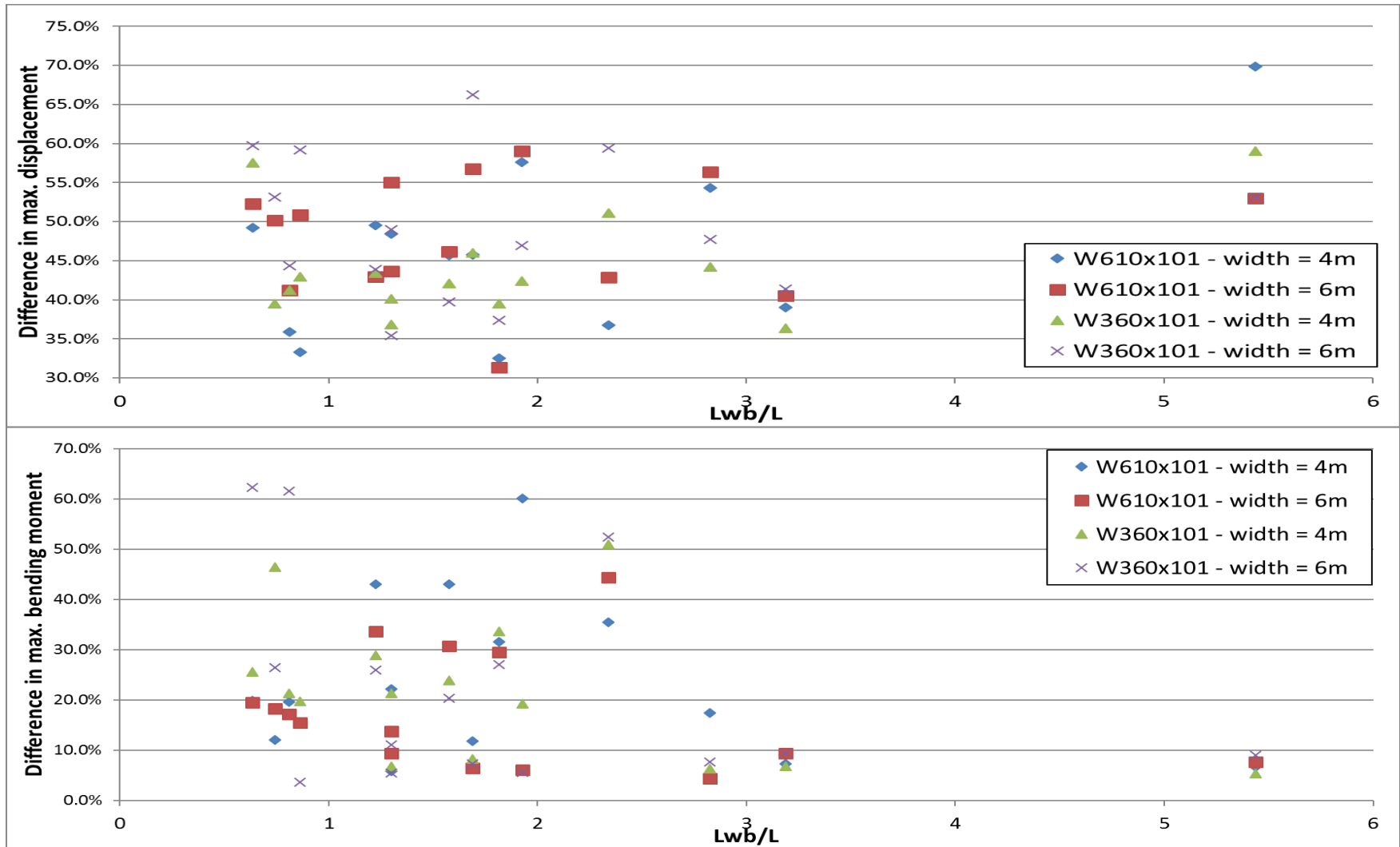


Figure 3.17. Difference in response for MDOF models subject to moving blast loads and uniform loads from TM 5-855

3- Most often the difference between the maximum displacements for travelling blast and simplified blast loads are greater when the loads are higher (larger tributary areas), but the trend is the opposite for the maximum bending moments. This is due to the fact that the higher loads cause yielding of the beams limiting their moments to only slightly above the plastic moments, while the displacements grow without any limitations after yield.

4- Other than the observed behavior noted in the foregoing, no distinct trend or pattern can be detected in the differences between the response measures for exact and equivalent loads and the difference values scatter randomly when plotted against the span ratios. The differences between the responses obtained for the travelling blast loads and for the equivalent loads are presented again in Table 3.11 for all of the cases analyzed. It will be noted that the error in UFC methodology grows with the span length, while in majority of cases this trend is reversed for the TM methodology.

Table 3.11. Differences beams response in travelling and equivalent uniform blast loads (MDOF models)

Case no.	Blast type	Span length (m)	Tributary width (m)	Beam section	UFC 3-340-02		TM 5-855	
					Error in max. displacement	Error in max. moment	Error in max. displacement	Error in max. moment
1		4			28.3%	28.1%	33.9%	33.8%
2	B 1	6			39.9%	40.7%	49.9%	50.8%
3		12			42.4%	15.3%	55.3%	22.7%
4		4	3	W610x101	43.4%	41.7%	41.6%	39.2%
5	B 2	6			56.8%	57.9%	47.8%	49.1%
6		12			55.0%	32.0%	45.0%	20.1%
7	B 3	4			196.0%	107.8%	58.8%	61.0%

Case no.	Blast type	Span length (m)	Tributary width (m)	Beam section	UFC 3-340-02		TM 5-855	
					Error in max. displacement	Error in max. moment	Error in max. displacement	Error in max. moment
8		6			235.2%	54.0%	51.4%	27.7%
9		12			295.2%	39.1%	37.3%	12.7%
10		4			318.9%	30.9%	61.6%	18.4%
11	B 4	6			409.9%	27.6%	55.5%	13.1%
12		12			699.2%	41.3%	39.4%	17.7%
13		4			240.9%	20.3%	80.3%	11.4%
14	B 5	6			292.7%	23.5%	44.4%	8.9%
15		12			557.7%	38.8%	38.1%	11.3%
16		4			33.8%	26.3%	37.9%	30.2%
17	B 1	6			41.3%	29.1%	52.1%	38.5%
18		12			47.2%	15.3%	60.3%	22.2%
19		4			49.2%	44.2%	52.4%	47.0%
20	B 2	6			55.3%	41.8%	47.6%	34.4%
21		12			59.7%	31.8%	49.6%	20.7%
22		4			232.2%	20.1%	60.9%	11.6%
23	B 3	6	6		284.4%	24.6%	55.7%	14.8%
24		12			412.6%	32.6%	53.2%	19.5%
25		4			342.7%	22.4%	60.7%	9.2%
26	B 4	6			452.0%	29.2%	58.4%	11.1%
27		12			883.5%	48.7%	57.8%	17.1%
28		4			198.3%	20.1%	59.7%	9.6%
29	B 5	6			291.4%	30.4%	43.8%	9.5%
30		12			585.4%	49.5%	46.2%	11.4%
31		4			36.2%	32.8%	40.0%	36.5%
32	B 1	6			40.7%	23.1%	51.6%	32.3%
33		12			47.9%	22.3%	61.1%	30.8%
34		4	3	W360x101	51.1%	51.8%	57.1%	57.8%
35	B 2	6			53.8%	36.2%	46.3%	29.2%
36		12			60.2%	38.9%	50.0%	27.9%
37	B 3	4			175.9%	54.8%	47.1%	25.5%

Case no.	Blast type	Span length (m)	Tributary width (m)	Beam section	UFC 3-340-02		TM 5-855	
					Error in max. displacement	Error in max. moment	Error in max. displacement	Error in max. moment
38		6			217.4%	46.3%	46.1%	23.3%
39		12			311.1%	73.6%	42.8%	48.4%
40		4			286.5%	16.3%	51.3%	6.6%
41	B 4	6			401.0%	26.8%	53.3%	13.9%
42		12			733.4%	42.9%	46.1%	22.0%
43		4			202.5%	16.7%	64.5%	8.9%
44	B 5	6			286.9%	21.6%	43.2%	7.9%
45		12			587.4%	35.6%	45.3%	9.9%
46		4			39.2%	29.3%	43.4%	33.1%
47	B 1	6			40.4%	21.5%	51.4%	30.5%
48		12			51.2%	57.2%	65.0%	71.1%
49		4			51.7%	40.6%	69.3%	56.8%
50	B 2	6			51.1%	31.1%	44.0%	24.7%
51		12			63.3%	74.8%	53.1%	63.4%
52		4			215.5%	15.0%	53.9%	7.6%
53	B 3	6	6		291.7%	25.4%	58.3%	16.6%
54		12			422.4%	40.1%	57.9%	29.0%
55		4			331.2%	21.6%	56.8%	9.1%
56	B 4	6			483.2%	28.3%	67.3%	10.7%
57		12			841.3%	35.4%	62.2%	9.3%
58		4			193.2%	20.0%	58.5%	9.3%
59	B 5	6			302.8%	30.9%	50.2%	11.3%
60		12			469.6%	33.3%	44.2%	6.9%

5-The other pattern that can be observed from the data presented in Table 3.11 is that the differences are larger for higher loads, contributed either by a larger tributary area or a higher blast magnitude.

6- In order to get a better understanding of the nature of the differences, the time-histories of the response for cases 1 and 15 are plotted in Figures 3.18 to 3.21.

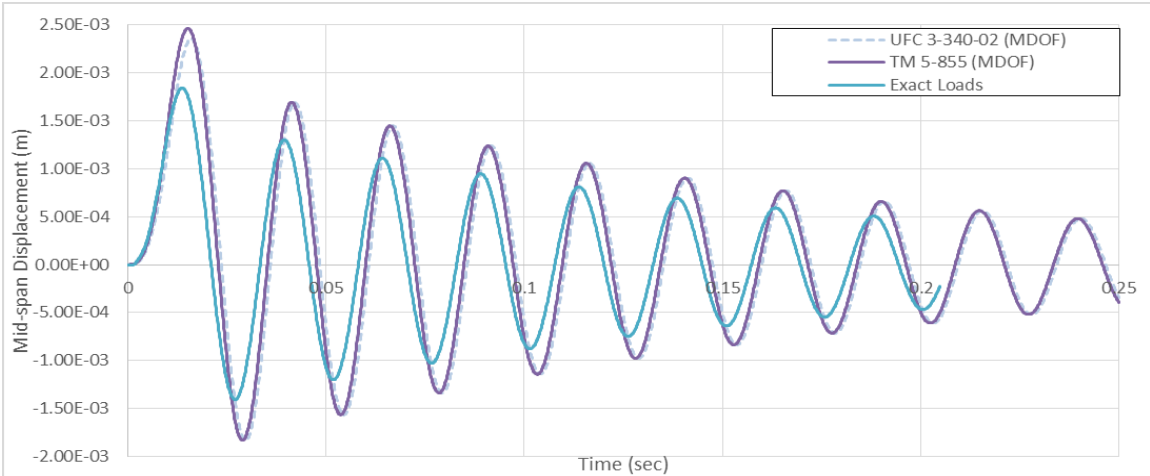


Figure 3.18. Midspan displacement time-history in simplified and travelling loads for Case 1

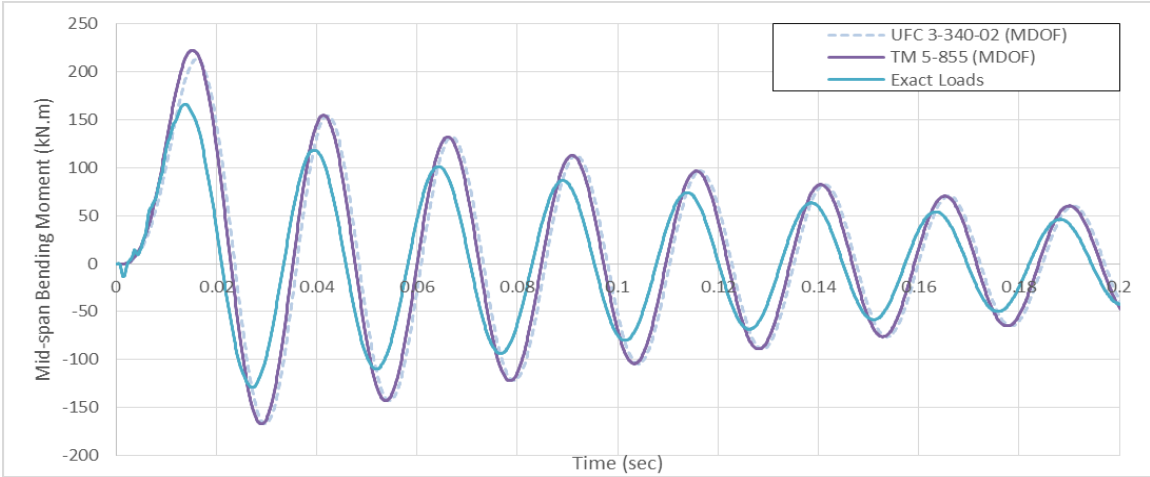


Figure 3.19. Midspan moment time-history in simplified and travelling loads for Case 1

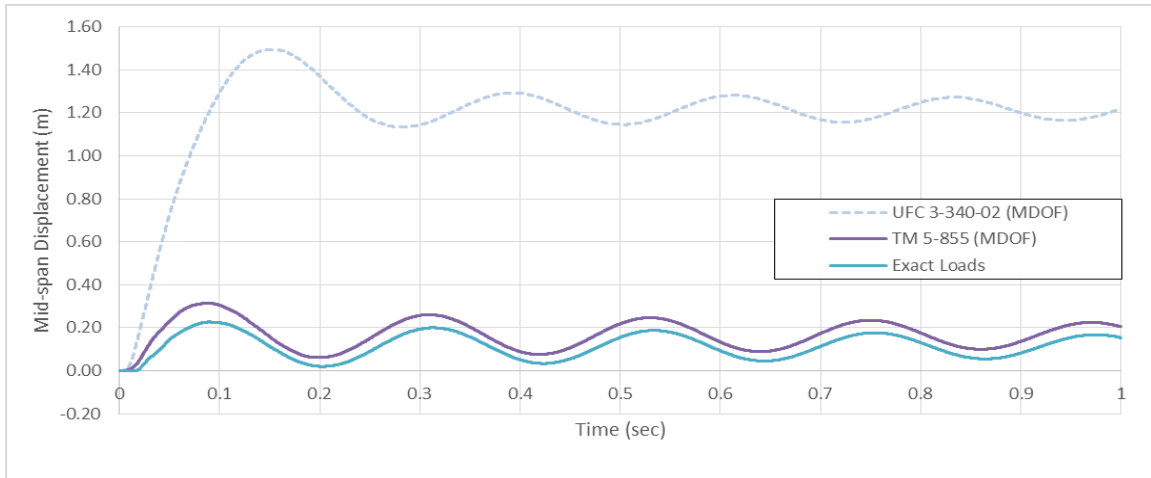


Figure 3.20. Midspan displacement time-history in simplified and travelling loads for Case 15

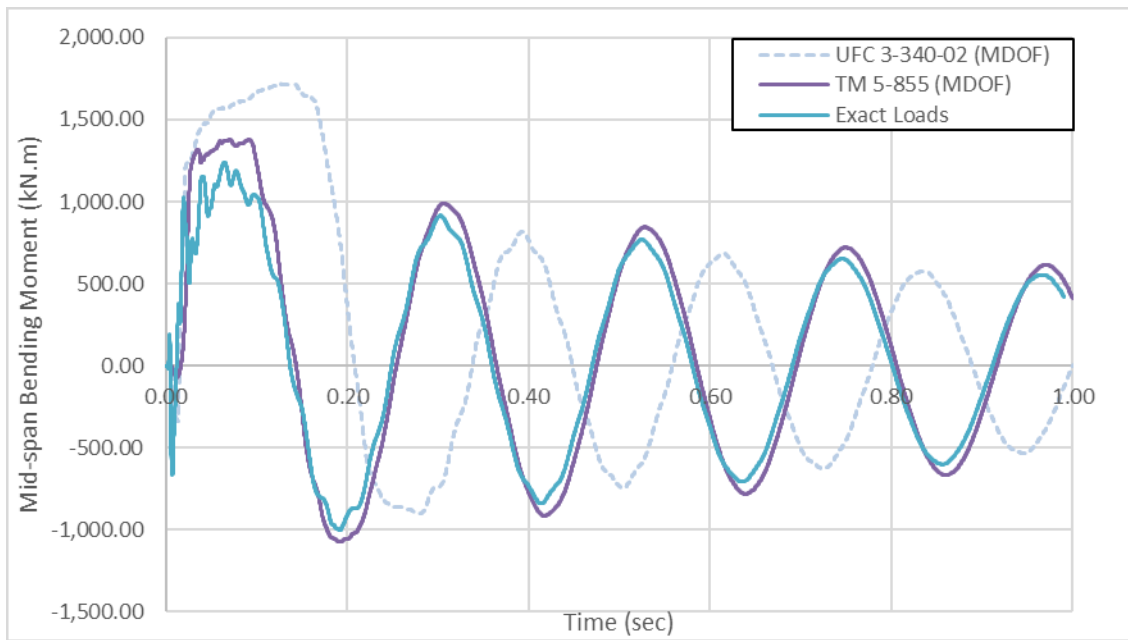


Figure 3.21. Midspan moment time-history in simplified and travelling loads for Case 15

The plots in Figures 3.18 to 3.21 confirm the observation that the differences between the more precise and simplified methodologies (especially UFC/ASCE method) increase with the magnitude of the blast. Also, the differences in the bending moment are much less than in the displacements. The other point that can be noted on a close examination of the response time-

histories is the small fluctuations in the response of beams to the moving load. This can be attributed to the contributions of modes of vibrations other than the first that get excited in this type of loading. On the other hand, the response plots for equivalent uniform loads are smoother, mainly because only the first mode of vibration contributes to the response.

7- Another observation that can be made is that for all analyzed cases, the maximum response of the beam occurs when the shock front has cleared the roof span. This is contrary to the TM 5-855 and UFC 3-340-02 methods (not explicitly in case of UFC) that use the location of a point D on the roof (the point at which the shockfront should be located to cause the maximum response) for the rise time of the simplified uniform loads. It is observed for the response analyses for travelling wave that in all cases, the response starts when the blast loads have almost cleared the span, and then the time it takes to peak depends on the period of the beams and whether the beam is pushed into nonlinearity. Generally, the peak of the response occurs approximately within one fourth of the beam period after the loads have cleared the span (as seen in Figure 3.18 and 3.20). This is contrary to the concepts described in the simplified methods.

3.3. Experimental Study

To further investigate the response of roof beams to a propagating blast wave, and also to verify the numerical results, several experimental tests are carried out as a part of this study. The experimental tests were used to investigate the accuracy of the detailed numerical analysis of response to a blast load traversing a roof element along the direction of blast wave propagation. The experimental tests were carried out at the facilities of Canadian Explosives

Research Laboratory (CERL), Natural Resources Canada in Ottawa, Canada. The details of the experimental design and setup as well as the test results are presented in this section.

3.3.1. Tests Setup

The maximum amount of explosive that can be used at the CERL test facilities is limited. A blast table designed for use with small explosive charges was used for the testing. The explosive charge mass and table size considerations dictated the dimensions of the experimental specimens and the test setup. The overall dimensions of the blast table were approximately 2.36 m (6'-9") by 1.2 m (4'-0"), as shown in Figure 3.22. According to the regulations and protocols used in the field experimentation, the maximum amount of the explosive could not be more than 100 grams of C4 explosive (120 g of TNT-equivalent mass).

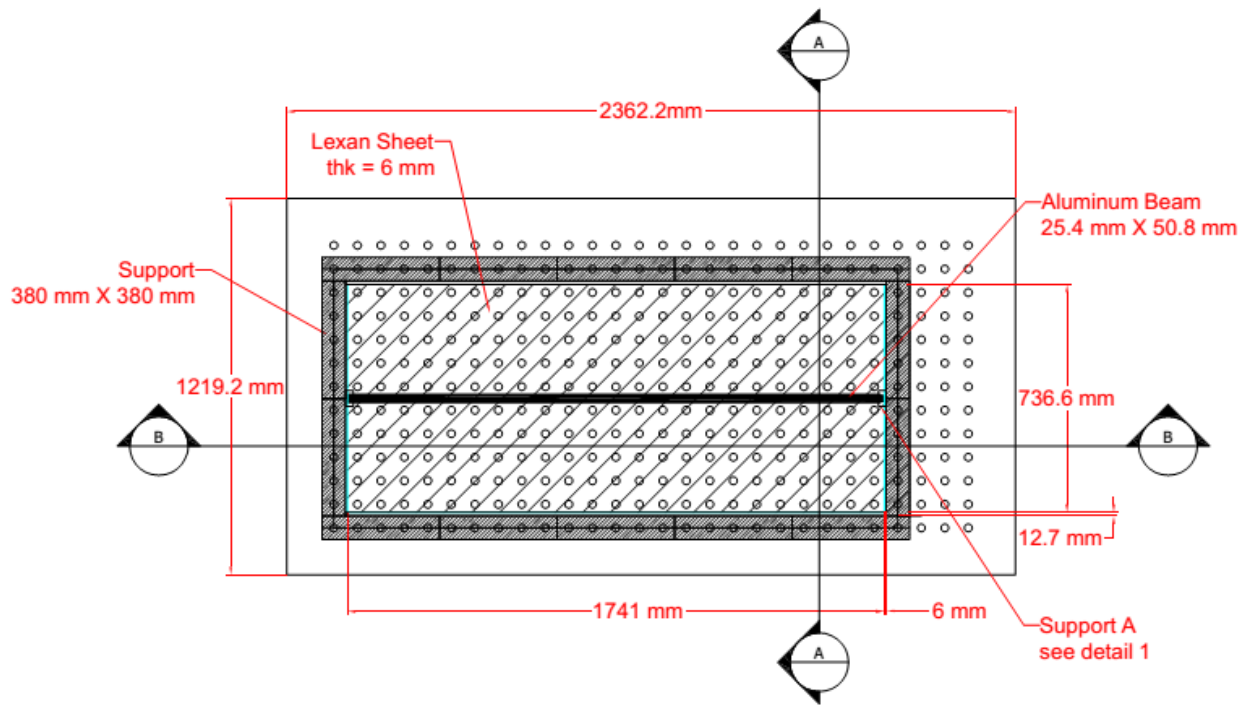


Figure 3.22. Plane view of blast table and the experimental setup

Since the explosions were going to be relatively small in scale, a small-scaled aluminum beam having a cross-section of 25×50 mm was used as the roof beam. The other properties of the aluminum roof beam, such as the support conditions and the span, were chosen to ensure that the beam response remained elastic throughout the test. The details of the experimental setup are shown in Figures 3.22 and Figure 3.23 in plan and elevation views, respectively. The completed field setup is shown in Figure 3.24.

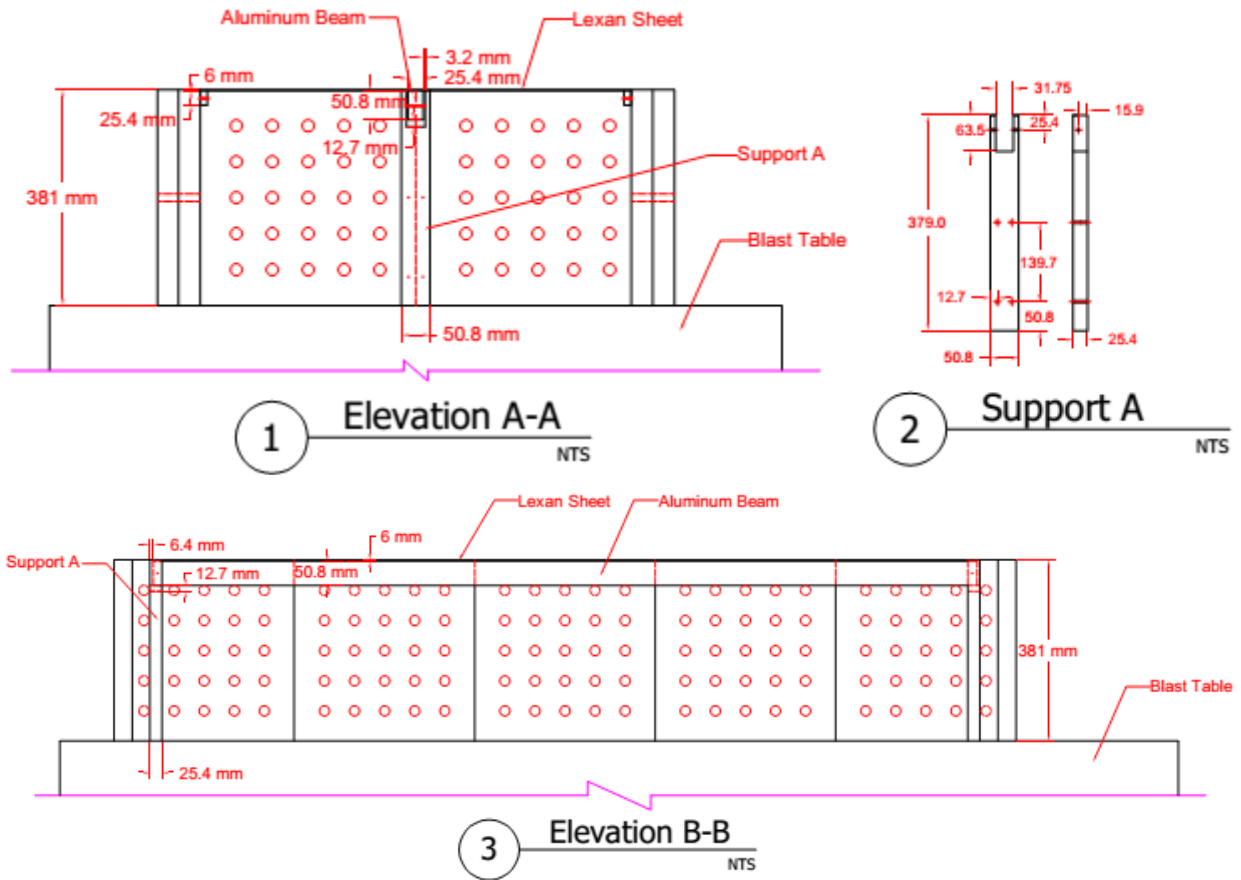


Figure 3.23. Elevation views of blast table and experimental setup



Figure 3.24. Experimental setup in the field

Instrumentation for the experimental tests included high-tension string potentiometers (string pots) attached to mid-span and quarter-span locations of the beam to capture the deflections of the beam. The string pots are designed to perform under very high accelerations, up to 90 times the acceleration of gravity¹. Also, Pico Coulomb (PCB) Piezoelectric pressure gauges were installed at five locations along the span of the roof beam and used to capture the pressure profile of the traversing blast wave. Figure 3.25 shows the location of the blast pressure gauges.

¹ Specifications are available online at http://celesco.com/_datasheets/mt3a.pdf.

A schematic plan of the instruments used in the tests is also shown in Figure 3.25. Figure 3.26 shows a photograph of the instrumentation installed on the blast table.

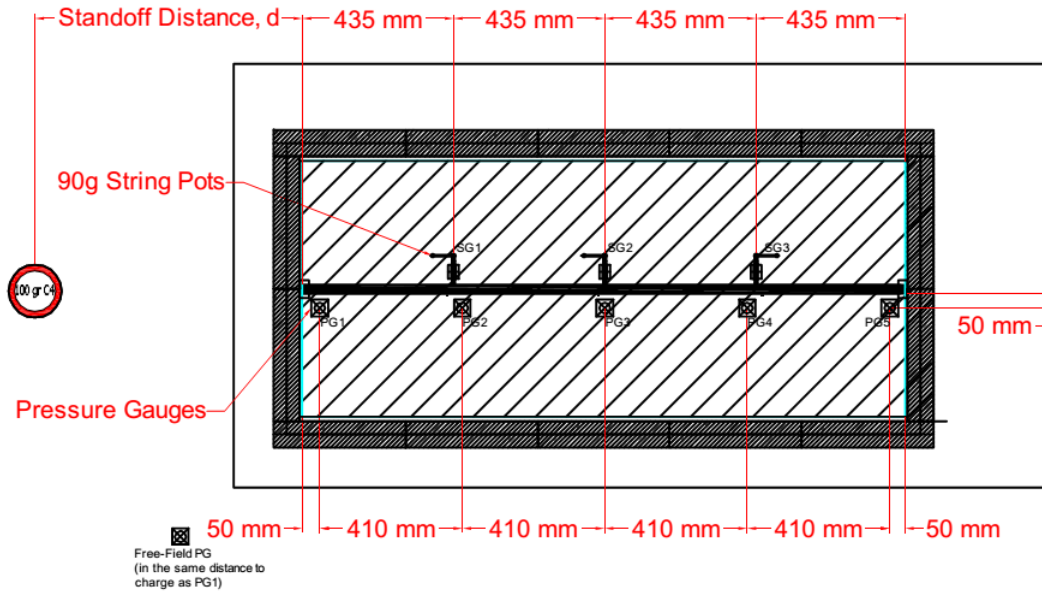


Figure 3.25. Plan of the measuring instruments in the test

The explosive charges were located at standoff distances, ranging from 250 mm to 1000 mm to the front edge of the roof. The elevation of the charges was slightly less than the roof elevation as shown in Figure 3.27, so that a clear path to the roof was avoided to ensure an incident (not reflected) pressure distribution on the roof plate.

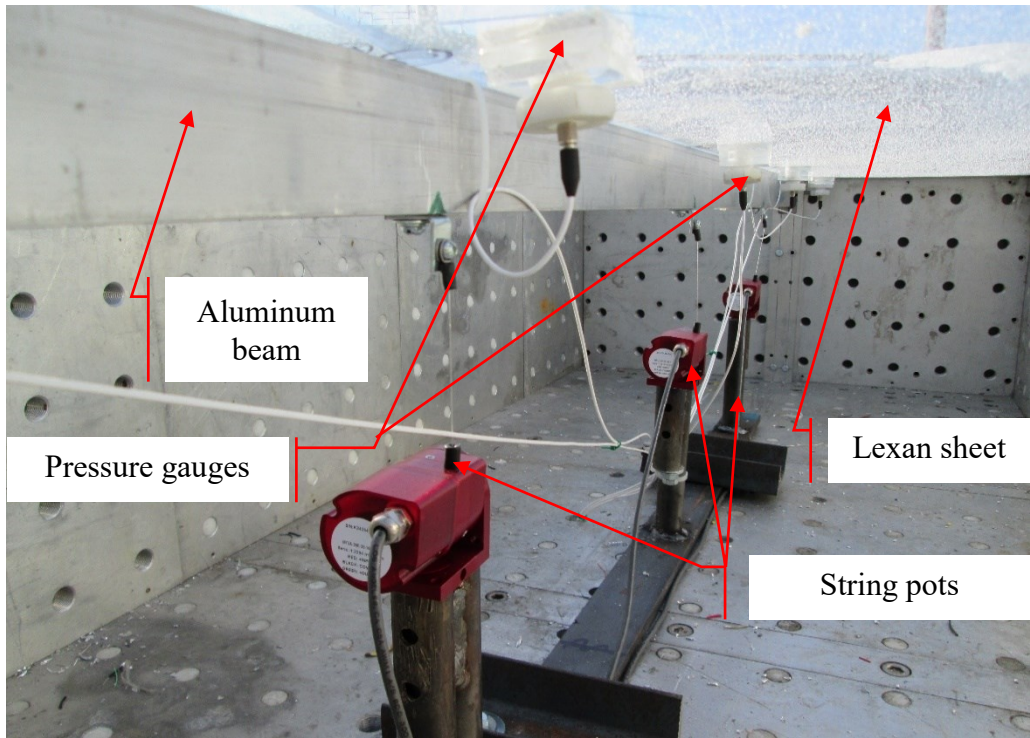


Figure 3.26. Inside view of the roof and measuring instruments in the tests

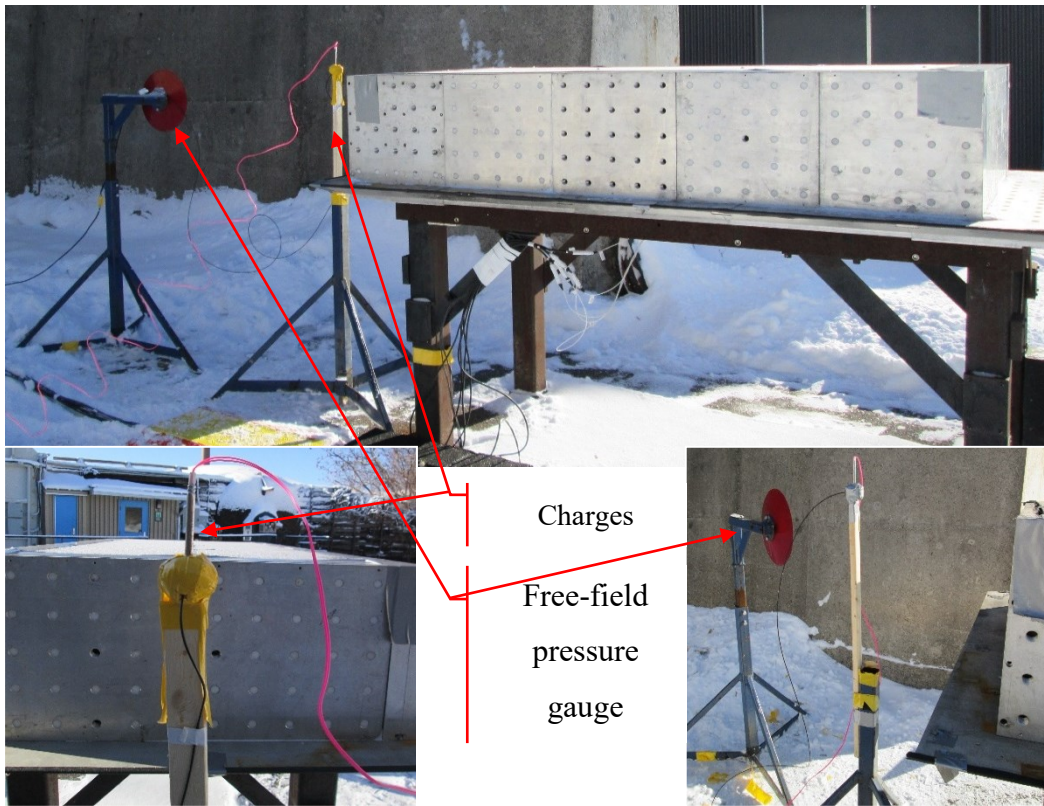


Figure 3.27. Completed setup for the tests in the field

3.3.2. Blast Scenarios

100 grams of C-4 explosive was selected as the charge mass and was detonated at 4 different standoff distances from the edge of the roof. The standoff distances used were 250, 500, 750 and 1000 mm from the roof edge. The pressure time-histories from the blast scenarios were calculated using CONWEP and compared to those measured during the tests. The comparisons are shown in Figure 3.28. The blast pressures at different points on the roof are obtained from Equation. 3.1. During the tests, some of the pressure gauges failed to capture the data, therefore only the results obtained from the gauges that functioned are compared with the CONWEP results.

As can be observed from Figure 3.28, the arrival times measured during experiments match those obtained from CONWEP reasonably well, while the peak pressures are slightly less consistent. In most cases, the experimental peak pressures are higher than the CONWEP values. The higher differences occur particularly at the closer ranges, that is, close to the front edge of the roof (PG1 gauge in Figure 3.25). This is on account of the expected turbulence from blast wave reflection and diffraction around the front face of the structure. Also, the negative phase of the experimental blast has been truncated for comparison with the CONWEP results.

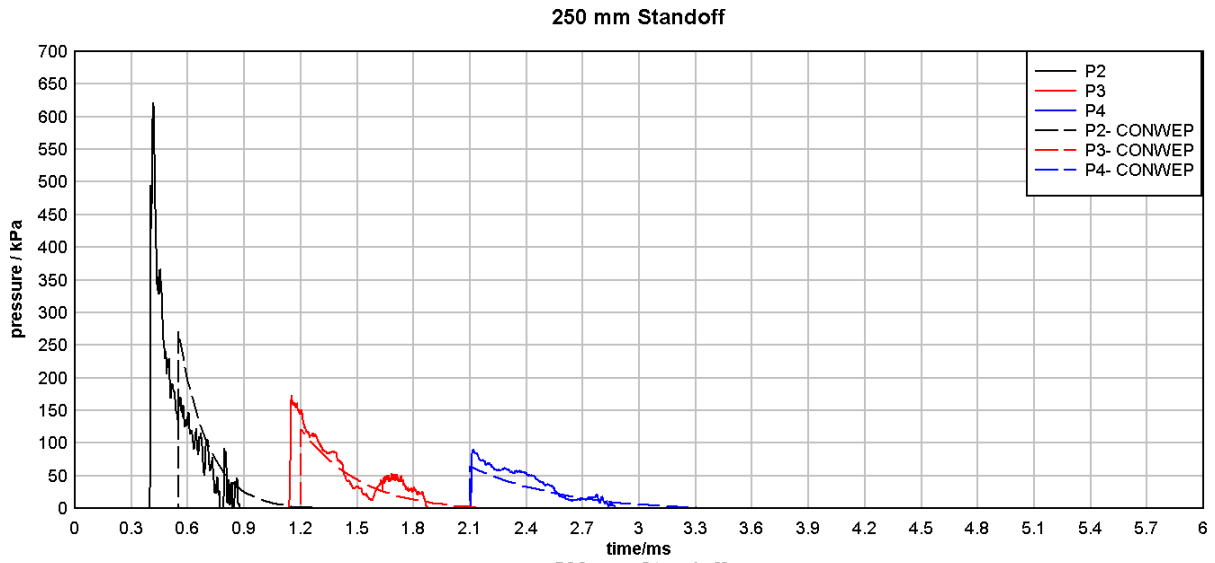


Figure 3.28. Comparison of measured pressures with those obtained from CONWEP

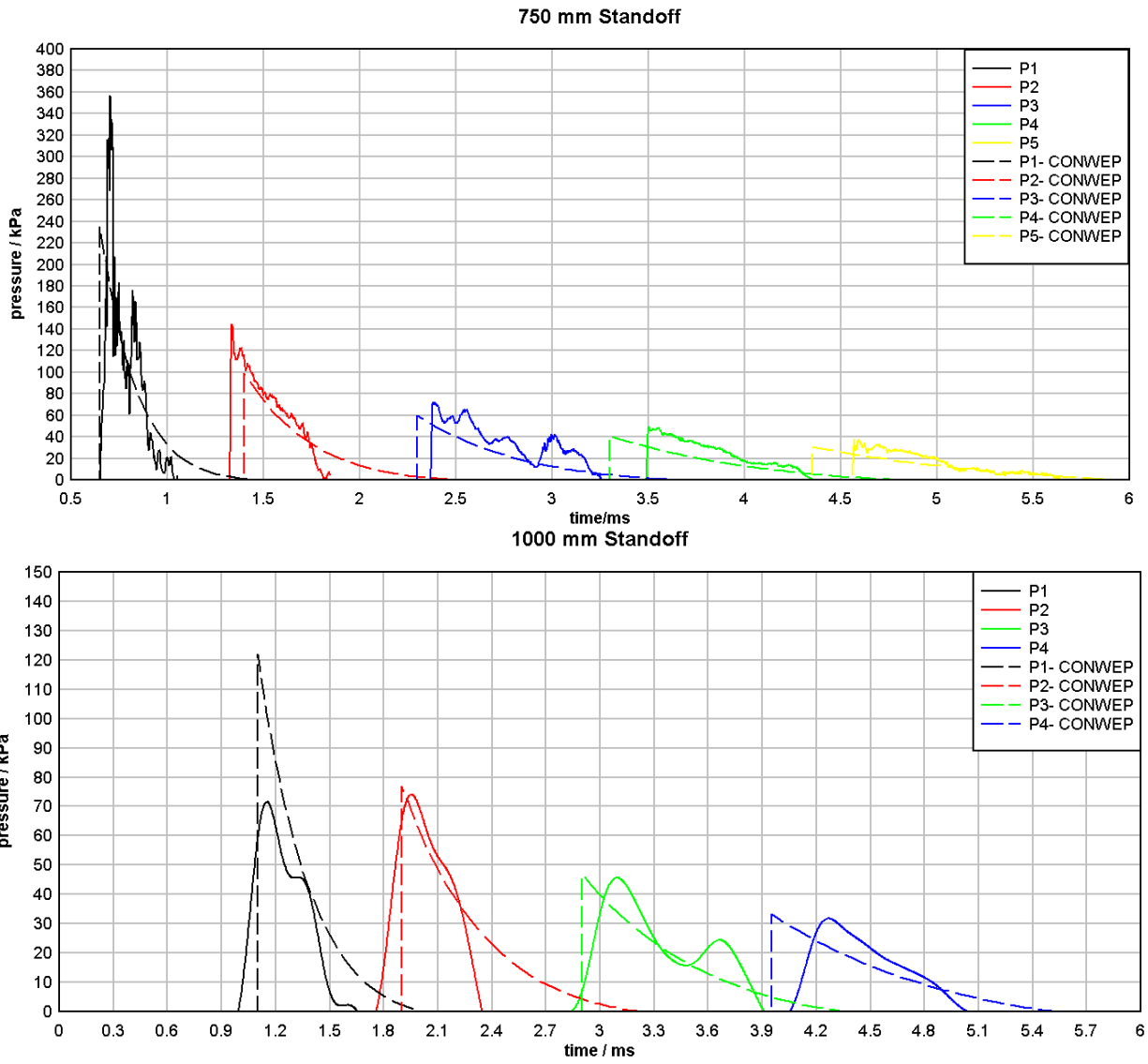


Figure 3.28 (Cont'd.) Comparison of measured pressures with those obtained from CONWEP

3.3.3. Numerical Simulation of the Experiments

The objective of the tests was to compare the test results with the results obtained from the numerical models. For such comparison, test cases are modeled using SDOF models and equivalent uniform loads, as well as the more detailed FE models and travelling blast loads. The characteristics of the analytical model used in the simulations are presented in Table 3.12. The SDOF and FE models described earlier in this chapter are generated and analyzed for the four

tested scenarios. The equivalent uniform loads are calculated based on both UFC/ASCE and TM 5-855 methodologies and are presented in Table 3.13 and Table 3.14.

Table 3.12. Characteristics of the analytical model for numerical simulation of the experiments

<i>Parameter</i>	<i>Value</i>
<i>Length of beam (L)</i>	1.7 m
<i>Tributary width (L_{tr})</i>	$\frac{0.7366}{2} m$
<i>End conditions</i>	simply-supported
<i>Modulus of Elasticity (E)</i>	69.0 GPa (Aluminum)
<i>Yield stress (F_y)</i>	275.0 MPa (Aluminum)
<i>Beam dimensions</i>	25 mm× 50 mm (Rectangular)
<i>Moment of inertia (I)</i>	260.42×10 ³ mm ⁴
<i>Max. yield moment (M_y)</i>	$\sigma_y \frac{I}{h/2} = 2.86 kN.m$
<i>Thickness of Lexan sheet (t_L)</i>	6 mm
<i>Mass per unit length (m)</i>	mass per length of beam + [mass per area of Lexan]·t _L ·L _{tr} = 6.027 kg / m

Table 3.13. Equivalent uniform loading for the experimental cases based on UFC/ASCE method

Test no.	Standoff (m)	Z _f (m/kg ^{1/3})	P _{sof} (kPa)	q _{of} (kPa)	C _D	t _{af} (msec)	t _{df} (msec)	L _{wf} (m)	L _{wf} /L	C _E - UFC	P _{max} (kPa)
1	0.25	0.54	3942	565.81	-0.20	0.0766	0.1587	0.312	0.179	0.134	416.827
2	0.5	1.08	951.4	196.08	-0.30	0.2641	0.9018	0.919	0.528	0.293	219.685
3	0.75	1.62	379.9	20.39	-0.40	0.5657	0.8456	0.589	0.339	0.211	72.122
4	1	2.15	198.1	4.80	-0.40	0.9656	0.924	0.514	0.295	0.191	35.961

Table 3.14. Equivalent uniform loading for the experimental cases based on TM 5-855 method

Test no.	Standoff (m)	Z _b (m/kg ^{1/3})	P _{sob} (kPa)	q _{ob} (kPa)	C _D	t _{ab} (msec)	t _{db} (msec)	L _{wb} (m)	L _{wb} /L	C _E - TM	P _{max} (kPa)
1	0.25	4.29	47.68	2.06	-0.40	3.158	1.537	0.619104	0.356	0.516	23.773
2	0.5	4.83	38.42	1.36	-0.40	3.797	1.609	0.629924	0.362	0.519	19.391
3	0.75	5.36	31.94	0.96	-0.40	4.454	1.673	0.641428	0.369	0.522	16.292
4	1	5.90	27.2	0.70	-0.40	5.123	1.731	0.653279	0.375	0.525	14.007

For assigning a realistic damping ratio to the numerical model, the responses of the beams in the field were examined and using logarithmic decrement of the peaks in two consecutive free-vibration cycles ($u_{max,n}$ and $u_{max,n+1}$), the damping ratios (ξ) were determined for the different experimental cases using Equation 3.6. The calculated damping ratios are 7.9%, 8.6%, 5.0% and 4.0% in cases 1 to 4 (standoff of 1000 mm to 250 mm), respectively.

$$\ln\left(\frac{u_{max,n}}{u_{max,n+1}}\right) = \frac{2\pi\xi}{\sqrt{1-\xi^2}} \quad (3.6)$$

The experimental and analytical results are compared in Figure 3.29 and Figure 3.30. In addition, the maximum responses of the beams for different scenarios obtained from the experiments and the numerical models are summarized in Table 3.15.

Table 3.15. Comparison of the maximum mid-span deflections obtained from numerical analyses and experiments

Test no.	Experimental results	MDOF model with travelling blast loads from CONWEP	MDOF results with pressures from experiments	SDOF model based on UFC/ASCE	SDOF model based on TM 5-855
1	11.97	19.67	- *	78.02	17.77
2	9.04	14.62	11.09	81.21	16.34
3	7.94	12.55	8.87	37.86	14.52
4	5.67	10.13	- *	24.00	13.43

* some pressure gauges were damaged, so carrying out this analysis was not possible.

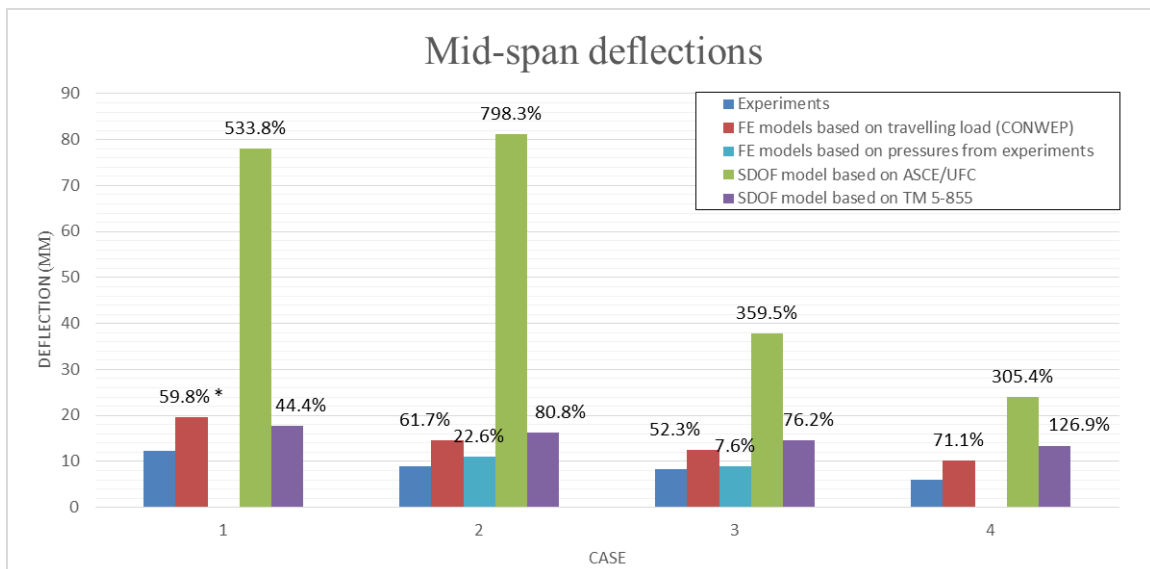


Figure 3.29. Results summary for the different cases

(* the labels show the difference with experimental results)

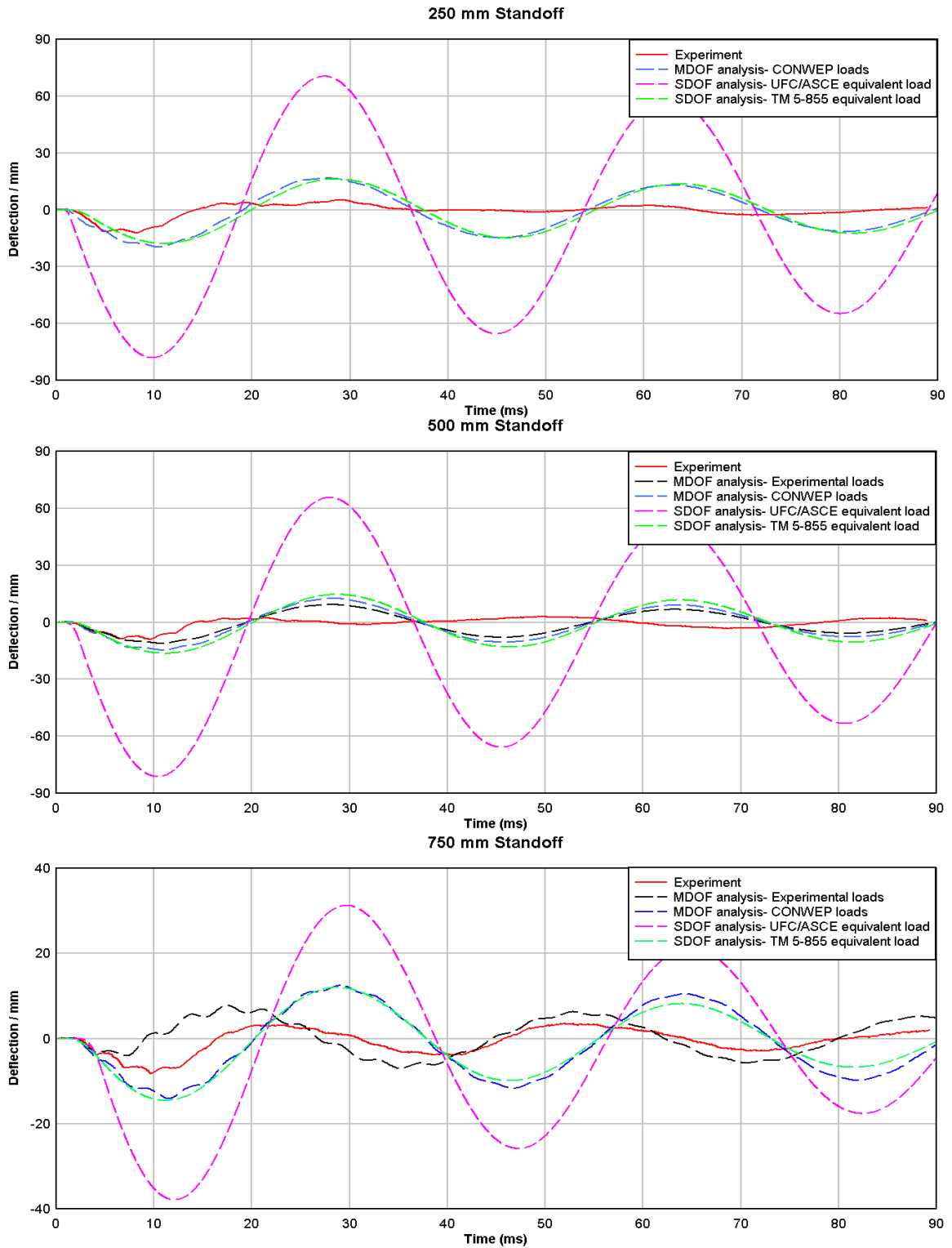


Figure 3.30. Comparison of mid-span deflections for different cases

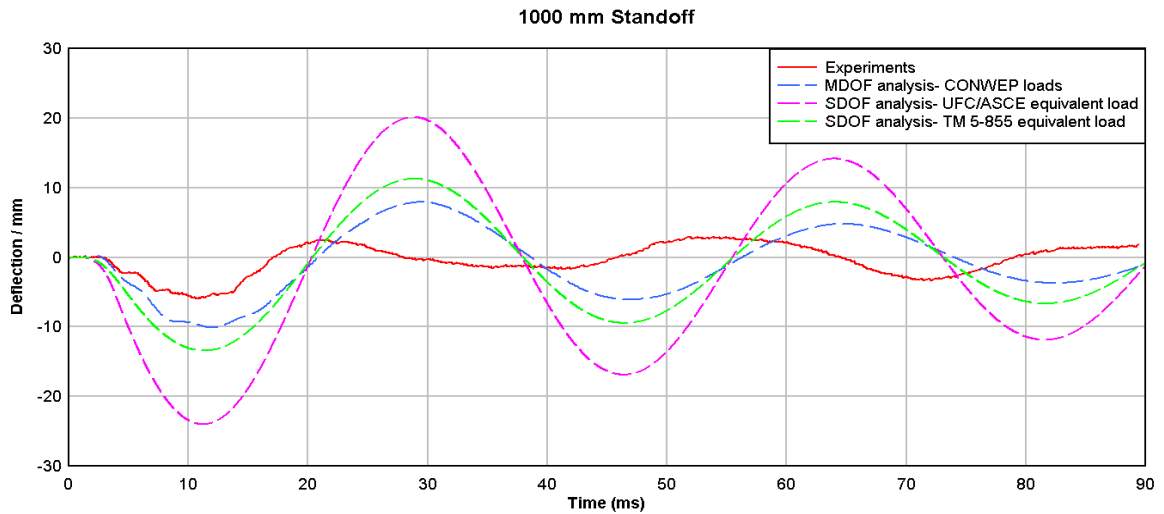


Figure 3.30. (Cont'd.) Comparison of mid-span deflections for different cases

3.3.4. Discussion and Conclusion

Several observations can be made and conclusions drawn from the results presented in the preceding paragraphs:

1. The difference between the pressure time-histories obtained from CONWEP and those obtained from the test are more pronounced for the shorter standoff distances (250 mm), and for the first pressure gauge (pressure time-history P1 recorded at gauge PG1). One of the reasons is the high turbulences near the edge of the roof, which can affect the recorded pressures significantly.
2. On comparing the measured response of the roof beam with that obtained from numerical simulations, it is observed that the vibration period of the system changed in the experiments throughout the duration of measurement. This implies a characteristic nonlinearity in the structure which can come from the connection of the Lexan sheets to the beam. However, the varying period of the

structure as measured in the tests (30.55 to 34.31 msec) and the periods of vibration obtained from the FE and SDOF models (35.20 and 35.11 msec respectively) are close. This proves that aside from the inherent nonlinearity in the connections, the numerical models capture the physical properties of the system with reasonable precision.

3. On comparing the peak responses of the structure measured in the experiments and those obtained from numerical simulations, it is observed that generally the results from FE (MDOF) models provide a closer match with the results of the experiments. It appears that the differences between the results of the MDOF models and the experiments are mostly because of the difference in the loading, because when the recorded pressures are used instead of CONWEP pressures, the accuracy of the numerical simulation improves significantly (errors going from 61.7% to 22.6% and 52.3% to 7.6% for standoff distances of 500 and 750 mm, respectively). It is therefore reasonable to conclude that the FE model with travelling blast loads, used in this research, is capable of capturing the response of the roof beams under blast loading.
4. Between the two equivalent uniform load methodologies, TM 5-855 provides the equivalent uniform loads that yield more accurate results. The use of equivalent loads determined from the other methodology (ASCE/UFC) results in large overestimation of the response. Although the scale of the experiments dictated to use the equivalent load coefficients at the margins of their applicable range, the results and trends observed are similar to the ones obtained in the previous

stages of this research. Thus, it is suggested that the equivalent loads specified in TM 855 be used to determine the response in cases where for some reason, the more accurate MDOF models with travelling loads cannot be employed.

5. In all of the experiments discussed here, it was observed that the maximum response of the beams occurred when the shockfront had cleared the whole beam span. This is contrary to what has been suggested in the TM 5-855 methodology, which defines a point on the roof at which the shockfront must be located to produce the maximum internal efforts in the beam.

3.4. Computer Code for Nonlinear Dynamic Analysis

As discussed earlier, when an equivalent uniformly distributed load methodology is used for analysis of the roof beams aligned perpendicular to the shockfront, the nature of the original problem which includes a propagation of the pressures is ignored. Therefore, despite very careful considerations and efforts in estimation of the equivalent loads, significant differences can occur between the response of the beams obtained from analyses using the more precise travelling wave model and the simplified methodologies based on equivalent uniform load. An easy to use computer code was therefore developed to analyze the response of the roof beams using the more precise travelling blast wave model. In this section, a description of the computer code and verification of the numerical analysis results obtained from the code against the corresponding results from the analyses presented in earlier parts of the thesis, are presented.

3.4.1. General flow of the code

The computer code referred to in the preceding paragraph was originally written in Matlab programming language, then converted to a standalone package that can be run on any computer. This code has a graphical user interface (GUI) and uses different subroutines for the analyses, from generating the blast load time-histories to dynamic analysis of the beams and post-processing the results. The required input data is supplied to the code via the designed GUI, as shown in Figure 3.31.

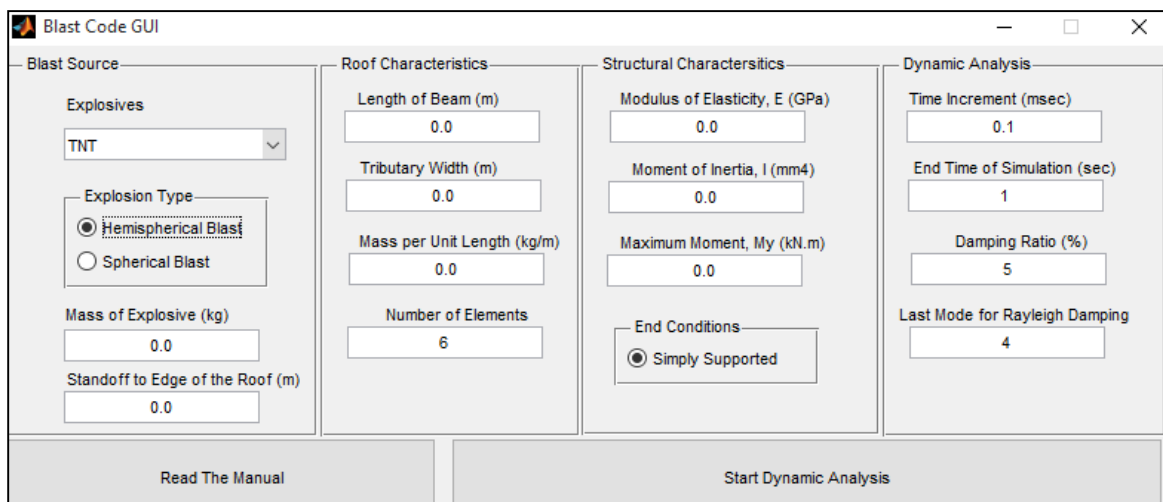


Figure 3.31. Snapshot of the input data in the designed computer code GUI

As shown in Figure 3.31, the input data required for the analysis are categorized into blast source data, roof and structural characteristics, and dynamic analysis inputs. The general flow of the code is shown in Figure 3.32. Different parts and subroutines used in the code are described in the following section.

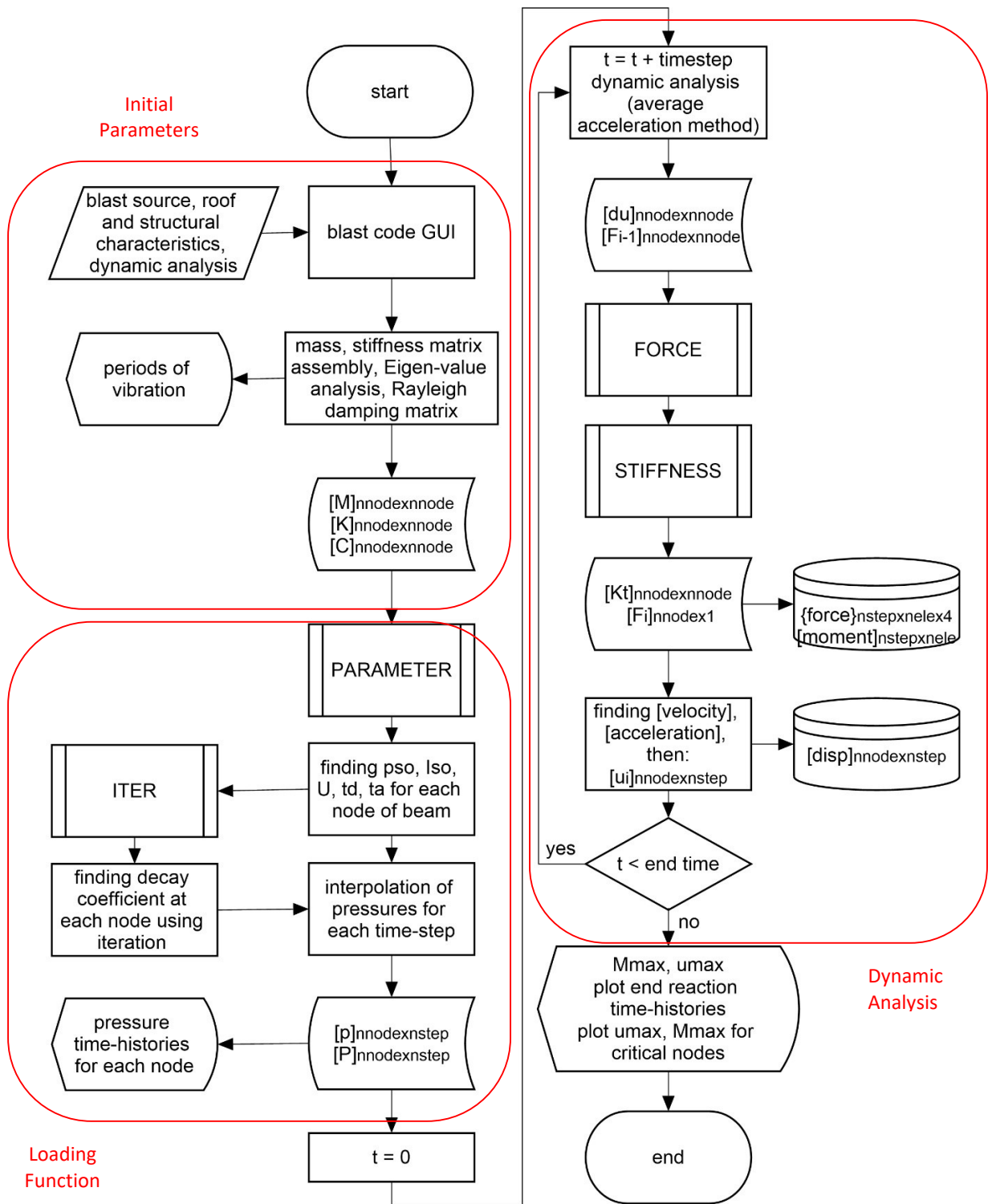


Figure 3.32. General flowchart of the written code for analysis of roof beams

3.4.2. Calculation of initial parameters

Based on the data input to the code via the designed GUI, several parameters that are used throughout the analysis are defined at the beginning of the code. These essential parameters include total number of time steps for analysis ($nstep$), the length of the elements, and the total number of nodes and elements ($nnode$ and $nele$ respectively).

Other parameters are defined at the start of the computation; they include the mass and stiffness matrices. A lumped mass matrix \mathbf{M} and element stiffness matrix \mathbf{K}^e based on elastic rotations and transverse deflections of the beam elements are generated.

Since the code is designed to carry out a nonlinear analysis, the global stiffness matrix \mathbf{K}_1 is assembled without using static condensation of the rotational DOF's. The assembly of the global stiffness matrix is carried out in the STIFFNESS subroutine.

After finding the global stiffness and mass matrices, an Eigen-value analysis is carried out and Rayleigh damping matrix \mathbf{C} is generated based on the initial stiffness matrix, and the desired damping ratio in the mode numbers input in the GUI. The damping matrix is formed using Equations 3.4 and 3.5.

3.4.3. Generation of loading function

After generating the mass, stiffness and damping matrices of the structure, the blast load time-histories to be applied to the transverse DOF's are generated. For this, a methodology similar to that discussed in section 3.2.3 is employed, where the blast shockfront is placed on each node on the beam ($inode$), and the blast pressures are calculated. The calculations are performed in subroutine PARAMETER.

Given the charge weight W in kg, and the stand-off distance x_j in m, the blast load parameters, namely the maximum pressure P_{so} in kPa, maximum impulse I_{so} in kPa-msec, the arrival time t_a in msec, and the duration of the exponential wave t_d in msec are determined by the subroutine PARAMETER using the simplified Kingery-Bulmarsh equations for hemispherical and spherical blasts (Swisdak 1994). Also, the dynamic pressure q_0 , and drag coefficient C_D are obtained from Equation 1.5 and Table 3.1 respectively. The TNT equivalency values for various explosives are used based on CONWEP. The exponential decay coefficient is determined by equating the maximum impulse to the area under the blast load. This is done in subroutine ITER.

After these calculations, an array of blast pressures is generated for each node using linear interpolation to find the pressures at the intermediate time-steps. Then, the pressure time-histories are multiplied by the tributary width of the roof beam and the element length to give the concentrated loads acting on the alternate nodes.

3.4.4. Dynamic Analysis

After defining the mass, initial stiffness and damping matrices, the dynamic analysis is carried out using the average acceleration method. The nonlinear behavior of the beam elements is considered using an elastic beam formulation with plastic hinges at the ends. The nonlinear behavior of the beams is considered as elastic-perfectly-plastic, which gives a conservative estimate of the response. The details of the dynamic analysis are discussed in the following.

3.4.4.1. Dynamic solver

Implicit numerical integration based on average acceleration method is used for the dynamic analysis of the MDOF system, so that the stability of the code is maintained regardless of the time step employed. In this regard. The flow of this process is presented in the following.

At each time-step i , the load increment vector $\Delta \mathbf{P}_i$ is calculated using Equation 3.7.

$$\Delta \mathbf{P}_i = \mathbf{P}_i - \mathbf{P}_{i-1} + \mathbf{M}(4/\Delta t) \dot{\mathbf{u}}_{i-1} + \mathbf{M} \ddot{\mathbf{u}}_{i-1} \quad (3.7)$$

Using the load increment and the tangential stiffness matrix from the previous time-step \mathbf{K}_{i-1}^t , the displacement increment and displacement vector are found from Equations 3.8 and 3.9.

$$\Delta \mathbf{u}_i = (\mathbf{K}_{i-1}^t)^{-1} \Delta \mathbf{P}_i \quad (3.8)$$

$$\mathbf{u}_i = \Delta \mathbf{u}_i + \mathbf{u}_{i-1} \quad (3.9)$$

Using the nodal displacements, and the stiffness forces from the previous time-step, the new element forces, and tangential stiffness matrices are determined and updated in the BEAMWITHHINGE subroutine, which is discussed in the following paragraphs. Also, the element forces are assembled into the global stiffness forces matrix \mathbf{F}_i^s . The new velocity and acceleration vectors are determined next from Equations 3.10 and 3.11 to be used in the analysis in the next time-step.

$$\dot{\mathbf{u}}_i = \dot{\mathbf{u}}_{i-1} + \Delta t (\mathbf{u}_i - \mathbf{u}_{i-1}) \quad (3.10)$$

$$\ddot{\mathbf{P}}_i - \mathbf{F}_i^S - \mathbf{C}\mathbf{u}_i \quad (3.11)$$

This procedure is repeated for the number of time-steps until the maximum time of the analysis is reached. At the end of each step, the elemental forces and nodal displacements are saved for post-processing the results. In this dynamic procedure, the iterations within each time-step are not carried out, since there is not much complexity in nonlinear behavior of the elements with elastic-perfectly-plastic hinges, and the error in calculation are not significant in this type of nonlinear behavior.

3.4.4.2. Nonlinear beam element

As mentioned in the preceding paragraph, the nonlinear behavior of the beams is modeled using an elastic beam with plastic hinges at the ends, a model that is commonly used in numerical codes for analysis of building structures, such as SAP2000, OPENSEES and DRAIN 2DX. The schematic view of this element is shown in Figure 3.33.

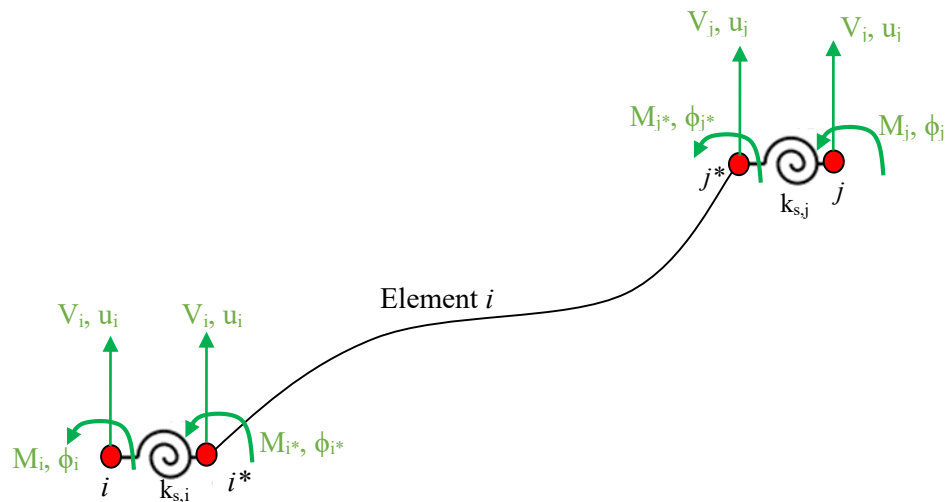


Figure 3.33. Elastic beam with plastic hinges at the end used in the code

The strategy to model the nonlinear behavior of the plastic hinges and their effect on the stiffness of the beam elements is based on the methodology described in Sekulovic and Nefovska-Danilovic (2004). The researchers investigated beam elements with two types of nonlinear hinges at the ends: one to consider the plasticity of the element and the other to consider the effect of the flexibility of the connection. The latter type is not used in the current code, since the connections between the beam elements are rigid, also there is no beam-column joints in the current model to consider the effect of axial loading.

In the concentrated plasticity model which is chosen for the current code, the behavior of the beam element is considered to be ideally elastic until the bending moments at the ends of the element reaches the moment capacity of the section, and the element becomes perfectly plastic, without any hardening. This is when the plastic hinge at the end of the element is formed. These plastic hinges are zero-length rotational springs connected to the end of the elastic beam elements as shown in Figure 3.33. Based on the assembly of the plastic hinges and elastic beams shown in Figure 3.33, the total rotations at the end nodes of the element (ϕ_i, ϕ_j) are the sum of rotations at the end of the elastic beam (ϕ_{i^*}, ϕ_{j^*}), and the rotation of the plastic hinges (ϕ_i^p, ϕ_j^p).

Elastic stiffness matrix for the beam element as shown in Equation 3.12 is used to relate the force and displacement parameters at i^* and j^* nodes.

$$\begin{Bmatrix} V_{i^*} = V_i \\ M_{i^*} \\ V_{j^*} = V_j \\ M_{j^*} \end{Bmatrix} = \begin{bmatrix} 12 & 6L & -12 & 6L \\ & 4L^2 & -6L & 2L^2 \\ & & 12 & -6L \\ \text{symm.} & & & 4L^2 \end{bmatrix} \begin{Bmatrix} u_{i^*} = u_i \\ \phi_{i^*} = \phi_i - \phi_i^p \\ u_{j^*} = u_j \\ \phi_{j^*} = \phi_j - \phi_j^p \end{Bmatrix} \quad (3.12)$$

As shown in Equation 3.13, the shear forces and transverse deflections remain unchanged after the formation of plastic hinges, and only the moments and rotations change. Therefore, it is possible to separate the moments from above equation to apply the effects of plastic hinges as presented in Equation 3.13.

$$\begin{Bmatrix} M_{i^*} \\ M_{j^*} \end{Bmatrix} = \frac{EI}{L^2} \begin{bmatrix} 6 & 4L & -6 & 2L \\ 6 & 2L & -6 & 4L \end{bmatrix} (\mathbf{q} - \mathbf{\Phi}^p), \quad \mathbf{q} = \begin{Bmatrix} \phi_i \\ \phi_j \end{Bmatrix}, \quad \mathbf{\Phi}^p = \begin{Bmatrix} \phi_i^p \\ \phi_j^p \end{Bmatrix} = \begin{Bmatrix} \frac{M_{i^*}}{k_{s,i}} \\ \frac{M_{j^*}}{k_{s,i}} \end{Bmatrix} \quad (3.13)$$

Equation 3.13 above can be simplified as Equation 3.14.

$$\begin{Bmatrix} M_{i^*} \\ M_{j^*} \end{Bmatrix} = \frac{EI}{\Delta L^2} \begin{bmatrix} 1+4\gamma_2 & -2\gamma_2 \\ -2\gamma_1 & 1+4\gamma_1 \end{bmatrix} \begin{bmatrix} 6 & 4L & -6 & 2L \\ 6 & 2L & -6 & 4L \end{bmatrix} \mathbf{q} \quad (3.14)$$

where,

$$\Delta = (1+4\gamma_i)(1+4\gamma_j) - 4\gamma_i\gamma_j, \quad \gamma_n = \frac{EI}{k_{s,n}}, n = i, j \quad (3.15)$$

Now the vector of plastic rotations, $\mathbf{\Phi}^p$ can be generated by Equation 3.16 using matrix $\mathbf{\Gamma}$ defined in Equation 3.17.

$$\Phi^p = \begin{Bmatrix} \phi_i^p \\ \phi_j^p \end{Bmatrix} = \begin{Bmatrix} \frac{M_{i^*}}{k_{s,i}} \\ \frac{M_{j^*}}{k_{s,j}} \end{Bmatrix} = \Gamma \mathbf{q} \quad (3.16)$$

$$\Gamma = \begin{bmatrix} \frac{6}{L}(4\gamma_1\gamma_2 + \gamma_1) & 4(3\gamma_1\gamma_2 + \gamma_1) & -\frac{6}{L}(4\gamma_1\gamma_2 + \gamma_1) & 2\gamma_1 \\ \frac{6}{L}(4\gamma_1\gamma_2 + \gamma_2) & 2\gamma_2 & -\frac{6}{L}(4\gamma_1\gamma_2 + \gamma_2) & 4(3\gamma_1\gamma_2 + \gamma_2) \end{bmatrix} \quad (3.17)$$

On assembling Equations 3.12-3.17 to generate the total stiffness matrix used in the finite element formulation, the stiffness matrix of the elastic beam with plastic hinges for element i is obtained as presented in Equation 3.18.

$$\mathbf{k}_i^t = \frac{EI}{\Delta L^3} \begin{bmatrix} 12(1 + \gamma_1 + \gamma_2) & 6(1 + 2\gamma_2) & -12(1 + \gamma_1 + \gamma_2) & 6(1 + 2\gamma_1) \\ & 4(1 + 3\gamma_2) & -6(1 + 2\gamma_2) & 2L^2 \\ & & 12(1 + \gamma_1 + \gamma_2) & -6(1 + 2\gamma_1) \\ \text{symm.} & & & 4(1 + 3\gamma_1) \end{bmatrix} \quad (3.18)$$

The subroutine, first compares the moments at the ends of the elements with the maximum moment capacity of the beams, and if the moments are greater than this maximum the nonlinear hinges are activated and a very small stiffness is assigned to the rotational springs. Otherwise, the rotational stiffness of the hinge is set to a very large value EI and included in the stiffness formulation of the beam. In the methodology used in this subroutine, it is possible to find the plastic rotations at the ends of the beam using Equation 3.18.

3.4.5. Summary of the assumptions

The general assumptions and range of application of the code is summarized in the following to give a better understanding of the algorithm:

1. The roof beam is simply supported.
2. The beam cross section and section strength are uniform across the length of the beam.
3. The roof mass is uniformly distributed.
4. The beam is modelled by a series of equal length elements with end plastic hinges.
5. The plastic hinges have elasto-plastic moment-rotation relationship.
6. The user specifies the number of elements. The program applies blast loads at the mid-points of these elements. For the purpose of analysis, the model actually uses twice the number of elements specified.
7. The negative phase of blast pressures is neglected in the program.

3.4.6. Validation and verification

The response to blast load for selected cases as obtained from the designed program is compared with that obtained by using program D2DX (Prakash et al. 1993). The blast load histories used in D2DX are identical to those generated by the proposed program. In all cases a perfect match is obtained between the two sets of results.

For demonstration, a 6-m long W610X101 steel beam supporting a 3m tributary width of concrete slab is selected. The number of elements is taken as 12. The blast loads are produced by a hemispherical explosive charge of 500 kg of TNT located at a distance of 20 m from the edge of the beam (Figure 3.34). A plastic moment capacity significantly smaller than the maximum moment attained in the elastic case is assigned to the beam to obtain the response for the inelastic case.

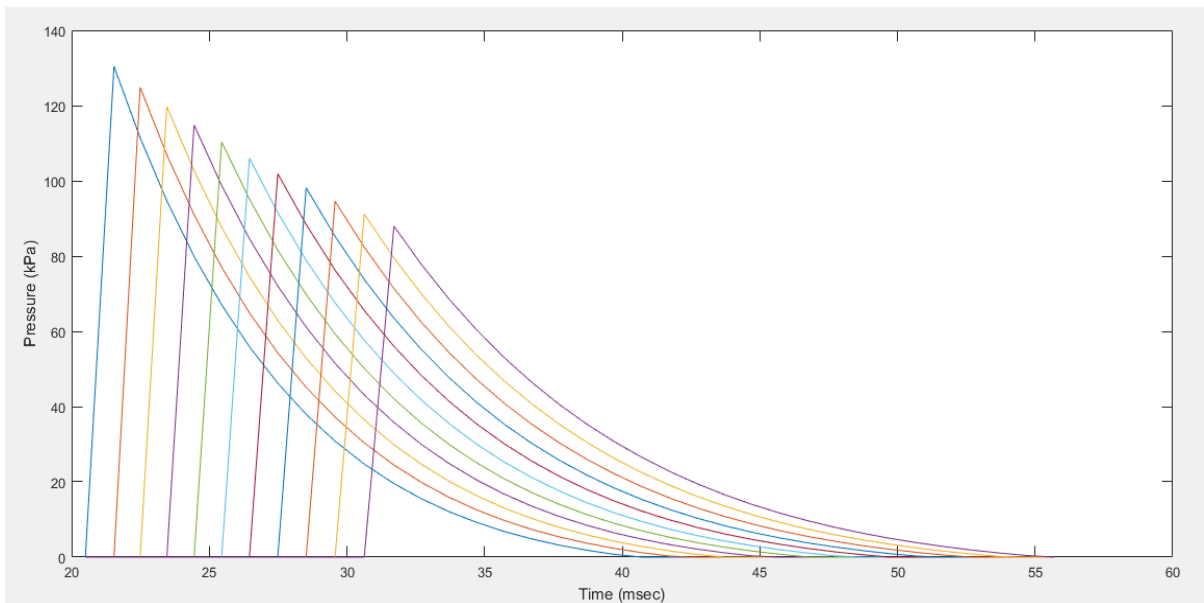


Figure 3.34. Blast pressure time histories for the internal nodes

The blast load parameters are derived from the Kingery-Bulmash polynomials for hemispherical blast. The parameter values calculated by the code for the case when the shock front is located at the front end of the beam are compared with those obtained from the program CONWEP (DoA 1986) in Table 3.16. It is observed that the two sets of values are very close to each other.

Table 3.16. Blast wave parameters for hemispherical 500 kg TNT at 20 m standoff

Parameter	Calculated by code	CONWEP
Peak incident pressure (<i>kPa</i>)	168.3	168.5
Time of arrival (<i>msec</i>)	20.60	20.59
Peak incident impulse (<i>kPa.msec</i>)	860.5	860.5
Positive phase duration time	18.44	18.44
Shock front velocity (<i>m/sec</i>)	529.7	530.1
Peak dynamic pressure (<i>kPa</i>)	80.69	80.67

The blast time-histories derived by the procedure described in Section 3.2.3 are shown in Figure 3.34.

In order to verify the results of the analysis, the same model is generated in D2DX code, using elastic beam elements with nonlinear hinges at the end (element type 2). The load time-histories generated by the designed code are applied to the model as point loads on the alternate nodes and a time history response analysis is carried out. The displacements at mid-span obtained from D2DX and the program are compared in Figure 3.35. In order to compare the results in the elastic range, the analysis has been repeated using an elastic element in D2DX and also by inputting a large value for moment capacity in the code GUI. The results are shown in Figure 3.35.

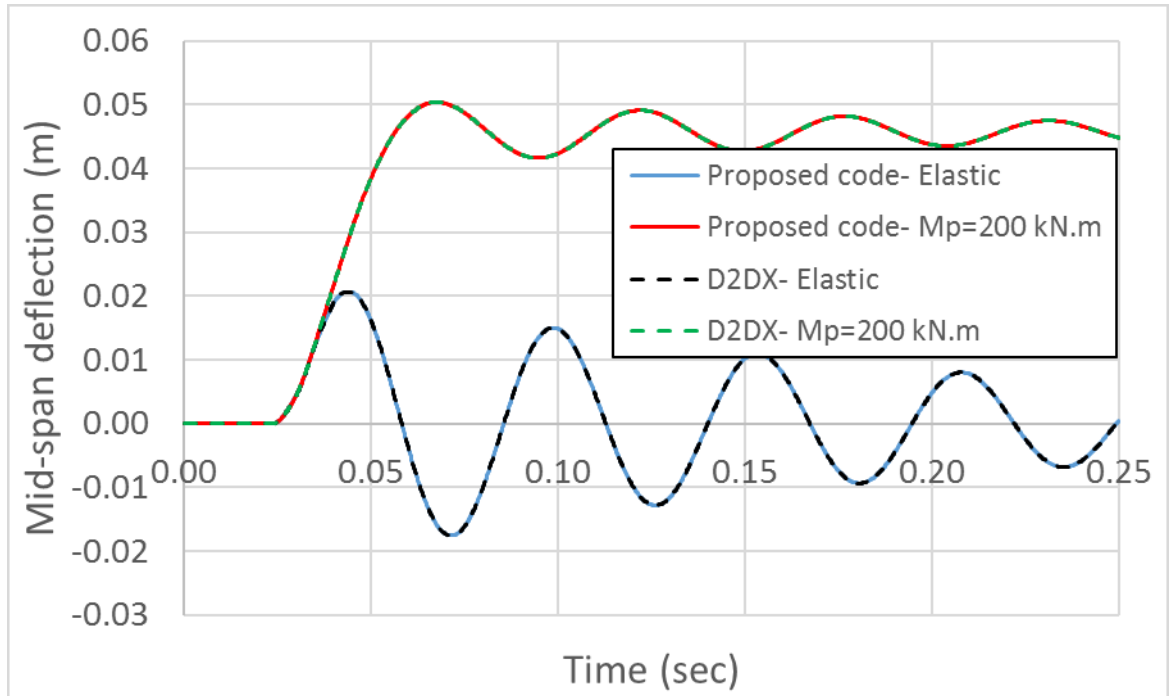


Figure 3.35. Comparison of mid-span deflections of 6-m beam obtained from computer code and D2DX

As seen from Figure 3.35 perfect match exists between the two sets of results in both the elastic and inelastic range.

3.5. Summary and Conclusion

In this chapter, the validity and accuracy of the methods traditionally used to estimate the response to blast load of side face and roof members which span in a direction perpendicular to the shock front are first examined. The methods are based on the representation of the blast load by a spatially uniform load whose magnitude varies with time. The response results are compared with those obtained from a more accurate analysis in which the blast load is derived from a travelling wave representation and the element under consideration is represented by a finite element model with multiple

degrees of freedom. It is shown that the two alternative traditional methods give responses of a roof beam that are not only vastly different from each other but are often grossly inaccurate.

In order to study the exact nature of the blast wave propagation over the span of the beams, a set of experimental tests were carried out. In these experimental tests, an aluminum beam is used as the roof beam which carries the propagating blast loads acting on a Plexiglass sheet attached to the beam. The experimental cases are modeled here numerically and by comparing the numerical and experimental results it is concluded that the step-by-step travelling load methodology can yield satisfactory results that are more precise in comparison to those obtained from the traditional methods using uniform loads.

Toward the end of the chapter a numerical code is described that requires for its input only a few parameters which can be easily input through a simple GUI developed for the purpose. Using this input, the program automatically performs all stages of the analysis beginning with the determination of the blast load parameters, generation of the blast load time histories, and the nonlinear time history dynamic analysis. In fact, the entire procedure is simpler than in the traditional simplified methods, which require the use of CONWEP as well as charts given in the manuals to generate the blast load parameters and the use of a code to carry out the SDOF nonlinear dynamic analysis for the equivalent uniform load based on such parameters.

Chapter 4. Global Response of Buildings to Blast Loading

4.1. Introduction

In the previous chapters, responses of structural members on the front face, side, and roof of a building were discussed. As outlined in Chapter 1, when a large blast interacts with a building, the blast wave can excite the lateral load resisting system of the structure and cause deformations in the structure. This type of behavior can be assessed by applying the blast loads on different sides of the structure and analyzing the dynamic behavior of the building.

Only a limited number of research studies have discussed different aspects of the global response of building structures under blast loading. Collapse mechanism of the buildings under blast was studied by Luccioni et al. (2004), where an actual terrorist attack on a reinforced concrete building was simulated using AUTODYN hydrocode. In that study, different stages of the event including detonation, shockwave propagation, interaction with the structure and collapse were reproduced. The cause of collapse was found to be the failure of gravity load bearing elements and progressive collapse of the building (Luccioni et al. 2004).

The potential for progressive collapse as well as the general structural response of two reinforced concrete buildings under blast was examined in a study by Saatcioglu et al. (2009) using both SDOF and MDOF analyses. In that study, two 10-story buildings with different structural systems, one having moment resisting frames and the other one having shear walls, each designed for two different seismicity levels, were analyzed for

their response to various blast load scenarios. These simulations were implemented by modelling individual members as two-dimensional beam-column elements in D2DX software using various simplifying assumptions. The local response of the columns of the buildings under the selected blast scenarios was also analyzed using SDOF models. Based on the results of the analyses, it was concluded that the seismic detailing and design of the structures improved their response to blast loads, however under significant blasts seismic detailing of the structures may not be sufficient.

Various parameters and assumptions govern the response of the structure. Therefore, it is necessary to study the different parameters and also the validity of the assumptions and simplifications that affect the global response of the structures to blast. In this chapter, the effects of different assumptions and parameters involved in the analysis of the dynamic response of structures to blast are studied for the case of a relatively severe blast load acting on a benchmark building studied by Saatcioglu et al. (2009). Also, the lateral deformations of the benchmark structure under blast load are compared to the lateral deformations caused by earthquake excitations.

4.2. Case Study of Global Response of a Building to Blast

This chapter deals with the simulation of the response of a 10-story reinforced concrete building, used as the benchmark in a previous study by Saatcioglu et al. (2009), to selected blast loads. The simulations in that study were based on several simplifications and general assumptions. The geometric properties of the building and element sections used here have been adopted from the previous research. However, since the material

models, detailing and other parameters are not similar, it is not expected that the response results obtained in the present study will be similar to those obtained in the previous research. In the present study, the response of the structures is determined from 2D and 3D nonlinear analyses using OpenSEES code. Also, more refined methodologies are used for the simulation of blast loads, and material and structural properties.

4.2.1. Geometric models

The geometry of the models used in the present study is based on the blast scenario and structural model shown in Figure 4.1, and on the floor plan of the building shown in Figure 4.2.

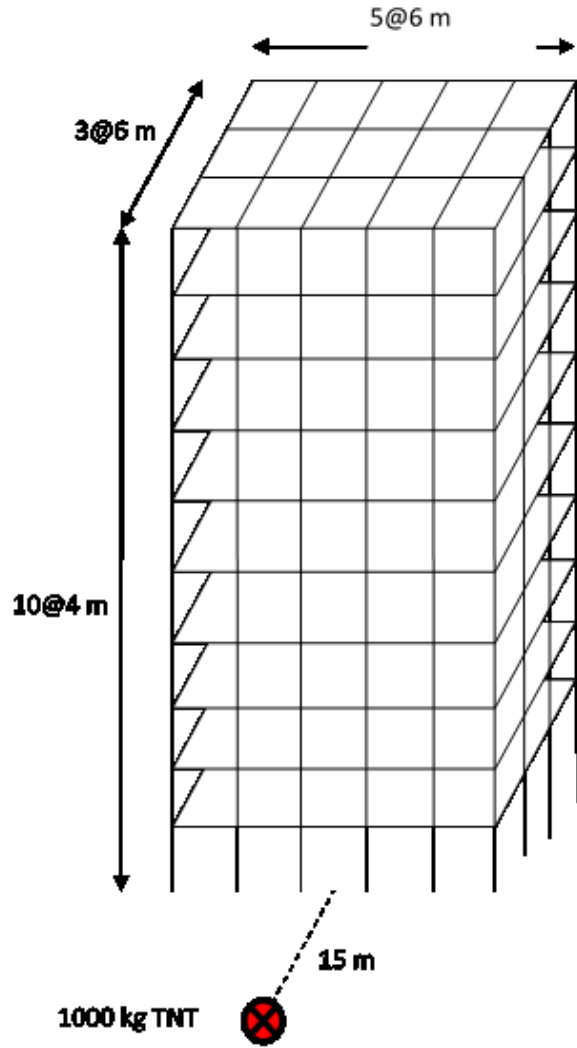


Figure 4.1. Geometrical model of the building and the blast source

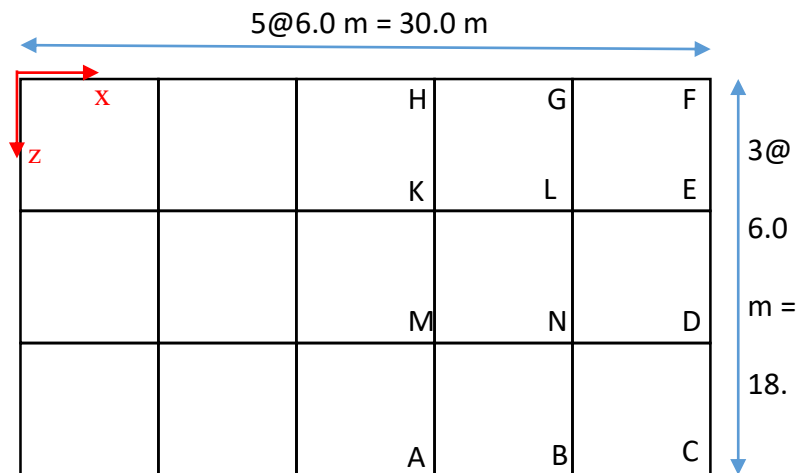


Figure 4.2. Floor plan of the building being studied

In the study by Saatcioglu et al. (2009), the building was designed for the earthquake hazard in two different cities: Vancouver and Ottawa, and for two different ductility capacities: high and moderate as defined in the National Building Code of Canada (NRCC 2010). The member sizes and capacities were considered to be the same for both hazard and ductility levels, and the only difference was in the detailing of the members. The same member sizes and reinforcements are considered in the current study. Also, only the moment frame building designed for moderate ductility is investigated.

For defining the geometry in the 3D model in OpenSEES, y axis is taken as being oriented along the height of the building, and the x and z axes are assumed to lie in the plan view of the building (Figure 4.2). All nodes at each level are constrained so as to simulate a rigid floor diaphragm. An additional node is defined at the center of mass of the floor, and is named as the master point. The nodes at the base level ($y=0$) are fully restrained along all degrees of freedom representing fully fixed supports for the columns.

For modelling the same building using a simpler 2D model, the frames oriented in the z direction (short dimension) of Figure 4.2 are selected, and interconnected through rigid links. Also, only 3 of the 6 frames are modeled because of the symmetry. The 2D model used in the analysis is shown in Figure 4.3.

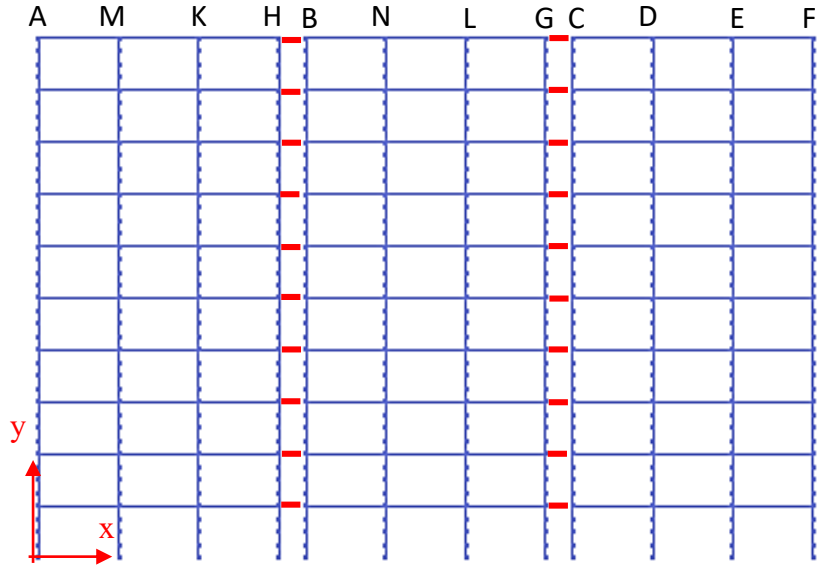


Figure 4.3. 2D model of the 10-story buildings

4.2.2. Material Models

For modeling the RC members including beams, columns and walls some verified models available in OpenSEES are used for both unconfined and confined concrete and for reinforcing steel bars as discussed in the following paragraphs.

4.2.2.1. Unconfined Concrete

For modeling unconfined concrete in the cover of the members, Hognestad's model (Hognestad, 1951) is used as described in Chapter 2. Based on the given property values for the concrete, and applying the dynamic increase factors (DoD 2008) and the material models in OpenSEES, the following parameters are derived:

$$\begin{aligned}
 f'_c = 30 \text{ MPa} & \Rightarrow E_c = E_t = 4700\sqrt{f'_c} = 25.74 \text{ GPa} \\
 f'_{cd} = DIF \cdot f'_c & \quad \& \quad DIF = 1.25 \Rightarrow f'_{cd} = 37.5 \text{ MPa} \\
 \varepsilon_0 = 2f'_{cd} / E_t & = 0.00291 \\
 \Rightarrow k = 169.2 & \quad \& \quad f'_{ca} = 0.85f'_{cd} = 31.875 \text{ MPa}
 \end{aligned}$$

4.2.2.2. Confined Concrete

For modeling the behavior of the confined concrete in the core of the members, concrete07 model in OpenSEES, based on Chang and Mander (1994), is used. The details of this material model are described in Chapter 2. The calculations for the properties of the confined concrete in the core of the members are presented in the following:

$$f'_{c0} = 30 \text{ MPa} \Rightarrow \boxed{E_c = 8200 f'_{c0}{}^{3/8} = 29.36 \text{ GPa}} \quad \& \quad f'_{cd} = DIF \cdot f'_{c0} = 37.5 \text{ MPa}$$
$$\varepsilon_{c0} = \frac{f'_{cd}{}^{1/4}}{1152.63} = 0.00215$$
$$\boxed{f_t = 0.62 \sqrt{f'_{cd}} = 3.8} \cong 0.1 f'_{cd} \quad \& \quad \boxed{\varepsilon_t = 2 f_t / E_c = 0.00026}$$

For deriving the properties of confined concrete, the detailing of the members and the transverse reinforcement should be known. The details of the reinforcement and confinement in the column members are described in detail in Chapter 2. The calculation for determining the transverse reinforcements in the beams are presented in the following paragraphs:

Beams in moderate ductility frames:

The calculations involved in determining the reinforcement for this case are carried out with reference to one of the intermediate beam sections, and will be generalized for other beams. A 300-mm wide by 450-mm deep section with 3-20M rebars at top and 2-20M bars at the bottom placed with 50-mm cover is selected. The requirement for selected level of ductility in the frames is to provide a minimum amount of transverse steel in the beam in its region close to the beam-column joint (possible plastic hinge

locations) as defined in Section 21.7.2.1 of the concrete design code CSA A23.3-04 (CSA, 2004):

$$\begin{aligned}
 &\text{Size at least: } 10\text{M} \Rightarrow A_{sv} = 100 \text{ mm}^2 \\
 &\text{Max. spacing, } s = \min \left\{ \begin{array}{l} d / 4 = 390 / 4 = 97.5 \text{ mm} \\ 8d_{b,\min} = 8 \times 20 = 160 \text{ mm} \\ 24d_{sv} = 24 \times 11.3 = 271.2 \text{ mm} \\ 300 \text{ mm} \end{array} \right\} = \text{say } 100 \text{ mm} \\
 &\text{Length of area, } d \leq L \leq 2d \quad \Rightarrow \text{say } \boxed{L = 750 \text{ mm}}
 \end{aligned}$$

The requirement for other regions of the beam length is given in Section 7.6.6 of the Code as:

$$\begin{aligned}
 &\text{Size assumed: } 10\text{M} \Rightarrow A_{sv} = 100 \text{ mm}^2 \\
 &s = \min \left\{ \begin{array}{l} d = 390 \text{ mm} \\ 16d_{b,\min} = 16 \times 20 = 320 \text{ mm} \\ 48d_{sv} = 48 \times 11.3 = 542.4 \text{ mm} \\ 300 \text{ mm} \end{array} \right\} = 300 \text{ mm}
 \end{aligned}$$

Based on the foregoing calculations, the details of the transverse reinforcement in the beams are selected as shown in Figure 4.4. After defining the transverse detailing of the beams, the properties of the confined concrete could be calculated as follows, based on the definition of effective confined core (Chang and Mander, 1994). The details of the model used here are presented in Chapter 2.

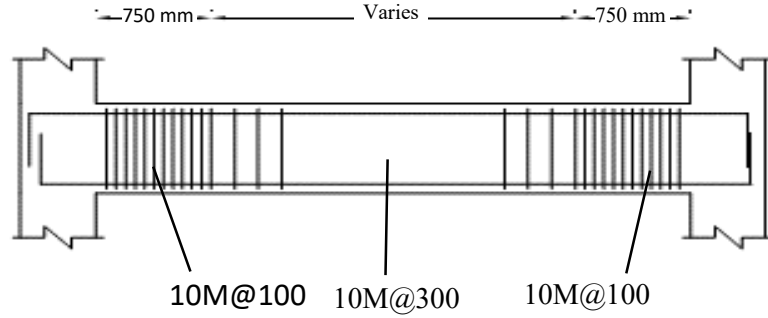


Figure 4.4. Details of transverse reinforcement in beams of moderate ductility frames

$$\begin{aligned}
 A_e &= \left(b_c d_c - \sum \frac{(w_i')^2}{6} \right) \left(1 - 0.5 \frac{s'}{b_c} \right) \left(1 - 0.5 \frac{s'}{d_c} \right) \\
 &= \left(180 \times 330 - 2 \times \frac{(70)^2}{6} \right) \left(1 - 0.5 \times \frac{80}{180} \right) \left(1 - 0.5 \times \frac{80}{330} \right) \\
 &= 35792.7 \text{ mm}^2
 \end{aligned}$$

$$A_{cc} = b_c d_c - A_{st} = 180 \times 330 - 5 \times 300 = 57900 \text{ mm}^2 \Rightarrow k_e = A_e / A_{cc} = 0.6182$$

$$\rho_x = \frac{A_{sx}}{s.d_c} = \frac{2 \times 100}{100 \times 330} = 6.06 \times 10^{-3} \quad \& \quad \rho_y = \frac{A_{sy}}{s.b_c} = \frac{2 \times 100}{100 \times 180} = 1.11 \times 10^{-2}$$

$$\text{confinement stress, } f_{lx}' = k_e \rho_x f_{yh} = 1.50 \text{ MPa} \quad \& \quad f_{ly}' = k_e \rho_y f_{yh} = 2.75 \text{ MPa}$$

$$q = f_{lx}' / f_{ly}' = 0.546 \quad \& \quad x' = \frac{f_{lx}' + f_{ly}'}{2f_{cd}'} = 0.057$$

$$A = 6.8886 - (0.6096 + 17.275q)e^{-4.989q} = 6.227 \quad \& \quad B = \frac{4.5}{\frac{5}{A}(0.9849 - 0.6306e^{-3.8939q}) - 0.1} = 7.14$$

$$k_1 = A \left(0.1 + \frac{0.9}{1 + Bx'} \right) = 4.566 \quad \Rightarrow \quad \boxed{f_{cc}' = f_{cd}'(1 + k_1 x') = 47.6 \text{ MPa}}$$

$$k_2 = 5k_1 = 22.83 \quad \Rightarrow \quad \boxed{\varepsilon_{cc} = \varepsilon_{c0}(1 + k_2 x') = 0.00505}$$

$$\boxed{x_n = 30} \quad \& \quad \boxed{x_p = 2} \quad n = \frac{E_c \varepsilon_{cc}}{f_{cc}'} = \frac{29.36 \times 10^3 \times 0.00632}{47.6} = 3.11 \quad \Rightarrow \quad \boxed{r = n / (n - 1) = 1.47}$$

The preceding calculations are for the end regions in the beams with special transverse reinforcement (100 mm spacing). The middle region of the beam with larger transverse

reinforcement spacing should be modelled by a different material model, for which the properties are calculated in the following.

$$\begin{aligned}
 A_e &= \left(b_c d_c - \sum \frac{(w'_i)^2}{6} \right) \left(1 - 0.5 \frac{s'}{b_c} \right) \left(1 - 0.5 \frac{s'}{d_c} \right) \\
 &= \left(180 \times 330 - 2 \times \frac{(70)^2}{6} \right) \left(1 - 0.5 \times \frac{280}{180} \right) \left(1 - 0.5 \times \frac{280}{330} \right) \\
 &= 6296.96 \text{ mm}^2
 \end{aligned}$$

$$A_{cc} = b_c d_c - A_{st} = 180 \times 330 - 5 \times 300 = 57900 \text{ mm}^2 \Rightarrow k_e = A_e / A_{cc} = 0.1088$$

$$\rho_x = \frac{A_{sx}}{s.d_c} = \frac{2 \times 100}{300 \times 330} = 2.02 \times 10^{-3} \quad \& \quad \rho_y = \frac{A_{sy}}{s.b_c} = \frac{2 \times 100}{300 \times 180} = 3.70 \times 10^{-3}$$

$$f'_{lx} = k_e \rho_x f_{yh} = 0.088 \text{ MPa} \quad \& \quad f'_{ly} = k_e \rho_y f_{yh} = 0.161 \text{ MPa}$$

$$q = f'_{lx} / f'_{ly} = 0.545 \quad \& \quad x' = \frac{f'_{lx} + f'_{ly}}{2f'_{cd}} = 7.63 \times 10^{-5}$$

As the confinement stress calculated above is very small, it can be concluded that the confinement effects are not so significant in the middle of the beams with relatively wider spacing of the transverse reinforcement. Therefore, the confinement effects are neglected in this region and the model is defined based on the concrete07 model for unconfined concrete model. The required model parameters are derived as follows:

$$f'_{c0} = 30 \text{ MPa} \Rightarrow E_c = 8200 f'_{c0}{}^{3/8} = 29.36 \text{ GPa} \quad \& \quad \boxed{f'_{cd} = DIF \cdot f'_{c0} = 37.5 \text{ MPa}}$$

$$\boxed{\varepsilon_{c0} = \frac{f'_{cd}{}^{1/4}}{1152.63} = 0.00215}$$

$$\boxed{f_t = 0.62 \sqrt{f'_{cd}} = 3.8} \cong 0.1 f'_{cd} \quad \& \quad \boxed{\varepsilon_t = 2 f_t / E_c = 0.00026}$$

$$\boxed{x_p = 2.0} \quad \boxed{x_n = 2.3} \quad \boxed{r = \frac{f'_{cd}}{5.2} - 1.9 = 5.31}$$

4.2.2.3. Reinforcing Steel

For the modeling of reinforcing steel, the Giuffre-Manegotto-Pinto material model without isotropic hardening is used (Filippou et al. 1983). This model is included in the OpenSEES code as steel02 model. Based on the given information on the steel rebar, the parameters used in this model are defined as follows:

$$\begin{aligned} f_y = 400 \text{ MPa} ; DIF = 1.23 &\Rightarrow \boxed{f_{yd} = 492 \text{ MPa}} \quad \boxed{E_s = 200 \text{ GPa}} \\ f_u = 500 \text{ MPa} ; DIF = 1.05 &\Rightarrow \boxed{f_{ud} = 525 \text{ MPa}} \\ \boxed{\varepsilon_y = f_{yd} / E_s = 0.00246} & \quad \boxed{\varepsilon_u = 0.035} \\ E_{sh} = \frac{f_{ud} - f_{yd}}{\varepsilon_u - \varepsilon_y} = 1014.14 \text{ MPa} &\Rightarrow \boxed{b_{sh} = \frac{E_{sh}}{E_s} = 0.0051} \end{aligned}$$

4.2.3. Structural Members Generation

After defining different material models as in the previous section, the member cross sections to be used in the analysis are constructed. The beams are divided into 3 different regions along their lengths, because of the different confinement levels. The columns are also detailed differently depending on the confinement level.

Different sections are built in the OpenSEES code using fibre elements as described in Table 4.1, and are prepared for moment-curvature analysis. The analysis provides an estimate of the yield curvature of each section ($\kappa_y = \frac{\varepsilon_y}{0.7d}$). The analysis is continued beyond yield until a ductility of $\mu=15$ is reached.

The columns in the frames are modeled similar to the beams; the axial loads on the columns are neglected. The sections are analyzed using zero length elements in

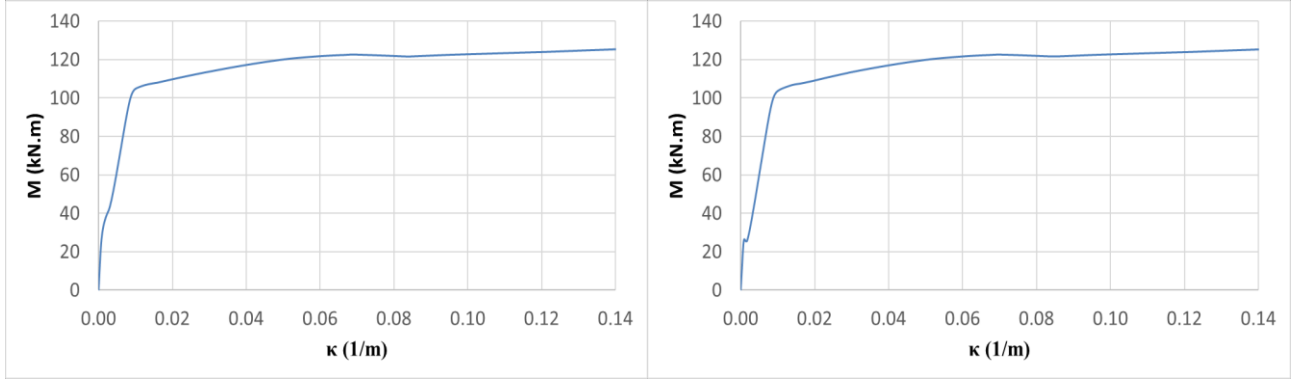
OpenSEES. Different parts of the sections are meshed, with finer meshes used in the confined core concrete.

Table 4.1. Definition of section properties for members

Member type	Section tag	Size	Long. rebar	Location	Detailing
Beam	1	300x450	3#25 top, 2#20 bot.	Interior, st. 1-9 and exterior st. 6-9	Special
	2				Regular
	3	300x400	3#20 top, 2#15 bot.	Interior and exterior st. 10	Special
	4				Regular
	5	300x500	3#25 top, 2#20 bot.	Interior st. 1-5	Special
	6				Regular
Column	7	350x350	8#20	Corner st. 6-10	Special
	8				Regular
	9	350x350	8#25	Corner st. 1-5	Special
	10				Regular
	11	400x400	8#20	Edge st. 6-10	Special
	12				Regular
	13	400x400	8#25	Edge st. 1-5	Special
	14				Regular
	15	500x500	12#20	Interior st. 6-10	Special
	16				Regular
	17	500x500	12#25	Interior st. 1-5	Special
	18				Regular

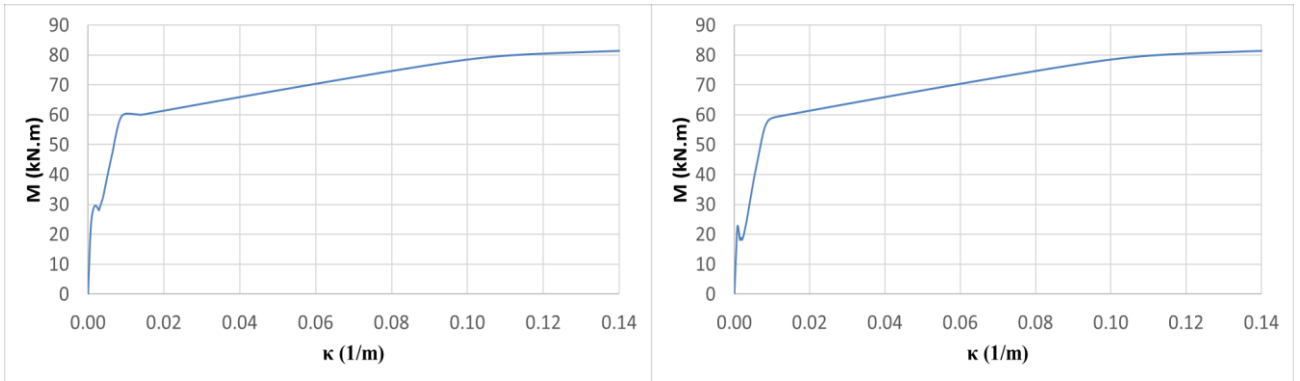
The results of the moment-curvature analyses for beams are shown in Figure 4.5. It is observed that the effect of a variation in the transverse reinforcement is not significant in the monotonic behavior of the beams; however, it is likely to make a bigger difference in cyclic and degrading behavior. The results of the analyses for column sections are presented in Figure 4.6. It may be noted that in this set of analyses, no axial load was applied to the column sections. Thus, the results are related to the pure bending capacity of the sections, also “reg.” and “sp.” designations refer to the specially

confined and regular portions of the sections, close to and far from the locations of potential plastic hinges, respectively.



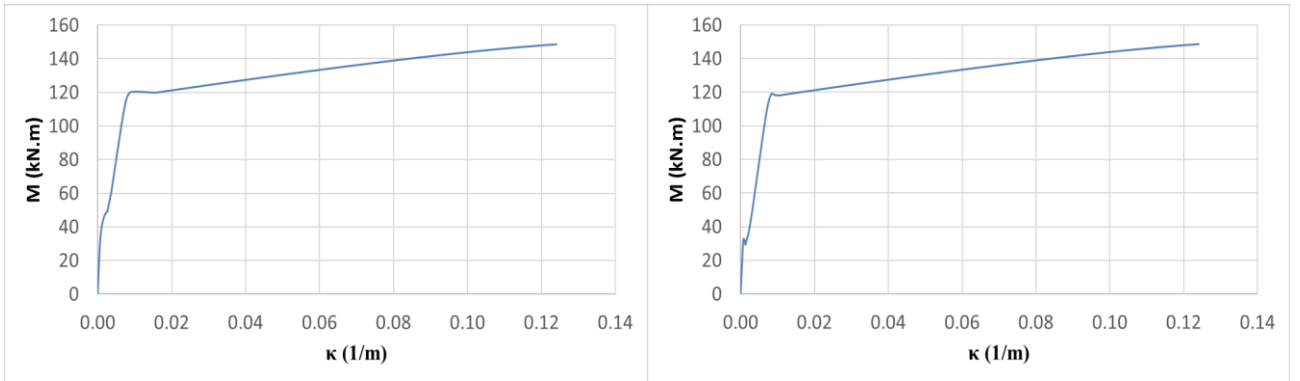
Section #1- 300x450- 3#25 top, 2#20 bot. – sp.

Section #2- 300x450- 3#25 top, 2#20 bot. – reg.



Section #3- 300x450- 3#20 top, 2#15 bot. – sp.

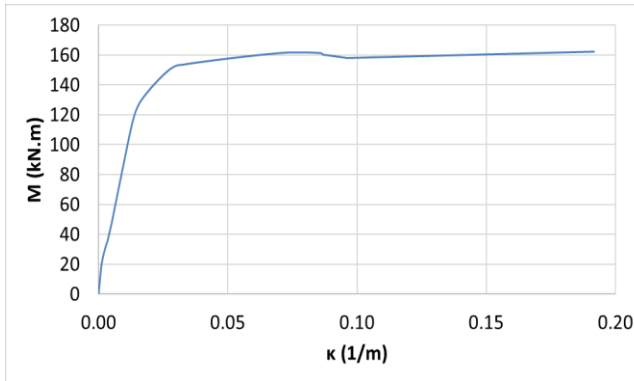
Section #4- 300x450- 3#20 top, 2#15 bot. – reg.



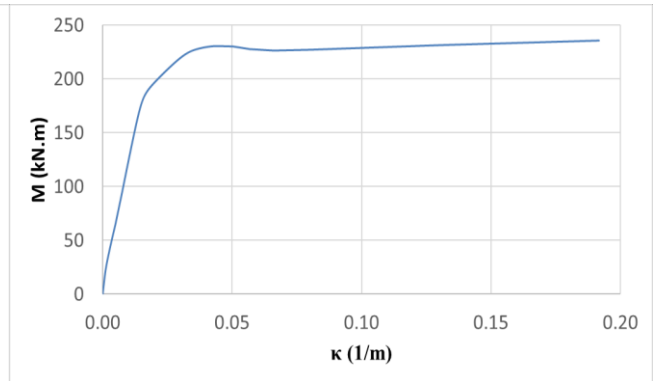
Section #5- 300x500- 3#25 top, 2#20 bot. – sp.

Section #6- 300x500- 3#25 top, 2#20 bot. – reg.

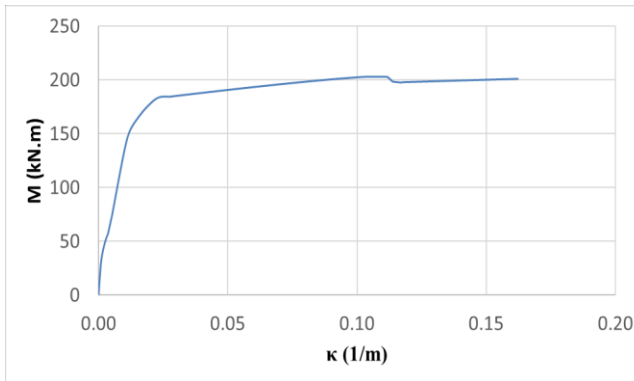
Figure 4.5. Results of the moment-curvature analysis of beam sections



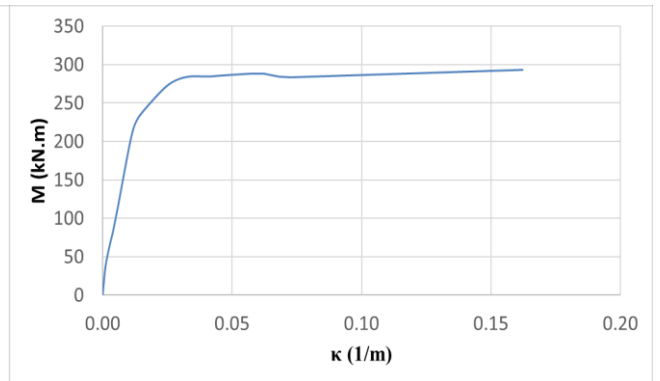
Section #7- 350x350- 8#20- sp.



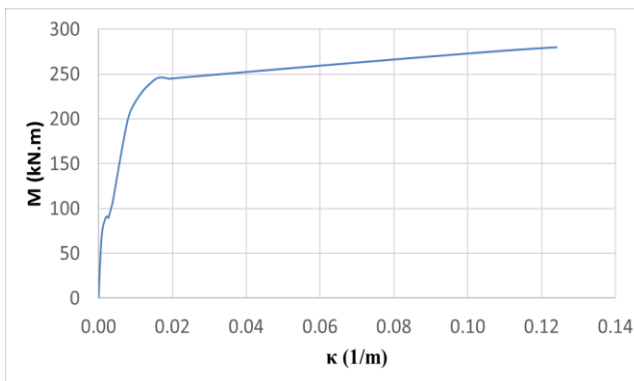
Section #9- 350x350- 8#25- sp.



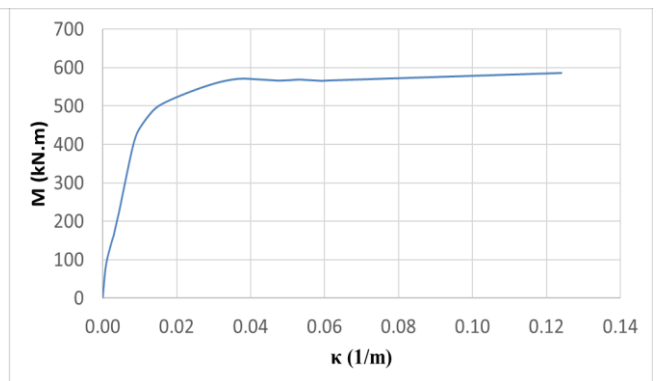
Section #11- 400x400- 8#20- sp.



Section #13- 400x400- 8#25- sp.



Section #15- 500x500- 12#20- sp.



Section #17- 500x500- 12#25- sp.

Figure 4.6. Results of the moment-curvature analysis of column sections

For comparison between the hysteretic and monotonic behavior of the members, cyclic moment-curvature analyses are carried out on several sections. The results for a sample beam and a sample column are shown in Figure 4.7. As observed from the figures, the

monotonic curves perfectly fit as the backbone curve for the hysteretic behavior. Also evident from the figure are the cyclically degrading properties of the RC section.

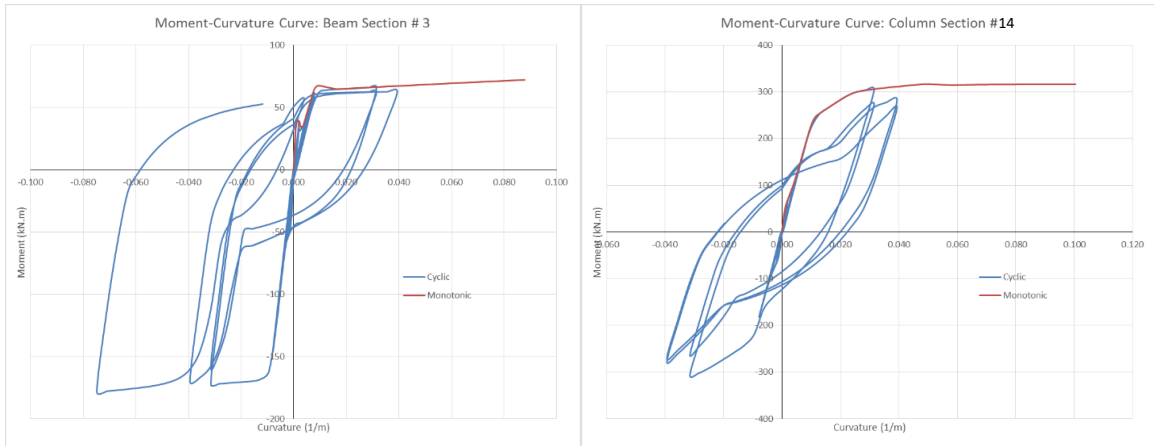


Figure 4.7. Hysteretic and monotonic moment- curvature behavior of sections

4.2.5. Blast Loading

The blast loading scenario selected for the current analysis is the hemispherical blast produced by the detonation of 1000 kg of TNT at a 15 m standoff distance from the longer face of the building, and located on its centerline as shown in Figure 4.1. It was observed during previous research study (Saatcioglu et al. 2009) that under this blast load the lower stories of the building undergo excessive drift and would be strained into the nonlinear range. The selection of the afore-mentioned blast load thus allows an examination of the nonlinear response behavior of the building.

The blast pressures are derived from CONWEP code for the front and back faces, sides, and the roof of the buildings. The front face pressures are derived considering the incidence angle of the blast wave. The pressures at beam/column joints (nodes) of the building are multiplied by the tributary areas, and the resulting forces are presented in

Tables 4.2 and 4.3. The tributary areas are calculated by assuming that the full area of the face is subjected to the blast pressure, contrary to what was assumed in the previous study (Saatcioglu, et al. 2009) where only half the area was considered, so as to account for the windows and door openings. There are two reasons for the assumption used here. First, if the building envelope is designed for blast, it has sufficient integrity and strength to withstand the loads and transmit them to the frames. The second reason is that the blast loads will be transmitted to the frames ultimately by the interior walls and barriers, even if the façade of the building is damaged and unable to transfer the load.

The parameters reported in the tables are arrival time, reflected pressure and impulse, incident pressure and impulse, tributary area, and forces on front, sides, and roof of the structure. The variation of blast pressure with time is idealized as a triangular impulse with a fictitious duration time $t_{df} = 2I/P$. For determining the shortest standoff distance from points on the side and back faces of the building, the path for the travel of the blast wave from the blast source to the point of interest on the building is defined as shown in Figure 4.8, and the minimum distance is calculated. as shown in the following.

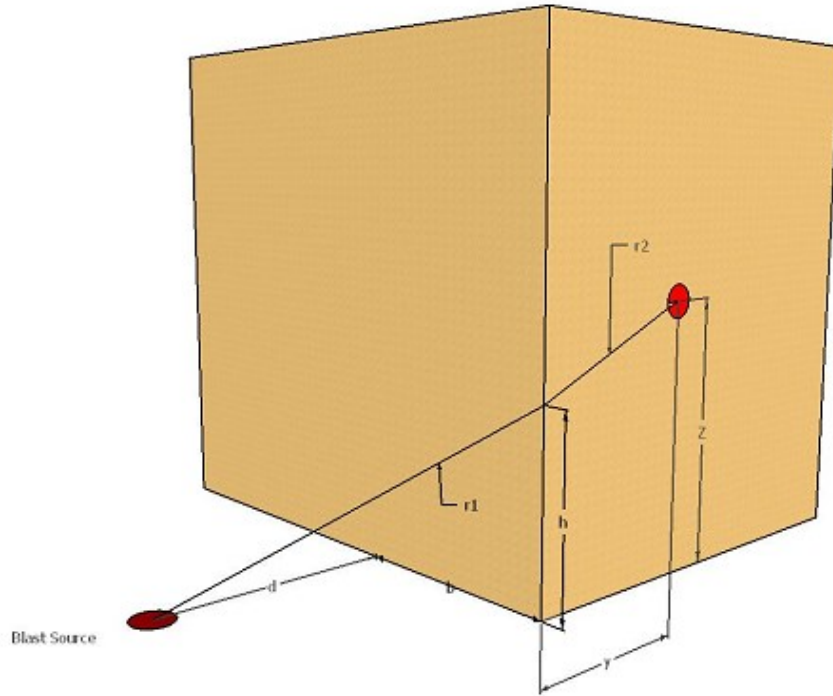


Figure 4.8. The shortest standoff distance for points on the side face

distance, $R = r_1 + r_2$

$$\Rightarrow R = \sqrt{b^2 + d^2 + h^2} + \sqrt{y^2 + (z - h)^2}$$

minimizing R: $\frac{dR}{dh} = 0 \Rightarrow \frac{h}{\sqrt{b^2 + d^2 + h^2}} + \frac{h - z}{\sqrt{y^2 + (z - h)^2}} = 0$

$$\Rightarrow h_{\min} = \frac{\pm yz\sqrt{b^2 + d^2} + (b^2 + d^2)z}{b^2 + d^2 - y^2}; \quad \text{name } D = \sqrt{b^2 + d^2}$$

$$h_{\min} = \frac{-yzD + D^2z}{D^2 - y^2}$$

$$\Rightarrow R_{\min} = \sqrt{D^2 + h_{\min}^2} + \sqrt{y^2 + (z - h_{\min})^2}$$

The same methodology is used for defining the shortest standoff to the points on the roof. The calculations and terminology are presented in the following.

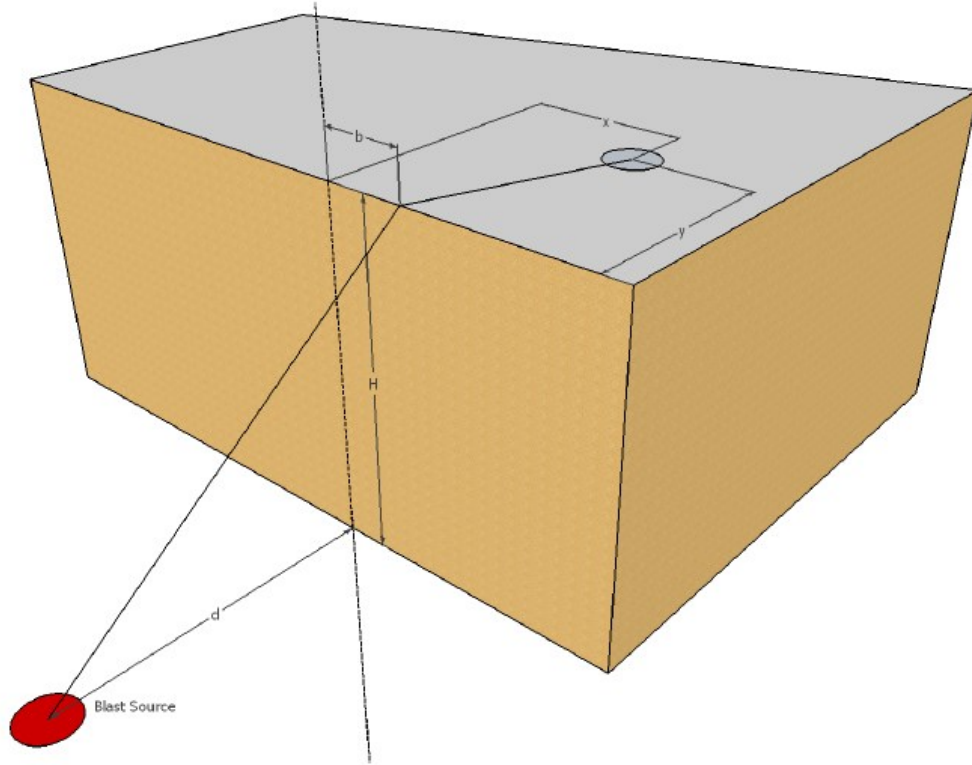


Figure 4.9. The shortest standoff distance for points on the roof

distance, $R = r_1 + r_2$

$$\vec{r}_1 = \begin{bmatrix} b \\ 0 \\ H \end{bmatrix} \quad \vec{r}_2 = \begin{bmatrix} x-b \\ y \\ 0 \end{bmatrix} \quad \Rightarrow R = \sqrt{H^2 + d^2 + b^2} + \sqrt{y^2 + (x-b)^2}$$

$$\text{minimizing } R: \frac{dR}{db} = 0 \Rightarrow \frac{b}{\sqrt{H^2 + d^2 + b^2}} + \frac{b-x}{\sqrt{y^2 + (x-b)^2}} = 0$$

$$\text{name } D = \sqrt{H^2 + d^2} \Rightarrow \boxed{b_{\min} = \frac{-yxD + D^2x}{D^2 - y^2}}$$

$$\Rightarrow R_{\min} = \sqrt{D^2 + b_{\min}^2} + \sqrt{y^2 + (x - b_{\min})^2}$$

The shortest distances for the blast wave to reach points on the side and back faces are also calculated using the relationships derived in the foregoing paragraphs.

Table 4.2. Peak blast loads on joints in front, side and back faces of the buildings

Point	Story	shortest distance (m)	h_{min} (m)	incident angle (deg.)	t_a (msec)	P_r (kPa)	I_r (kPa.msec)	P_{so} (kPa)	I_{so} (kPa.msec)	F_z (kN)	F_x (kN)
A				18.4	10.9	2049.3	4635.9	-	-	49183.2	-
B				33.3	13.8	1298.5	3560.3	-	-	31164	-
C				46.0	19.5	635.6	2512	20	1470.7	7627.2	240
D	1	27.5	3.1	-	30.6	-	-	14.8	1135.3	-	355.2
E	1	33.5	2.6	-	43.1	-	-	12.6	934.6	-	302.4
F	1	39.4	2.2	-	56.9	-	-	10.9	799.1	130.8	130.8
G	1	45.4		-	71.4	-	-	9.2	699.9	220.8	-
H	1	51.4		-	86.5	-	-	7.8	622.9	187.2	-
A				29.7	12.9	1478.7	3839.1	-	-	35488.8	-
B				38.8	15.7	1060.8	3112.6	-	-	25459.2	-
C				48.6	21.4	495.9	2303.3	18.6	1392.7	5950.8	223.2
D	2	28.4	6.2	-	32.8	-	-	14.3	1091	-	343.2
E	2	34.2	5.1	-	45.6	-	-	12.3	905.9	-	295.2
F	2	40.0	4.3	-	59.5	-	-	10.6	778.8	127.2	127.2
G	2	46.0		-	74.2	-	-	8.9	684.4	213.6	-
H	2	52.0		-	89.3	-	-	7.6	610.5	182.4	-
A				39.5	16	1029.4	3052.7	-	-	24705.6	-
B				45.0	18.9	701.5	2594.2	-	-	16836	-
C				52.0	24.5	382.5	2042.1	16.9	1289.3	4590	202.8
D	3	29.7	9.4	-	36.3	-	-	13.6	1030.2	-	326.4
E	3	35.3	7.7	-	49.4	-	-	11.8	865.4	-	283.2
F	3	41.0	6.5	-	63.6	-	-	10.1	749.4	121.2	121.2
G	3	47.0		-	78.4	-	-	8.5	661.8	204	-

Point	Story	shortest distance (m)	h _{min} (m)	incident angle (deg.)	t _a (msec)	P _r (kPa)	I _r (kPa.msec)	P _{so} (kPa)	I _{so} (kPa.msec)	F _z (kN)	F _x (kN)
H		53.0		-	93.7	-	-	7.3	592.3	175.2	-
A				47.3	20.4	562.4	2410	-	-	13497.6	-
B				50.7	22	420.9	2141.6	-	-	10101.6	-
C				55.6	28.6	294.7	1780.9	15.4	1178.5	3536.4	184.8
D	4	31.6	12.5	-	41	-	-	12.9	962.1	-	309.6
E		36.9	10.2	-	54.5	-	-	11.2	818.6	-	268.8
F		42.4	8.7	-	63.6	-	-	10.1	749.4	121.2	121.2
G		48.4		-	84	-	-	8	634.6	192	-
H		54.4		-	99.4	-	-	7.1	570.2	170.4	-
A				53.4	26	345.3	1938.6	-	-	8287.2	-
B				55.6	28.6	294.7	1780.9	-	-	7072.8	-
C				59.0	33.8	231.3	1549.2	14.1	1072.3	2775.6	169.2
D	5	33.8	15.6	-	46.7	-	-	12.1	893.5	-	290.4
E		38.8	12.8	-	60.7	-	-	10.4	769.9	-	249.6
F		44.0	10.8	-	75.4	-	-	8.8	677.6	105.6	105.6
G		50.0		-	90.6	-	-	7.5	605.1	180	-
H		56.0		-	106.2	-	-	0	0	0	-
A				58.2	32.4	245.8	1604.3	-	-	5899.2	-
B				59.7	34.8	220.7	1509.1	-	-	5296.8	-
C				62.1	39.7	182	1358.3	13.1	979.6	2184	157.2
D	6	36.3	18.7	-	53.1	-	-	11.3	830.8	-	271.2
E		41.0	15.3	-	63.6	-	-	10.1	749.4	-	242.4
F		46.0	13.0	-	72.4	-	-	9.1	694.2	109.2	109.2
G		52.0		-	87.5	-	-	7.7	618.4	184.8	-
H		58.0		-	103.1	-	-	7	557	168	-

Point	Story	shortest distance (m)	h _{min} (m)	incident angle (deg.)	t _a (msec)	P _r (kPa)	I _r (kPa.msec)	P _{so} (kPa)	I _{so} (kPa.msec)	F _z (kN)	F _x (kN)
A				62.0	39.5	183.5	1364.2	-	-	4404	-
B				63.0	41.8	168.3	1302.6	-	-	4039.2	-
C				64.7	46.5	144.4	1200.2	12.2	896	1732.8	146.4
D	7	39.0	21.8	-	60.7	-	-	10.4	769.9	-	249.6
E		43.4	17.9	-	66	-	-	9.8	733.2	-	235.2
F		48.2	15.1	-	84	-	-	8	634.6	96	96
G		54.2		-	99.4	-	-	7.1	570.2	170.4	-
H		60.2		-	0	-	-	0	0	0	-
A				65.0	47.4	140.4	1182.5	-	-	3369.6	-
B				65.7	49.7	131.3	1141.1	-	-	3151.2	-
C				67.0	54.1	116.4	1069.1	11.2	822.7	1396.8	134.4
D	8	42.0	24.9	-	63.6	-	-	10.1	749.4	-	242.4
E		46.1	20.4	-	72.4	-	-	9.1	694.2	-	218.4
F		50.6	17.3	-	90.6	-	-	7.5	605.1	90	90
G		56.6		-	100	-	-	7.1	576.1	170.4	-
H		62.6		-		-	-	0	0	0	-
A				67.5	55.7	112.2	1044.1	-	-	2692.8	-
B				68.0	57.8	108.3	1015.3	-	-	2599.2	-
C				69.0	62.1	100.5	961.6	10.3	759.5	1206	123.6
D	9	45.1	28.1	-	70.2	-	-	9.4	707.2	-	225.6
E		49.0	23.0	-	84	-	-	8	634.6	-	192
F		53.2	19.5	-	99.4	-	-	7.1	570.2	85.2	85.2
G		59.2		-	103.1	-	-	7	557	168	-
H		65.2		-		-	-	0		0	-
A	10			69.5	64.6	96.4	934.4	-	-	1156.8	-

Point	Story	shortest distance (m)	h_{min} (m)	incident angle (deg.)	t_a (msec)	P_r (kPa)	I_r (kPa.msec)	P_{so} (kPa)	I_{so} (kPa.msec)	F_z (kN)	F_x (kN)
B				69.9	66.7	93	911.6	-	-	1116	-
C				70.7	70.7	86.8	872.3	9.3	704.3	520.8	55.8
D		48.4	31.2	-	84	-	-	8	634.6	-	96
E		52.0	25.5	-	87.5	-	-	7.7	618.4	-	92.4
F		56.0	21.6	-	97.9	-	-	7.1	576.1	42.6	42.6
G		62.0		-				0		0	-
H		68.0		-				0		0	-

Table 4.3. Peak blast loads on joints in the roof

Point	X (m)	Y (m)	shortest distance (m)	b_{min} (m)	t_a (msec)	P_{so} (kPa)	I_{so} (kPa.msec)	Area (m ²)	F_y (kN)
A	3	0	42.8	-	64.6	10	742.8	18	180
B	9	0	43.7	-	66.7	9.7	728.5	18	174.6
C	15	0	45.3	-	70.7	9.3	704.3	9	83.7
D	15	6	51.0	13.2	85.8	7.8	626.4	18	140.4
E	15	12	56.7	11.7	99.7	7.1	569.3	18	127.8
F	15	18	62.5	10.6	-	0	-	9	0
G	9	18	61.4	6.3	-	0	-	18	0
H	3	18	60.8	2.1	-	0	-	18	0
M	3	6	48.8	2.6	79.4	8.4	656.7	36	302.4
N	9	6	49.5	7.9	81.2	8.2	647.9	36	295.2
K	3	12	54.8	2.3	94.7	7.3	588.2	36	262.8
L	9	12	55.5	7.0	96.6	7.2	581.1	36	259.2

4.2.6. General Model Preparations and Modifications

After defining the geometry and sections, the basic analytical model is modified and the complementary options and properties of the structure defined, as discussed in this section.

In the 3D model of the structure, torsional stiffness of the sections needs to be defined. However, since the torsional stiffness of reinforced concrete members after initial cracking is negligible, a very small number is assigned as the torsional stiffness of all members.

It was found that analysis using force-based beam elements to represent the beams and columns could not proceed far into the nonlinear range because of the very large loads, and high ductility demands, especially in columns. Displacement-based elements are therefore used in the analysis to obtain the full extent of response. For obtaining higher accuracy with the force-based elements, 5 integration points are assigned to all fibre sections in order to accommodate nonlinear curvature distribution in the length. The displacement-based elements are meshed and divided into 4 sub-elements over the length.

The weight of the structure is assigned as a uniformly distributed dead load that acts on the beams. Such dead load includes the self-weight of the beam and a portion of the weight of the concrete slab whose thickness is assumed as 150 mm. In these calculations, the mass density of the concrete is considered to be 2400 kg/m^3 .

To account for large deformations in the structure, the P-Delta effect on the columns is considered in the analysis. This is accomplished in the OpenSEES code by defining P-Delta geometric transformation for the columns, even though a linear coordinate transformation is assigned to the beams. The gravity load is applied to the structure in a static linear pattern, and the analysis time is reset for the rest of the study.

Before carrying out a static pushover and dynamic blast load analysis of the structure, an Eigen-value analysis is carried out to obtain the periods of the structure, and to look for any singularity in the model. The period of vibration the structure in the direction of application of blast loads are found to be the same in both force-based and displacement-based element models, being 2.016 and 2.012 in 3D and 2D models, respectively.

4.2.7. Static Pushover Analysis

The monotonic behavior of the 3D model is analyzed using static pushover analysis. For this purpose, the pattern of loads in the pushover analysis is assumed to be proportional to the distribution of the weight of the floors, which in this case implies a regular triangular distribution. The loads are applied at the master nodes of the diaphragms on each floor and gradually increased until the final displacement of the monitored node at the top floor reaches 15% of the building height.

The pushover analysis, which uses a displacement-controlled, force-incremented procedure is carried out in step increment of 1 mm, and different outputs are collected and processed statistically for the purpose of study. The pushover curves obtained from

the analysis are shown in Figure 4.10. The analysis using force-based beam column elements had to be stopped before reaching the desired top displacement because of high nonlinearities in the members; however, the portion of the curve shown in the figure is adequate for giving a general idea of the nature of response of the structure. For obtaining the complete pushover curve until total collapse of the structure, it was found necessary to use displacement-based elements. The results are shown for different modeling methodologies in Figure 4.10.

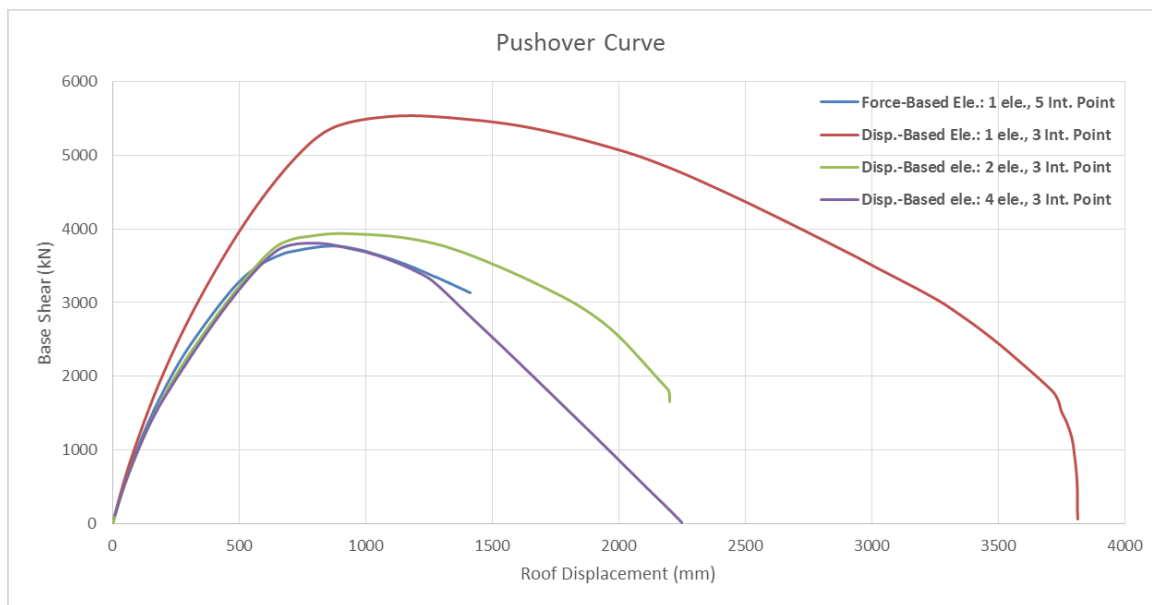


Figure 4.10. Pushover curve for moderate ductility moment resisting frame using different elements

As seen from the figure, the results obtained from forced-based element model are similar to those obtained with finely meshed displacement-based element model. The plots show that the maximum base shear, which is equal to approximately 3800 kN, occurs at a roof displacement of almost 900 mm, corresponding to 2.25% total drift. The final monitored displacement obtained from the forced-based model is 1.41 m, despite

a very long computational time having been used. This is just 3.5% the total height of the building, which may not be sufficient for an analysis for high impact loads. For this reason, finely meshed displacement-based elements are selected to be used in the simulations.

4.2.8. Dynamic Analysis and Results

Dynamic analyses are carried out for several different patterns of blast loads. The patterns include: progressive step-by-step distribution on the building, loads applied at all stories simultaneously without considering the time lag between the arrival of blast wave at different points on the building, and loading of the whole building at the same time to represent a planar shock front. In addition, two different assumptions are made for the loading area of the structure's surface: as 100% or 50%. These sets of analyses are carried out to assess the difference between the results obtained from various loading models.

For exact loading of the structure, different load time-histories are applied at each beam-column joint. This makes the input files very large, exceeding the limits of the OpenSEES code. Therefore, for running the full analysis, it was necessary to break up the code into parts for parallel processing using OpenSEES MP and SP parallel engines. One way to reduce the size of the problem and to make it more efficient is to use a 2D model, when justified. The accuracy with which such a model will provide an estimate of the response is examined and the observations are presented in the following paragraphs.

In each case, the dynamic analysis, is performed by means of step-by-step integration using Newmark's average acceleration algorithm. Mass, stiffness, and proportional Rayleigh damping are considered in the analysis. A damping coefficient of 5% is selected for modes 1 and 4. The nonlinear iterative procedure is implemented using modified Newton-Raphson methodology. The analysis time step is varied from 0.1 msec to 0.001 msec depending on the number of iterations required to achieve convergence, leading to a very high computation effort even with the simplified loads.

4.2.8.1. 2D and 3D Modelling Techniques

Dynamic blast analyses are carried out on both 3D and 2D models. In the 3D model, the response of ductile moment frame building to progressive step-by-step loads on front, back, and side surface is assessed, while the 2D model is analyzed for the front and roof loads. For each of the analysis types, models using displacement-based elements were constructed.

For the 2D model, rigid link elements are used for constraining the displacements of the frames. Since only the translational displacement constraints are needed, bar (truss) type elements are used at each floor level in the space between adjacent frames (red lines in Figure 4.3). Different variations of the blast loads are applied to each node separately with the predefined time-history. The command line for modeling these type of links is shown below. The other structural setups and features are the same as those discussed in the previous sections.

```
rigidLink bar $nodeI $nodeJ
```

The results obtained from the two sets of analyses, 2D and 3D, are very close. The deformation time-history of the monitored node at the top of the building is shown in Figure 4.11. The drift ratios for the floors are compared in Figure 4.12.

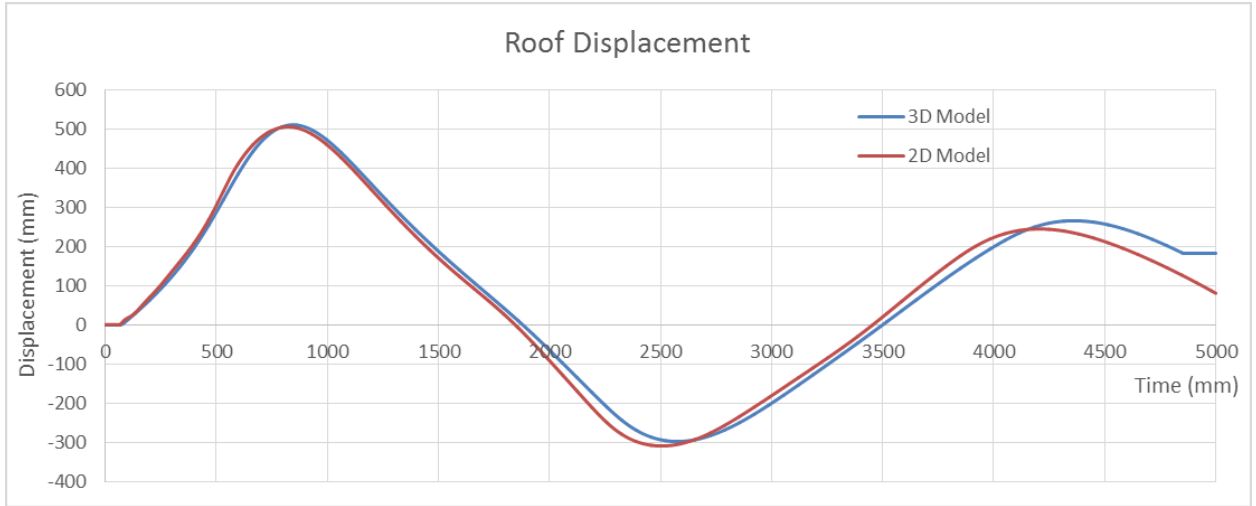


Figure 4.11. Top floor displacement in 2D and 3D model

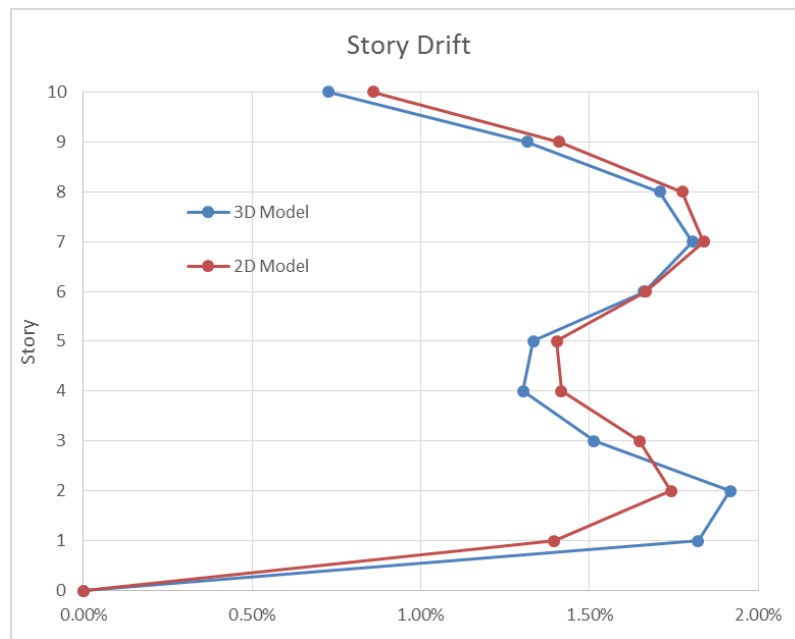


Figure 4.12. Maximum story drift ratios in 2D and 3D model

As is obvious from the results shown in Figures 4.11 and 4.12, the 2D model is capable of providing a good estimate of the response in this case study, while being considerably

more efficient. Consequently, the 2D model is used in all further studies, the results of which are presented here. However, it should be noted that in other examples with more complex asymmetrical geometries, where torsion can affect the response of the structure in blast, the difference between 2D and 3D model can be higher.

4.2.8.2. Blast Load Patterns

As discussed earlier, the blast load can be applied to the structure in different patterns.

The blast pressures are derived from CONWEP code for the front and back faces, sides and the roof of the buildings. Three different blast load patterns are used in this study as follows:

1- Progressive loading: This type of loading is used in both a 2D and a 3D analysis described in the previous section and is based on Tables 4.2 and 4.3, the blast load being applied at each beam-column joint on all faces of the building. The load time-history is determined based on the tributary area supported by the joint, the actual range between the centre of explosive charge and the joint under consideration, and where applicable, the angle of incidence between the wave front and the supported tributary area. The loading on a joint begins at the time the blast wave arrives at the joint. This loading is similar to the actual non-planar blast loading experienced by the structure.

2- Simplified progressive loading- with incident angle: This loading is used in the 2D analysis. The loads are applied only on the front face of the building. At each story level the beam-column joint closest to the charge is selected. The blast load parameters including range, angle of incidence, and arrival time are determined with respect to the

selected joint. The blast pressure corresponding to these parameters is determined and is assumed to be the same for all joints at the story level under consideration. The blast pressure is converted into load at the joint based on the tributary area supported by the joint. The blast pressure time-history properties in this pattern are summarized in Table 4.4.

Table 4.4. Simplified progressive blast pressures, with incident angles

Story	Range (m)	Time of arrival, t_a (msec)	Incidence angle (deg.)	Peak reflected pressure, P_r (kPa)	Reflected impulse, I_r (kPa.msec)	Fictitious duration, t_d (msec)
1	15.52	10.55	14.93	2200	4825.7	4.39
2	17.00	12.51	28.07	1573.2	3974	5.05
3	19.21	15.73	38.66	1059.2	3115.3	5.88
4	21.93	20.12	46.85	585.8	2443.9	8.34
5	25.00	25.58	53.13	353.1	1961.7	11.11
6	28.30	31.97	57.99	250	1620.2	12.96
7	31.76	39.16	61.82	185.8	1373.4	14.78
8	35.34	47.04	64.89	141.9	1189.4	16.76
9	39.00	55.47	67.38	112.8	1048.3	18.59
10	42.72	64.36	69.44	96.8	936.8	19.36

3- Simplified progressive loading- without incident angle: This loading is used in the 2D analysis as well and the loads are applied only on the front face of the building. The pressure time-histories are generated based on the shortest range of each story to the centre of explosive charge without considering the incident angle. The blast pressure is assumed to be the same for all joints at the story level under consideration, and is converted into load at the joint based on its tributary area. The blast pressure time-history properties in this pattern are summarized in Table 4.5.

Table 4.5. Simplified progressive blast pressures, without incident angles

Story	Range (m)	Time of arrival, t_a (msec)	Peak reflected pressure, P_r (kPa)	Reflected impulse, I_r (kPa.msec)	Fictitious duration, t_d (msec)
1	15.52	10.55	2281	4987	4.37
2	17.00	12.51	1730	4448	5.14
3	19.21	15.73	1193	3823	6.41
4	21.93	20.12	802.1	3253	8.11
5	25.00	25.58	547.5	2780	10.16
6	28.30	31.97	387.1	2401	12.41
7	31.76	39.16	284.7	2099	14.75
8	35.34	47.04	217.5	1856	17.07
9	39.00	55.47	171.9	1659	19.30
10	42.72	64.36	140	1497	21.39

4- Planar shock front loading: This loading is also used in a 2D analysis. Again, the loads are applied only on the front face. The stand-off distance is taken as the shortest distance between the charge and the front face of the building. The angle of incidence is taken as being zero. The blast pressure-time history determined from these parameters is then assumed to act over the entire front face, and the blast loads on individual joints are calculated using the corresponding tributary areas. The blast pressure time-history properties in this pattern are summarized in Table 4.6.

Table 4.6. Planar shock front loading pressures

Story	Range (m)	Time of arrival, t_a (msec)	Peak reflected pressure, P_r (kPa)	Reflected impulse, I_r (kPa.msec)	Fictitious duration, t_d (msec)
1-10	15	9.896	2529	5207	4.12

These patterns of loading are the most commonly used, and each is justifiable in some situations. The load patterns are applied separately to the structural model of the moderate-ductility frame and the results are compared in Figure 4.13 and 4.14. In applying the loads in these models, it has been assumed that the loaded area of the structure is the full facade area and all the loads are transmitted to the frames.

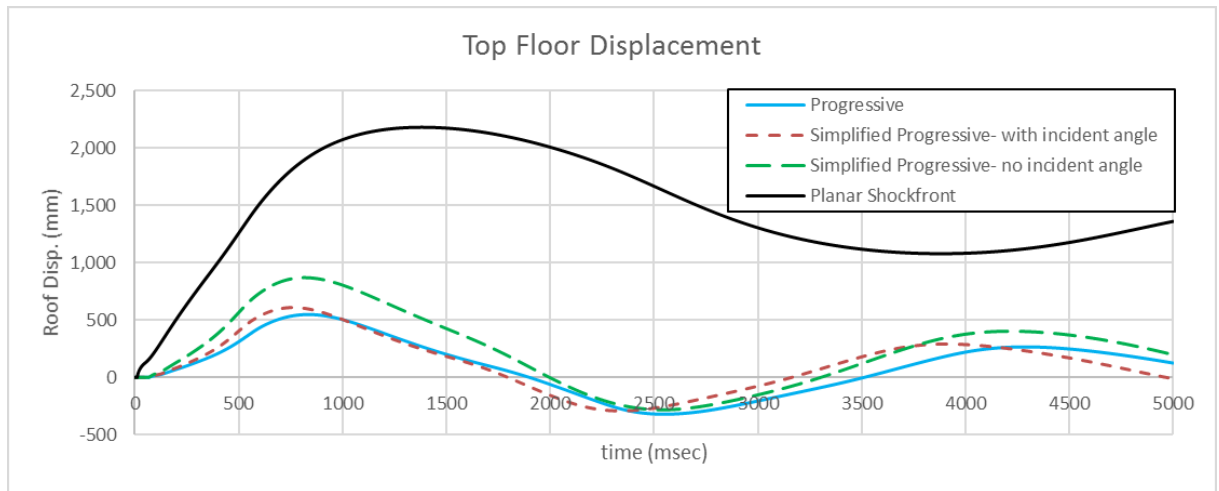


Figure 4.13. Top floor displacement for different types of loading patterns

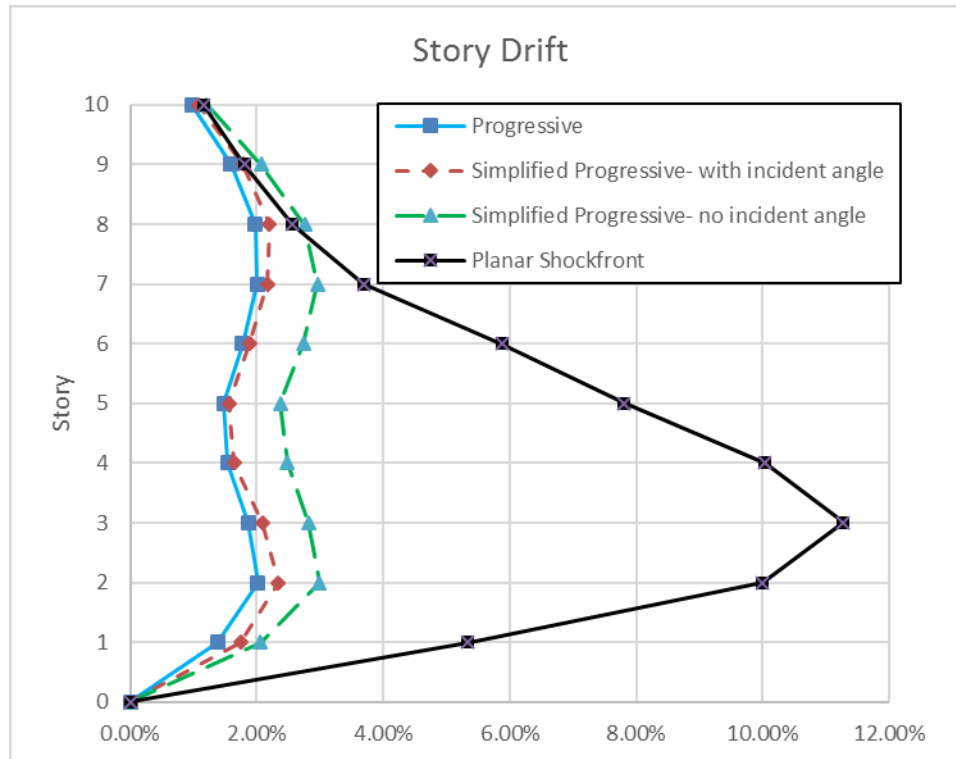


Figure 4.14. Maximum story drift ratios for different types of loading patterns

As can be seen in Figures 4.13 and 4.14, the response of the models to progressive and simplified progressive loading based on the smallest incident angles are quite similar.

The planar shockfront assumption results a much higher demand on the structure and is overly conservative. The use of the simplified progressive loads in the analysis is thus justified and would lead to considerable saving in the analysis time and in the effort since it will not be necessary to calculate the exact distance and incident angle for each node in a story. Also, for the selected symmetrical mid-rise building and the selected blast scenarios, the loads on the sides, roof and back of the structure are relatively small and may be neglected in determining the global response of the building. The blast loading on the back face acts at a later time during the response of the building and has

a much smaller magnitude (up to 1/100) in comparison with the reflected pressure on the front face

4.2.8.3. Cladding and Transmitted Load Effects

Another important factor in the response of the structures is the integrity of the cladding and its ability to transmit the blast pressures on the surface of the building to the frames. If the building has been designed for blast, it is more likely that the exterior surfaces remain intact when the blast pressure acts on them. However, if the design basis blast load is exceeded, some of windows and other façade elements could fail and only a portion of the surface is exposed to blast pressure and the load on the frames is reduced.

To assess the sensitivity of the response of the structure to the reduction in the exposed area, two models, one in which the full surface area is exposed to the blast and the other in which only half of the area is exposed, are analyzed (under progressive loading scenario) to determine their response. The results are compared in Figure 4.15 and 4.16.

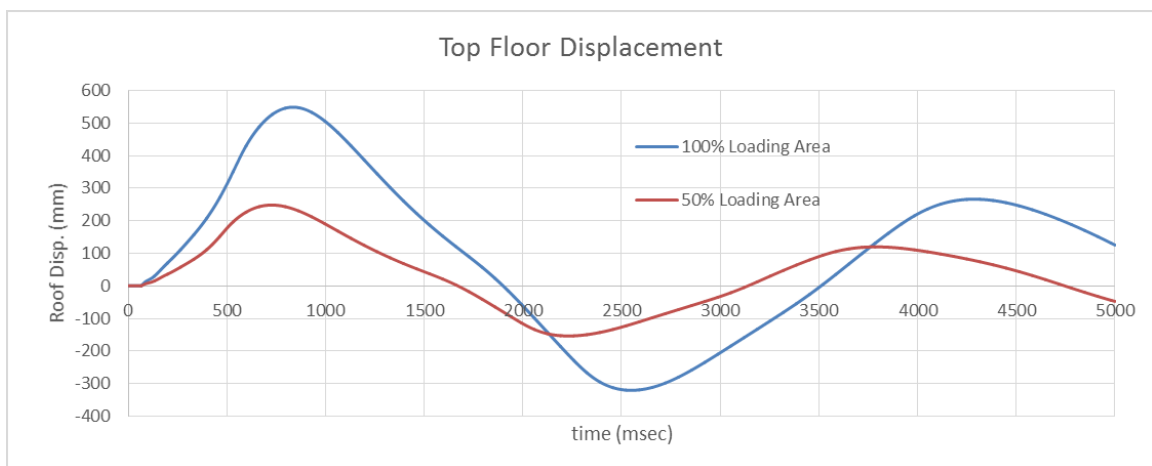


Figure 4.15. Top floor displacement for different types of loading area

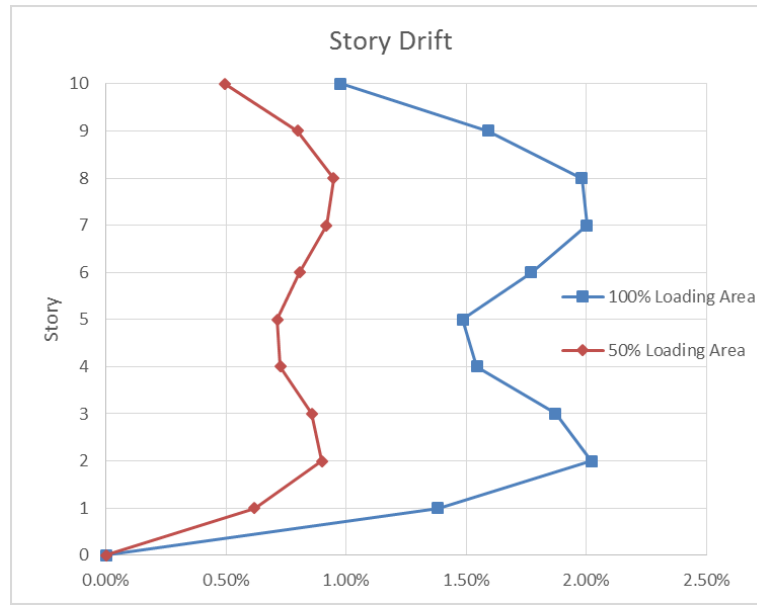


Figure 4.16. Maximum story drift ratios for different types of loading area

As seen from Figure 4.15, the top deflection in the model with 50% loaded area is slightly less than 50% of the model in which full area is considered. This implies that the integrity of the cladding and the exterior surfaces of the building play an important role in the response of the structure to blast loads. It is, therefore, important that a reasonable assumption be made for the tributary areas that contribute to the loads on columns and stories.

4.2.8.4. Comparison of the response of an isolated column to that of the same column as a part of the global model

As described in Chapters 1 and 2, the vulnerability of building structures to blast loading is traditionally assessed on the basis of the analyses of individual elements. In such analyses, it is usually assumed, especially for the columns, that the ends of the element do not displace in the lateral direction during loading. Thus, the member being analysed is considered as fixed-fixed or pinned-pinned. However, as observed from the analysis of

the global behavior of the building, lateral story drifts occur as a result of blast loading, which means that the ends of the columns do, in fact, displace in the lateral direction. This is contrary to the assumption made in modelling an individual column such that the ends are laterally restrained. An investigation is therefore carried out to determine how much the ends of the columns displace and how such displacement affects the response of the columns.

The first story exterior columns are selected for the analysis of their response to the blast loads produced by the explosion of a 1000 kg charge located at 15 m, a charge that is identical to that used in the global response analysis. The blast pressure properties at the mid-height of columns are calculated based on the range and incident angles for the individual columns and are presented in Table 4.7.

Table 4.7. Blast load properties applied on first story column

Column	A1	B1	C1
Standoff (m)	15.4	17.6	21.6
Incident angle ($^{\circ}$)	13.5	31.6	45.3
Time of arrival (msec)	10.4	13.4	19.1
Reflected pressure (kPa)	2266.2	1388.7	682.1
Fictitious duration time (msec)	4.3	5.3	7.5

The columns that are individually analysed under the blast loads presented in Table 4.7 have the same attributes and gravity loads as they possess in the global building response model. The columns are divided into 16 sub-elements (15 internal nodes) each

and blast loads are applied uniformly at the nodes in the same fashion as described earlier in Chapter 2. The blast loads are based on the range and incident angle of the mid-height of the columns.

The time-histories of the mid-height deflections in the columns analysed individually and the deflections at the first story (top end of columns) produced by the progressive loading pattern in the global model are compared at the in Figure 4.17.

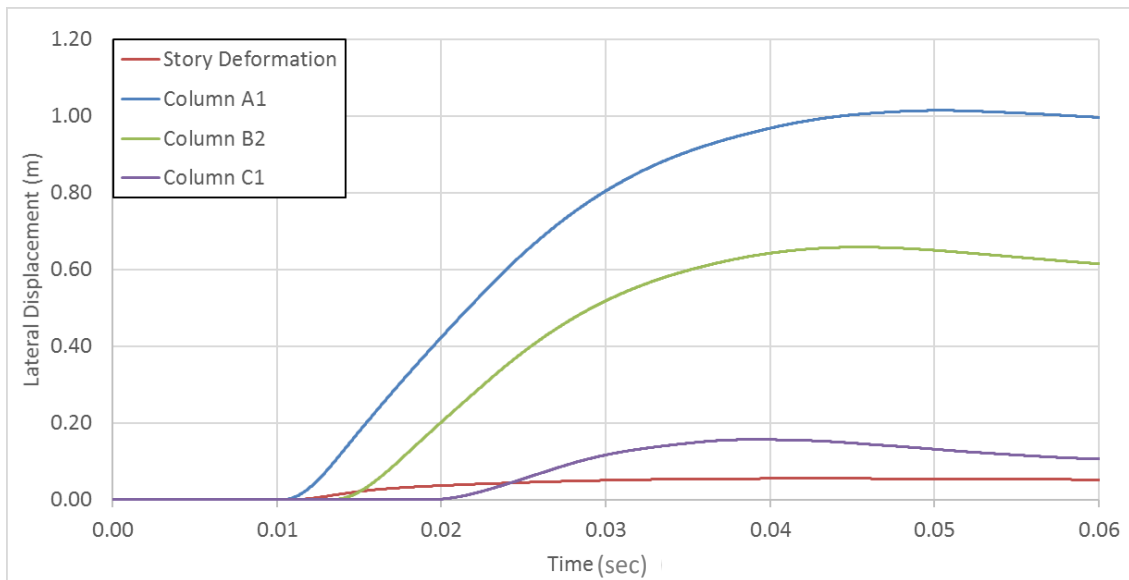


Figure 4.17. Response at mid-height in individual columns versus first story displacement in the global model

As observed from Figure 4.17, the lateral displacements (mid-height displacements) in the columns and the story drifts (top ends of columns) start at about the same time. Although the story deflections are much smaller than the local displacements in the columns, the assumption of a laterally restrained end for the columns is not quite accurate.

In order to compare the response of an isolated column to the response of the same column as part of the global model, the global response analysis is repeated, but with a different loading pattern. In this new pattern, the blast loads are applied at the mid-height of the columns as well as at beam-column joints at story levels. The reflected pressure time-histories at the two locations are derived using the range and incident angle of the column mid-heights and story levels, respectively. The tributary areas used to convert the blast pressures to loads are shown in Figure 4.18 for a typical frame. This type of loading should be able to capture both the individual deformations of the exterior columns and the lateral story drift of the building. In fact, to improve the validity of the comparison the number of internal nodes of a column at which the blast forces are applied should be identical between the isolated column and when the same column is part of the global model. This is covered in a later part of this chapter.

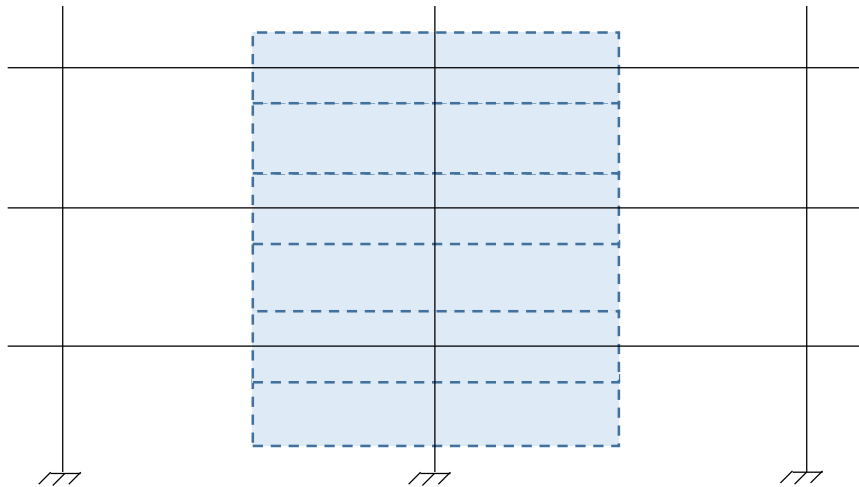


Figure 4.18. Loading areas for a typical frame

The lateral displacements at column mid-heights and at story levels produced by the new loading pattern are shown in Figure 4.19, and are compared with the mid-height

deflections of the columns in individual models, and also with the story drifts of the building under the previously described exact progressive loading. A comparison of the maximum responses is also presented in Table 4.8. The maximum story drifts under the two types of loading are shown in Figure 4.20.

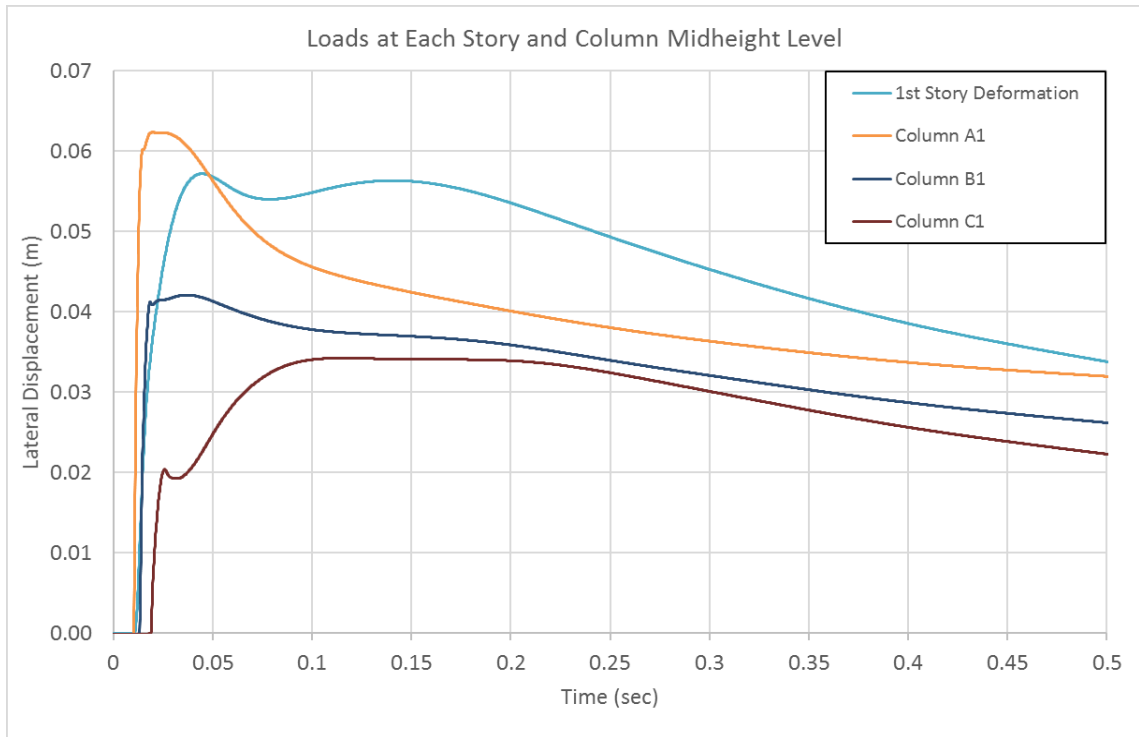


Figure 4.19. Lateral displacements at mid-heights of individual columns and the first story (columns end) deformations in the global model in which the loads are applied at both column mid-heights and at story levels

Table 4.8. Comparison of lateral deflections at individual column mid-heights, and when they are part of the global model with loads applied at both story and mid-height levels

Deflection location	Column A1		Column B1		Column C1		Story 1 level deflection	
	Individual	Global	Individual	Global	Individual	Global	All loads at story level	Loads at story and mid-height level
Max. lateral displacement (mm)	1013.9	65.1	657.8	44.3	156.8	36.3	55.3	59.5

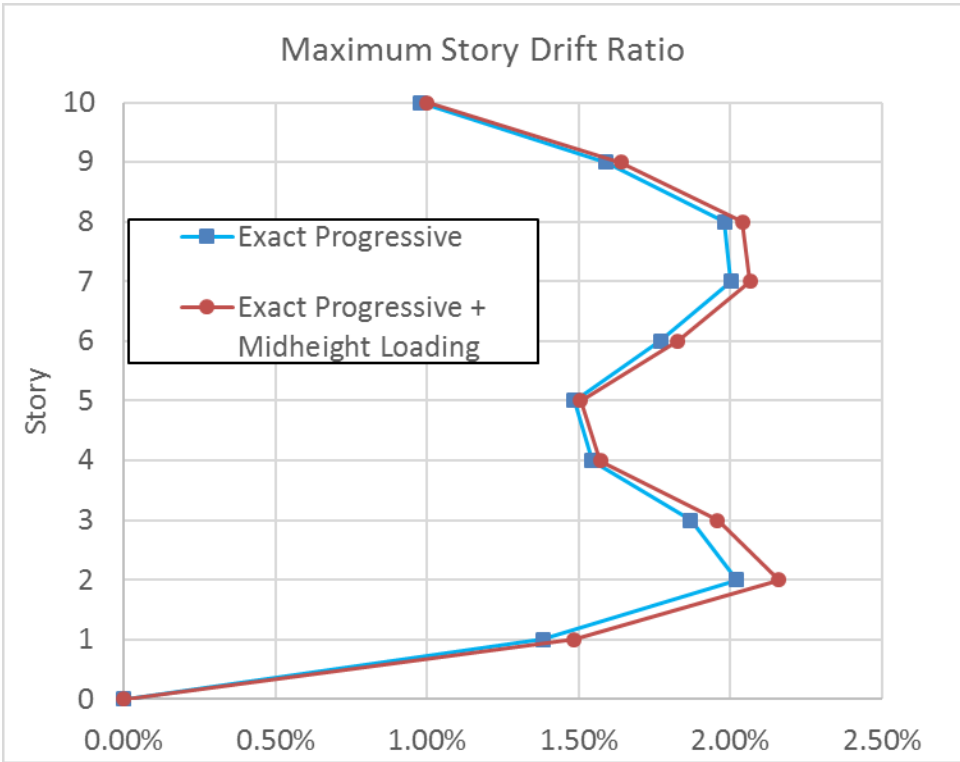


Figure 4.20. Comparison of maximum story drifts under progressive loading with loads applied at story levels or at both story and mid-height levels

As observed in Figure 4.20, the story drifts and therefore the global response of the building remain relatively unchanged when the blast loads are split between the story levels and the column mid-heights. In order to have a better review of the displacement

patterns that occur in the global response, the deformed shape (at the peak displacements) of the first story columns analysed in the global model with loads split between the story levels and column mid-heights are shown in Figure 4.21. The maximum chord displacements in the columns obtained in the global analysis are reported in Table 4.9. Also shown for comparison are the maximum displacements in the columns analysed individually (with fixed ends) under the same loads.

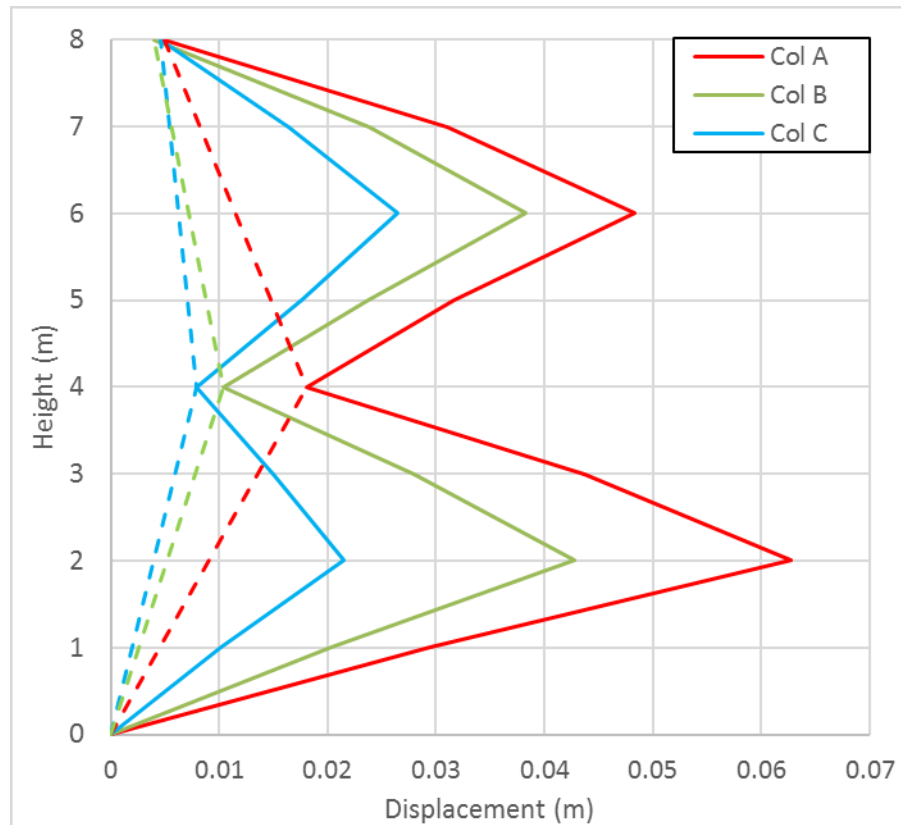


Figure 4.21. Deformed shape of 1st and 2nd story columns at the time mid-height chord deflections in 1st story columns peak in global response (dashed lines are chord deflections which are deduced from total deflections of columns to be compared to individual results)

Table 4.9. Maximum chord displacements of 1st story columns in global model compared to maximum mid-height column deflections in individual model

Deflection location	Column A1		Column B1		Column C1	
Model	Individual	Global	Individual	Global	Individual	Global
Max. lateral displacement (mm)	1013.9	53.7	657.8	37.6	156.8	17.5

The mid-height deflections of the columns are much smaller when the columns are treated as part of the global model of the structure, but when the columns are modelled as individual elements with fixed ends considerably higher deflections are obtained. As stated earlier, it might be reasoned that this difference could be because of the difference between the how the column loads are applied in the two models, since in the individual column model 15 internal nodes are loaded while in the global model only one internal node is loaded with tributary area equal to half of the column height multiplied by the tributary width. In order to eliminate this possible source of difference, the first and second story columns in the global model are divided into the same 16 elements and loads are applied to each node in the same fashion as in the individual column model. Thus, the column and cladding masses are lumped at these 15 nodes as well as at the nodes at story levels. The model was analysed and the maximum lateral deflections for the first story are reported in Table 4.10. These results are compared with the results of the analysis of the previous global model in which only four sub-elements were present in each of the columns in the first two stories.

Table 4.10. Maximum displacements of 1st story columns in global models with 4 and 16 sub-elements

Deflection location	Column A1		Column B1		Column C1		Story level	
Sub-elements in each column	16	4	16	4	16	4	16	4
Max. lateral displacement (mm)	71.3	65.1	48.2	44.3	38.1	36.3	62.1	59.5

As shown by the data presented in Table 4.10, use of 16 elements and therefore giving a greater portion of the loads to the columns instead of to the story levels, does not affect the response in a significant manner.

The response results presented here show that the individual model of the columns yields highly conservative values of the mid-height displacement, compared to those obtained from a global model.

The results shown above are all under the same blast scenario, namely 1000 kg TNT at 15 m. The results of the individual member analysis show that all the three columns become nonlinear throughout their length and have excessive lateral displacements.

The columns have clearly failed under these loads. Even in the global analysis excessive nonlinearity is present in the columns, where the plasticity has spread to large areas of the columns. For instance, it was observed in column A1 in the global model that in 13 of the 16 sub-elements, the tensile rebar strain exceeds the yielding strain. When gravity load carrying members experience such nonlinearity the building is likely to collapse. Therefore, it can be reasoned that the comparison between the global and

individual responses is exaggerated because of the excessive nonlinearity and failure of the columns.

In order to have a better comparison between the global and individual models, the same building is subjected to a smaller blast scenario of hemispherical 500 kg TNT at 30 m standoff from the building. The blast load characteristics are determined for the beam-column nodes and the column mid-heights in the building façade closest to the blast charges based on the range and incident angle of each node. Since both the charge mass (500 kg) is smaller and the standoff distance (30 m) is larger in this blast scenario than in the previous scenario (1000 kg at 15 m), it is obvious that the effects of side and roof blast loads are even smaller, therefore these loads are neglected in this scenario and only the front face of the building is loaded with the progressive blast pattern. All other parameters of both global and individual models are considered in exactly the same manner as earlier. The columns in the first and second story of the global model and also in the individual model are discretized into 16 sub-elements (15 degrees of freedom), and the other beam and column elements are discretized into 4 sub-elements. The blast loads based on the mid-height of the columns in the first story, which are used in the individual model are presented in Table 4.11. The blast loads are applied uniformly to all the internal nodes of the columns.

Table 4.11. Blast load properties applied on first story column in 500 kg TNT at 30 m
standoff

Column	A1	B1	C1
Standoff (m)	30.2	31.4	33.6
Incident angle ($^{\circ}$)	6.9	17.1	26.8
Time of arrival (msec)	42.3	45.1	50.3
Reflected pressure (kPa)	180.0	164.2	140.4
Fictitious duration time (msec)	15.0	15.3	15.9

Both global and individual models are analysed for their response to the specified load. The chord displacements of the columns in the front face of the building in the global model are determined as described earlier and are compared to the displacements of the single columns modeled individually. The displaced shape of the first story columns relative to the chords in the global model at the time the chord displacements peak is compared to the displaced shape of the columns modeled individually in Figure 4.22.

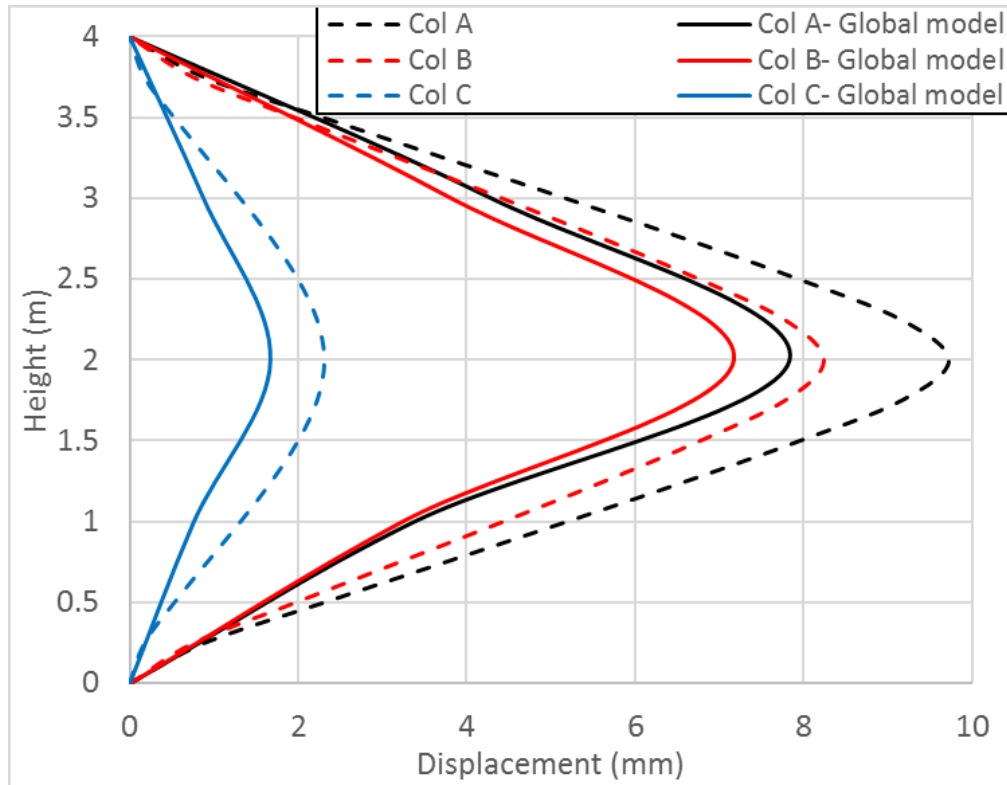


Figure 4.22. Comparison of deformed shape of peak 1st story columns chord displacements versus deflections in single columns modeled individually

As can be seen from Figure 4.22, the chord displacements of the columns in the global model and the displacements of the individual columns are quite close. This comparison, however, shows that the individual model still estimates the column displacements in a conservative way. The maximum support rotation in this scenario is 0.3 degrees for column A1 in the individual model, which indicates the columns are still in the stage of low intensity (superficial) damages.

By comparing the response of the columns in global and individual (element-by-element) models in the two blast scenarios analysed here, a conclusion can be drawn that the individual models estimate the displacements conservatively compared to

when the whole building is modeled. The difference between the results of the two models is more significant when the columns are in a more severe response stage (i.e. blow out stage). However, in the case of reasonable and smaller damage stages of the columns, the two models do not differ in results substantially. Therefore, it can be reasoned that the use of individual element models (traditional member-by-member analysis) is justified and reasonably accurate, since in designing a building against blast it would be ensured that columns do not suffer major damage. On the other hand, if an existing building is being evaluated for its resistance to blast loads, a global analysis would be recommended.

Another important observation from the results of these simulations is that the maximum deflections at the column mid-height and at story level do not occur at the same time. As observed from Figure 4.19, at the time the mid-height deflections are at the peak in the first blast scenario, the story level deflection is less than 20 mm, which is well below the peak story drifts (almost 60 mm). The peak column mid-height deflections occur in the early stages of the response (14.6 msec for Column A1, 18.3 msec for Column B1 and 25.5 msec for Column C1). On the other hand, the maximum deflections in the first story level occur at 140 msec in the analysis (see Figure 4.19). The deflected shape of the first and second story columns at the time the first story drifts peak is presented in Figure 4.23.

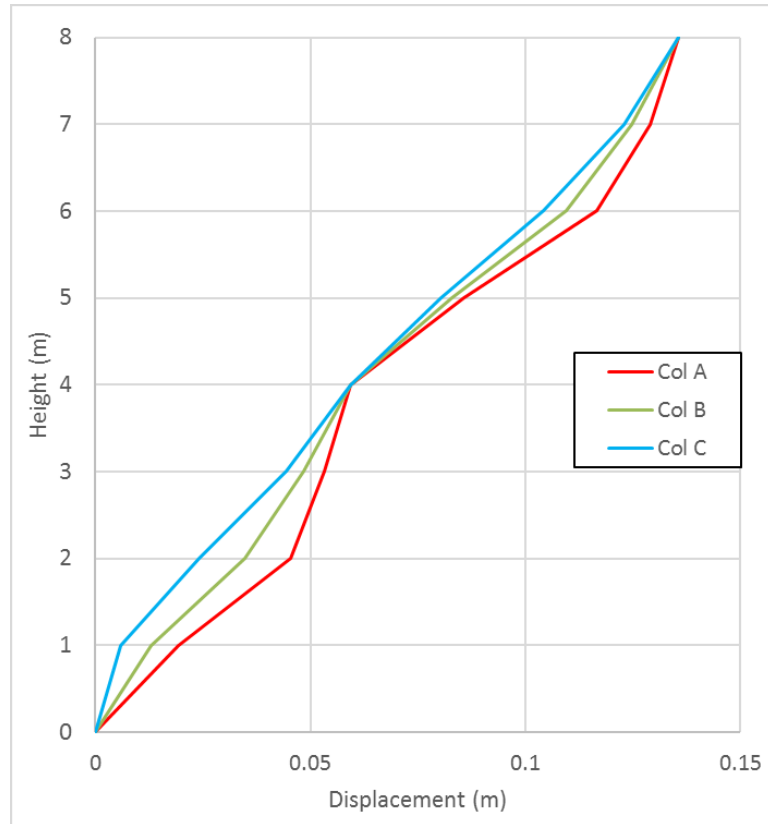


Figure 4.23. Deformed shape of 1st and 2nd story columns at the time 1st story deflections peak in global model in 1000 kg TNT at 15 m scenario

As seen from Figure 4.23, the global response of the building (story sway) is more dominant than the local response (mid-height deflections of columns) and the pattern of the deflections in the building and the columns shows this fact.

At the end, it should be mentioned that in reality, the portion of the loading incident on the columns can even be smaller than what has been assumed here, since the tributary areas contributing to the loads on the individual columns are usually less than the total supported panels because of the two way actions in each loaded panel as shown in Figure 4.24. Thus the assumption made in splitting the loads between the story levels and mid-heights in global models is not far from the reality.

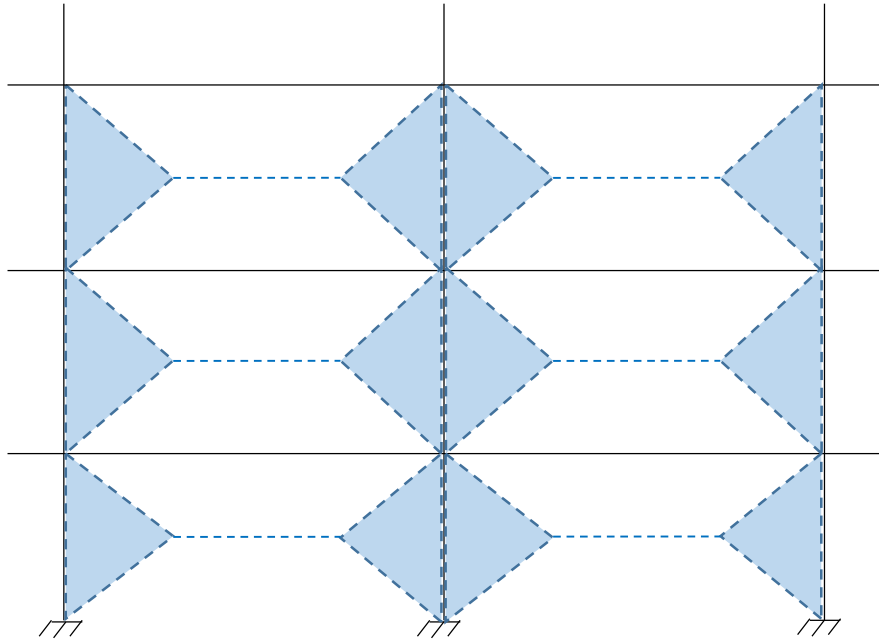


Figure 4.24. Tributary area of the columns subject to blast loads

4.2.8.5. Comparison with the deflections produced under earthquake loads

In this Section, the global response of the structure to blast loading is compared with its response to earthquake forces for which the lateral load resisting system was originally designed. For this purpose, the lateral deformations and story drifts under the progressive blast load pattern are compared to those obtained when the structure is subjected to 10 different earthquake time-histories. Out of the 10 selected time histories of earthquake ground motions, five are scaled so that their response spectra are compatible with the uniform hazard spectrum (UHS) for Montreal in eastern Canada, while the other five are scaled so that their response spectra match the UHS for Vancouver in western Canada. The synthetic time-histories, namely E6C1, E6C13, E6C15, E6C18 and E6C42 to represent the hazard for Montreal and M6C1, M6C2, M6C26, M6C31 and M6C38 to represent the hazard for Vancouver, are extracted from the

database of ground motions generated by Atkinson (2009). The eastern ground motion time-histories need to be scaled by scale factors of 0.55, 0.74, 0.56, 0.61 and 1.01, respectively for the time-histories mentioned above, in order for their spectra to match the UHS for Montreal. The scale factors to be applied to the western ground motions are 0.78, 0.87, 1.19, 0.99 and 1.43, respectively for the time-histories mentioned above, for their spectra to match the UHS for Vancouver. The scaled ground motions are shown in Figures 4.25 and 4.26.

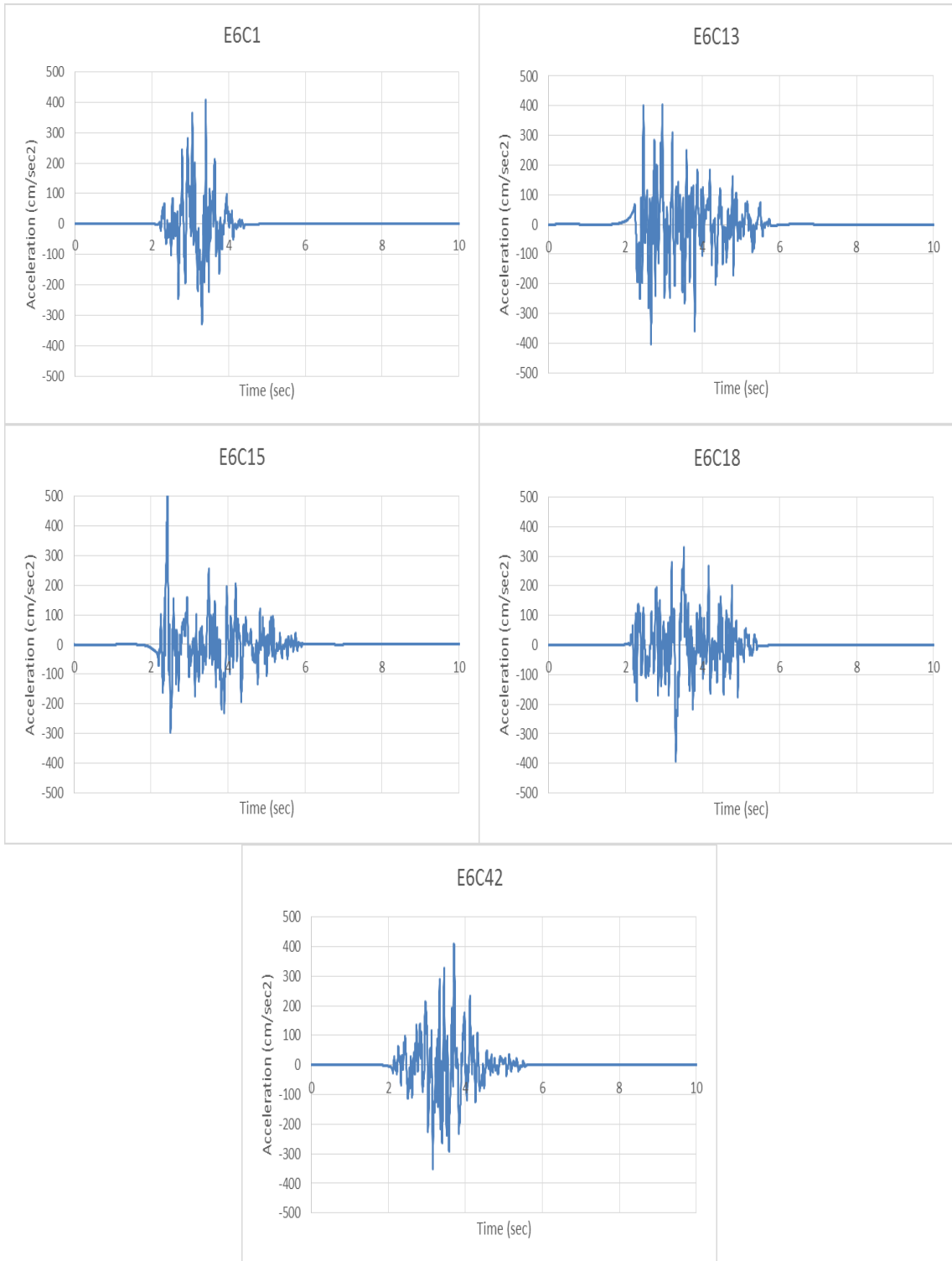


Figure 4.25. Scaled ground motion time-histories for the eastern Canada (Atkinson 2009)

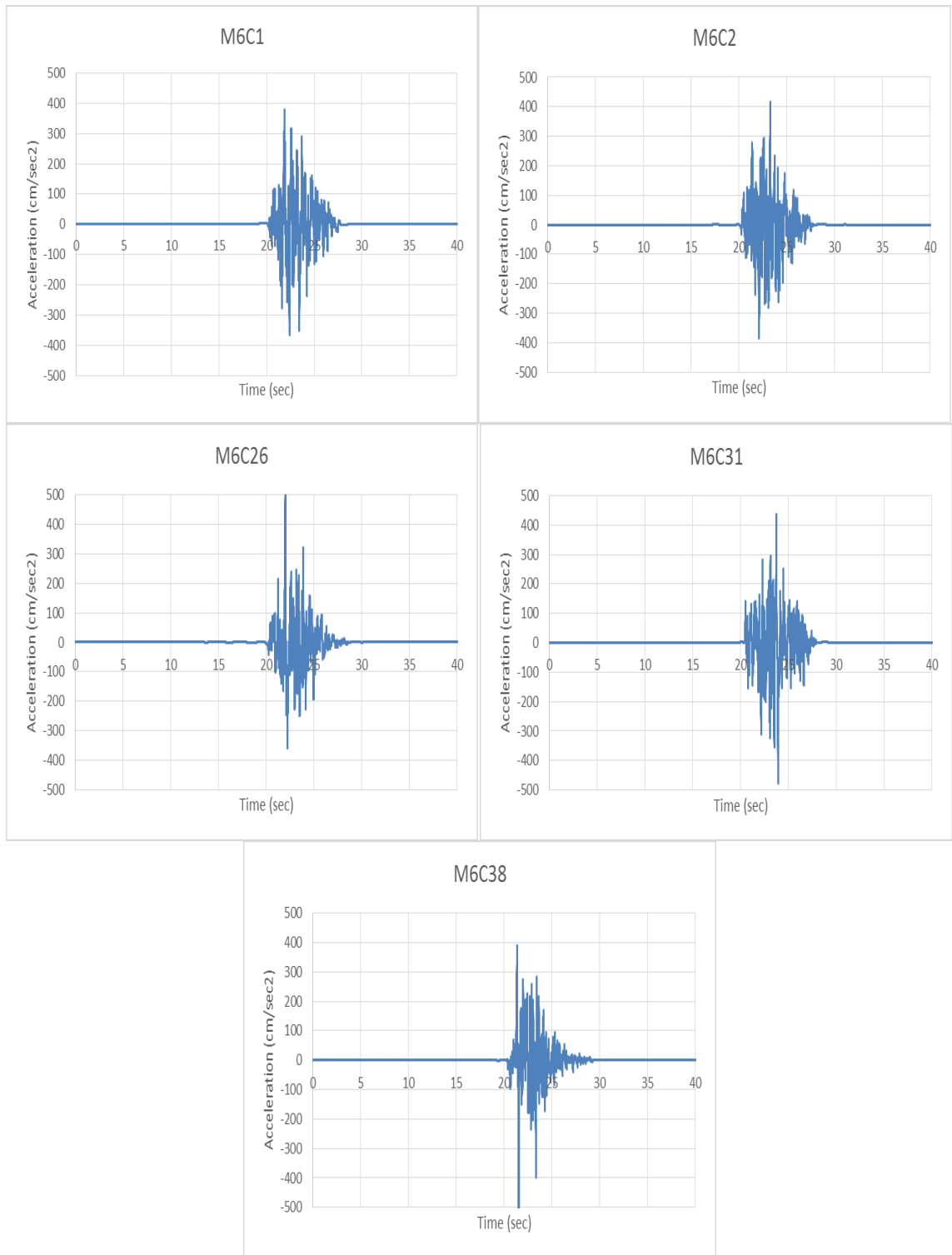


Figure 4.26. Scaled ground motion time-histories for the western Canada (Atkinson 2009)

In order to analyse the response of the structure to the selected earthquake records, the material models need to be modified, since the strain rate effects and dynamic increase factors are not applicable. The revised material models are obtained by a procedure similar to that described in Chapter 2 and section 4.2.2 and are presented in the following.

- **Unconfined concrete:**

$$f'_c = 30 \text{ MPa} \Rightarrow E_c = 4700\sqrt{f'_c} = 25.74 \text{ GPa}$$

$$\varepsilon_0 = 2f'_c / E_c = 0.00233$$

$$\Rightarrow k = 102.04 \text{ \& } f'_{ca} = 0.85f'_c = 25.5 \text{ MPa}$$

- **Confined concrete:**

$$f'_{c0} = 30 \text{ MPa} \Rightarrow E_c = 8200f'_{c0}{}^{3/8} = 29.36 \text{ GPa}$$

$$\varepsilon_{c0} = \frac{f'_c{}^{1/4}}{1152.63} = 0.00203$$

$$f_t = 0.62\sqrt{f'_c} = 3.4 \text{ \& } \varepsilon_t = 2f_t / E_c = 0.00023$$

- **Special regions in moderate ductility columns:**

$$\begin{aligned} \text{effective confined area, } A_e &= \left(b_c d_c - \sum \frac{(w'_i)^2}{6} \right) \left(1 - 0.5 \frac{s'}{b_c} \right) \left(1 - 0.5 \frac{s'}{d_c} \right) \\ &= \left(275 \times 275 - 8 \times \frac{(112.5)^2}{6} \right) \left(1 - 0.5 \times \frac{125}{275} \right) \left(1 - 0.5 \times \frac{125}{275} \right) \\ &= 33448.66 \text{ mm}^2 \end{aligned}$$

$$\text{concrete core area, } A_{cc} = b_c d_c - A_{st} = 275 \times 275 - 8 \times 500 = 71625 \text{ mm}^2 \Rightarrow k_e = A_e / A_{cc} = 0.467$$

$$\rho_x = \rho_y = \frac{A_{sx}}{s.d_c} = \frac{3 \times 200}{150 \times 275} = 1.45 \times 10^{-2} \Rightarrow \text{confinement stress, } f'_l = k_e \rho_x f_{yh} = 2.72 \text{ MPa}$$

$$q = f_{lx}' / f_{ly}' = 1.0 \quad \& \quad x' = \frac{f_{lx}' + f_{ly}'}{2f_c'} = 0.090$$

$$A = 6.8886 - (0.6096 + 17.275q)e^{-4.989q} = 6.767 \quad \& \quad B = \frac{4.5}{\frac{5}{A}(0.9849 - 0.6306e^{-3.8939q}) - 0.1} = 7.28$$

$$k_1 = A\left(0.1 + \frac{0.9}{1 + Bx'}\right) = 4.67 \quad \Rightarrow \quad \boxed{f_{cc}' = f_c'(1 + k_1x') = 42.61 \text{ MPa}}$$

$$k_2 = 5k_1 = 23.35 \quad \Rightarrow \quad \boxed{\varepsilon_{cc} = \varepsilon_{c0}(1 + k_2x') = 0.0063}$$

$$\boxed{x_n = 30} \& \boxed{x_p = 2} \quad n = \frac{E_c \varepsilon_{cc}}{f_{cc}'} = \frac{29.36 \times 10^3 \times 0.0063}{42.61} = 4.34 \quad \Rightarrow \quad \boxed{r = n / (n - 1) = 1.3}$$

- **Special regions in moderate ductility beams:**

$$\begin{aligned} \text{effective confined area, } A_e &= \left(b_c d_c - \sum \frac{(w_i')^2}{6} \right) \left(1 - 0.5 \frac{s'}{b_c} \right) \left(1 - 0.5 \frac{s'}{d_c} \right) \\ &= \left(180 \times 330 - 2 \times \frac{(70)^2}{6} \right) \left(1 - 0.5 \times \frac{80}{180} \right) \left(1 - 0.5 \times \frac{80}{330} \right) \\ &= 35792.7 \text{ mm}^2 \end{aligned}$$

concrete core area, $A_{cc} = b_c d_c - A_{st} = 180 \times 330 - 5 \times 300 = 57900 \text{ mm}^2 \Rightarrow k_e = A_e / A_{cc} = 0.6182$

$$\rho_x = \frac{A_{sx}}{s.d_c} = \frac{2 \times 100}{100 \times 330} = 6.06 \times 10^{-3} \quad \& \quad \rho_y = \frac{A_{sy}}{s.b_c} = \frac{2 \times 100}{100 \times 180} = 1.11 \times 10^{-2}$$

confinement stress, $f'_{lx} = k_e \rho_x f_{yh} = 1.50 \text{ MPa}$ & $f'_{ly} = k_e \rho_y f_{yh} = 2.75 \text{ MPa}$

$$q = f'_{lx} / f'_{ly} = 0.546 \quad \& \quad x' = \frac{f'_{lx} + f'_{ly}}{2f'_{cd}} = 0.054$$

$$A = 6.8886 - (0.6096 + 17.275q)e^{-4.989q} = 6.227 \quad \& \quad B = \frac{4.5}{\frac{5}{A}(0.9849 - 0.6306e^{-3.8939q}) - 0.1} = 7.14$$

$$k_1 = A(0.1 + \frac{0.9}{1 + Bx'}) = 4.67 \quad \Rightarrow \quad \boxed{f'_{cc} = f'_c(1 + k_1x') = 37.56 \text{ MPa}}$$

$$k_2 = 5k_1 = 23.35 \quad \Rightarrow \quad \boxed{\varepsilon_{cc} = \varepsilon_{c0}(1 + k_2x') = 0.0046}$$

$$\boxed{x_n = 30} \quad \& \quad \boxed{x_p = 2} \quad n = \frac{E_c \varepsilon_{cc}}{f'_{cc}} = \frac{29.36 \times 10^3 \times 0.0046}{37.56} = 3.6 \quad \Rightarrow \quad \boxed{r = n / (n - 1) = 1.38}$$

- Other regions in moderate ductility beams and columns:

$$f'_c = 30 \text{ MPa} \quad \Rightarrow \quad E_c = 8200 f'^{3/8}_c = 29.36 \text{ GPa}$$

$$\boxed{\varepsilon_{c0} = \frac{f'^{1/4}_c}{1152.63} = 0.00203}$$

$$\boxed{f_t = 0.62\sqrt{f'_c} = 3.4} \quad \& \quad \boxed{\varepsilon_t = 2f_t / E_c = 0.00023}$$

$$\boxed{x_p = 2.0} \quad \boxed{x_n = 2.3} \quad \boxed{r = \frac{f'_c}{5.2} - 1.9 = 3.9}$$

- **Reinforcing steel:**

$$\boxed{f_y = 400 \text{ MPa}} \quad , \quad \boxed{E_s = 200 \text{ GPa}} \quad \boxed{\varepsilon_y = f_y / E_s = 0.002}$$

$$\boxed{f_u = 500 \text{ MPa}} \quad ; \quad \boxed{\varepsilon_u = 0.035}$$

$$E_{sh} = \frac{f_{ud} - f_{yd}}{\varepsilon_u - \varepsilon_y} = 3030.3 \text{ MPa} \quad \Rightarrow \quad \boxed{b_{sh} = \frac{E_{sh}}{E_s} = 0.015}$$

Using the new material properties described in the foregoing, the seismic time-history analyses are carried out in OpenSEES using UniformExcitation, 5% damping ratio and a time-step of 0.001 sec throughout the analysis. The results in terms of lateral story drifts are collected for comparison with those obtained in the blast load analysis.

Since the seismicity levels selected here are not too high, in order for the response to be comparable, another smaller blast scenario was selected to be applied to the structure. Thus, in addition to the 1000 kg TNT at 15 m standoff scenario, a second blast scenario consisting of 1000 kg TNT at 30 m standoff from the building was selected. The blast loads on the building are calculated from CONWEP, assuming a similar pattern for all the nodes in each story, and considering the range and incidence angle to be those of the point in each story that is nearest to the charge (simplified progressive with incident angles). The blast pressures and other required properties for loading of the structure in this scenario are presented in Table 4.12. For the 1000-kg-at-15-m blast scenario, the loads are applied in the same simplified fashion to the structure as calculated in Table 4.4 and the response results are obtained. The response to blast loads is compared with the response to earthquake forces in Figure 4.27.

Table 4.12. Simplified progressive blast loads (considering incident angle for each story)

applied to structure from 1000 kg at 30 m scenario

Story	Shortest range (m)	Incidence angle ($^{\circ}$)	Time of arrival, t_a (msec)	Peak reflected pressure, P_r (kPa)	Reflected impulse, I_r (kPa.msec)	Fictitious duration, t_d (msec)
1	30.27	7.59	36.00	317.27	2181.29	13.75
2	31.05	14.93	37.64	282.07	2012.95	14.27
3	32.31	21.80	40.34	235.33	1778.57	15.12
4	34.00	28.07	44.04	187.54	1521.86	16.23
5	36.06	33.69	48.67	145.62	1278.08	17.55
6	38.42	38.66	54.11	111.90	1064.48	19.02
7	41.04	43.03	60.31	86.24	887.90	20.59
8	43.86	46.85	67.14	67.30	746.10	22.17
9	46.86	50.19	74.55	53.36	634.51	23.78
10	50.00	53.13	82.45	43.16	546.94	25.34

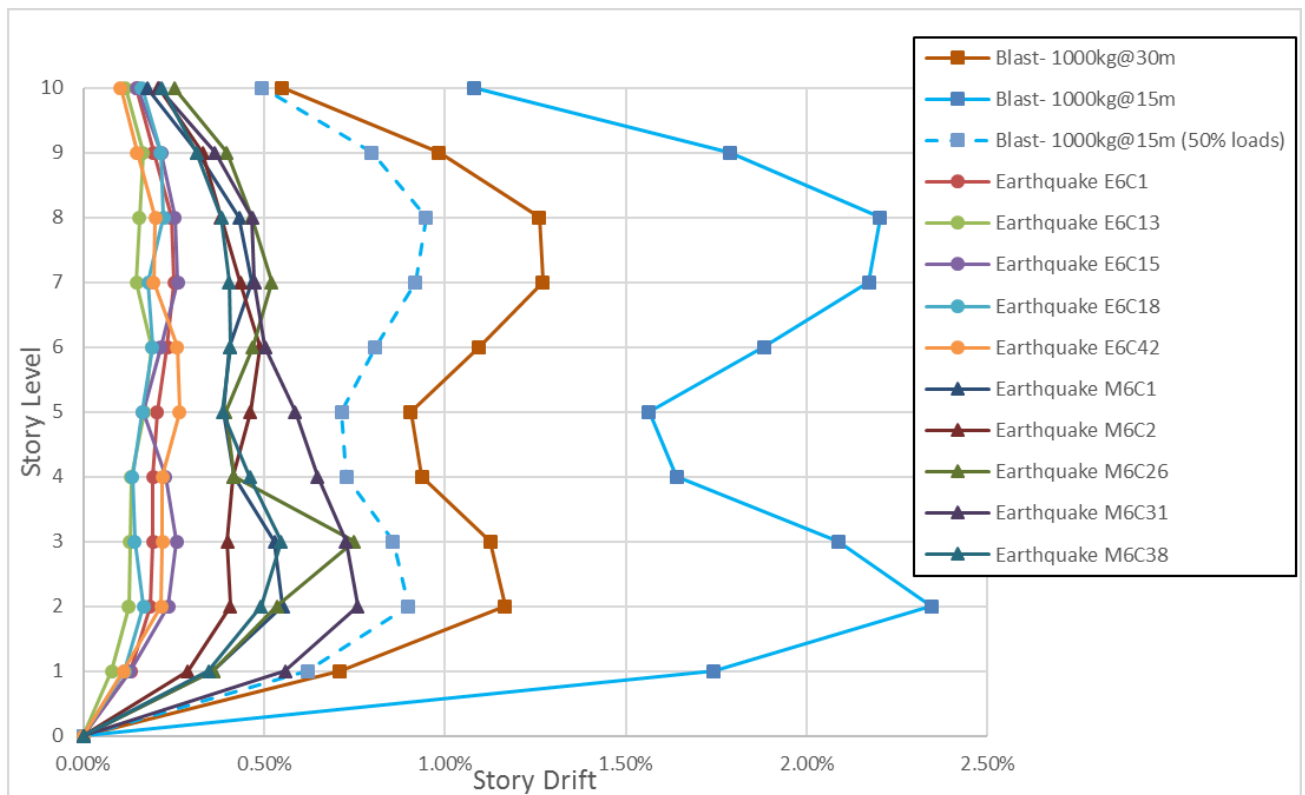


Figure 4.27. Maximum story drift ratios obtained from earthquake and blast analyses

The results presented in Figure 4.27 show that the maximum story drift ratios under blast loads are much higher than those obtained from the analyses for both eastern and western Canada earthquake time-histories. Since the response of the building to earthquake loads is quite low (much less than allowable in the seismic design), there is the likelihood that the design of the building was not governed by earthquake forces, and that instead gravity loads were the governing loads. Even the ground motions representing the seismic hazard for Vancouver do not cause any significant lateral displacement in the structure. On the other hand, even the smaller blast scenario (30-m standoff) pushes the structure into nonlinearity, and the larger blast scenario (15-m-standoff) pushes the structure above allowable lateral story drifts specified by the code of 2% (NRCC, 2010). It should be noted that the blast scenarios selected here are not extreme cases, as the 1000 kg TNT charge at standoff of 15 m or 30 m is expected to result in heavy damage performance category (USACE, 2010). The heavy damage performance of the building is expected under the design basis earthquake, namely “collapse prevention” (NRCC, 2010).

Based on the foregoing observations, it may be reasoned that the blast loads may force the structure to deform laterally with magnitudes of deformations that are similar to or higher than those under seismic action. It would therefore be necessary for the designers to check the lateral deformations and the global response of the buildings under blast loads, in the same fashion as for earthquake forces.

4.3. Summary and Conclusions

Different aspects of global response of building structures are analyzed in a case study of a 10 story RC moment frame building structure. The building is analyzed for its response to a selected blast scenario. It is noted that for a regular building and symmetrical loading, such as those in the present study, a 2D model is adequate for determining the response. The 2D model reduces the computational effort significantly, and with the use of proper modeling technique as illustrated in this thesis it provides the accuracy needed in the analysis.

Among the different patterns used to represent the blast loads acting on the building, simultaneous loading of all components at a story level based on the shortest range to the story leads to a response that is quite close to that obtained from the progressive loading pattern. In fact, for the type of system studied here the differences in the blast loads on individual points in each stories based on the difference in their distance to charge as well as the incident angle of the blast pressure with the surface can be ignored without significantly compromising the accuracy of results. On the other hand, it is observed that the assumption of planar shock front for the blast waves, which implies simultaneous loading of the entire building, leads to excessive and unrealistic (up to 4 times) deformations in the structure.

The integrity of the outer surfaces and claddings has an important role in the response of the structure. If the envelop of the building fails and is not able to transmit the blast forces to the frames, the response is likely to drop drastically. However, in that case the

failure of the peripheral elements and windows would by itself present a big safety hazard. This issue should be considered in the designs and assessments of the safety and risks associated with action of blast loads on the structure.

In the traditional practice, it is generally assumed that the response of individual columns on the front face of the building, rather than the global response is more critical. It is further assumed that the individual columns can be analysed for their response by using a model of the isolated column in which the boundary conditions are assumed to be some combination of fixed and pinned, but laterally restrained. For high blast loads, the response of an isolated column is much larger than the response of the same column when it is treated as a part of the global model. This is mainly on account of the inelasticity introduced in the columns, and to some extent because of the assumption of lateral restraint at the boundaries of the column. When the blast loads are modest, so that the column remains elastic the difference between the response of an isolated column and when it is part of the global model is not large, although isolated column response is still conservative. In a new design the columns will be sized so as not to deform into the inelastic range under the expected blast load. This is to safeguard the vertical gravity carrying components against damage. In this situation, response analysis of isolated column model would provide acceptable, although somewhat conservative results. On the other hand, when an existing building is being evaluated for its resistance to blast, a global analysis may be necessary to obtaining realistic results, particularly when the isolated column analysis shows that the column becomes inelastic.

Global analysis is also useful to verify that the story drifts are within acceptable limits and that P- Δ effects are not critical.

For a comparison of the response of the selected building under earthquake and blast forces, the building is subjected to 10 different earthquake ground motions representing two different hazard levels (eastern and western regions of Canada). The lateral deformations of the structure under earthquake forces are compared to those obtained under two different realistic blast scenarios. The comparison shows that the lateral story drifts produced by blast loading are significantly larger than the corresponding seismic drifts.

In general, the present study demonstrates the importance of carrying out an analysis of the response of global model of the building structure under blast loading. A detailed model of the building structure in addition to the element-by-element analysis of the critical members, can lead to a better understanding of the response. Also, the lateral deformations and drifts of the building structures could be comparable to and even more significant than those under seismic loads.

Chapter 5. Summary and conclusions

5.1 Introduction

Among the many different types of loads a building structure experiences, are the blast loads produced by explosions, accidental or manmade. Until recently, design of buildings to resist blast loads was a military concern. However, with an increase in terrorist activity many civilian structures are now designed so that they are able to sustain blast loads.

Designing for blast loads involves an understanding of the nature of blast loads and the analysis of structures for their response to such loads. Empirical expressions based on observation of the magnitude and variation of blast loads has been derived and are now widely used. However, considerable uncertainty exists in the determination of blast loads. Because of such uncertainty, traditional methods of the analysis of structures for their response to blast loads are based on simplified analysis of highly idealized models of the building components. In addition, it is believed that the more critical response from the point of view of design is that of individual components so that global response need not be studied.

The present research includes a critical review of the traditional methods of blast load analysis of structural components. Also examined is the nature of global response to blast loads and whether such response may be critical in some cases. Attempt is made to develop new methods of analysis, which could provide a comparatively more precise estimation of the response, without making the analysis too complex. The study

assumes that the available expressions for determining the blast loads are adequate. The scope of the study is limited to the effect of far field explosions; the impact of an explosion in close proximity of the building is not studied.

A summary of the research carried out and the conclusions drawn is presented in the following sections. Individual sections deal with the following cases:

1. Response of the columns on the front face of the building relative to the centre of explosion: A general conclusion in this part is that by using more advanced numerical tools, engineers can capture the response of columns to blast loading more accurately. Various in-depth suggestions are presented in Chapter 2, also in the next section of the thesis to support this conclusion.
2. Response of the elements of structures perpendicular to the shock front, such as roof beams spanning in the perpendicular direction: A general conclusion is that the current simplified methodologies are not accurate and engineers should use the more accurate methodology described and suggested by this thesis for these types of beams. Also, a new analytical tool is presented which can facilitate this idea and methodology with very small computational cost.
3. Global response of the building: As a general conclusion, it is suggested a global response analysis model should be a part of design or analysis of buildings in blast loading. The lateral deformations of the buildings, response of critical members as part of the whole building can be very important to be analysed in this model. More detailed and in-depth suggestions in this regard are presented in the following section.

Also, presented are more detailed conclusions and some recommendations for future research in the area of response analysis dealt with in the present study in the following.

5.2. Summary and conclusion on response of columns to blast loading

Response of columns to blast loads is traditionally assessed using SDOF systems. The use of idealized SDOF models was originally suggested, considering the high uncertainty involved in the determination of blast loads. This simplified methodology is still used as a common means of analysing the blast load effects on columns of buildings. However, methods of analysis that could provide comparatively more precise estimates of response, with limited or no increase in the complexity of analysis, would be quite useful. In fact, civilian structures, originally designed for economy and aesthetics, are now also likely to be subjected to blast loads. Thus, blast load retrofit of such structures would be required, and it would be important to undertake a more detailed analysis before scarce resources are expended on retrofit. Evidently, there is a need to carry out a critical review of the traditional methodologies and models, and to determine whether it is still justified to use the simplifying assumptions.

For a critical review of the traditional methods of analysis as well as to determine what factors had important bearing on the response of columns, response of two rectangular RC columns with different dimensions to five different blast loads was determined.

Fixed dynamic increase factors and confinement effects were considered in modeling the columns. First, the columns having an axial load equal to 12.5% of the ultimate axial load capacity ($f'_c A_g$) were modeled using fibre elements and 15 translational degrees of freedom (the column being divided into 16 sub-elements).

To study the effect of shear deformation on response models with and without the consideration of shear deformations were analysed. It was observed that the maximum displacements in the models with shear deformations were slightly greater (up to 12%) than those in the models without shear deformation. This difference was more pronounced in the columns with larger dimensions (11.3% compared to 5.3% for columns with smaller dimension). This would be expected because the shear deformations are more important in deeper sections. The differences in the maximum moments (at mid-height and ends) and end shears of the columns varied randomly, but were within 5% percent of the calculated values in the models with no shear deformations.

Next, the effect of number of degrees of freedom on the analysis of blast load response of columns was studied for RC columns modeled using fibre elements with different numbers of degrees of freedom. Also included for the purpose of comparison were the response results obtained from the analysis of a traditional single degree of freedom system. Columns under an axial load equal to 12.5% of the axial load capacity were modeled using one to 25 degrees of freedom (DOF) and analysed for their response to five different blast scenarios. The simulations showed that the maximum displacements, as well as the maximum bending moments, could be predicted with good accuracy even when only a small number of DOF's were used (up to 25% error in SDOF model and 10% error in models with five DOF's or more). The maximum end shear was more sensitive to the number of DOF's used (up to 70% underestimation in SDOF model and up to 20%

underestimation even in models with 15 DOF's, compared to the results of the columns modeled with 25 DOF's).

The effects of axial load level and $P-\delta$ in response of single columns to blast load was next analysed. For this purpose, the RC columns described in the previous paragraphs, modelled using fibre element and 15 DOF's, were subjected to the five selected blast scenarios. The axial load on the columns was varied from 12.5% to 40% of the nominal axial load capacity. These simulations were carried out with and without considering the second order effects ($P-\delta$ effects). The comparative study showed that under smaller axial loads, $P-\delta$ effects were not significant (less than 5% increase in displacement), while under higher blast loads and higher axial load levels, the simulations considering $P-\delta$ effects resulted in higher responses by up to 40% comparing to in case when the $P-\delta$ effects were not considered. An increase in the axial load decreased the deflections of the columns under smaller blast loads, but it did not have any significant effect when the columns were experiencing higher deformations under higher blast loads.

In analysing an individual column in the building for its response to blast loads, certain assumptions must be made in respect of the end conditions in the column model. The column could be modelled as being pinned-pinned or fixed-fixed. The actual end conditions of a column in a building would be quite different. To get some appreciation for the effect of variations in the end conditions, as well as of the variation of the blast load with height because of the variation in the blast range, the response of a continuous two-story column was analysed, where the first and second story columns were subjected to different blast scenarios. First, different load patterns ranging from

uniform and simultaneous load over the entire two-story height to segment by segment loading were applied to the columns. It was shown that loading the column in each story with a uniform load based on the charge distance to the mid-height of that story provided reasonable estimates of the response. Comparison of the response of the columns in the continuous model to those for individual single column models showed that the traditional element-by-element analysis of single columns underestimates the response of the column in the first story by up to 45%, while overestimating the response of the column in the upper story by up to 20%.

At the end of Chapter 2 of the thesis, the response results obtained from the numerical models used throughout the chapter were verified against experimental results obtained from the published literature. The experimental cases selected were from the RC columns tested at the University of Ottawa's shock tube facility. Comparison of the responses found from the numerical analysis of MDOF models with 15 DOF's and the experiments showed an acceptable match between the two sets of results. This indicates that the models used can be trusted for the cases analyzed here, where the members do not suffer from direct shockfront damages or shear failures as a result of near-field blasts.

The following conclusions can be drawn based on the results obtained from the analytical studies mentioned in the previous paragraphs:

- 1- The effect of shear deformations in the response of columns, in the cases that do not lead to shear failure can be ignored.

2- Selection of the number of degrees of freedom in modeling the columns for blast load analysis is important. A SDOF model can capture the maximum deformations of the members with reasonable accuracy, but if the end reactions (moment and shear) are to be estimated, a MDOF model with at least 15 DOF's would be required.

3- Under smaller blast loads (in the elastic response range), the response of columns reduces under higher levels of axial loads.

4- The secondary effects of deformations ($P-\delta$ effects) may be important in the analysis of the columns, especially if the members are under moderate or high axial loads.

5- Response of continuous (multi-story) columns can be different from the response of the same columns modeled individually. Analysis of global response would be required for a detailed assessment of the effect of continuity and the lateral restraints provided by frame action. This is dealt with more fully in Chapter 4 of the thesis.

5.3. Summary and conclusion on response of roof beams to blast loading

When a building is subjected to blast loads, the beams on the roof or sides of building spanning in a direction perpendicular to the blast shockfront experience pressures that can vary significantly along their span. This propagation of blast loads along the span of the beams makes the analysis of the response of such of beams to blast loading quite challenging. These beams have been traditionally analysed using simplified equivalent uniformly-distributed blast loads. The accuracy of these methodologies have been studied in Chapter 3 of the thesis.

Two different steel roof beams with different tributary widths were selected for the analysis of their response to five different far-field blast scenarios. The beams were modelled using SDOF and MDOF (fibre elements) models based either on simplified equivalent uniform loads (obtained by two different methodologies, UFC 3-340-02 and TM 5-855) or on a travelling blast wave. When the beams were under equivalent uniform loads, the difference between results of SDOF and MDOF models were not substantial (less than 25% and in most cases less than 10%). However, the comparison between results of MDOF models under equivalent uniform loads and travelling loads showed major differences in maximum displacements (up to 840% for UFC 3-340-02 and 70% for TM 5-855 method) and also in maximum bending moments (106% for UFC 3-340-02 and 62% for TM 5-855 method).

An experimental study was conducted to study the exact nature of the blast load on a roof beam. An aluminum beam holding a roof plate made of plexiglas was subjected to a small scale blast load. For the purpose of comparison, the experimental set up was modeled and analysed numerically. A study of the numerical and experimental results showed that the step-by-step travelling load methodology can yield more reasonable estimates of the response in comparison to that obtained from the traditional uniform load analysis.

A nonlinear dynamic analysis code was developed for determining the response of the beams on the roof or sides of the buildings to travelling blast loads. A simple and user-friendly GUI was designed for the computer code. The program uses a simple input and carries out all stages of the analysis from the determination of the blast load to the

computation of response. Application of the computer code to determine the response is quite straightforward and, in fact, less time consuming than even an analysis using comparatively less accurate traditional equivalent uniform load methodologies and a SDOF model. This could be considered a very useful contribution in this subject.

The following significant conclusions can be drawn based on the results obtained from the studies mentioned in the previous paragraphs:

1- Use of the existing simplified equivalent uniform load methodologies for simulation of the response of side and roof beams that are perpendicular to the shock front may lead to large overestimation of the response. In fact, the simplified equivalent uniform load methodologies studied here often provide vastly different results.

2- The errors involved in an analysis based on equivalent uniform load could be attributed to two sources: (a) the inability of a uniform load to represent the load imposed by a travelling pressure wave, which varies with both the spatial and temporal coordinate, and (2) use of a SDOF freedom model rather than a MDOF model.

Comparison of the results of response analysis under the same uniform load but with two different models, a SDOF model and a MDOF model, shows that a SDOF model does not usually lead to significant loss of accuracy, except in the cases where the response is highly nonlinear. In those cases, the simplified definition of plastic moments based on the current codes results in large differences in the response (up to 25%) when compared with the results of MDOF analysis. Thus, in most cases it is the inability of the

uniform load to represent a travelling load is the primary cause of inaccuracy in the uniform load analysis.

3- The application of the more realistic traveling blast loads on a MDOF model for the analysis of roof and side beams is not any more time consuming than the use of a SDOF model and an equivalent uniform load. At the same time, analysis for a travelling blast load provides more reliable and comparably more accurate estimates of response. The methodology can be implemented through commonly available structural design programs, such as SAP2000, ETABS, etc.

4- The nonlinear dynamic code developed as part of the research, further simplifies the analysis of travelling loads. The program uses MDOF models with the number of DOF's selected by the user and performs all steps in the analysis from the determination of the blast load parameters to the calculation of the traveling blast load time-histories and the time histories of response.

5.4. Summary and conclusion on global response of buildings to blast loading

Response of building structures is traditionally assessed by an element-by-element analysis, which consists of modeling critical structural members individually and analysing their response under blast loading. Only a few research studies have focussed on the global response and deformations of buildings under blast, and whether the blast loads can excite or even overwhelm the lateral load resisting system of the buildings.

Different aspects of global response of buildings were studied through the analysis of a 10-story RC moment frame building structure subjected to selected set of blast scenario.

It was shown that for the regular symmetrical problem selected, the 2D models were much more efficient and at the same time accurate enough. Two-dimensional analysis was therefore used throughout the study reported in Chapter 4. Different patterns of blast load distribution were applied to the building, ranging from a uniform loading produced by a planar shockfront to loading of each beam-column node in the building based on its own range and incident angle.

It was shown that assumption of the planar shockfront led to excessive and unrealistic (up to 4 times the more accurate predictions based on the application of blast loads that were dependent on the different range and incident angles of different nodes) inter-story deformations in the structure. For the type of building geometry selected in the study, all of the loads at any story level could be based on the standoff distance and incident angle of the point on the story nearest to the charge, neglecting the horizontal distribution of the loads, without any significant loss of accuracy. The integrity of the outer surfaces and claddings was shown to have an important role in the response of the structure. Therefore, failure of the building envelope should be considered in the design and assessment of the safety and risks associated with action of blast loads on the structure.

In the current practice, the individual columns are analysed for their response by using a model of the isolated column, in which the boundary conditions are assumed to be some combination of fixed and pinned, but laterally restrained. In Chapter 4, it was shown that for high blast loads, the response of an individually modeled column was much larger than the response of the same column when it was treated as a part of the

global model. When the blast loads were moderate, such that the column remained elastic, the difference between the response of an isolated column and when it was part of the global model, was not substantial, although isolated column response was still conservative. Therefore, it was suggested that response analysis of isolated column model could provide acceptable results in the design of new buildings, but in the assessment of an existing building, global analysis may be necessary for obtaining realistic results, particularly when the isolated column analysis shows that the column becomes inelastic. The global analysis of buildings for blast loads is also useful in verifying whether the story drifts are within acceptable limits, and that the P- Δ effects are not critical.

At the end, response of the selected building under earthquake and blast forces were compared. The building was subjected to 10 different earthquake ground motions representing two different hazard levels in Canada. The comparison showed that the lateral story drifts produced by blast loading were significantly larger than the corresponding seismic drifts. Thus, consideration of global response of the buildings to blast loads can be worthwhile in the design and response assessment procedures.

The following conclusions can be drawn based on the results obtained from the studies in this chapter, mentioned in the previous paragraphs:

- 1- Global response of building structures to blast loads can be important, even if progressive collapse phenomenon does not occur.

2- Blast loads can overwhelm the lateral load resisting system of building structures, by imposing large inter-story drifts in the buildings. These drifts can be even more significant than the probable drifts caused by the design level earthquakes.

3- Response of columns in the front face of buildings to blast loads when the global response of buildings and story drifts are considered can be different than when the columns are analysed individually. Therefore, modeling of the whole building structure provides a more reliable estimate of the response.

4 - When the blast loads are modest, so that the column remains elastic the difference between the response of an isolated column and when it is part of the global model is not large, although isolated column response is still conservative. In a new design the columns will be sized so as not to deform into the highly inelastic range under the expected blast load. This is to safeguard the vertical gravity carrying components against damage. In this situation, response analysis of isolated column model would provide acceptable, although somewhat conservative results. On the other hand, when an existing building is being evaluated for its resistance to blast, a global analysis may be necessary to obtain realistic results, particularly when the isolated column analysis shows that the column becomes inelastic. Global analysis is also useful to verify that the story drifts are within acceptable limits and that $P-\Delta$ effects are not critical.

5- In determining the global response of the buildings to blast loads, if the geometry of the building and the location of blast source are symmetrical, a two-dimensional can efficiently and accurately capture the response.

6- Assumption of a planar shockfront to determine the blast loads, especially in the cases when the charge standoff from the building is not large, imposes unrealistically large loads on the building, which results in overestimation of the response. To obtain a realistic estimate of the response, the blast load to be applied at each beam-column joint must be based on that joint's own range and incident angle. Also it is observed that for a typical symmetrical mid-rise building, the loading of sides and roof of the building does not affect the global response significantly.

7- In analysing global response of buildings to blast loads, the integrity of claddings is important; partial or full collapse of the cladding can drastically change the results. Therefore, a good understanding of the possible failure of the building envelope and its impact on the transmission of the blast loads to structural frames is essential.

5.5. Recommendations for future research

5.5.1. General Recommendations

As observed throughout the thesis, in all of the cases considered under different parts of the present study, the main focus has been on the response of building structures and their components to far-field blast loads. It will be worthwhile to continue the same research approach and include various aspects of structural response to near-field and close-in blast loads. However, using near-field instead of the far-field blasts brings new challenges to the work, which need special care in the simulations. For instance, the model should be able to capture various failure modes that can result from direct action of the shockfront, including shear failure which is common in near-field and close-in

blasts. Thus, a more comprehensive model, such as high fidelity physics-based finite elements model, should be used.

Another simplification used throughout the present study was using a constant dynamic increase factor. Although in analysing the local response of the columns and roof beams, the models used were verified against experimental data, a more accurate simulation could use strain-rate dependant increase factors. It is suggested that the effects of using variable increase factors for the strength of both steel and concrete be studied in future research.

The recommendations mentioned in the foregoing are relevant to all three topics covered in the present study. More specific recommendations related to the individual topics are outlined in the following.

5.4.2. Further Research on Column Response to Blast Loading

Response of the columns to blast loading is a topic that has been the subject of many studies. Thus, there is not much that can be recommended for additional research.

Almost all of the aspects of the response have been studied as reported in the literature, and in the present work. The beam column fibre element model used here appears to be capable of simulating the response of the members under blast loading.

The only limitation of this model is that the shear failure cannot be captured. Therefore, it is recommended that a novel methodology to implement the shear failure mode and nonlinearities in this type of elements and models be developed.

5.4.3. Further Research on Roof Beam Response to Blast Loading

- It is suggested that a series of larger scale experimental tests be carried out to study the response of the roof beams to blast loading. The literature in this field, specifically on experimental data, is rather scarce. Conducting a large scale experimental study would be an important step in developing a better understanding of the phenomenon.
- It is also suggested that the analyses of roof beams for their response to blast load be carried out with different end conditions, such as continuous or fixed ends. Also, the accuracy of the current and any suggested equivalent uniform loads should be tested on the beams with different end conditions.
- The computer code developed as part of this thesis can be updated to include various parameters such as different end conditions and also continuity of the members. Another recommendation in this regard is to implement strain-rate effects and strain hardening in the analysis.

5.4.4. Further Research on Global Response of Buildings to Blast Loading

- The approach used in the global analysis carried out as a part of this study, can be applied to different buildings with various heights, different materials, and different lateral load resisting systems. Such research could provide useful insight into the global effects of blast loading.
- In general, due to the eccentricity of the blast source with respect to the building, or irregularity in the building geometry, stiffness and mass, the blast loads may cause torsion in the buildings. Depending on the irregularities mentioned, the magnitude of

the torsional moment may be high and may lead to overstress in the lateral load resisting system. These torsional effects were not considered in the current study, since the building was regular, and the blast charges were located at the axis of symmetry of the building. it is recommended that the effects of the torsion caused by aforementioned sources be studied.

- There still exist some doubts regarding the nature and magnitude of loading of the buildings due to blast, specifically in the distribution of the loads between the floor levels and the columns. Therefore, it is suggested that more detailed simulations be carried out using high fidelity finite element models, or/and large scale experimental tests to obtain a better understanding of the situation.

References

- Abladey, L., and Braimah, A. 2014. Near-field Explosion Effects on the Behaviour of Reinforced Concrete Columns: A Numerical Investigation, *International Journal of Protective Structures*: 5(4), 475–500.
- ACI. 2014. Report for the Design of Concrete Structures for Blast Effects, ACI Committee 370 Report, 1st Printing, ISBN: 978-0-87031-898-6, USA.
- ASCE. 2010. Design of Blast Resistant Buildings in Petrochemical Facilities, ASCE Task Committee on Blast Resistant Design, 2nd Edition. Reston, Virginia, USA.
- ASCE/SEI. 2010. Minimum Design Loads for Buildings and Other Structures, ASCE/SEI 7-10 Standard. 3rd Printing. USA.
- Atkinson, G.M. 2009. Earthquake Time Histories Compatible with the 2005 NBCC Uniform Hazard Spectrum, *Canadian Journal of Civil Engineering*.
- Biggs, J.M. 1964. Introduction to structural dynamics, McGraw-Hill, New York, USA.
- Burrell, R. P., Aoude, H. and Saatcioglu, M. 2014. Response of SFRC Columns under Blast Loads. *J. of Str. Eng. ASCE*. DOI: 10.1061/(ASCE)ST.1943-541X.0001186.
- Canadian Standards Association (CSA). 2004. CAN CSA A23.3-04 Design of concrete structures. Rexdale, Ontario.
- Chang, G.A., and Mander, J.B. 1994. Seismic Energy Based Fatigue Damage Analysis of Bridge Columns: Part 1 – Evaluation of Seismic Capacity. NCEER Technical Report No. NCEER-94-0006. State University of New York, USA.
- Crawford, J. E., Morrill, K. B., and Magallanes, J. M. 2014. Protective Design for Columns against Close-in Blast Effects. *Structures Congress, ASCE*. 131–142.

- Crawford, J. E. and Morrill, K. B. 2015. Failure Modes for RC Columns Subjected to Blast Loadings that Must Be Considered in Design. 11th International Conference on Shock & Impact Loads on Structures. Ottawa, Canada.
- DoA (US Department of the Army). 1986. Fundamentals of Protective Design for Conventional Weapons, TM 5-855-1, USA.
- DoD (US Department of Defense). 2008. Structures to Resist the Effects of Accidental Explosions, UFC 3-340-02 (TM 5-1300, NAVFAC P-397, AFR 88-22), USA.
- DoD (US Department of Defense). 2009. Design of Buildings to Resist Progressive Collapse, UFC 4-023-03 (Changes applied in 2013), USA.
- Ebeling, R.M., Green, R.A. and French, S.E. 1997. Accuracy of response of single degree of freedom systems to ground motion. Technical Report ITL-97-7. U.S. Army Engineer Waterways Experiment Station. USA.
- El-Dakhakhni, W. W., Changiz Rezaei S. H., Mekky W. F. and Razaqpur A. G. 2009. Response sensitivity of blast-loaded reinforced concrete structures to the number of degrees of freedom. Canadian Journal of Civil Engineering 36(8): 1305-1320.
- El-Dakhakhni, W. W., Mekky, W. F., & Changiz-Rezaei, S. H. 2009. Vulnerability Screening and Capacity Assessment of Reinforced Concrete Columns Subjected to Blast. Journal of Performance of Constructed Facilities, ASCE. 23(5), 353-365. DOI: 10.1061/(ASCE)CF.1943-5509.0000015.
- Filippou, F. C., Popov, E. P. and Bertero, V. V. 1983. Effects of Bond Deterioration on Hysteretic Behavior of Reinforced Concrete Joints. Report EERC 83-19. Earthquake Engineering Research Center. UC Berkeley, USA.

- Glasstone, S. and Dolan, P. J. 1977. The Effects of Nuclear Weapons, 3rd Edition, Energy Research and Development Administration, USA.
- Hognestad, E. 1951. A study on combined bending and axial load in reinforced concrete members. Engineering Experiment Station. Univ. of Illinois at Urbana-Champaign, IL. pp. 43-46.
- Humar, J. L. 2012. Dynamic of Structures, 3rd edition, CRC Press/Balkema, Taylor and Francis Publication, London, UK.
- Jan, S. F. and Gurbuz, O. 2008. Dynamic Nonlinear Finite Element Analysis of Blast Resistant Concrete Buildings in Petrochemical Facilities, Proceedings of Structures Congress 2008, ASCE Research Library, USA.
- Luccioni, B. M., Ambrosini, R.D. and Danesi, R.F. 2004. Analysis of Building Collapse under Blast Loads. Engineering Structures. volume 26, pp. 63-71. Elsevier.
- Magnusson, J. 2007. Structural concrete elements subjected to air blast loading. Licentiate thesis in KTH, Department of Civil and Architectural Engineering. Sweden.
- Mays, G.C. and Smith, P.D. 1995. Blast effects on buildings. Thomas Telford Publication. UK.
- McClendon, M. A. 2007. Blast Resistant Design for Roof Systems. MSc. Dissertation. University of Missouri-Columbia, USA.
- Nassr, A. A., Razaqpur, A. G., Tait, M. J., Campidelli, M., and Foo, S. 2012. Single and multi-degree of freedom analysis of steel beams under blast loading. Nuclear Engineering and Design, 242, 63–77. DOI: 10.1016/j.nucengdes.2011.10.020.

- Nassr, A. A., Asce, A. M., Razaqpur, A. G., Tait, M. J., Campidelli, M., and Foo, S. 2013. Dynamic Response of Steel Columns Subjected to Blast Loading. *J. of Str. Eng. ASCE*, 1–15. DOI: 10.1061/(ASCE)ST.1943-541X.0000920.
- Neuenhofer, A. and Filippou, F. C. 1997. Evaluation of nonlinear frame finite-element models. *Journal of Structural Engineering*, 123(7): 958–966.
- National Research Council of Canada (NRCC). 2010. National building code of Canada. Associate Committee on the National Building Code. Ottawa, ON.
- Prakash, V., Powell, G. and Campbell, S. 1993. DRAIN 2D User Guide V 1.10. University of California at Berkeley, CA.
- Razaqpur, A.G., Mekky, W.F., Tolba, A.F., El-Dakhakhni, W.W., Foo, S. and Contestabile, E. 2007. Numerical analysis of the response of blast loaded GFRP retrofitted concrete slabs. *Proceedings of the 1st Specialty Conference on Disaster Mitigation*. Calgary, AL.
- Saatcioglu, M. Ozbakkaloglu, T. Naumoski, N. and Lloyd, A. 2009. Response of Earthquake-Resistant Reinforced-Concrete Buildings to Blast Loading. *Canadian Journal of Civil Engineering*. 36(8), 1378–1390. DOI: 10.1139/L09-089.
- Saatcioglu, M., Lloyd, A., and Jacques, E. 2011. Focused Research for the Development of a CSA Standard on Design and Assessment of Buildings Subjected to Blast Loads. Hazard Mitigation and Disaster Management Research Centre Publication, Univ. of Ottawa, Ottawa.
- Smith, S. McCann, D. and Kamara, M. 2009. Blast Resistant Design Guide for Reinforced Concrete Structures, Report EB090. Portland Cement Association, USA.

- Smith, P. D. and Hetherington, J. G. 1994. Blast and Ballistic Loading of Structures, Butterworth-Heinemann Ltd., Oxford, UK.
- Smith, R.S.H. and Tso, W.K. 2002. Inconsistency of force-based design procedure. Journal of Seismology and Earthquake Engineering (JSEE): 4(1). pp. 47-54.
- Swisdak, M.M.J. 1994. Simplified Kingery Airblast Calculations. Proceedings of the 26th Department of Defense (DoD), Explosives Safety Seminar, Miami, USA.
- Tadepalli, T. and Mullen, C. 2008. Design Parameters Governing Performance of Proceedings of Structures Congress 2008, ASCE Research Library.
- US Army Corps of Engineers (USACE). 2010, Conventional Construction Standoff Distances for the Low and Very Low Levels of Protection. PDC Technical Report 10-01. USA.